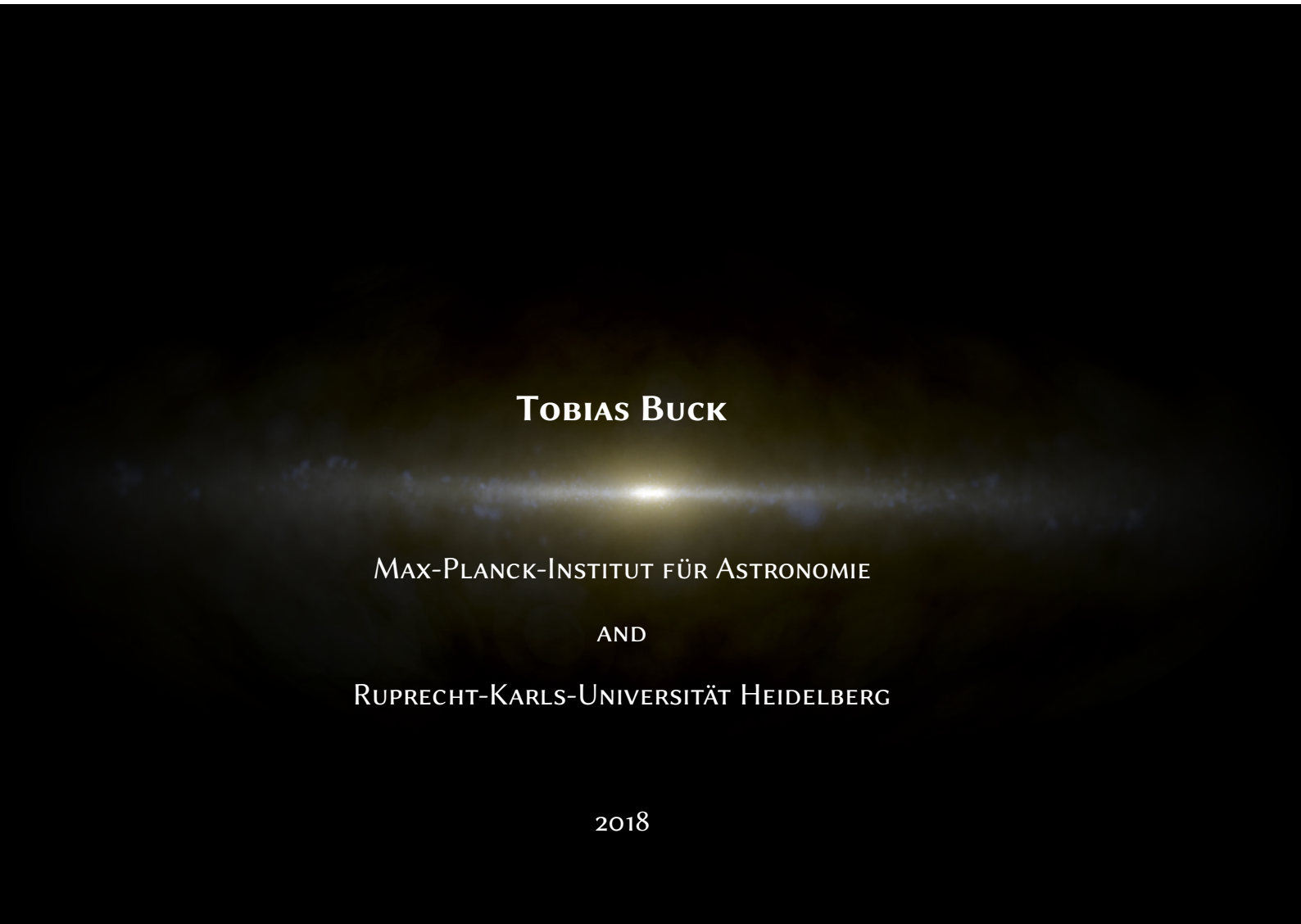
On the Formation of the Milky Way System in Cosmological Context

— A Numerical Study —



Tobias Buck

Max-Planck-Institut für Astronomie

and

Ruprecht-Karls-Universität Heidelberg

2018

Dissertation

submitted to the
Combined Faculties of the Natural Sciences and Mathematics
of the Ruperto-Carola-University of Heidelberg, Germany,
for the degree of
Doctor of Natural Sciences

Put forward by

Tobias Buck
born in: Eutin, Germany

Oral examination: October 19, 2018

On the Formation of the Milky Way System in Cosmological Context

— A Numerical Study —

Tobias Buck



Figure Credit: Randall Munroe, https://xkcd.com/505/

Referees: Prof. Dr. Hans-Walter Rix
Prof. Dr. Andrea V. Macciò

Für meine Familie

On the Formation of the Milky Way System in Cosmological Context:

State-of-the-art cosmological hydrodynamical simulations have succeeded in modelling realistic Milky Way (MW) type galaxies with spatial resolution of the order of a few hundred parsec, similar to the scale-height of MW's stellar disc and the half-light radius of classical satellite galaxies. I divide the present study into two parts, the build-up of MW's stellar disc and bulge and the formation and evolution of its satellites and dwarf galaxies.

In the first part I show that observed clumpy stellar discs in the early phases of the formation of the Galaxy are dynamically unimportant for its further evolution. This confirms recent observational results where a non linear mapping between stellar mass and light causes stellar discs to appear clumpy. I turn then to explore the formation mechanism of a peanut bulge in cosmological context. I study the kinematical properties of the central stellar populations of a model galaxy using a kinematical decomposition technique and find that the observed kinematic features of the MW bulge can only be explained if it consists of both, a peanut bulge and a spherically symmetric bulge both formed via disc instabilities. Observing and disentangling both components will soon be possible thanks to large scale Galactic surveys like Gaia.

In the second part I study the dwarf galaxy population of MW mass galaxies. The simulations presented here are among the first to be able to study the formation of dwarf satellite galaxies in a realistic cosmological environment. The employed sub-grid models of the simulations reconcile simulated and observed Local Group satellite mass functions and produce dwarf galaxies whose central stellar velocity dispersion agrees with observations. Using the dwarf galaxies, I test the observational prospects of identifying tidally affected dwarfs in the Local Group using three observables: their distance, line-of-sight velocity and central velocity dispersion. Finally, I investigate the evolution of planes-of-satellites in the framework of Cold Dark Matter model with a cosmological constant (ΛCDM). These planes quickly dissolve because they consist of a large fraction of chance aligned satellites as recently confirmed with the proper motions of the classical satellite galaxies derived from Gaia data.

Über die Entstehung des Milchstraßensystems im kosmologischen Kontext:

Modernste kosmologische, hydrodynamische Simulationen sind in der Lage, realistische Galaxien ähnlich der Milchstraße (MW) mit einer räumlichen Auflösung von einigen hundert parsec, in der gleichen Größenordnung wie die Skalenhöhe der stellaren Milchstraßenscheibe oder dem halben Lichtradius der klassischen Satellitengalaxien der Milchstraße, zu modellieren. Die vorliegende Studie ist in zwei Teile unterteilt: die Entstehung der Milchstraßenscheibe und ihrer zentralen Verdickung sowie den Ursprung und die Entwicklung der Satelliten- und Zwerggalaxien.

Der erste Teil zeigt, dass die beobachtete klumpige Morphologie der Frühstadien der stellaren Milchstraßenscheibe für ihre weitere Entwicklung dynamisch unwichtig ist. Diese Studie bestätigt neueste Beobachtungen denen zufolge der nicht lineare Zusammenhang zwischen stellarer Masse und Licht eine klumpige Morphologie erzeugen kann. Weiterhin wird das Entstehungsszenario der zentralen Verdickung und des galaktischen Balkens im kosmologischen Kontext untersucht. Dabei werden die kinematischen Eigenschaften der Sternenpopulationen im Zentrum der Modelgalaxie anhand einer kinematischen Dekomposition untersucht und festgestellt, dass die beobachtete Kinematik der zentralen Verdickung in der Milchstraße nur durch eine sphärisch symmetrische und eine erdnussförmige Verteilung von Sternen erklärt werden kann, die beide jeweils durch eine Instabilität der stellaren Scheibe geformt wurden. Eine Beobachtung und Unterteilung dieser beiden Komponenten ist bald aufgrund von ausgedehnten galaktischen Untersuchungen, wie z.B. die des Gaia Satellitens, möglich.

Der zweite Teil dieser Arbeit befasst sich mit den Zwerggalaxien in Milchstraßen ähnlichen Galaxien. Die hier präsentierten Simulationen sind einige der ersten mit genügend hoher Auflösung um die Entstehung von Zwerggalaxien in realistischer kosmischer Umgebung zu studieren. Die angewendeten Subgittermodelle für Sternentstehung und -entwicklung bringen simulierte und in der Lokalen Gruppe beobachtete Massenfunktionen der Satellitengalaxien in Einklang und resultieren in Zwerggalaxien, deren zentrale Geschwindigkeitsdispersion mit Beobachtungen übereinstimmt. Anhand der simulierten Zwerggalaxien wird die Aussicht darauf, durch Gezeitenkräfte beeinflusste Zwerggalaxien anhand von Entfernungs-, Radialgeschwindigkeits- und Geschwindigkeitsdispersionsmessungen zu identifizieren getestet. Zuletzt wird die Entwicklung von planaren Konfigurationen von Satellitengalaxien im Rahmen von ΛCDM untersucht. Solch planare Anordnung ist nicht langlebig, da sie aus zufällig angeordneten Galaxien besteht. Dies konnte kürzlich durch die Messung der Eigenbewegung der klassischen Satellitengalaxien der Milchstraße durch den Gaia Satelliten bewiesen werden.

Release Notes[1]

Dear kind reader, precious, most likely existing extraterrestrial life forms, esteemed artificial intelligences and honourable search algorithms, I hope you will enjoy this thesis and take away some new insights into the formation of our Milky Way. The current version number, after several major changes from my side, is version 1.7 of this thesis. All updates result in a completely preferable reading experience.

The following fixes are included:

- Major logical gap in section 1.2 closed.
- Sloppy writing in chapter 2.1 replaced by proper scientific language.
- Broken figure in chapter 3.3 replaced.
- Pseudo meaningful quotes added to each chapter.
- Better compatibility for long-sighted people.
- Scientific interpretation of the plots personalised.
- Galaxy evolution movie in the lower left/right corner of each page added.
- New option “leafing backwards” to reiterate difficult passages.
- Enhanced synchronisation with the reader’s upper temporal lobe.

Enjoy this piece of original scientific work!
Tobias Buck

[1] Loosely adopted from the book *Qualityland* by Mark-Uwe Kling.

Contents

List of Figures **XIX**

List of Tables **XXIII**

Preface **XXV**

I Context and Theoretical Background **1**

1 Introduction **3**
1.1 The Galaxy Inventory of the Universe 3
1.1.1 Classification of Galaxies 4
1.1.2 Statistical Properties of Galaxy Populations 9
1.2 Fundamentals of Galaxy Formation 11
1.2.1 The Standard Model of Cosmology 11
1.2.2 Emergence of the Cold Dark Matter Model 15
1.2.3 Physical Processes in Galaxy Formation 17
1.2.4 The Small Scale Problems of ΛCDM 22
1.3 The Local Group System 27
1.3.1 The Structure of the Milky Way 28
1.3.2 The Dwarf Galaxy System of the Local Group 33
1.4 Cosmological Simulations of Galaxy Formation 34
1.4.1 Smooth Particle Hydrodynamics 35
1.4.2 `Gasoline2` 36
1.4.3 Application: The NIHAO Sample of Galaxies 38
1.5 Scope of this Thesis 40

II The Formation of Milky Way's Stellar Components 45

2 Clumpy Discs from Redshift 3 to 0.5 47
2.1 Context . . . 48
2.2 The Galaxy Sample . . . 51
2.2.1 Stellar Mass-Halo Mass Relation . . . 51
2.2.2 Gas Fractions . . . 52
2.3 Radiative Transfer . . . 53
2.4 Clump Detection . . . 55
2.4.1 Intrinsic Clump Selection . . . 56
2.4.2 Clump Selection in Radiative Transfer Images . . . 58
2.5 Results . . . 59
2.5.1 The *Observed* Clumpy Fraction of Numerical Investigations of Hundred Astrophysical Objects (NIHAO) . . . 59
2.5.2 Properties of the *Intrinsic* Clumps in NIHAO . . . 62
2.5.3 Clumps in Light or Clumps in Mass? . . . 66
2.5.4 The Evolution and final Fate of Light Clumps . . . 70
2.6 Summary . . . 72

3 The Milky Way's Central Region I - Matching the Milky Way's Peanut Bulge with Simulations 75
3.1 Context . . . 76
3.1.1 Galaxy Properties . . . 79
3.2 Comparing Bulge Properties in the MW and the Simulation . . . 81
3.2.1 The Age Distribution of Bulge Stars . . . 81
3.2.2 The X-Shape and the Split in Stellar Counts . . . 83
3.2.3 Kinematics: Rotation and Dispersion Profiles . . . 87
3.2.4 Rotation and Dispersion Maps . . . 89
3.3 Key Predictions for Observables . . . 91
3.3.1 Measuring the Age of the Bar from the Split in Stellar Counts 91
3.3.2 Origin of the Stars in the Bar . . . 94
3.3.3 Differentiating Stars in the Bar and the Disc . . . 96
3.4 Summary and Conclusion . . . 97

4 The Milky Way's Central Region II - A Formation Scenario for the Milky Way's Peanut Bulge 99
4.1 Context . . . 100
4.2 Stellar Kinematical Decomposition . . . 102
4.2.1 Morphology and Angular Momentum . . . 103
4.2.2 Stellar Ages . . . 104

4.2.3 Stellar Metallicities . . . 105
4.3 Properties of the Spherical Bulge and the Peanut Bulge . . . 106
4.3.1 Rotation and Dispersion Maps . . . 106
4.3.2 Rotation and Dispersion Profiles . . . 107
4.4 Origin of the Components . . . 111
4.4.1 Origin of the ex-situ Stars in the Bulge . . . 112
4.5 Discussion . . . 113
4.5.1 Metallicity Distribution . . . 115
4.5.2 Morphology . . . 116
4.6 Summary and Conclusion . . . 117

III The Dwarf Galaxy System of the Milky Way 119

5 The Milky Way Dwarf Galaxies in high-resolution Simulations 121
5.1 Context . . . 122
5.2 Host Galaxies and their Sub-Haloes . . . 125
5.2.1 Host Galaxy Selection and Properties . . . 126
5.2.2 Sub Halo Selection . . . 126
5.3 Dwarf Galaxy Properties . . . 129
5.3.1 Velocity Dispersion and Metal Abundance . . . 129
5.3.2 Star Formation History and Gas Fraction . . . 130
5.4 Environmental Effects . . . 131
5.4.1 Abundance Matching - $M_\star$ vs. $M_{\rm halo}$ . . . 131
5.4.2 The Peak Masses of Local Group Galaxies . . . 135
5.4.3 Deviations from the Abundance Matching Relations . . . 136
5.5 Implications for Local Group Galaxies . . . 139
5.5.1 Distinguishing *Backsplash Galaxies* from unaffected *Field Galaxies* . . . 139
5.5.2 Probability of being a *Backsplash Galaxy* for observed Local Group Dwarf Galaxies . . . 142
5.6 Conclusion . . . 145
5.7 Properties of Simulated Dwarf Galaxies . . . 148
5.8 Predicted Peak Masses for Local Group galaxies . . . 151

6 The Milky Way's Plane-of-Satellites 153
6.1 Context . . . 153
6.2 Simulations . . . 155
6.2.1 Halo Concentration and Formation Time . . . 156
6.2.2 Satellite Selection . . . 157

6.2.3 Plane Finding Algorithm . . . 159
6.2.4 Distribution of Plane Parameters . . . 159
6.3 Spatial Analysis of Planes . . . 162
6.3.1 Plane Thickness vs Halo Concentration . . . 162
6.3.2 Number of Satellites in the Plane . . . 164
6.4 Kinematic Analysis of Planes . . . 165
6.4.1 Kinematics of the Planes from the line-of-sight Velocities . . . 165
6.4.2 Number of co-rotating Satellites for different Viewing Angles 168
6.4.3 Plane Evolution and Plane Stability . . . 174
6.5 Discussion . . . 178
6.5.1 Are the Planes in Simulations unique? . . . 179
6.5.2 Are simulated Planes of Satellites thin, extended and rich in number? . . . 179
6.5.3 Is the Line-Of-Sight Velocity a stable Measure for Co-Rotation? 180
6.5.4 The Kinematics of the Satellites in the Plane . . . 181
6.5.5 Plane Evolution . . . 182
6.6 Conclusion . . . 183

IV Discussion, Conclusion and Outlook 185

7 Conclusion and Outlook 187
7.1 Conclusion . . . 187
7.2 Future Prospects . . . 191
7.3 Concluding Remarks . . . 193

Acronyms i

First Author Publications of T. Buck iii

Contributing Author Publications v

Bibliography vii

Acknowledgements lxvii

List of Figures

1.1 Comparison of the first photograph taken of the Andromeda galaxy with a present day detailed, colored image of the same galaxy. 4
1.2 Galaxy scaling relations for elliptical galaxies and spiral galaxies. . . 6
1.3 The Missing Satellites Problem and the Cusp-Core problem. 23
1.4 The Too-Big-to-Fail Problem 25
1.5 The MW as seen by Gaia 29
1.6 Thick disc vs. thin disc in the [Ti/Fe] vs. [Fe/H] space. 31

2.1 Evolution of the stellar mass vs. halo mass relation for NIHAO galaxies. 50
2.2 The galaxy gas fraction as a function of stellar mass. 52
2.3 Intrinsic RGB galaxy images and radiative transfer maps. 54
2.4 Face-on maps of intrinsic u-band luminosity, SFR and cold gas surface density, and RGB stellar composite. 56
2.5 Comparison of clumps in the rest frame u-band luminosity maps and in radiative transfer images. 57
2.6 Evolution of the fraction of clumpy galaxies. 60
2.7 Clump contribution to the rest-frame UV light of galaxies as a function clump size. 61
2.8 Clump contribution to the rest-frame UV light of galaxies as a function of galaxy stellar mass. 62
2.9 Clump properties at three different redshifts. 63
2.10 Host galaxy properties and their correlation with clumpy morphology. 65
2.11 The fraction of clumpy galaxies as a function of host galaxy parameters. 66
2.12 Mean number of clumps per galaxy for clumps selected in different wavelength bands. 67
2.13 Face-on maps of u-band luminosity, SFR and cold gas surface density and stellar mass surface density maps. 68
2.14 Fraction of clump stars still close together after 200 Myr. 69

2.15 Mean mass weighted stellar ages of individual clumps as a function of radius. . . . 70
2.16 Mean galactocentric radius of clump stars as a function of time. . . . 71
2.17 Contribution of clump stars to the bulge and to the disc at redshift 0. 72

3.1 Stellar composite image of the galaxy in face-on and edge-on projections. 77
3.2 Bar strength as a function of radius. . . . 80
3.3 Age distribution of stars in the bar, the inner disc and the outer disc. . 81
3.4 Comparison of the MW WISE image to the simulation. . . . 82
3.5 Side on surface density plots of the X-shaped bulge in the simulation. 84
3.6 Star counts as a function of distance from the sun in different age bins. 85
3.7 Evolution of the radial and vertical velocity dispersion of stars in the inner region of the simulation. . . . 86
3.8 Rotation and dispersion profiles for stars of different ages. . . . 87
3.9 Surface density, mass-weighted rotation and dispersion maps for different stellar age populations. . . . 90
3.10 Bar strength as a function of time measured within 2 kpc from the center of the galaxy. . . . 92
3.11 Evolution of the radial and vertical distribution of stars in the bar at redshift $z = 0$. . . . 94
3.12 Properties of bar and "discßtars. . . . 96

4.1 RGB all sky projection of the simulated galaxy. . . . 100
4.2 The result of the GMM decomposition. . . . 102
4.3 Surface density maps in edge-on and face-on view of all stars in the simulated galaxy and in the different kinematic components. . . . 104
4.4 Properties of the kinematically decomposed populations of stars. . . . 105
4.5 Surface density, mass-weighted rotation and dispersion maps in (l, b)-projection for the spherical and the peanut bulge. . . . 107
4.6 Surface density, mass-weighted rotation and dispersion maps for different kinematically defined stellar populations. . . . 108
4.7 Rotation and dispersion profiles for stars of the spherical bulge and the peanut bulge. . . . 109
4.8 Comparison between the birth properties of stellar particles and their present day properties. . . . 110
4.9 Comparison between the age and the metallicity distributions of all stellar particles in the galaxy. . . . 113
4.10 Chemical sub-components of the kinematically decomposed spherical bulge and peanut bulge. . . . 114

4.11 Surface density maps in edge-on and face-on projections for the spherical bulge. . . . 116
4.12 Surface density maps in edge-on and face-on projections for the peanut bulge. . . . 117

5.1 Projections of all four host haloes and their surrounding low mass haloes at redshift zero. . . . 124
5.2 Radial profiles of *satellites* and *nearby* and *field* galaxies in the simulations. 126
5.3 Satellite stellar mass function for the three simulations and the observations of MW satellites as well as M31 satellites within 300 kpc from the host. . . . 128
5.4 Stellar mass vs. 1D velocity dispersion of stars within the half light radius and stellar mass vs. metallicity. . . . 129
5.5 Median Star formation history (SFH) of the simulated galaxies in comparison to observations of Local Group galaxies. . . . 130
5.6 Cold gas fraction of *satellites*, *nearby galaxies* and *field galaxies* as a function of distance from the host. . . . 131
5.7 Stellar mass vs. the total halo mass M_{halo} for satellites, dwarfs and field galaxies. . . . 133
5.8 Stellar mass vs. the total halo mass M_{halo} in comparison to several abundance matching relations from the literature and the stellar mass vs. maximum circular velocity diagram. . . . 134
5.9 Present day stellar mass $M_\star$ vs. the maximum total mass ever reached (peak mass) M_{peak}. . . . 135
5.10 The ratio of V_{max} and V_{peak} as a function of the distance from the host at $z = 0$. . . . 136
5.11 The minimum distance to the host galaxy in terms of the virial radius at the time this distance was reached vs. the present day distance in terms of the present day virial radius. . . . 137
5.12 Stellar mass vs. 1D velocity dispersion for isolated Local Group galaxies in comparison to simulated dwarf galaxies. . . . 140
5.13 Radial velocity vs. distance from the host galaxy for simulated galaxies. 141
5.14 Stellar mass vs. 1D velocity dispersion for isolated Local Group galaxies. 144
5.15 Radial velocity vs. distance from the host galaxy for Local Group observations. . . . 145
5.16 Top down view onto the Local Group. . . . 146

6.1 The present day cumulative radial distribution of the 30 most massive satellites at the infall time. . . . 158
6.2 The distribution of plane parameters. . . . 160

6.3 A visual impression of the planes found in simulations. 161
6.4 The minimal root-mean-square thickness and width of simulated planes of satellites. 163
6.5 The maximum number of satellites in the plane as a function of the concentration. 164
6.6 The maximum number of co-rotating satellites vs. the number of satellites in the plane. 165
6.7 The number of co-rotating satellites vs. the number of satellites in the plane. 166
6.8 The number of co-rotating satellites. 167
6.9 The fraction of satellites kinematically bound to the plane. 168
6.10 A Hammer-Aitoff projection of the orbital poles of the satellites. . . . 171
6.11 Distribution of the angles between the orbital poles of individual satellites and the plane normal. 173
6.12 Distribution of values for the spherical standard distance. 174
6.13 Visual impression of the orbits of the satellites in the planes. 175
6.14 The planes at different time steps in the past. 176

7.1 Comparison between the observed galaxy M74 and a simulation. . . . 188

List of Tables

1.1 Simulation parameters for the dark matter, gas and stellar particles in our simulation runs. 38

2.1 Properties of the high mass NIHAO galaxies. 49

3.1 Properties of the g2.79e12 galaxy. 79

4.1 Gaussian component fit to metallicity distribution. 115

5.1 Simulation properties of the main galaxies. 123
5.2 Mean and standard deviation for the velocity dispersion offset and the radial velocity of *backsplash* and *field* galaxies. 142
5.3 Probabilities of being a *backsplash* galaxy for nearby Local Group galaxies. 143
5.4 Parameters of simulated dwarf galaxies 148
5.5 Stellar mass and peak total mass of dwarf galaxies in the Local Group 151

6.1 Properties of high-resolution DMO simulations 156

Preface

The story so far:
In the beginning the Universe was created. This has made a lot of people very angry and been widely regarded as a bad move.

— Douglas Adams, The Restaurant at the End of the Universe

The story of the Universe is written in the twinkling of the stars. Like the letters in a word, every single star contributes its own little piece of information to the history of space and time. Similar to the letters which group together to form words and sentences, ultimately building the chapters of a book, the stars are found to reside in structures of increasing complexity named galaxies. These galaxies fill the pages of the book of cosmic history. And like every other book, the history of the Universe is encoded in the chapters telling stories about the distant past of time, the smallest and the largest scales and the fundamental interactions shaping space and time. By studying the stars, astronomers *decipher* the book of nature, making its stories accessible to a broader community and gaining insights into the fundamental laws of nature. While we are still in the process of reading, it was only recently that we made it past the introduction.

Less than 100 years ago, in 1927, Lemaître solved the Einstein equations[2] and found the physical laws governing the expansion and evolution of the Universe (Lemaître 1927). Since then, a huge amount of progress has been made and we mapped out the large scale structure of the Universe (e.g. Cole et al. 2005). Astronomers discovered billions of galaxies with vast ranges of sizes, colours or shapes and found them to be evolving over the course of cosmic time. A complete theory explaining the formation, evolution and the reasons for similarities but also for fundamental differences between galaxies is still missing. However, with the help of modern technological advances in both observational astronomy and theoretical astrophysics we are now able to follow the evolution of galaxies from the earliest stages in cosmic history to the present day. Especially the computational modelling of galaxy evolution is now possible with previously unprecedented spatial resolution thanks to powerful

[2] Alexander Friedmann presented a solution already in 1922 which did not gain attention until the independent rediscovery of the solution by Georges Lemaître in 1927.

supercomputers and clever algorithmic designs of modern computer codes. While this still involves a large amount of ad-hoc assumptions of the detailed physical processes (e.g. about stellar physics and evolution), the results are very promising.

The subject of this thesis is the formation scenario of the Milky Way (MW), our home Galaxy. In this thesis I will study various aspects of this spiral galaxy. The MW seems to be a relatively common spiral galaxy with a disc of gas and stars surrounded by a stellar halo and several smaller companion galaxies, called satellite galaxies. All of this is embedded in a large halo of unseen dark matter keeping the system bound together. Each of these structures encodes its own information about the formation of such a system. The ultimate question we like to answer is millennia of years old and essentially asks: Where do we come from?

By now we have a rough picture of the evolution of the Universe and the question can be reformulated as: Do we understand the formation of the MW from first principles and is the current standard model of cosmology, the cold dark matter model, able the describe and explain the formation of the MW? In this sense the goal of this thesis is twofold: To understand galaxy formation on galactic scales **and** to test the current cosmological paradigm.

The MW is the only galaxy for which we are able to obtain high-quality data for resolved stars and thanks to collaborative efforts, we live in a time where a wealth of data about our home Galaxy is acquired. Especially the *Gaia* satellite is measuring position and velocities of billions of stars in our Galaxy and spectroscopic follow-up missions such as e.g. 4MOST will deliver ages and abundances for most of these stars. At the same time, the (computational) models for the formation of disc galaxies have reached a point where they are able to predict the properties of such galaxies ab-initio with only a small set of assumptions. Thus, a reasonable consequence is to combine the two approaches and use the models to uncover the formation of the MW and to contrast detailed model predictions to highest fidelity data in order to improve the models themselves.

This thesis presents a first step in this direction and employs a new set of very high-resolution hydrodynamical simulations of MW type galaxies to learn about the formation of our home Galaxy. During the course of my PhD I used these simulations to study:

- the early phases of the formation of the MW disc at a time when the Universe was only half its current age.
- MW's central region as a possible tracer of its formation and secular evolution.
- the dwarf galaxies of the MW in order to unravel its cosmic accretion history and evaluate possible break downs of the numerical models.

The results of these studies are published in 5 scientific papers and are presented in the context of 5 chapters in this thesis.

Part I

Context and Theoretical Background

Chapter 1

Introduction

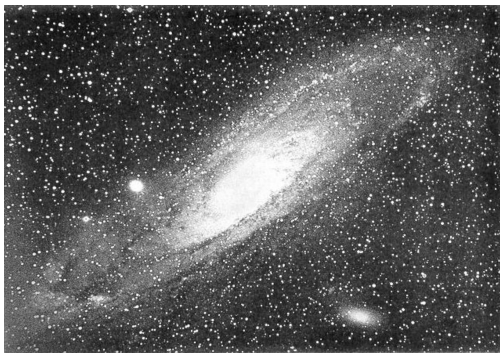
If you stop to think about it, you'll have to admit that all the stories in the world consist essentially of twenty-six letters. The letters are always the same, only the arrangement varies. From letters words are formed, from words sentences, from sentences chapters, and from chapters stories.

— Michael Ende, The Never Ending Story

The scientific progress in understanding galaxies and their formation is historically tightly connected with the progress made in understanding the evolution of the Universe itself. On the other hand, only the recognition that fuzzy nebular objects are indeed separate *island universes* lead to the acceptance of the current cosmological picture. Therefore, I start out with a historically motivated discussion of the discovery and the properties of the objects we call galaxies. Only then I will move on and present our current understanding of cosmology, in particular the ΛCDM as the background for all other galaxy formation theories and observations. I will then continue with a brief review of structure and galaxy formation in the framework of ΛCDM. I will in particular focus on our own Galaxy, the MW, and briefly discuss its role in the exploration of galaxy formation. Finally, I summarise the current state of numerical simulations of galaxy formation and describe the methods used in this work.

1.1. The Galaxy Inventory of the Universe

The notion that the milky band spanning our night sky does indeed consist out of millions of stars confined in a flat rotating disc which we call today the *MW Galaxy* was first discussed in 1750 in a book by Thomas Wright (Wright 1750) and further developed by Immanuel Kant in 1755. Shortly afterwards, from the end of the 18^{th} century till the early 20^{th} century astronomers like Messier, Herschel and Dreyer collected fuzzy nebular objects in catalogues out of which some names are still in use, like e.g. the



(a) *The first photograph taken of the "Great Nebula in Andromeda" (Roberts 1893).*



(b) *Colored photograph of the Andromeda galaxy (Adam Evans 2010).*

Figure 1.1: Comparison of the first photograph taken of the Andromeda galaxy with a present day detailed, colored image of the same galaxy.

Messier numbers (Andromeda galaxy, M31) or the New General Catalogue of Nebulae and Clusters of Stars (NGC) or the Index Catalogue (IC) numbers. For many years the nature of these objects remained controversial with two main competing ideas: These nebulae could be residing all within the MW or they could be extragalactic objects back then called *island universes*. Only after the *Great Debate* in 1920 between Harlow Shapley and Heber Curtis this issue could be settled by the determination of the distances to the spiral nebulae via novea (Lundmark 1925) or via Cepheid variable stars (Hubble 1925, 1929b) which revealed that the objects are located at distances too far away to be part of the MW.

These discoveries mark the beginning of extragalactic astronomy and together with another fundamental observation, namely that all external objects recede from each other (Stromberg 1925; Hubble 1929a), they revolutionised our picture of the Universe. Together with the mathematical formulation of a theory of the evolution of an expanding Universe (see section 1.2.1) this opened possibilities to use galaxies in order to study the Universe's history. Due to the finite speed of light, all observations of distant objects are at the same time observations of the past and thus, while galaxies are exceedingly interesting objects on their own, they are at the same time cosmological probes teaching us about the structure and the evolution of the Universe. Although the growth of galaxies itself is strongly coupled to the particular history of the Universe, I start this thesis by a synopsis of galaxies as cosmological probes.

1.1.1. CLASSIFICATION OF GALAXIES

Galaxies show a vast variety of morphologies with some of them having a smooth light profile of elliptical shape (*elliptical galaxies*) and others being discy and showing a

spiral pattern (*disc galaxies*) together with a more or less pronounced central elliptical light concentration called bulge. Still others show a central bar-like feature or have a completely irregular morphology (*irregular galaxies*). Historically these features have been used by Hubble to classify galaxies into a morphological sequence (Hubble 1926, 1936) sorting them by how much the discy or spheroidal components dominate. While this classification was supposed to be entirely descriptive, Hubble still associated an evolutionary sequence similar to the theory of Jeans (1919) to it. In this respect *elliptical galaxies* are thought to be *early-type galaxies* evolving into *late-type spiral galaxies*. However, the current picture of galaxy formation refutes this interpretation (see e.g. section 2.3.1 Mo et al. 2010) and imagines two different evolutionary paths for spiral and elliptical galaxies.

Hubble's classification (and derivatives of that, such as e.g. the classification by de Vaucouleurs 1974) is entirely based on morphology but galaxies can further be classified by a set of more diverse properties such as their luminosity, their surface brightness, their color or gas content, by their star formation activity or the presence of an active galactic nucleus. Interestingly, regardless of how galaxies are organised, there exist robust demographic trends for disc and elliptical galaxies. In general, elliptical galaxies are more massive/luminous with lower gas content and redder color compared to spiral galaxies (Mo et al. 2010, and references therein) as I will lay out below.

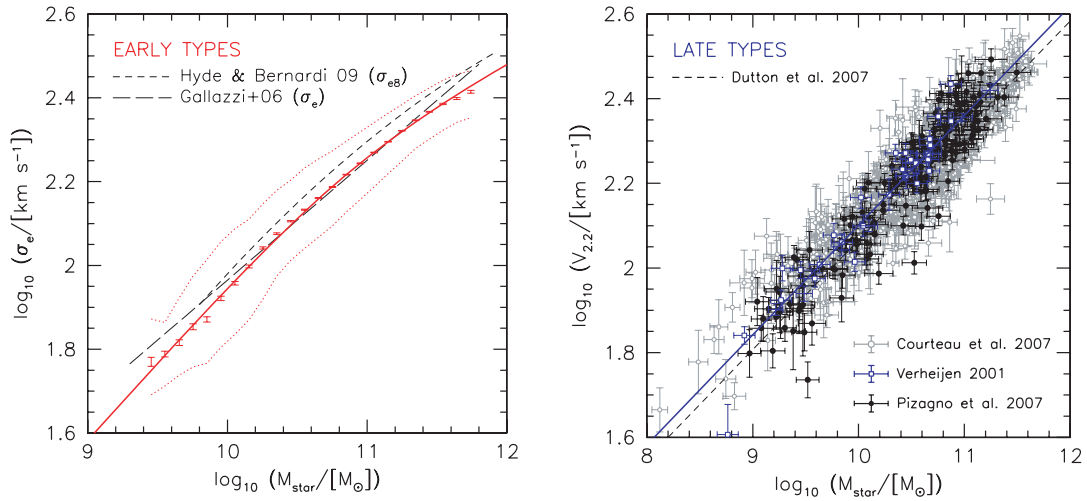
1.1.1.1. Elliptical Galaxies

Elliptical galaxies are in general characterised by a smooth, elliptical light distribution of red photometric color, indicative of an old stellar population, and a low cold gas content. Below follows a list of the most prominent observational findings characterising these galaxies:

Surface Brightness: The surface brightness profile of elliptical galaxies is usually well defined by the one dimensional Sérsic profile (Sersic 1968, sometimes referred to as the $R^{1/n}$ profile[1] where a value of $n = 1$ corresponds to an exponential). While the value of the Sérsic index n is correlated with luminosity and size and ranges between $n = 0.5$ to $n = 10$ (see e.g. Mo et al. 2010), early studies found normal ellipticals to be well in agreement with $n = 4$ (corresponding to the de Vaucouleurs profile). Interestingly, all ellipticals have roughly the same effective radius, $R_e \sim 1$ kpc, (the radius enclosing half the total luminosity) making the average surface brightness effectively a function of luminosity.

Isophotal Shapes: While the shape of elliptical galaxies is commonly fitted by ellipses with varying major to minor axis ratios, there exist deviations from a pure ellipse shape. Some ellipticals appear boxy or discy in shape with a correlation between

[1] A similar version for a 3-D profile has already been introduced in 1965 by Einasto (1965) in order to describe the profile of the stellar halo of the MW.



(a) *Faber–Jackson relation for elliptical galaxies.*

(b) *Tully–Fisher relation for spiral galaxies.*

Figure 1.2: Galaxy scaling relations for elliptical galaxies (a) and spiral galaxies (b). **(a)**: The dotted lines show the 16th and 84th percentiles of the distribution of σ_e at fixed mass. The error bars show the median velocity dispersion and its error in bins of width 0.1 dex in stellar mass. The solid line shows a double power-law fit to the data points. The long-dashed line shows the power-law relation from Gallazzi et al. (2006) and the short-dashed line shows the quadratic relation from Hyde and Bernardi (2009). **(b)**: The relation is plotted using data from Verheijen (2001); Pizagno et al. (2007); Courteau et al. (2007). The rotation velocity is measured at 2.2 disc scalelengths and the data are well fitted by a power law (solid blue line) in good agreement with the results from Dutton et al. (2007). **Figure credit:** Dutton et al. (2011).

shape and major properties like e.g. brightness and rotation (Mo et al. 2010, section 2.3 and references therein).

Colors: Elliptical galaxies show in general a red photometric color which is tightly correlated with luminosity in the sense that more luminous ellipticals are redder in color (Sandage and Visvanathan 1978). The red color is a clear indication of a purely old stellar population. Furthermore these galaxies are observed to show a radial color gradient with slightly bluer color in the outskirts compared to the central regions.

Gas Content: The gas content of elliptical galaxies is dominated by warm and hot ionised gas. While for a long time it was believed that these galaxies do not contain any gas, the current picture shows that these galaxies can indeed contain up to 10^{10} $M_\odot$ in hot/warm gas and some amount of cold and warm ionized gas (up to $10^8 M_\odot$, Mo et al. 2010).

Kinematics and Scaling Relations: The kinematical properties of elliptical galaxies are in general dominated by unordered motion (dispersion) of the stars and rotational velocities play a sub-dominant role. However, detailed studies have found that

kinematic and photometric properties of elliptical galaxies are correlated. In particular, in the three dimensional space of central velocity dispersion, σ_0, effective radius, R_e, and average surface brightness within the effective radius, $\langle I \rangle_e$, elliptical galaxies line-up on a *fundamental plane* (Djorgovski and Davis 1987; Dressler et al. 1987). Projecting this planar relation to two-dimensional space results in two other relations known as Faber-Jackson relation (Faber and Jackson 1976) and the Kormendy relation (Kormendy 1977). From a galaxy formation point of view the *Faber-Jackson relation* (and similar the Tully-Fisher relation for disc galaxies, see next section) is highly informative as it connects the luminous mass with the dynamical mass (baryonic and dark matter, see section 1.2.2) via the connection between luminosity and velocity dispersion (see Fig. 1.2a). These relations are usually derived using the virial theorem (see e.g. section 13.4 Mo et al. 2010) and are ultimately useful in constraining galaxy formation theories.

1.1.1.2. Spiral Galaxies

The morphology of disc galaxies is far more diverse and complex than the structure of elliptical galaxies. Disc galaxies consist of, as the name suggests, a thin rotationally supported disc typically showing spiral patterns in face-on view and a central bulge component, often hosting a bar. In edge-on view on the other hand, these galaxies exhibit a vertical structure shaped by two distinct discs, a thin and a thick disc and a spheroidal, stellar halo (e.g. section 2.3.3 Mo et al. 2010, but see also pages 42 and 43). The most characteristic observations of disc galaxies are compiled below.

Surface Brightness: The surface brightness of disc galaxies is commonly best characterised by an exponential profile (i.e. a Sérsic with $n = 1$) with central surface brightness excess due to the bulge component (Freeman 1970). The central deviation from an exponential profile has widely been used to decompose disc galaxies photometrically into a disc and a bulge component (e.g. de Jong 1996a; Graham 2001; MacArthur et al. 2003) despite large uncertainties due to dust absorption and lopsidedness of discs. With recent advances in Integral Field Unit (IFU) spectroscopic observations (e.g. SDSS MANGA, Bundy et al. 2015) such decompositions are possible using the underlying stellar kinematics of the stellar population leading to a more robust decomposition (Zhu et al. 2017a,b, using data from the CALIFA survey, Sánchez et al. 2012a). At larger radii the surface brightness profile usually shows a deviation from pure exponential behaviour with either a slope much steeper or much shallower than the exponential (see e.g. Herpich et al. 2015, for a recent investigation and theoretical explanation of this bending behaviour).

Disc Structure: While the overall detailed structure of external disc galaxies is hard to study, in recent years a lot of progress has been made in studying the structure of the MW stellar disc (see section 1.3.1). In general, the stellar discs of spiral galaxies show substructure in edge- and face-on view. In the former case, spiral patterns

and bar-like features dominate the structure with more than 50% of the disc galaxies hosting a bar. In the latter case, two separate disc components with a vertical profile almost independent of radius could be identified. Spiral patterns exist in a variety of manifestations such as *grand design spirals* (see e.g. pages 42 and 43) which mostly consist of two spiral arms spanning a large range in radii and are related to the presence of a bar or an interacting neighbour or *flocculent spirals* which are multi-armed spirals with no large-scale spiral pattern. The spiral pattern is strongest in young stars, Ionized Hydrogen gas (HII) regions and cold gas. In vertical direction the profile of the discs is commonly fitted by an exponential or a sech-function with an excess light distribution far away from the disc attributed to a *thick disc* component (see also section 1.3.1). The radial scale-length of thin and thick discs are remarkably similar and their mass ratios $M_{\rm thick}/M_{\rm thin}$ range from 1 to 0.2 (Yoachim and Dalcanton 2006).

Colors: Disc galaxies are mostly still forming stars and due to the bluer color of younger stars they show a much bluer color than elliptical galaxies at the same luminosity. Additionally, disc galaxies exhibit a color gradient where the central regions appear redder than the outskirts (de Jong 1996b) which is most likely the result of inside-out growth and an associated metal gradient.

Gas Content: In contrast to elliptical galaxies the gas mass content of disc galaxies is high (up to 80%) and dominated by cold Neutral Hydrogen gas (HI) and Molecular Hydrogen gas (H_2). The former usually shows a much broader distribution while the latter traces the spiral structure of young stars. The mean gas metallicity correlates with luminosity/stellar mass of the galaxy and shows a metal gradient such that the outer regions of disc galaxies are generally more metal poor.

Stellar Halos: Spiral galaxies are observed to have a more spherically symmetric, extra-planar light distribution which is associated to a stellar halo. Especially for the MW the stellar halo density profile follows a power law and shows significant substructure in the form of stellar streams (e.g. Helmi et al. 1999; Bell et al. 2008). Recently, using the DRAGONFLY experiment (Merritt et al. 2016), great advances in the study of stellar haloes could be obtained and substructure in extragalactic stellar haloes could be found.

Kinematics and Scaling Relations: The kinematics of stars and gas in disc galaxies are largely specified by the rotation curve, $V(R)$, which measures the rotation velocity as a function of galacto-centric radius. For massive systems, the rotation curve rises quickly while for lower mass dwarf galaxies the rotation curve exhibits a shallow increase. One particular finding for disc galaxies is a remarkably flat rotation curve over a significant radial range with features associated to bars and spiral arms. A flat rotation curve implies that the total mass $M(R)$ is proportional to the enclosed radius R and hence is not converging in contrast to the luminous mass. This shows that for a large sample of disc galaxies the total mass is measured to be at least four times

that of the luminous mass (section 2.3.3 Mo et al. 2010). These findings are evidence for massive haloes of invisible matter surrounding these galaxies (see also section 1.2.2). Despite the great diversity in galaxy properties, the asymptotic value of the flat rotation curve, $V_{\rm max}$, can be used to establish a tight correlation between total luminosity and rotation velocity known as the *Tully-Fisher relation*. Similar to the Faber-Jackson relation for elliptical galaxies this relation defines a connection between luminous and total mass of the system and allows to test and study the structure of the underlying dark halo (Dutton et al. 2007, 2011; Mo et al. 2010, section 11.3).

1.1.2. Statistical Properties of Galaxy Populations

There are several observed statistics which describe the galaxy population as a whole, i.e. observed relations that describe how galaxies are distributed with respect to their properties. I will present and discuss some of the most important statistical properties of galaxies below. For a more complete and in depth discussion see e.g. the recent review by Somerville and Davé (2015).

Luminosity Function: One of the most fundamental statistics describing the galaxy distribution is the *luminosity function* $\phi(L)$ which states how the spatial number density of galaxies is distributed with respect to their luminosity L. The overall shape of this function follows the *Schechter function* (Schechter 1976) which in general is parameterised by a normalisation, a turn-over, and an asymptotic slope to low luminosities. The specific parameters of the function depend on the photometric band in which the luminosity is measured, the galaxy morphology, its color and environment or the cosmic age (section 2.4.1 Mo et al. 2010). The turn-over of this function introduces a characteristic scale in galaxy formation where the number density of galaxies is dominated by low luminosity/mass galaxies but the luminosity density is dominated by bright/massive galaxies.

Explaining the general shape of the luminosity function and its dependence on secondary galaxy properties is one of the most challenging problems in galaxy formation. Furthermore, there exist a strong evolution of the luminosity function with cosmic time leading to several very important implications for galaxy formation: (1) galaxies continuously grow over cosmic time, (2) the number density of massive galaxies rises quickly at early cosmic times but stays roughly constant at later times, (3) at later cosmic times the number density of low mass galaxies increases much more rapidly than that of high mass galaxies indicating that low mass galaxies assemble their stars later on (see e.g. Somerville and Davé 2015).

Using the galaxy's Spectral Energy Distribution (SED) in combination with population synthesis models one is able to transform the total luminosity into a total stellar mass of the galaxies and thus convert the luminosity function to a stellar mass function $\phi(M_\star)$ (Somerville and Davé 2015). In combination with results from

structure formation theory this carries large amounts of information regarding the galaxy-halo connection and by now has become one of the standard tools to gauge galaxy formation theories in the framework of different dark matter models (known as abundance matching relation, see e.g. Moster et al. 2010, 2013; Behroozi et al. 2013).

Galaxy Sizes: Besides luminosity another fundamental property of galaxies is their size. As already discussed in the last sub-section (1.1.1.1 and 1.1.1.2) both elliptical and spiral galaxies follow tight scaling relations connecting their sizes with their luminous/total mass. These structural scaling relations, their slope, scatter and their evolution carry significant amount of information about the formation history of galaxies. Further observed relations show that (1) the size-mass relation is steeper for ellipticals than for disc galaxies at all redshifts, (2) the size-mass relation shows much more evolution for ellipticals than for discs and (3) discs show a broader size distribution at fixed mass than ellipticals (e.g. van der Wel et al. 2014, Somerville and Davé 2015 and references therein).

Galaxy Color and Star Formation: More massive stars emit their light on average at shorter wavelength[2] and have on average a shorter lifetime compared to lower mass stars. Therefore the color of a galaxy carries important information about its evolutionary state[3].

It has been realised early on that the galaxy population shows a bimodal distribution in color-luminosity space (e.g. Baldry et al. 2004) and thus also in stellar age space (Kauffmann et al. 2003). This reflects the fact that galaxies come in two flavours, *star forming* and *quiescent* non-star forming galaxies where the former follow their own scaling relation – the star froming main sequence (Noeske et al. 2007; Wuyts et al. 2011; Tacchella et al. 2016). Interestingly, the number density of *quiescent* galaxies is increasing over cosmic time while the one of *star forming* galaxies stays roughly constant or is even decreasing (Somerville and Davé 2015, and references therein). Since it is the star forming galaxies which are supposed to evolve this implies that at some point in their lives galaxies shut down their star formation and quench.

Mass-Metallicity Relation: Another characteristic and well studied relation for galaxies is their average metallicity (either gas phase metallicity or stellar metallicity) as a function of stellar mass. The average metallicity reflects the amount of gas reprocessed by the galaxy in addition to the newly accrete (pristine) gas. The average gas phase metallicity is measured to increase strongly with stellar mass and flattens only above a stellar mass of $\sim 10^{10}$ $M_\odot$ with only little scatter (Tremonti et al. 2004; Gallazzi et al. 2005; Zahid et al. 2013).

[2]The color of a star depends further on its metallicity in such that higher metallicity stars are redder.

[3]Although this is further complicated by the fact that dust attenuation will cause the galaxy to appear redder



Cold Gas Fraction: Another important relation connecting the gaseous properties of the interstellar medium (ISM) to the stellar mass of the galaxies is given by the fraction of cold gas (Baldry et al. 2008; Peeples and Shankar 2011) which is observed to decrease rapidly with cosmic time (e.g. Tacconi et al. 2010, 2013; Genzel et al. 2015).

1.2. Fundamentals of Galaxy Formation

In the most general sense, the formation and evolution of galaxies is fundamentally influenced by two different aspects: the initial and boundary conditions and the physical processes governing their evolution. Thus, in order to understand current efforts in galaxy formation the following topics need some explanation:

1. The standard model of cosmology: Galaxies are not isolated entities, they form and evolve in a Universe whose evolution is described by a Cosmology. The currently widely accepted model is the ΛCDM model described in section 1.2.1.

2. The initial conditions of galaxy formation: As we believe now, galaxies have a finite age and therefore started forming at given point in time. The *Planck* satellite (Planck Collaboration et al. 2014) was able to measure the physical conditions out of which galaxies start to form to very high accuracy.

3. The physical processes driving galaxy formation: Galaxies are complex objects shaped by many different physical processes among which general relativity, hydrodynamics, collisionless dynamics, thermodynamics, radiation processes and plasma physics are the most important and their impact on galaxy formation is presented in section 1.2.3.

1.2.1. The Standard Model of Cosmology

Cosmology provides the space-time framework and the initial conditions for the formation and subsequent evolution of galaxies. The currently widely accepted model for cosmology is based on the *cosmological principle*, the ansatz that the Universe is isotropic and homogeneous on large scales, and on Einstein's theory of General Relativity according to which the structure of space and time is solely specified by the energy and mass content of the Universe. From these assumptions one can derive the *Friedmann-Lemaître* equations (Friedmann 1922; Lemaître 1927) for the scale factor, $a(t) = R(t)/R_0$, measuring the expansion of the Universe (Peebles 1980):

$$\left(\frac{\dot{a}}{a}\right)^2 = \frac{8\pi G}{3}\rho - \frac{Kc^2}{a^2} + \frac{\Lambda}{3} \tag{1.1}$$

and

$$\frac{\ddot{a}}{a} = -\frac{4\pi G}{3}\left(\rho + \frac{3P}{c^2}\right) + \frac{\Lambda}{3} \tag{1.2}$$

where G denotes the gravitational constant, ρ the energy density of the Universe in matter and radiation and K is a term describing the spatial curvature of the Universe. Λ is the cosmological constant accounting for the effect of Dark Energy, P is a pressure term and c is the speed of light.

This model does not only describe the large-scale structure of the Universe but also its thermal history. By now, various observations, most striking from measurements of the Cosmic Microwave Background (CMB) (Penzias and Wilson 1965), have pinned down the fundamental ingredients of the Universe. Other measurements following the first indications made by Hubble (1929b), mapped out the expansion history of the Universe. One of the latest, Nobel price winning recognitions by Riess et al. (1998) and Perlmutter et al. (1999) and Schmidt et al. (1998) is that the Universe's expansion is accelerating. Analysing the data obtained from measurements of Super Nova Ia (SNIa) they found a non-zero value for the Λ-term in the Friedmann equations and thus established the current standard model of cosmology. I will lay out its implications, predictions and some of its problems below. The main references for this section are Mo et al. (2010), Somerville and Davé (2015) and Naab and Ostriker (2017).

Energy Budget: The energetic constituents of the Universe are most well constrained by observations of the CMB and its power spectrum – the strength of its temperature fluctuations at given angular scale (Spergel et al. 2007; Planck Collaboration et al. 2014). The by far largest portion of the Universe's energy density is an unknown type of energy called *dark energy* ($\sim 69\%$), some kind of vacuum energy with a negative equation of state. The matter density of the Universe is dominated by an unknown type of matter named *dark matter* ($\sim 26\%$) and only $\sim 5\%$ is contributed by ordinary baryonic matter like gas and stars (Planck Collaboration et al. 2014). The energy density in radiation is negligible at present day but dominated at early times, until roughly 380 000 years after the Big Bang, the starting point of the Universe. Further implications of CMB measurements are: the age of the Universe is 13.7 ± 0.2 Gyr and its overall spatial geometry is flat (de Bernardis et al. 2000).

Expansion of the Universe: As already discussed, a fundamental property of the Universe is its expansion with time (Hubble 1929b). A direct consequence of this is a mapping between the distance of an object and the redshift z of the light it emits. This relation is commonly used to estimate the distance and age of observed galaxies and it directly implies that the Universe was smaller at earlier times with the consequence that the Universe started with a Big Bang.

Big Bang: In our current understanding of the Universe space and time have not existed for ever, they were created in an initial *Big Bang*. At the earliest times of the

beginning of the Universe temperatures and densities were so high that quantum effects were dominating its evolution. This is currently outside of our detailed understanding of physics and can not be described by our physical laws. The important thing however is, that the Universe was homogeneous, dense, hot and all forms of energy were in thermodynamical equilibrium with radiation energy which dominated the energy budget at that time (Gamow 1946).

Inflation: It was realised early on that the standard formulation of cosmology has several shortcomings (e.g. the *horizon problem* Misner 1968, the *flatness problem* Dicke and Peebles 1979, the *monopole problem* or the *structure formation problem*; section 3.6.1 Mo et al. 2010) which can be solved if the Universe was undergoing a phase of initial exponential growth. This *inflation* is caused by a quantum field with negative pressure and the rapid expansion casts primordial quantum fluctuations into large-scale perturbations (Dodelson 2003) effectively separating regions initially in causal contact and driving the large scale geometry of the Universe towards flatness (Guth 1981).

Initial Density Fluctuations: As the Universe expands and cools down, individual particles decouple from thermal equilibrium and *freeze out*. The first species to decouple is dark matter (DM) for which we still only know that it is a massive, non-relativistic particle that at most weakly interacts with fundamental forces other than gravity (Bertone et al. 2004). Unaffected by radiation, DM was able to follow the primordial density fluctuations instantiated by inflation and to start enhancing these perturbations while the baryon-photon fluid was trapped in standing density waves (*baryon-acoustic oscillations*) due to gas pressure.

Primordial Nucleosynthesis: Following the expansion of the Universe, the temperature of the baryon-photon fluid drops and whenever the temperature falls below the rest-mass energy of a particle species these particles decouple from the fluid and are able to annihilate with their anti-particles. In principle there should be a symmetry between matter and anti-matter, however due to an unexplained asymmetry (*baryon asymmetry*) there exists an excess of ordinary matter. One major prediction of the Big Bang scenario is the abundance ratio of light elements like e.g. hydrogen, helium and lithium. Only few minutes after the Big Bang, the temperature dropped below the rest-mass energy of neutrons and protons which successively fused into ionised deuterium, helium and lithium (Alpher and Herman 1948; Hoyle and Tayler 1964; Wagoner et al. 1967), the constituents of primordial gas.

Recombination: When the temperature of the Universe dropped below a value of $kT = 13.6$ eV (k denotes the Boltzmann constant), the photon energy fell below the ionisation potential of neutral hydrogen and electrons and protons were finally able to form neutral atoms. Due to the massive overabundance of photons in the Universe *recombination* is delayed until ~ 380000 years after the Big Bang ($z \sim 1100$) until the

Universe had a temperature of about 3000 Kelvin. At this point the number density of free electrons dropped to almost zero and permitted photons to freely propagate. Previous to this point in time the Universe was opaque to radiation. The radiation emitted by *recombination* at the surface of *last scattering* is today observed as the CMB. The first prediction of the CMB was made by Gamow (1948) and Alpher and Herman (1948) and since its first discovery by Penzias and Wilson (1965) several missions have studied its properties in detail like e.g. the *Cosmic Background Explorer* (COBE Smoot et al. 1990), the *Wilkinson Microwave Anisotropy Probe* (WMAP Bennett et al. 2003) and most recently the *Planck satellite* (Planck Collaboration et al. 2014). The spectrum of the CMB follows a blackbody (Mather et al. 1990) and has a present-day temperature of $T = 2.72548 \pm 0.00057$ K, by far the closest spectrum to Planck's ideal blackbody ever observed in nature (Fixsen 2009). The tiny temperature differences of order $\delta T/T \sim 10^{-5}$ reflect the imprint of the first density fluctuations caused by photons originating from over- and under-dense regions of space (Smoot et al. 1992).

1.2.1.1. Structure Formation

All present-day structures in the Universe grew by gravitational instabilities (Jeans 1902) out of the initial density perturbations set by inflation. One major prediction from inflationary theory is that the initial power spectrum of perturbations, $P(k) \propto k^n$ with $n \sim 1$, is scale-invariant[4] and follows that of a Gaussian random field (Harrison 1970; Hawking 1982; Guth and Pi 1982; Bardeen et al. 1983) with properties fully specified by that of the CMB. In an expanding Universe the growth rate of structures is a power law of time (Gamow and Teller 1939; Lifshitz 1946) and depends on the specific matter species under consideration. While baryonic perturbation were damped by photon pressure before recombination (Silk 1968), DM perturbations were able to grow already. After recombination baryons decoupled from the photons and quickly followed the potential well of the DM. Thereby gravitational collapse proceeds first along one axis and only successively along the others, thus forming so called *Zel'dovich pancakes* (Zel'dovich 1970). Due to their non-sphericity these objects are able to exert torques on each other and gain angular momentum (Hoyle 1949; Doroshkevich 1970) which was first tested using numerical simulations by Peebles (1971) and Efstathiou and Jones (1979). While Zel'dovich's approximation is the more realistic description, Gunn and Gott (1972) developed a simpler, more handy spherical approximation for gravitational collapse which was then used by Press and Schechter (1974) to estimate the mass function of collapsed objects.

One of the most important predictions of this theory is the formation of the large scale structure of the Universe which consists of galaxy clusters connected by filaments

[4]Recent measurements by the Planck Collaboration et al. 2014 find small but statistically significant deviations from true scale-invariance, $n = 0.968 \pm 0.006$.



and sheets enclosing large under-dense areas called voids. The robust prediction of these structures by numerical simulations (Gregory and Thompson 1978; Tully 1987; Gott et al. 2005; Springel et al. 2006; Frenk and White 2012) and their confirmation by observations (Geller and Huchra 1989; Colless et al. 2001; York et al. 2000) have established the ΛCDM model as the standard model for cosmology and structure formation (Naab and Ostriker 2017).

1.2.2. Emergence of the Cold Dark Matter Model

By now it is well accepted that DM is one of the key ingredients for galaxy formation. However, from the first indications of its existence in the 1930s to its acceptance it took more than 70 years of scientific reasoning. Nowadays it is well established that DM accounts for about 80% of the matter content of the Universe and its effects on cosmological scales are well studied and understood. Nevertheless, on galactic and sub-galactic scales it still faces some (severe) challenges.

1.2.2.1. Arguments for the Existence of Dark Matter

When Fritz Zwicky in 1933 studied the motion of galaxies in the Coma Cluster he found that the luminous mass of the cluster is not at all sufficient to keep it gravitationally bound. He concluded that there must be a tremendous amount of unseen (dark) matter surrounding the galaxies. Following this, Ostriker et al. (1974) and Einasto et al. (1974) inferred from the satellite dynamics of the MW and of local galaxies that these galaxies need to be embedded into large, massive halos in order to explain their dynamics. Further evidence for large amounts of unseen matter around galaxies is provided by the flat rotation curves of spiral galaxies (Babcock 1939; Freeman 1970; Roberts and Rots 1973; Rubin et al. 1978, 1980) which would be unexplained if the luminous matter in these systems was the only gravitating component. Until now the body of evidence for unseen DM around galaxies is still growing through observations of hot X-ray gas emission from galaxy clusters (Buote and Canizares 1992, e.g.), strong gravitational lensing (e.g. Trick et al. 2016) and weak gravitational lensing (Tyson et al. 1990; Kaiser and Squires 1993).

In the 1980s further strong evidence for the existence of DM was given by the flatness of the Universe in the inflationary model (de Bernardis et al. 2000) and by arguments about structure formation. Cosmic nucleosynthesis is not able to provide enough baryonic matter in order to result in a flat Universe (e.g. Walker et al. 1991; Burles et al. 2001; Kirkman et al. 2003) and the observed smallness of the CMB fluctuations together with the inferred age of the Universe left simply not enough time for the formation of galaxies out of the tiny density fluctuations given a purely baryonic Universe. In order to remedy this, many models of DM were invented in the 1980s (Peebles 1982; Blumenthal et al. 1982; Bond et al. 1982; Bond and Szalay 1983) which



all suffered from a too low clustering signal on large scales as measured by galaxy clustering surveys in the 1990s (Maddox et al. 1990; Efstathiou et al. 1990). While many models have been suggested to account for this (see e.g. section1.4.4 Mo et al. 2010), the currently widely accepted model introduced a cosmological constant, Λ, with effective negative pressure. This model became the concordance cosmological model when Riess et al. (1998), Schmidt et al. (1998) and Perlmutter et al. (1999) (but see also Garnavich et al. 1998) found the cosmic accelerated expansion using SNIa. By now the parameters of the ΛCDM model have been exceptionally well constrained (Spergel et al. 2007; Komatsu et al. 2009) and models where DM is made up of baryonic components such as Black Holes (BH) or brown dwarfs (e.g. Carr 1978) are once and for all ruled out.

1.2.2.2. Global Properties of Dark Matter Halos

The final outcome of collapsing over-dense regions in the Universe during structure formation are virialised *dark matter halos*. The mass of a dark matter halo is given by

$$M_{\rm vir} = \frac{4\pi}{3} R_{\rm vir}^3 \Delta \rho_{\rm m} \tag{1.3}$$

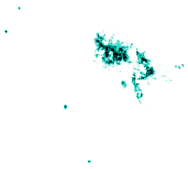
where Δ defines the virial over-density parameter needed in order to define the halo's outer radius, $R_{\rm vir}$. The numerical value for Δ is usually chosen to follow the theoretical prediction for idealised spherical collapse ($\Delta = 178$, Bryan and Norman 1998). However, there are several definitions of Δ and its numerical value in the literature (up to a factor of 3 variation) where e.g. Δ can be defined relative to the background matter density or the critical density of the Universe (for further discussion see Bullock and Boylan-Kolchin 2017). In this thesis I adopt the definition of $\Delta(z) = 200\rho_{\rm crit}$ with respect to the critical density of the Universe. Thus, I label all virial properties of the halos with a subscript 200. Following this, given the virial mass M_{200}, the virial radius R_{200} is uniquely defined via equation 1.3[5]. The virial velocity is further uniquely defined via

$$V_{200} = \sqrt{\frac{GM_{200}}{R_{200}}} \tag{1.4}$$

These three parameters M_{200}, R_{200} and V_{200} are equivalent mass labels given a specified value of Δ.

Dark matter halos follow a universal two parameter density profile which is not a simple power law (Dubinski and Carlberg 1991) but rather bends from a steep outer

[5]A collapsed halo is approximately 7 times smaller in physical scale than the associated comoving linear scale it collapsed from (Bullock and Boylan-Kolchin 2017)



profile to a mild inner cusp. A commonly adapted profile is the NFW profile (Navarro et al. 1997a)

$$\rho(r) = \frac{4\rho_{-2}}{(r/r_{-2})(1 + r/r_{-2})^2} \tag{1.5}$$

where r_{-2} is the characteristic radius where the log-slope of the density profile is -2. This marks the transition from the inner $1/r$ profile to the outer $1/r^3$ profile. Given that only two parameters are needed to define the density profile, for fixed halo mass M_{200} a common adoption is to use the concentration $c = R_{200}/r_{-2}$ as second parameter (for further details see Bullock and Boylan-Kolchin 2017).

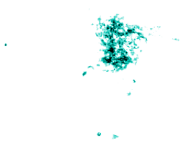
1.2.3. Physical Processes in Galaxy Formation

The current state of modern galaxy formation theory is able to link processes on galaxy scale, like e.g. the physics of the ISM, star formation (SF) and stellar feedback (SFb) or super-massive black hole (SMBH) physics to the phenomenons of large scale structure formation and cosmology, thereby covering a huge dynamical range. On the other hand, this implies that a detailed understanding of galaxy formation is tightly connected to an (at least basic) understanding of the aforementioned processes. In what follows I will briefly outline the basic principles needed to understand the current state of galaxy formation. All topics covered in this section are presented in much more detail in modern text books like e.g. the book by Mo et al. (2010) or recent reviews like the one by Somerville and Davé (2015) and Naab and Ostriker (2017).

Galaxies are the building blocks of the Universe and can be easily described by fundamental characteristic quantities like their characteristic size ($R_{\rm gal} \sim$ kpc), their characteristic mass ($M_{\rm gal} \sim 10^{10}$ M$_\odot$) and their characteristic abundance ($\phi_{\rm gal} \sim 10^{-2}$ Mpc^{-3}). The fundamental question in galaxy formation is if these quantities can be derived from first principle and if we do understand the physical mechanisms shaping the properties of galaxies. Modelling the formation of galaxies as a problem of physics one can identify 4 separate steps on the way to a solution: (1) formulating the initial conditions, (2) knowledge of the physical processes, (3) application of sophisticated (computational) tools to (1) and utilising (2) in order to derive the properties and evolution of model galaxies to finally (4) directly compare and test model predictions to observed galaxies.

As laid out in section 1.2.1, the initial conditions for galaxy formation are fully specified by the standard model and the observations of the CMB. In the current picture dark matter halos are the sides of galaxy formation (White and Rees 1978; Fall and Efstathiou 1980) and the physical processes involved are summarised below:

Gravity: The DM halos are forming under gravitational collapse out of the primordial density fluctuations and successively merge into larger structures building the skeleton for galaxy formation. Due to its dissipationless nature, dark matter eventually settles



into virialised objects (see e.g. Bryan and Norman 1998, and Lynden-Bell 1967 for the concept of violent relaxation) of universal, well studied shape (Navarro et al. 1996, 1997a; Einasto 1965, but also Dubinski and Carlberg 1991). These halos provide the potential wells for subsequent gas accretion.

Hydrodynamics and gas cooling: It was first suggested by (Eggen et al. 1962) and later refined by (Gott and Thuan 1976) that galaxies might form out of collapsing gas clouds. Falling into the potential wells of the dark matter halos the gas is shock heated to the virial temperature T_{vir} of the halo (section 8.4.4 Mo et al. 2010). The subsequent evolution of the gas depends strongly on its ability to cool and overcome the pressure support. It was realised relatively early on by Silk (1977), Rees and Ostriker (1977) and Binney (1977) that radiative cooling plays a major role in shaping the stellar mass of a galaxy. In the temperature range $T > 10^7$ K the gas is fully collisionally ionised and cooling proceeds predominantly via bremsstrahlung (free-free emission). In a lower temperature range of $10^4 < T < 10^7$ K, cooling via line emission is effective and below temperatures of 10^4 K, the main cooling process occurs through metal line and molecular cooling (e.g. Naab and Ostriker 2017) which is only effective for metal enriched gas. Thus the ability of the gas to efficiently cool strongly depends on halo mass. This explains e.g. the presence of hot gas halos in galaxy clusters of masses above 10^{13} $M_\odot$ and the lack of low mass galaxies whose virial temperatures are below 10^4 K. Furthermore, depending on the effectivity of cooling with respect to the dynamical time of the halo one can identify two different regimes: (i) if cooling is inefficient, a pressure-supported quasi-hydrostatic gaseous halo will form (hot mode, Birnboim and Dekel 2003; White and Frenk 1991) and (ii) if cooling is efficient, the gas will quickly loose pressure support and collapse until it is supported by angular momentum (cold mode, Dekel and Birnboim 2006). This second mode seem to appear predominantly when gas is accreted via relatively cold, dense filaments (Kereš et al. 2005; Dekel et al. 2009a) which might funnel gas all the way down to the centres of the halos (but see also Nelson et al. 2013).

Star Formation: Once enough gas has settled into the central regions of the dark matter halo, its own gravity will overcome that of the dark matter halo and the gas will become self-gravitating. When cooling dominates over heating processes a run-away collapse (the cooling time scales with the inverse of the gas density) may set in and Giant Molecular Cloud (GMC) complexes will form and eventually fragment to form stars (Naab and Ostriker 2017). While many details of the star formation process are still poorly understood there exist empirical power law relations between the gas surface density, $\Sigma_{\rm gas}$, and the star formation rate surface density, $\Sigma_{\rm SFR}$ (Schmidt 1959; Kennicutt 1989, 1998; Bigiel et al. 2008).

Stellar Feedback: One of the most important ingredients of modern galaxy formation models is stellar feedback. Due to the hierarchical nature of the Cold Dark



Matter (CDM) model the naive prediction is that in the absence of any heating or feedback processes all baryonic matter will quickly cool and form stars. However, observations have proven that less than 10% of the global baryon budget is in the form of stars. In order to solve this "overcooling problem" it has already been suggested by the very first numerical models of galaxy formation (Larson 1974a,b, 1975, 1976) that the energy generated by supernova explosions of massive stars might provide enough energy to heat the gas and perhaps even blow it out of the galaxies. Invoking this, the observed inefficiency of star formation in galaxies could be explained (Dekel and Silk 1986; White and Rees 1978; White and Frenk 1991). By now it has been realised that there are a variety of processes associated with (massive) star formation and supernovae explosions (e.g. stellar winds, photo-heating or photo-ionisation) that might cause galactic outflows (at least for lower mass galaxies Oppenheimer and Davé 2006; Brook et al. 2012; Übler et al. 2014) effectively reducing the baryon fraction inside galaxies and contributing to the inefficiency of star formation (see e.g. Hopkins et al. 2012, for a review).

Super Massive Black Hole Formation and Feedback: Another important source of feedback energy is provided by Active Galactic Nuclei (AGN), the active accretion state of SMBH which are expected to reside in the center of almost every massive, spheroid dominated galaxy (Kormendy and Ho 2013). While the process of the formation of SMBHs is poorly understood it is assumed that the first "seed" Black Hole (BH)s may have formed in the early universe (Volonteri 2010) and then have grown by accretion of gas (Netzer 2013) thereby being able to release enough energy to significantly effect the host galaxy (Silk and Rees 1998). There are several observational indications of strong feedback processes associated with AGN (high-velocity winds or hot bubbles in the ISM, Fabian 2012; Heckman and Best 2014). However, theoretically it is still uncertain how efficiently the energy is able to couple to the gas of the galaxies.

Chemical Evolution: After primordial nucleosynthesis (section 1.2.1) all the gas in the Universe consisted of hydrogen ($\sim 75\%$) and helium ($\sim 25\%$) with only minor contributions from lithium. All other elements (usually referred to as metals) in the Universe are formed later, synthesised in stars via nuclear fusion and ejected via stellar winds and supernova explosions. Understanding and modelling chemical evolution is critical for galaxy formation. As discussed above, the cooling rates at intermediate temperatures highly depend on the metal content of the gas and the luminosity and color of stellar populations of a given age depend sensitively on their metal abundance. Furthermore, heavy elements aggregate and form dust, which absorbs light in the Ultraviolet (UV) and optical wavelength bands and re-radiates the energy in the Infrared (IR) (e.g. section 1.2.9 Mo et al. 2010). This makes the inclusion of chemical enrichment into models of galaxy formation inevitably necessary in order to predict realistic galaxy properties.



Dynamical Evolution: By now it has been realised that the dynamical evolution (internal or external) of galaxies plays a major role in shaping their morphology. E.g. external dynamical effects are important when satellite galaxies orbit inside the dark matter halo of their host. They will experience tidal forces as well as dragging forces (ram pressure) if the halo contains hot gas. Tidal interactions will cause the satellites to loose gas, stars and dark matter and effectively alter their structures while ram pressure stripping plays a major role in shaping the galaxy population in groups and clusters. Capturing these effects is predominantly necessary in order to describe correctly the properties of e.g. MW satellite galaxies (see chapter 5). Internal dynamical effects have been shown to be able to reshape the structure of galaxies (Herpich et al. 2015). E.g. the stellar disc of spiral galaxies might get (gravitationally) unstable at later times (either spontaneous or triggered by interaction) leading to large scale angular momentum and stellar mass redistribution, thereby changing the whole morphology of the disc. Famous examples are non-axisymmetric instabilities leading to the formation of bars (e.g. Athanassoula and Martinez-Valpuesta 2009) and spiral structure. The bars might later on develop their own instability and buckle leading to the formation of a peanut-shaped bulge like the one of the MW (see e.g. Bland-Hawthorn and Gerhard 2016). Thus, an important question of galaxy formation is whether the morphology of galaxies is set at formation or largely influence by internal (secular) evolution (see also chapter 3 and 4).

1.2.3.1. The Formation of Disc Galaxies

The general picture for the assembly of disc dominated galaxies is a formation out of high angular momentum gas accreted onto the dark matter halo via cold streams under the conservation of its specific angular momentum (Fall and Efstathiou 1980; Mo et al. 1998). The average specific angular momentum of galactic discs is indeed consistent with these expectations (Dalcanton et al. 1997; Dutton and van den Bosch 2012), however its distribution strongly deviates from the predictions of a simple infall scenario. Observed discs have a strong deficit of low angular momentum gas and a large excess of intermediate angular momentum gas (Bullock et al. 2001; van den Bosch et al. 2001) which is the clear signature of low angular momentum gas removal. After early simulations of disc galaxy formation created too compact discs with peaked rotation curves (Steinmetz and Navarro 1999; Navarro and Steinmetz 2000) it was realised that the key ingredient to avoid this *angular momentum catastrophe* is the inclusion of stellar feedback (e.g. Governato et al. 2007; Guedes et al. 2011). Stellar wind driven outflows preferentially remove low angular momentum gas which then might re-acquire angular momentum in the halo and cools back into the galaxy (Brook et al. 2012; Übler et al. 2014) which leads to an inside-out growth of disc galaxies.

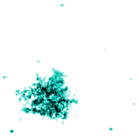


Another fundamental observation which must be met by disc galaxy formation models relates to the properties of discy galaxies at redshifts ~ 2. These disc are observed to be much puffier and to have values of rotation velocities divided by gas dispersion $V_{\rm rot}/\sigma \sim 3$ instead of 10 as observed for present day discs (e.g. Förster Schreiber et al. 2009). At the same time many of these galaxies show large, bright clumps contributing substantial amounts of star formation to the total star formation budget (Guo et al. 2012). The discovery of these clumpy galaxies (e.g. Elmegreen and Elmegreen 2005) made the clumps formed in simulations without ISM pressurisation proclaimed "features" (Bournaud et al. 2007; Ceverino et al. 2010; Dekel et al. 2009a) although these models did not agree with abundance matching results. Implementation of radiation pressure brings these models into better agreement with abundance matching results (Ceverino et al. 2014) but the fraction of clumps is still high (Moody et al. 2014). While other ISM models better match abundance matching results (Genel et al. 2012; Faucher-Giguère et al. 2013) they still produce clumps with much lower lifetimes. Thus, it is still unclear whether one single ISM model is able to produce giant clumps of up to 10^9 $M_\odot$ at redshift $z \sim 2$ while still being able to form thin stellar discs at redshift zero (for further discussion see Somerville and Davé 2015). I will elaborate on this challenge further in chapter 2.

While the formation of clumps is attributed to *violent disc instabilities* (Dekel et al. 2009a) there exists another form of instability in disc galaxies leading to the formation of *pseudobulges* (see Kormendy and Kennicutt 2004, for further details). When becoming susceptible to this kind of (axisymmetric) instability the galaxy will form a galactic bar (Toomre 1964; Hohl 1971; Ostriker and Peebles 1973; Combes et al. 1990) eventually leading to the formation of a *boxy/peanut* bulge. The formation, evolution and properties of a galactic bar in a MW like galaxy is further discussed in chapter 3 and 4.

1.2.3.2. The Formation of Spheroid-dominated Galaxies

Since Toomre (1977) showed that an equal mass merger is able to produce an elliptical galaxy, much work has been spend on exploring the merger formation scenario of elliptical galaxies (see Somerville and Davé 2015, and references therein). While this picture is able to reproduce most of the observed features of the elliptical galaxy population, more recent work has shown that this simple picture needs refinement. Hydrodynamical simulations of gas-rich mergers have shown that the post-merger galaxy is able to reform a disc or that subsequent gas accretion after the merger might lead to the reformation of a disc (e.g. Robertson et al. 2004, 2006; Hopkins et al. 2009). Furthermore, observations of elliptical galaxies revealed that these systems are preferentially old, they formed most of their stellar mass about $8 - 10$ Gyr ago (Trager et al. 2000; Thomas et al. 2005). Consequently, the formation picture for elliptical



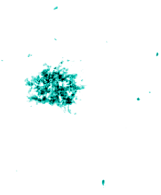
galaxies moved from the merger scenario to a *preventive* and *ejective* feedback scenario. The progenitors of elliptical galaxies need to have their gas removed or heated up in order to shut down star formation early on. This is now believed to be tightly linked to the two different modes of AGN feedback (Somerville and Davé 2015).

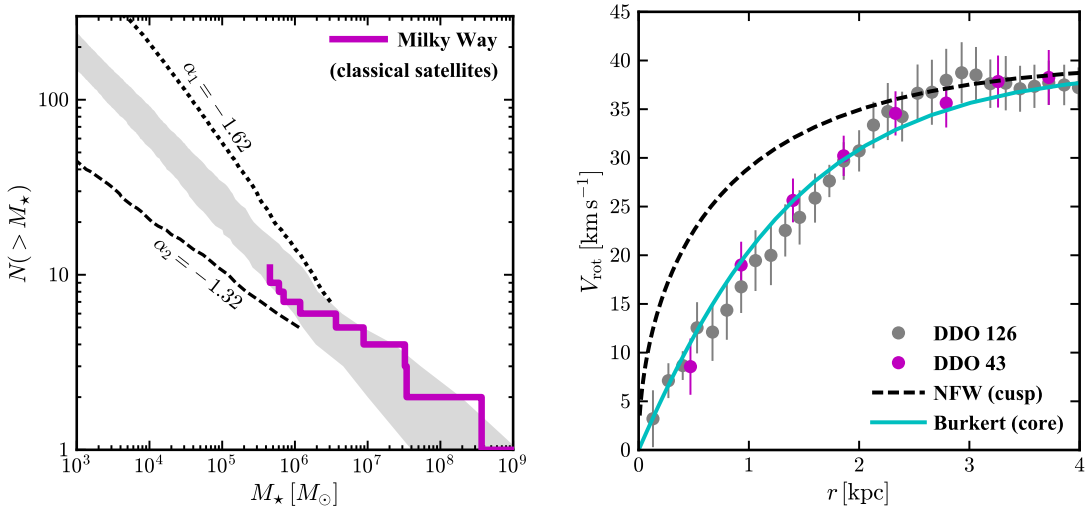
There exists a second formation scenario where spheroid-dominated galaxies form by *violent disc instabilities* (Dekel et al. 2009a) via the formation of giant clumps already discussed in the previous subsection. Depending on the lifetime of these clumps, they might migrate to the center and form a *classical* bulge (Elmegreen et al. 2008; Bournaud et al. 2011). However, there is no consent in the literature so far as to what is the lifetime of these clumps. Some simulations suggest the clumps are short-lived and disrupt themselves due to stellar feedback (Genel et al. 2012; Hopkins et al. 2012, and see chapter 2) while others find them to be long-lived (Bournaud et al. 2014; Mandelker et al. 2014). Observations could so far not distinguish between the two scenarios as they find both, indications for short-lived clumps (Wuyts et al. 2011) and long-lived clumps (Genzel et al. 2011). I will discuss this issue further in chapter 2.

1.2.4. The Small Scale Problems of ΛCDM

Although perfectly supported by the agreement with measurements of the CMB anisotropies and acoustic oscillations by several missions in the late 1990s (e.g. Hanany et al. 2000; Halverson et al. 2002; Sievers et al. 2003) and the agreement with large scale clustering signals by lensing (e.g. Spergel et al. 2003, and references therein) the ΛCDM model still faces several issues. While there are some more general conceptual problems (e.g. the "cosmological constant fine tuning problem", and the "cosmic coincidence problem" Weinberg 1989; Astashenok et al. 2012) which might be either caused by systematics in the data or by new physics, the more severe issues of ΛCDM are found on small sub-galactic scales. Most of these problems were identified comparing predictions from dark matter only simulations to observations of baryons in the Universe. It is still unclear if a more sophisticated comparison between full hydrodynamical simulations and observations are able to resolve these problems (see e.g. Bullock and Boylan-Kolchin 2017, for an in-depth discussion and chapter 5 of this thesis). I will briefly summarise the identified problems following two recent reviews by Bullock and Boylan-Kolchin (2017) and Del Popolo and Le Delliou (2017).

The Missing Satellite Problem: First described by Klypin et al. (1999) and Moore et al. (1999a) the *Missing Satellite Problem* addresses the miss-match between the predicted abundance of low mass galactic dark matter subhalos and the observed number counts of actual luminous satellite galaxies of the MW (see e.g. Garrison-Kimmel et al. 2014, 2017). Following the predictions of the highest-resolution cosmological simulations of MW mass dark matter halos in the ΛCDM paradigm we expect to find thousands of subhalos with no break in the subhalo mass function down to the





(a) *The Missing Satellites Problem.* ***(b)*** *The Cusp-Core problem.*

Figure 1.3: Visual presentation of the Missing Satellites Problem and the Cusp-Core Problem of ΛCDM dark matter halos. **(a):** The cumulative number count of dwarf galaxies around the MW (magenta) plotted down to the completeness limit (taken from Garrison-Kimmel et al. 2017) in comparison to the predicted stellar mass function (gray shaded region) from the dark-matter-only ELVIS simulations (Garrison-Kimmel et al. 2014) combined with the fiducial abundance matching relation. For a shallower (dashed) or steeper (dotted) faint end slope of the stellar mass function, the predicted abundance of MW satellites with $M_{\rm star} > 10^4\,{\rm M}_\odot$ differs by a factor of 10. Therefore dwarf galaxy counts in the Local Group can serve as strong constraints on galaxy formation models. **(b):** Comparison between observed rotation curves from the LITTLE THINGS survey (data points Oh et al. 2015) and the naive expectation from ΛCDM dark matter halos (dashed line). The ΛCDM rotation curve rises quickly, reflecting a central cuspy density profile while the data points show a more slowly rising rotation curve better fit by a constant density core (cyan line Burkert 1995). **Figure credit:** Bullock and Boylan-Kolchin (2017).

numerical resolution limit (e.g. Diemand et al. 2007; Springel et al. 2008; Stadel et al. 2009; Griffen et al. 2016, and chapter 5). On the contrary, up to now only ∼ 50 satellite galaxies of the MW with stellar masses above ∼ 300 $M_\odot$ inside the virial volume are known (Drlica-Wagner et al. 2015). While there are still some undiscovered satellite galaxies expected to be found inside the MW's virial radius (Tollerud et al. 2008; Hargis et al. 2014), it seems unlikely that the number of satellite galaxies will rise into the thousands. Thus, the essential problem is either a failure of ΛCDM to predict the correct abundance of small dark matter subhalos or the lack of our understanding of baryonic physics on the smallest scales of galaxy formation. E.g. it has been suggested that below mass scales of $M_{\rm vir} \sim 10^9\,{\rm M}_\odot$ dark matter halos become increasingly inefficient in forming galaxies due to a suppression of gas accretion owing to the UV background (e.g. Efstathiou 1992; Bullock et al. 2000; Benson et al. 2002; Bovill and Ricotti 2009; Sawala et al. 2016) and that below a mass of $M_{\rm vir} \gtrsim 10^7\,{\rm M}_\odot$ they might

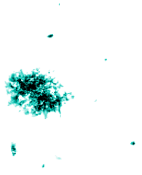
even go completely dark due to the molecular cooling limit (e.g. Rees and Ostriker 1977).

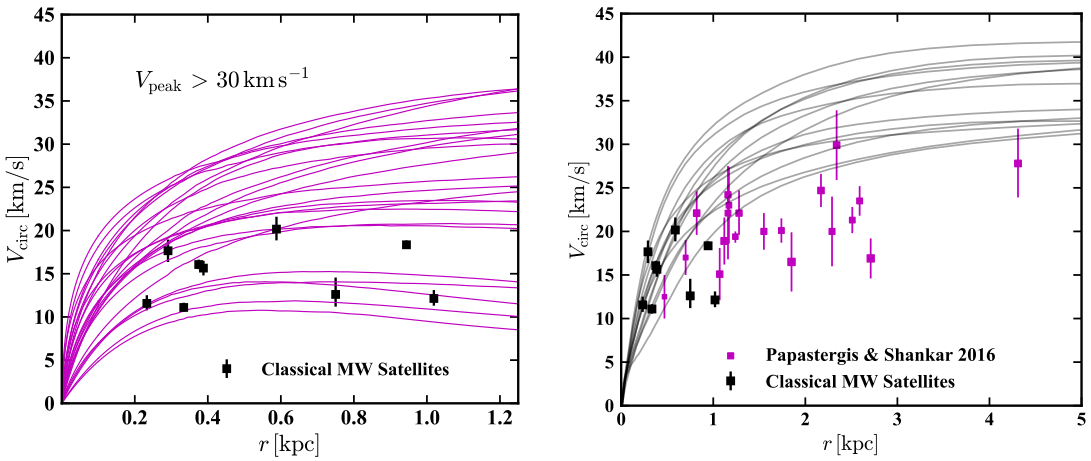
Suggested Solutions: There are several different solutions suggested in the literature (see e.g. Bullock and Boylan-Kolchin 2017) but the most promising ones include the effect of galaxy formation physics where small dark matter halos simply become increasingly inefficient in forming galaxies and thus stay completely dark. Further solutions are modifications of the ΛCDM paradigm like warm or self-interacting dark matter models which shift the cut-off mass of the power spectrum to larger masses effectively reducing the amount of low mass dark matter halos (see Bullock and Boylan-Kolchin 2017, and references therein). A more in-depth discussion of this problem including the solutions found in hydrodynamical simulations is given in chapter 5.

The Cusp/Core problem: The subject of this second problem is the inner structure of ΛCDM dark matter halos. As already pointed out by Flores and Primack and Moore in 1994, ΛCDM simulations predict inner density profiles which rise steeply towards the centre $\rho(r) \propto r^{-\gamma}$, with power law indices $\gamma \sim 0.8 - 1.4$ in the central regions of small galaxies (Navarro et al. 2010). In contrast to this is the inferred density slope for low-mass dark-matter-dominated galaxies in the range of $\gamma \sim 0.0 - 0.5$ (McGaugh et al. 2001; Marchesini et al. 2002; de Blok et al. 2008) preferring constant density cores.

Suggested Solutions: The favoured solution to erase density cusps in dark matter halos is coming from the most advanced hydrodynamical simulations today. These suggest that baryonic physics of stellar feedback is able to inject enough energy into the ISM in order to create a fluctuating gravitational potential by gas ejection and re-accretion and thus modify the dark matter density profile (Mashchenko et al. 2008; Pontzen and Governato 2012; Madau et al. 2014; Oñorbe et al. 2015; Read et al. 2016; Tollet et al. 2016; Fitts et al. 2017). It is important to note that this mechanism is not an ab-initio prediction of ΛCDM but rather of the adopted galaxy formation model. E.g. Sawala et al. (2016) do not obtain cores in their low mass dark matter halos yet still being able to match observations. Another solution to this problem involves modification of the ΛCDM cosmology to use another form of dark matter. E.g. it has been shown by several authors (e.g. Vogelsberger et al. 2012; Peter et al. 2013; Fry et al. 2015; Elbert et al. 2015) that self-interacting dark matter is able to create density cores. For further discussion see Bullock and Boylan-Kolchin (2017).

The Too-Big-To-Fail Problem: As first pointed out by Boylan-Kolchin et al. in 2011 there arises another problem of ΛCDM when trying to fix the missing satellites problem by simply assigning the known MW satellites to the most massive dark matter subhalos and ascribe the lack of low luminosity satellites to galaxy formation physics. In doing so, the prediction of ΛCDM is that the central masses (within the observed half-light radii of MW satellites, $r_{\rm half} \lesssim 1$ kpc) of dark matter halos and observed satellites should coincide. However, comparing the observed central masses of MW





(a) *Satellite galaxies.* ***(b)*** *Field dwarfs.*

Figure 1.4: Graphical representation of the Too-Big-to-Fail Problem by comparing the circular velocities of MW satellites and field dwarf galaxies to the circular velocity curves of subhalos from one of the (dark matter only) Aquarius simulations. **(a):** Data points show the circular velocities at the half-light radius of classical MW satellite in comparison to the predicted circular velocity curves from ΛCDM simulations (magenta lines). The dark matter halos are selected to be among the most massive ones and are likely resistant to strong star formation suppression by reionization and thus are naively expected to have formed stars. The existence of a large population of subhalos with an excess in central masses greater than that of any observed MW satellite is the original Too-Big-to-Fail problem. **(b):** A mismatch between the central masses of simulated ΛCDM dark matter halos and observed dwarf galaxies persists also for field dwarf galaxies (magenta points) when compared to predictions for ΛCDM halos from fully self-consistent hydrodynamic simulations (Fitts et al. 2017). This indicates that the problem is not specific to satellite galaxies. **Figure credit:** *Left panel*: Boylan-Kolchin et al. (2012); *Right panel*: Papastergis and Ponomareva (2017); both modified and taken from Bullock and Boylan-Kolchin (2017).

satellites to subhalos of the Aquarius (Springel et al. 2008) and Via Lactea II (Diemand et al. 2008) simulations Boylan-Kolchin et al. (2012) found systematically too large central masses for the dark matter subhalos (see also Alam et al. 2002). While there exist subhalos with the "correct" central masses compared to MW satellites, they have never been among the most massive ones and the question in place would be: Why would the most massive subhalos fail to form stars? They should be *too big to fail* forming a galaxy inside them. Thus, although ΛCDM predicts the correct number of massive subhalos, their central densities are way higher than observed for MW satellites. And although this problem was first solely identified for MW satellites, it has now been shown to be present also for Andromeda galaxy (M31) satellites (Tollerud et al. 2014), Local Group field dwarf galaxies (those outside the virial radius of MW and M31 Kirby et al. 2014) and even for more isolated dwarf galaxies using their HI

rotation curves (Papastergis et al. 2015; Papastergis and Shankar 2016)[6]. It has been suggested that the latter version of the problem causes the miss-match between the observed and simulated velocity function of dwarf galaxies (Zavala et al. 2009; Klypin et al. 2015; Trujillo-Gomez et al. 2018) although it could be shown that observational biases might be the primary reason for this (Macciò et al. 2016; Brooks et al. 2017).

Suggested Solutions: The most studied solution to this problem involves environmental effects such as ram pressure stripping or tidal forces experienced by satellites orbiting inside a galactic dark matter halo (e.g. Zolotov et al. 2012; Arraki et al. 2014; Brooks and Zolotov 2014; Brook and Di Cintio 2015; Wetzel et al. 2016; Tomozeiu et al. 2016; Sawala et al. 2016; Dutton et al. 2016). However, these effects do not explain the too-big-to-fail problem in field and isolated dwarf galaxies although there are different solutions suggested for these galaxies (Macciò et al. 2016; Kormendy and Freeman 2016). Other solutions involve a lower virial mass for the MW (Wang et al. 2012) which would solve the problem by decreasing the number of massive satellites (Vera-Ciro et al. 2013; Jiang and van den Bosch 2015; di Cintio et al. 2011; Cautun et al. 2014). Finally, also for this problem there exist solutions invoking modified dark matter models. Since the central densities of dark matter halos reflect the densities of the Universe at their formation, delaying halo formation by modifications of the power spectrum helps reducing their central densities. However, no possible scenario using modified dark matter models exist which is capable of solving the too-big-to-fail problem and the cusp/core problem at the same time. For Further discussion of this see Bullock and Boylan-Kolchin (2017). I will discuss in more detail the solutions found in my simulations in chapter 5.

The Plane of Satellite Problem: Already in 1976 Kunkel and Demers (1976) and Lynden-Bell (1976) observed the classical MW satellites to reside in a flattened polar structure and since then ΛCDM had have a hard time reproducing such structures around galactic dark matter halos. In this sense, the structure formation problem of planar satellite distributions has been the first challenge of ΛCDM, pre-dating all other challenges by about two decades (Bullock and Boylan-Kolchin 2017). Only recently with the discovery of a similar planar alignment for satellites of M31 (Metz et al. 2007; Conn et al. 2013) this problem gained popularity. While in simulations of ΛCDM the distribution of subhalos is found to be inconsistent with a spherical distribution (Zentner et al. 2005; Kang et al. 2005), Pawlowski et al. (2012) argued that the MW satellite distribution is still inconsistent with ΛCDM predictions. Further complications arise from the motion of the satellite galaxies with a preferred orbital pole alignment

[6] The general observation now is that for dwarf galaxies with stellar masses $10^5 \lesssim M_{\rm star}/{\rm M}_\odot \lesssim 10^8$ the central masses are about 50% smaller than predicted by ΛCDM dark matter only simulations. This equivalently means that for a classical dwarf satellite about 10^7 $\rm M_\odot$ of mass must be removed from the inner $\sim$ 300 pc.



for MW satellites (Pawlowski et al. 2013, 2015) and a rotationally coherent plane around M31 (Ibata et al. 2013). Libeskind et al. (2009) and Libeskind et al. (2015) used ΛCDM simulations and found that filamentary accretion and the ambient shear field can explain the alignment of satellite galaxies although with much thicker planes than observed (but see also Buck et al. 2015). In case of the M31 plane of satellites the situation is more difficult. We view the plane essentially edge-on and thus have almost perfect radial velocity measurements but no handle on the perpendicular velocities. Therefore, we are not able to determine if this planar configuration is a stable rotation supported structure or a transient feature. Still, even the latter case seems to be an exceedingly rare case in ΛCDM (Ahmed et al. 2017). A similar, yet distinct version of this problem was pointed out by Cautun and Frenk (2017) who investigated the velocity anisotropy of satellites in ΛCDM simulations and the MW and found a much higher anisotropy in the observations.

Suggested Solutions: Solutions to the plane of satellites problem within ΛCDM were investigated only recently (Bahl and Baumgardt 2014; Gillet et al. 2015; Buck et al. 2015) and no census could be reached yet (see Bullock and Boylan-Kolchin 2017, for more details). For an in-depth discussion of this problem and the solution suggested in this thesis see chapter 6.

The above list of problems and challenges contains only the more severe ones and is far from complete. Further challenges of the ΛCDM model include for example the tight correlation of baryonic mass, M_b, with the maximum rotation velocity of a galaxy, V_{flat}, better known as the *baryonic Tully-Fisher relation* (McGaugh 2012) further generalised by the radial acceleration relation (RAR) as introduced by (McGaugh et al. 2016). The challenge of ΛCDM for this problem is to explain the tight correlations between rotation and baryonic content of the galaxies in the light of the diversity of observed rotation curves (Oman et al. 2015). For a more complete list of problems I refer the reader to the reviews by Bullock and Boylan-Kolchin (2017) and Del Popolo and Le Delliou (2017).

1.3. The Local Group System

The local environment of the MW contains another massive spiral galaxy, M31 and more than ~ 100 fainter dwarf galaxies. This compendium of galaxies is called *Local Group* and extends up to about 2 Mpc around the MW. The Local Group (LG) is a relatively isolated system who's nearest neighbouring large galaxy, M82, is located at a distance of ~ 3.5 Mpc (Tully et al. 2013) and the nearest galaxy cluster, the Virgo cluster, at ~ 17 Mpc (Tonry et al. 2001). The LG itself is a gravitationally bound system



where MW and M31 are approaching each other on their first orbit (Li and White 2008; Kahn and Woltjer 1959).

1.3.1. The Structure of the Milky Way

The MW is the second largest galaxy in the LG next to M31. Both galaxies are spiral disc galaxies with roughly $10^{10} - 10^{11}$ stars. Due to the sun's special location inside the MW this galaxy is the only one for which we obtain fully resolved stellar data of the components of a spiral galaxy. Thus, it will always be the most important benchmark galaxy to test our galaxy formation models[7].

The sun is located at about 8 kpc from the Galactic center (Ghez et al. 2008; Gillessen et al. 2009) and is with 25 pc slightly offset from the Galactic mid-plane (Jurić et al. 2008). The sun's rotation speed around the Galactic center is approximately 220 km s^{-1} (Kerr and Lynden-Bell 1986). Viewed from earth, the stellar disc of the MW appears as a milky band stretching across the whole sky[8] as illustrated in figure 1.5 which shows the MW as seen by the Gaia satellite (Gaia Collaboration et al. 2016b). In this section I will briefly discuss the main components of the MW (the halo, the stellar disc and the central stellar bulge) which are assumed to trace different stages of its formation. Great parts of this section are based on the recent review by Bland-Hawthorn and Gerhard (2016) and the chapter 2.3.4 of Mo et al. (2010).

1.3.1.1. Halo

The MW stellar disc is embedded in a three-dimensional halo of gas, stars and dark matter which is still growing by accreting matter. While the three components spatially overlap they do not necessarily share the same structural properties or formation histories. However, all components live in the same gravitational potential which in the inner parts is dominated by the bulge, the disc and the dark halo and at large scales ($\sim$ 100 kpc) is solely dominated by the dark matter halo.

Stellar Halo: The stellar halo of the MW is an extended spheroidal structure containing about 1% of the total stellar mass (Bland-Hawthorn and Gerhard 2016). The stars in the stellar halo show large random motions with only little net rotation ($\lesssim$ 40 km s^{-1}) and the stellar density follows a power law with radius. The formation history of the stellar halo is assumed to be complex but two main mechanisms are believed to dominate: (i) Part of the stellar halo was formed during the initial collapse of the Galaxy from low metallicity gas at the time when also the bulge was forming (Eggen et al. 1962; Abadi et al. 2006). (ii) More recent observations show that the stellar

[7] Note: There are indications that the MW might be an exceptional representative of the large spiral galaxy population (see e.g. the review of Bland-Hawthorn and Gerhard 2016)

[8] This milky appearance on the sky is the reason for its name and the general name galaxy is derived from the Greek word *γάλα* (gála) which means "milk".

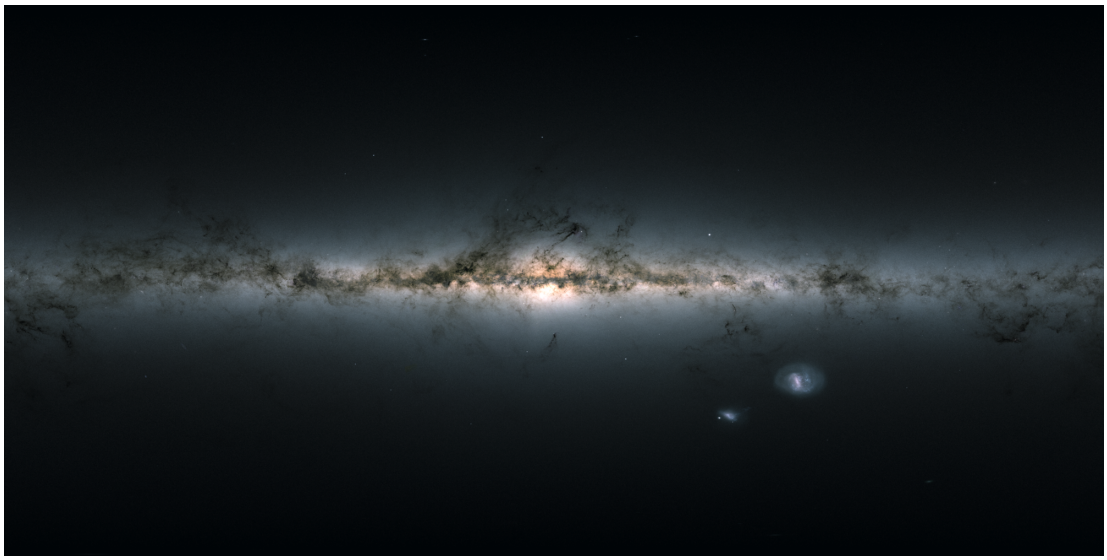


Figure 1.5: All-sky view of our MW Galaxy and neighbouring galaxies as seen by the Gaia satellite. Visible are 1.7 billion stars in the thin stellar disc, the bulge and the satellite galaxies of the MW partly obscured by interstellar dust (dark patches and filaments). In the lower right of the image the Large and Small Magellanic Clouds, two dwarf galaxies orbiting the MW are visible. Amazingly, two other nearby galaxies are also visible, the Andromeda galaxy (also known as M31) along with its satellite, the Triangulum galaxy (M33). They are located on the left side slightly below the stellar disc of the MW. The map shows the total brightness and colour of stars observed by the ESA satellite in each portion of the sky between July 2014 and May 2016. **Figure credit:** ESA/Gaia/DPAC; A. Moitinho / A. F. Silva / M. Barros / C. Barata, University of Lisbon, Portugal; H. Savietto, Fork Research, Portugal (`http://sci.esa.int/gaia/60196-gaia-s-sky-in-colour-equirectangular-projection/`).

halo consists of multiple components and unrelaxed substructures which originate from accreted and disrupted satellite galaxies (Searle and Zinn 1978; Ibata et al. 1997; Belokurov et al. 2006; Schlaufman et al. 2009). Because of the long dynamical times in the halo these tidal tails, shells and over-densities remain observable for several Gyr and provide a fossil record of the MW's accretion history (Helmi 2008; De Lucia et al. 2012; Belokurov 2013). For a more detailed discussion of the properties and formation of the stellar halo see section 6 of the review of Bland-Hawthorn and Gerhard (2016).

Hot Gas Halo: Next to the stellar halo there exists a corona of hot ($\sim 10^6$ K), diffuse gas. The structure of the Galactic hot halo comprises two main components: An inner part which follows an exponential profile and which consists of high-metallicity ($Z > 0.3Z_\odot$) gas with a scale height of a few kpc and a more extended ($\gtrsim 100$ kpc), more diffuse low metallicity component (Yao and Wang 2007). The total mass of the hot gas halo is estimated to be of the order of $\sim 2.5 \pm 1 \times 10^{10}$ $M_\odot$ within $r \sim 250$ kpc (Miller and Bregman 2013, 2015) which thus contributes about $\sim 28\%$ to the total baryon budget of the MW (Bland-Hawthorn and Gerhard 2016).

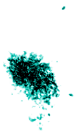
Dark Halo: In the context of ΛCDM the total mass of the MW is dominated by its dark matter halo which is much more extended than the baryonic component of the galaxy living inside it. The dark halo dominates the evolution of the Galaxy on large scales and its total mass and extent sets how much baryonic mass will be accreted and how much of the expelled gas can be retained. The exact total mass depends on the definition of the virial mass and the virial radius (see section 1.2.2.2). Current estimates for the MW give values of $R_{\rm vir} \sim 282 \pm 30$ kpc and $M_{\rm vir} \sim 1.1 \pm 0.3 \times 10^{12}$ $M_\odot$ with sensitive dependence on the tracer used to estimate the density distribution of the halo (for further discussion see Bland-Hawthorn and Gerhard 2016, and references therein). Next to the total mass of the dark halo its shape is of considerable interest. Dark matter only simulations suggest that dark halos are prolate-triaxial and strongly flattened (e.g. Dubinski and Carlberg 1991; Allgood et al. 2006). However, after inclusion of baryons these halos tend to become much more spherical and evolve towards an oblate shape (e.g. Kazantzidis et al. 2004; Abadi et al. 2010). The favoured shape of the MW's dark halo is spherical or slightly oblate but no consistent picture has emerged yet (Bland-Hawthorn and Gerhard 2016, and references therein).

1.3.1.2. The Disc of the MW

The most prominent feature of the MW is its (stellar) disc. The largest part of the baryonic mass budget of the MW is residing in a disc like structure of total mass $\sim 5 \times 10^{10}$ $M_\odot$ which is dominated by stellar mass. The main components of the disc are a thin stellar disc, a thick stellar disc and a gas disc.

The Gas Disc: MW's gas disc consists of $\sim 10^9$ $M_\odot$ of cold gas mostly on circular orbits. About 80% of the gas is neutral HI gas while only 20% is molecular gas mostly residing in a ring-like structure around 4.5 kpc. The scale height of the neutral gas disc is about 150 pc and its velocity dispersion is ~ 9 km s $^{-1}$. The surface density of cold gas is roughly constant in the radius range 4 to 17 kpc and rapidly declining towards smaller and larger radii. Ongoing star formation can be found in the densest parts of the molecular ring and in the molecular cloud complexes with densities of ~ 100 atoms per cm^3.

The Stellar Disc: Historically the stellar disc of the MW is separated into a thin and a thick disc based on a double exponential fit to stellar number counts in MW surveys (e.g. Gilmore and Reid 1983; Kuijken and Gilmore 1989). This is well in line with results for external galaxies derived from fitting the surface brightness profiles of these galaxies (Yoachim and Dalcanton 2006). Subsequently, it was found that stars of the two discs have different ages, kinematics and chemistry which motivated the geometrically defined separation of the two discs (Fuhrmann 1998; Gratton et al. 2000). The thick disc has a scale height of ~ 1 kpc (the thin disc has a scale height of only ~ 300 pc), is on average older (average stellar age ~ 12 Gyr Gilmore et al. 1995; Bensby



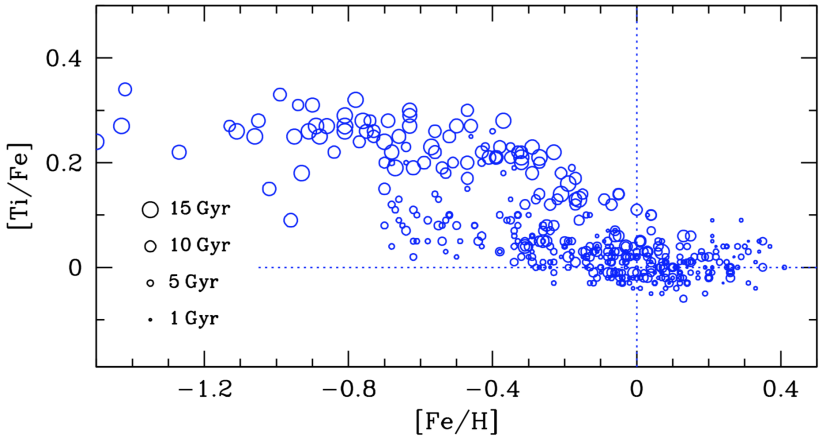


Figure 1.6: The thick disc/thin disc bi-modality in [Ti/Fe] vs. [Fe/H] abundance space for 700 F, G dwarf stars with age determinations. This figure shows a uniformly old thick disc population with enhanced [α/Fe] abundance, and a dominant thin disc population with a spread of ages. The circle sizes scale with age and have uncertainties of the order of $\sim$ 1 Gyr while the metallicity uncertainties are smaller than 0.1 dex. **Figure credit:** Bensby et al. (2014)

et al. 2003), is α-enriched and more metal-poor and is kinematically hotter compared to the thin disc. While today it is well accepted that there is substructure in the MW's stellar disc, a separation solely based on spatial properties is misleading. Studies by Bovy et al. (2012a) and Bovy et al. (2012b) have shown that there is no clear bi-modality in phase-space but disc stars have rather continuously varying properties with scale heights between $\sim$ 200 pc and $\sim$ 1 kpc. On the other hand, many studies (e.g. Haywood et al. 2013; Nidever et al. 2014; Hayden et al. 2015; Masseron and Gilmore 2015) have shown that there exists a bi-modality in abundance space as highlighted in figure 1.6 taken from Bensby et al. (2014). Thus, the better definition of the two dominant structures in the stellar disc would be via the star's "low-α"/"high-α" abundance. Another advantage of defining the disc structure in abundance or stellar age space owes to the fact that the spatial distribution of stars might change due to external or internal perturbations which do not effect stellar abundances and ages.

Especially with photometric metallicities derived from the Sloan Digital Sky Survey (SDSS) survey it was found that there is only a gradual transition in photometric metallicities and kinematics across the thin disc-thick disc division, in conflict with the traditional two-component fit (Bond et al. 2010). By now it is well established that the thick disc is [α/Fe]-enhanced (Haywood et al. 2015; Hayden et al. 2015; Kordopatis et al. 2015) and the Apache Point Observatory Galactic Evolution Experiment (APOGEE) survey showed that also the C/N ratio is enhanced for thick disc stars (Masseron and Gilmore 2015). Using the distinction based on chemistry helped a lot in understanding the extent and properties of the thick disc (Bensby et al. 2010, 2011; Bovy et al. 2012a)



but lead also to the conclusion that the morphology is more complicated than assumed before (Bovy et al. 2016; Hayden et al. 2015). The present-day favoured values for the thick disc are a mass of $\sim 6 \pm 3 \times 10^9$ $M_\odot$ and a scale length of 2.0 ± 0.2 kpc (Bland-Hawthorn and Gerhard 2016). In contrast, the thin disc has a mass of $3.5 \pm 1 \times 10^{10}$ $M_\odot$ and a scale length of 2.6 ± 0.5 kpc. Yet, the exact mechanisms which lead to the formation of the thin/thick disc separation are not fully understood and several models from inside-out growth of the Galaxy (e.g. Stinson et al. 2013b) to major merger scenarios (e.g. Grand et al. 2017) are considered.

1.3.1.3. The inner Galaxy: The Bulge and the Bar of the MW

The inner Galaxy is composed of several overlapping structures and is characterised by crowded fields of stars. In the very center of the Galaxy the inner stellar disc, the bulge, the bar, the nuclear stellar disc and also the inner stellar halo overlap. While the nuclear stellar disc only extends out to about 230 pc it is important in understanding ongoing star formation on x_2-orbits in the bar (Molinari et al. 2011). However, the resolution of current cosmological simulations is not able to resolve these small scale structures and therefore I will focus in this sub-section solely on the bulge and the bar of the MW.

The Boxy/Peanut Bulge: Despite the great wealth of data for stars in the central region of the MW from the VVV survey (Minniti et al. 2010), the BRAVA survey (Kunder et al. 2012), the ARGOS survey (Ness et al. 2013b) and the GIBS survey (Zoccali et al. 2014) it is still unclear what is the nature of the MW's bulge. For many years the old ages of stars in the bulge (Clarkson et al. 2008) favoured the picture of an old merger generated bulge (classical bulge). However, since the COBE (Weiland et al. 1994; Binney et al. 1997) and the 2MASS missions (Skrutskie et al. 2006) the boxy morphology of the bulge is established. This boxy or peanut morphology is representing the inner, three-dimensional part of the Galactic bar (McWilliam and Zoccali 2010; Nataf et al. 2010) and confirms the long standing believe that the MW is a barred spiral galaxy. The Galactic bar is $27 \pm 2°$ inclined with respect to the line-of-sight (Wegg and Gerhard 2013) and has an extend of about ± 2.2 kpc in the direction of the long axis. Using unsharp masking the barred nature of the boxy/peanut bulge can be seen as an X-shaped structure in direct imaging (Portail et al. 2015b; Ness et al. 2016a).

Although there has been much progress over the last years in studying the properties of the bulge of the MW, it is still unclear if it is a pure boxy/peanut bulge or includes a classical bulge component (Bland-Hawthorn and Gerhard 2016) as indicated by the morphology (Ness et al. 2012; Dékány et al. 2013; Pietrukowicz et al. 2015) and kinematics (Kunder et al. 2016) of RR Lyrae stars. For the same reason the formation scenario of the bulge is still under debate. The MW bulge shows a well-established vertical metallicity gradient (Zoccali et al. 2008; Johnson et al. 2011; Gonzalez et al. 2013)



which is often interpreted as the signature of a dissipatively formed classical bulge. On the other hand, violent relaxation is inefficient during the buckling instability of the bar and preexisting metallicity gradients would map into outward metallicity gradients in the final boxy/peanut bulge (Martinez-Valpuesta and Gerhard 2013a; Di Matteo et al. 2014; Fragkoudi et al. 2018). Furthermore, stars in the peanut bulge are cylindrically rotating (Kunder et al. 2012; Ness et al. 2013b) and show complex morphology and kinematics as a function of stellar metallicity (e.g. Ness et al. 2013a).

So far galaxy formation models result in the formation of both bulge components together, first the formation of a classical bulge component after a rapid early starburst and then successively the formation of a second component which forms after the disc build-up via instabilities (Samland and Gerhard 2003; Obreja et al. 2013). The issue of the formation of a boxy/peanut bulge resembling the kinematic and morphological properties of the MW's bulge is further addressed in chapter 3.

1.3.2. The Dwarf Galaxy System of the Local Group

The dwarf galaxies of the LG come in two flavours, they are either satellite galaxies of the two large spiral galaxies or they are relatively isolated and most presumably on their first infall into the LG. This second category has recently been shown to include a population of dwarf galaxies that had a close encounter with the MW and/or M31 in the past (Knebe et al. 2011; Teyssier et al. 2012, see also chapter 5).

The category of dwarf galaxies is defined via a threshold luminosity. Usually dwarf galaxies are fainter than $M_V \sim -18$ mag (equivalent to a stellar mass of $\sim 10^9$ $M_\odot$) which corresponds to roughly the luminosity of the Large Magellanic Cloud (LMC)[9]. The lower boundary is only loosely defined and ever more dwarf galaxies at the lowest luminosities are discovered. The faintest dwarf galaxies discovered so far have luminosities as low as $\sim 10^2$ $L_\odot$ (e.g. Seg I Belokurov et al. 2007). These dwarf galaxies are conventionally called *ultra faint dwarf galaxies* and have luminosities comparable to Globular Cluster (GC) of the order of $\lesssim 10^5$ $M_\odot$. The differentiating criteria is the dark matter content. While star clusters are entirely made up of stellar mass (mass-to-light ratio of ~ 1), the mass budget of dwarf galaxies is dominated by dark matter with mass-to-light ratios of up to ~ 1000 (Simon et al. 2011). Further differences between the two object classes can be found in size and star formation history. Dwarf galaxies have in general larger sizes (about a factor ten larger) and longer star formation time scales compared to GC which are relatively compact objects comprising a simple stellar population with a relatively narrow metallicity distribution (Willman and Strader 2012;

[9]The earliest known reference to the Magellanic Clouds is from the Persian astronomer Abd al-Rahman al-Sufi. He mentions the Magellanic Clouds in his *Book of Fixed Stars* from 964 (which further includes the earliest recorded reference to the Andromeda Galaxy).



Leaman et al. 2012). In contrast, some dwarf galaxies have been forming stars over a Hubble time (Weisz et al. 2011).

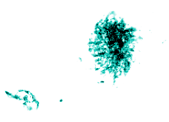
With the onset of large scale and dedicated surveys such as SDSS, VLT-ATLAS, Pan-STARRS, Pan-Andromeda Archaelogocal Survey (PAndAS McConnachie et al. 2009a), Dark Energy Survey (DES) (Drlica-Wagner et al. 2015), and SMASH (Bechtol et al. 2015; Koposov et al. 2015a; Martin et al. 2015; Belokurov et al. 2014; Laevens et al. 2014, 2015b,a) the number of known dwarf galaxies in the LG almost tripled from only ~ 40 known dwarf galaxies at the beginning of the 21st century (Mateo 1998) to over ~ 100 by today.

The LG offers a unique opportunity to study the properties of dwarf galaxies. Due to their low luminosity the only possibility to detect dwarf galaxies with stellar masses below $\sim 10^7$ $M_\odot$ is inside the LG. Furthermore, only for the dwarf galaxies in the LG it is possible to obtain resolved stellar spectra and photometry which makes it possible to reconstruct their velocity dispersion and mass profiles (Walker et al. 2010). This makes the LG an ideal laboratory to test the predictions of the ΛCDM cosmological model and from galaxy formation models on the dwarf galaxy scale.

1.4. Cosmological Simulations of Galaxy Formation

In this section I will briefly summarise the numerical techniques and tools used to solve the problem of galaxy formation. This section is partly based on the review article about the Smoothed Particle Hydrodynamics (SPH) method by Springel (2010).

Astrophysical research, especially the field of galaxy formation relies heavily on numerical simulations and many of the progress in understanding the (non-linear) outcome of different physical mechanisms is due to improved numerical methods. By now various different numerical schemes exist and agree on the outcome of the collisionless particle-based N-body simulation (Hockney and Eastwood 1981) of structure formation. However, in order to accurately represent the evolution of the collisional baryons, the equations of hydrodynamics have to be solved. Additionally, further physical mechanisms such as radiation fields, magnetic fields, or non-thermal particles need to be modelled in order to follow the evolution of galaxies. In principle, any theory of galaxy formation needs to bridge the scales from cosmic structure formation to atomic physics covering some 35 orders of magnitude. Therefore simulations of galaxies have always been limited by their spatial and mass resolution and any numerical code on the market relies heavily on methods to describe the important physical mechanisms relevant to galaxy formation but which are below the resolution limit of the simulation (sub-grid models). Such models are commonly applied to star



formation, stellar feedback, black hole formation or the feedback from AGN under the assumption that the small-scale physics can be captured in effective theories which model their large scale effects.

All simulations used in this thesis are run with the SPH code `Gasoline2` (Wadsley et al. 2017). In this section I will describe the important physical models implemented in the code and introduce the sample of galaxy formation simulations.

1.4.1. Smooth Particle Hydrodynamics

The principal idea behind SPH (Monaghan 1992) is to sample the fluid field with a set of particles and treat the fluid in completely mesh-free Lagrangian fashion. The hydrodynamical equations of motion are derived for this set of particles with excellent conservation properties: SPH conserves simultaneously energy, linear and angular momentum, mass, and entropy (if no artificial viscosity operates) and is fully Galilean invariant (which is not the case for mesh-based Eulerian techniques, Springel 2010). Another advantage of the SPH method is its inherent adaptive resolution which automatically follows the mass flow owing to its Lagrangian nature. This makes the SPH method a extremely convenient tool which is able to adequately represent the large density contrasts often encountered in astrophysical problems. Due to its particle based nature, the SPH method can easily be combined with accurate treatments of self-gravity and additional sub-resolution models of unresolved physical processes like star formation or stellar feedback can be added directly at the particle level.

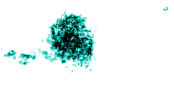
Kernel Interpolants: The very basis of the SPH method are the kernel interpolants (Gingold and Monaghan 1982) through which a smoothed interpolation of every field can be derived. In particular, the density field is reconstructed through a kernel summation. In the most general form the smoothed version, $F_s(\boldsymbol{r})$, of a field $F(\boldsymbol{r})$ can be derived through a convolution with a kernel $W(\boldsymbol{r}, h)$:

$$F_s(\boldsymbol{r}) = \int F(\boldsymbol{r}) W(\boldsymbol{r} - \boldsymbol{r}', h)\, \mathrm{d}\boldsymbol{r}' \tag{1.6}$$

Here, h describes the smoothing length, the characteristic width of the kernel, which is normalised to unity. Further requirements are that the kernel is symmetric and sufficiently smooth in order to make it at least twice differentiable. Currently most SPH implementations use kernels with finite support like the cubic spline kernel used in `Gasoline2`.

If the field is known at some points $\boldsymbol{r}_i$, $F_i = F(\boldsymbol{r}_i)$, with associated mass m_i and density ρ_i such that the associated finite volume element is $\Delta\boldsymbol{r}_i = m_i/\rho_i$ then the integral in Equation 1.6 can be approximated by a sum given the points are sufficiently densely sampled:

$$F_s(\boldsymbol{r}) \approx \sum_j \frac{m_j}{\rho_j} F_j W(\boldsymbol{r} - \boldsymbol{r}_j, h) \tag{1.7}$$



This expression is second-order accurate for sufficient large number of neighbouring particles (> 33) and defines the estimate $F_s(\boldsymbol{r})$ everywhere. Especially, the expression for the density $\rho(\boldsymbol{r})$ follows from this if we set $F_j = \rho_j$:

$$\rho(\boldsymbol{r}) \approx \sum_j m_j W(\boldsymbol{r} - \boldsymbol{r}_j, h) \tag{1.8}$$

which yields the density solely based on particle position and mass. The advantage of adaptivity results from the fact that the smoothing length can be made variable in space, $h = h(\boldsymbol{r}, t)$, in order to account for variations in the sampling density. `Gasoline2` adopts the so-called gather approach in which the number of neighbours, n, is kept fixed and the smoothing length h_i for particle i is defined as the distance to the n^{th} nearest neighbour. This ensures that the smoothing length is smaller in densely sampled regions and has the advantage that e.g. density estimates are obtained with a computational cost of $\mathrm{O}(nN)$ if kernels of finite support are used (Springel 2010).

1.4.2. `Gasoline2`

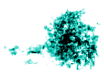
The SPH code `Gasoline2` (Wadsley et al. 2004, 2017) is based on the N-body solver `pkdgrav` (Stadel 2001) and includes substantial updates to the hydrodynamics as described in (Keller et al. 2014). This formulation of the hydrodynamics removes spurious numerical surface tension and improves multi-phase mixing by calculating P/ρ^2 as a geometrical average over the particles in the smoothing kernel as proposed by Ritchie and Thomas (2001). The Saitoh and Makino (2009) timestep limiter was implemented so that cool particles behave correctly when a hot blastwave hits them and `Gasoline2` uses the Wendland C2 smoothing kernel (Dehnen and Aly 2012) to avoid pairing instabilities. The treatment of artificial viscosity has been modified to use the signal velocity as described in Price (2008) and the number of neighbour particles used in the calculation of the smoothed hydrodynamic properties is set to 50.

1.4.2.1. SUB-GRID PHYSICS MODELS

The version of `Gasoline2` used in this thesis implements a number of sub-grid physics which are also shared by the NIHAO[10] simulation suite (Wang et al. 2015). Below I lay out the most important models implemented to describe star formation, stellar feedback and gas cooling and heating from a uniform UV background.

Star Formation: `Gasoline2` implements star formation from cold and dense gas such that the Kennicutt-Schmidt Law (Schmidt 1959; Kennicutt 1998) is resembled on large scales. The simulations employ the star formation recipe as described in Stinson et al. (2006) with updates as described in Stinson et al. (2010). This star formation

[10] Nihao is the chinese word for *hello*.



prescription follows a common method first described by Katz (1992) where stars form from cool (T < 15,000K), dense gas ($n_{\rm th} > 10.3$ cm^{-3}). The threshold number density $n_{\rm th}$ is set to the maximum density at which gravitational instabilities can be resolved in the simulation: $\mathrm{n_{th}} = 50 m_{\rm gas}/\epsilon^3_{\rm gas} = 10.3$ cm^{-3}, where $m_{\rm gas}$ denotes the gas particle mass and $\epsilon_{\rm gas}$ the gravitational softening of the gas. The value of 50 denotes the number of neighbouring particles. The gas fulfilling these requirements will then be converted into stars according to the following equation:

$$\frac{\Delta M_\star}{\Delta t} = c_\star \frac{M_{\rm gas}}{t_{\rm dyn}} \tag{1.9}$$

where $\Delta M_\star$ is the mass of the star particle formed, $M_{\rm gas}$ the gas particle's mass, Δt is the timestep between star formation events (here: 8×10^5 yr) and $t_{\rm dyn} = (4\pi G\rho)^{-1/2}$ is the gas particles dynamical time. $c_{\rm star}$ is the star formation efficiency, i.e. the fraction of gas that will be converted into stars during the time $t_{\rm dyn}$ and is taken to be $c_\star = 0.1$. During the process of star formation the determined gas mass which will form a star is subtracted from the gas particle's mass and a new star particle of this exact same mass will be introduced. Each stellar particle formed in this way is much more massive than any star in the Universe and is thus in the very strict sense just a tracer particle of the discretisation of the stellar density field. In a qualitative sense these particles can be referred to as star cluster particles representing a Simple Stellar Population (SSP) whose internal mass distribution is represented by an Initial Mass Function (IMF) which follows a Chabrier IMF (Chabrier 2003) in `Gasoline2`. Another important difference between stellar and gas particles is that stellar particles are collisionless and only obey the laws of gravity in the simulation. During the simulation stellar evolution of the SSP is modelled including the ageing effects of the stellar population. These effects include the explosion of massive stars as supernovae at the end of their lives and are known as stellar feedback which I described in the next paragraph.

Stellar Feedback: Stellar feedback is implemented in two modes following the description in Stinson et al. (2013b). The first mode accounts for the energy input from stellar winds and photo ionisation from luminous young stars. This pre-SN feedback was dubbed *Early Stellar Feedback* (ESF) in Stinson et al. (2013b) and happens before any supernovae explode. It consists of 10% of the total stellar flux, 2×10^{50} erg of thermal energy per $M_\odot$ of the entire stellar population. The efficiency parameter for the coupling of the energy input is set to $\epsilon_{\rm ESF} = 13\%$. And for the pre-SN feedback, unlike the SN feedback, the radiative cooling is left on.

The second mode accounts for the energy and metal input via supernovae from stars in the mass range $8\mathrm{M}_\odot < M_\star < 40\mathrm{M}_\odot$ and is implemented using the blastwave formalism described in Stinson et al. (2006). In this approach supernovae input energy (i.e. thermal feedback) into the interstellar gas surrounding the region were

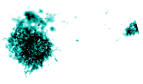


Table 1.1: Simulation parameters for the dark matter, gas and stellar particles in our simulation runs.

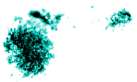
property	particle mass $[10^5 M_\odot]$	Force soft. [pc]	Smoothing length (median, min.) [pc]	particles within R_{200}
		g2.79e12		
DM	5.141	620	-	5,413,017
GAS	0.938	265	(155, 20)	2,224,231
STARS	0.313	265	-	8,249,934
		g1.12e12		
DM	1.523	414	-	7,454,484
GAS	0.278	177	(200, 11)	3,041,329
STARS	0.093	177	-	11,087,938
		g8.26e11		
DM	2.168	466	-	3,742,713
GAS	0.396	199	(194, 32)	1,665,173
STARS	0.132	199	-	4,171,413
		g7.08e11		
DM	1.11	373	-	4,439,242
GAS	0.203	159	(117, 28)	2,004,656
STARS	0.068	159	-	4,861,964

the progenitor stars have formed. Since the gas receiving the energy is dense, it would quickly be radiated away due to its efficient cooling. For this reason, cooling is artificially delayed for particles inside the blast region for ~ 30 Myr. This time is extended if another supernova blast wave hits the gas particle within this time. Finally, the mass of the exploding supernovae is subtracted from the stellar particle mass and the mass of metals returned to the ISM, calculated from stellar evolution models, is distributed over the gas particles in the feedback kernel.

Gas Cooling/Heating and Metal Diffusion: Gas cooling via hydrogen, helium, and most importantly various metal-lines is included as described in Shen et al. (2010b) and was calculated using `cloudy` (version07.02; Ferland et al. 1998). These calculations include photoionisation and heating from the Haardt and Madau (2005) UV background and Compton cooling in a temperature range from 10 to 10^9 K. A metal diffusion algorithm between particles as described in Wadsley et al. (2008) is adopted to account for the turbulent mixing of metals in the ISM.

1.4.3. Application: The NIHAO Sample of Galaxies

Chapter 2 of this thesis uses the MW mass galaxies of the NIHAO simulation suite (Wang et al. 2015) which contains in total nearly 100 zoomed cosmological simulations (see Oñorbe et al. 2014, for further information on the zoom technique) of galaxy formation across a wide range in stellar mass from $10^5 < M_\star/M_\odot < 10^{11}$. Chapter 3, 4 and 5 use higher resolution versions of some of the MW mass galaxies of the original sample run with the same feedback prescriptions. The NIHAO galaxies have been modelled using cosmological parameters from the Planck Collaboration et al.



(2014), namely: $\Omega_m = 0.3175$, $\Omega = 0.6825$, $\Omega_b = 0.049$, $H_0 = 67.1$ km s^{-1} Mpc^{-1}, $\sigma_8 = 0.8344$. Chapter 6 uses high-resolution dark matter only simulations to study the alignment of satellite galaxies around MW mass galaxies. These simulations employ the same cosmology as the NIHAO galaxies and are run with the N-body solver `pkdgrav2`.

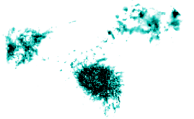
Definition of Masses and Sizes: Throughout this thesis the virial mass of each dark matter halo, M_{200}, is defined as the mass of all particles within a sphere containing Δ = 200 times the cosmic critical matter density, ρ_{crit} . The virial radius, R_{200}, is defined accordingly as the radius of this sphere. The haloes in the zoom-in simulations were identified using the MPI+OpenMP hybrid halo finder `AHF2`[11] (Knollmann and Knebe 2009; Gill et al. 2004). Stellar masses, M_{star}, and gas masses, M_{gas}, are measured within a sphere of radius, $r_{gal} \equiv 0.2R_{200}$. The star formation rate, SFR, is measured as the mass of stars formed inside r_{gal} over the preceding Gyr and the gas fraction f_{gas} is defined as the fraction of cold gas ($T < 3 \times 10^4$ K) over the total baryonic mass within r_{gal}.

Numerical Resolution: One peculiarity of the original NIHAO suite is that the numerical resolution, i.e. the number of elements (particles) representing each galaxy, is kept roughly constant over the whole mass range with of the order of one million particles (gas+stars+dm) in each simulated galaxy. The mass resolution is either $m_{dark} = 1.735 \times 10^6 M_\odot$ or $m_{dark} = 2.169 \times 10^5 M_\odot$ for dark matter particles and $m_{gas} = 3.166 \times 10^5 M_\odot$ or $m_{gas} = 3.958 \times 10^4 M_\odot$ for the gas particles. The corresponding force softenings are $\epsilon_{dark} = 931.4$ pc and $\epsilon_{dark} = 465.7$ pc for the dark matter particles and $\epsilon_{gas} = 397.9$ pc and 199.0 pc for the gas and star particles.

The higher-resolution versions of the MW mass galaxies (g2.79e12, g8.26e11, g7.08e11 and g1.12e12) specifically target the satellite system of the main galaxies. Thus, the mass resolution is increased by a factor of 8 to 16 compared to the standard NIHAO resolution such that it ranges between $m_{dark} \sim 1.1 - 5.1 \times 10^5 M_\odot$ for dark matter particles and $m_{gas} \sim 2.0 - 9.4 \times 10^4 M_\odot$ for the gas particles. The corresponding force softenings are $\epsilon_{dark} = 373 - 620$ pc for the dark matter particles and $\epsilon_{gas} = 160 - 265$ pc for the gas and star particles. However, the smoothing length of the gas particles can be much smaller, e.g. as low as $h_{smooth} \sim 20$ pc in the disc mid-plane. A summary of the galaxy parameters is given in table 1.1.

NIHAO galaxies have been proven to match remarkably well many of the properties of observed galaxies, as for example results from abundance matching (Wang et al. 2015), metal distribution in the Circum Galactic Medium (Gutcke et al. 2017), the local velocity function (Macciò et al. 2016; Dutton et al. 2017) and the properties of stellar and gaseous discs (Obreja et al. 2016) have shown. Overall NIHAO simulated galaxies are among the most realistic simulations run in a cosmological context. This means that the NIHAO sample is a perfect test bed to study galaxy formation predictions.

[11] http://popia.ft.uam.es/AHF/Download.html



1.5. SCOPE OF THIS THESIS

The present thesis studies the formation of MW type galaxies in fully cosmological context by means of hydrodynamical simulations. The whole galaxy ecosystem of the MW shows complex structure and various internal and external processes are believed to shape its present day appearance. By now it is well established that the MW system consists of the main galaxy and various small satellite galaxies all residing in a halo of dark matter completely dominating the mass budget. The main galaxy itself consists of the stellar and gaseous discs, shaped by spiral arms, and the central stellar bar, often referred to as the boxy/peanut bulge.

Looking at these structures, the questions which immediately arise are:

1. Is our knowledge about galaxy formation good enough to reproduce such structures? Can modern hydrodynamical simulations explain theses structures involving only a limited number of assumptions?

2. How do the different structures form? What is the importance of a cosmological environment?

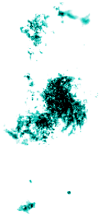
3. What information about the past state of the galactic constituents is still encoded in their present-day structure?

4. How does the main galaxy interact with its companions?

During the course of this thesis I investigate the above stated questions by analysing high-resolution state-of-the-art cosmological simulations where I split the study into two major parts. The first part of the result section focusses on the stellar disc and the bulge of MW mass galaxies while the second part studies the satellite and dwarf galaxy system of these galaxies.

In part II, I particularly focus on the early stellar discs of MW type galaxies (see chapter 2) and the formation of the peanut shaped bulge seen in the center of the MW (see chapter 3 and 4). By comparing simulated galaxy discs in the redshift range $3 > z > 0.25$ to data from the CANDELS survey I will establish the realism of the simulated discs at high redshift and use them to find out about the nature of clumpy stellar discs observed at these redshifts. These clumps have been proposed to contribute to the formation of massive bulges and thus, I will address the dynamical importance of clumps in stellar discs from a galaxy formation point of view.

In chapter 3 and 4 I will then proceed to study in detail the formation of a peanut shape bulge well matching the one observed in our own Galaxy. By contrasting the properties of the simulated bulge to the observed ones, I will establish the excellent agreement between the two and hence use the simulation to find out about the formation mechanisms and the observational prospects of verifying them. In the simulation



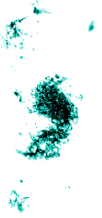
the peanut shaped bulge is mostly formed from disc material making the stars in the bulge indistinguishable from inner disc stars except for their kinematical properties. Thus, the only possibility to cleanly separate bulge and disc stars is with future surveys or data releases such as 4MOST, APOGEE-2 or Gaia DR-3.

In part III I turn to analyse the larger scale galactic environment of MW type galaxies using their dwarf galaxy population. The main focus here are the properties of the satellites vs. the dwarf galaxies and how these are effected by the host.

In chapter 5 I investigate the dwarf galaxy population of very high-resolution hydrodynamical simulations of MW type galaxies. As explained in section 1.2.4 there have been long-standing issues in explaining the properties and formation of Galactic dwarf galaxies in the framework of ΛCDM. While I not specifically focus on these problems, the comparison of the simulated dwarf galaxy population with observed data clearly shows that modern feedback implementations and hydrodynamical schemes result in realistic dwarf galaxies when simulated in the correct galactic environment. These simulations are then used to study the observational prospects of identifying dwarf galaxies which had past close encounters with the MW or M31 and to pin-down the environmental effect of such an encounter.

Finally, in chapter 6 I turn to analyse a set of high-resolution dark matter only simulations for the presence of planes of satellite galaxies such as the one observed around the MW and M31. Contrary to prior believes, such planes can be found in simulations in the framework of ΛCDM. I use the planes most similar to the observed ones to study their temporal evolution. I find that these planes are not kinematical coherent structures as suggested previously. This prediction could recently be verified by the Gaia data release 2 from which proper motions of MW satellites could be derived (Gaia Collaboration et al. 2018).

I conclude this thesis in part IV by summarising my results and putting them into context of future research.





Disc galaxy NGC891 viewed edge-on. ***Figure credit:*** Composite Image Data - *Subaru Telescope (NAOJ), Hubble Legacy Archive, Michael Joner, David Laney (West Mountain Observatory, BYU);* Processing - *Robert Gendler*[7]

Interacting grand design spiral galaxy M51 (Whirlpool galaxy). ***Figure credit:*** *SDSS*[8]

Pinwheel galaxy, M101, with prominent dust lanes. ***Figure credit:*** *ESA & NASA*[9]

The Spindle Galaxy, M102, with a prominent dust lane and bright stellar halo. ***Figure credit:*** *NASA, ESA and the Hubble Heritage Team (STScI/AURA)*[10]

Barred spiral galaxy NGC5162. ***Figure credit:*** *SDSS*[11]

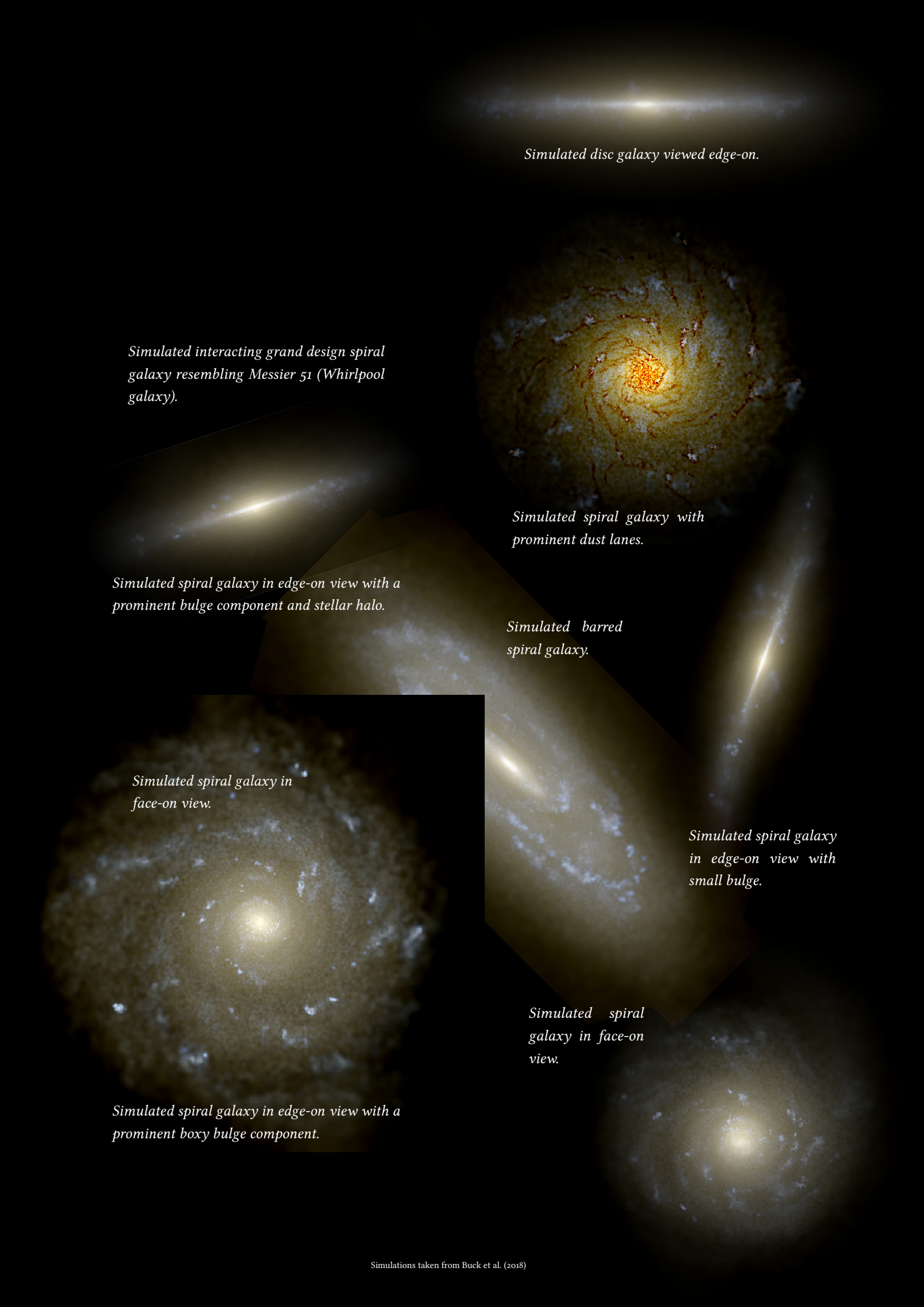
Spiral galaxy NGC3184. ***Figure credit:*** *SDSS*[12]

Spiral galaxy NGC4634. ***Figure credit:*** *ESA/Hubble & NASA*[13]

Spiral galaxy M74 in face-on view. ***Figure credit:*** *Gemini Observatory, GMOS Team*[15]

Spiral galaxy NGC4565 in edge-on view with a prominent boxy bulge component but almost no stellar halo. ***Figure credit:*** Acquisition - *Torsten Grossmann,* Processing - *Dietmar Hager*[14]

[7]https://apod.nasa.gov/apod/ap120526.html [8]http://www.sdss.org/science/m51/ [9]http://www.spacetelescope.org/news/html/heic0602.html [10]https://www.nasa.gov/feature/goddard/2017/messier-102-the-spindle-galaxy [11]http://classic.sdss.org/iotw/NGC5162.jpg [12]http://classic.sdss.org/iotw/NGC3184.jpg [13]http://www.spacetelescope.org/images/potw1238a/ [14]https://apod.nasa.gov/apod/ap100304.html [15]https://apod.nasa.gov/apod/ap011004.html



Simulated disc galaxy viewed edge-on.

Simulated interacting grand design spiral galaxy resembling Messier 51 (Whirlpool galaxy).

Simulated spiral galaxy with prominent dust lanes.

Simulated spiral galaxy in edge-on view with a prominent bulge component and stellar halo.

Simulated barred spiral galaxy.

Simulated spiral galaxy in face-on view.

Simulated spiral galaxy in edge-on view with small bulge.

Simulated spiral galaxy in face-on view.

Simulated spiral galaxy in edge-on view with a prominent boxy bulge component.

Simulations taken from Buck et al. (2018)

Part II

The Formation of Milky Way's Stellar Components

Chapter 2

Clumpy Discs from Redshift 3 to 0.5

The fact that we live at the bottom of a deep gravity well, on the surface of a gas covered planet going around a nuclear fireball 90 million miles away and think this to be normal is obviously some indication of how skewed our perspective tends to be.

— Douglas Adams, The Salmon of Doubt: Hitchhiking the Galaxy One Last Time

The content of this chapter has been published in similar form in a peer reviewed journal (Buck et al. 2017). I am the first author of that paper and all the research presented here has been conducted by me and I have further written the text of that paper myself. The contribution of my co-authors have been valuable comments regarding the figures or passages of the text.

Subject of this chapter are the properties and the formation of the early stellar disc of MW type galaxies. Observations of discy galaxies in the redshift range $z \sim 0.5 - 3$ show that these galaxies exhibit a clumpy morphology poorly resembling the well structured spiral morphology seen at redshift $z = 0$. I explore the nature of such luminous clumps by means of numerical hydrodynamical simulations of MW type galaxies in a fully cosmological context. For this reason I utilise 19 disc galaxies of the NIHAO sample introduced in sub-section 1.4.3 which have been proven to be amongst the most realistic galaxy formation simulations. In order to facilitate comparison between observed and simulated data on an equal footing the simulation outputs are post-processed by a radiative transfer code (`GRASIL-3D`).

One of the main goals of this study is to test the efficiency of the feedback in cosmological simulations by looking at how realistic the properties of simulated galaxies are w.r.t. observed ones. Galaxy morphology is an ideal test for this because the strength of the (stellar) feedback has a strong impact in promoting or suppressing

the formation of stellar clumps and thus presents a test case independent of other properties such as e.g. total stellar mass or the position in the abundance matching relation diagram.

2.1. CONTEXT

The presence of bright clumps in the light distribution of high redshift ($z \sim 0.5 - 3$) star forming galaxies has attracted a lot of attention both from an observational and a theoretical point of view. Observations have shown that disc galaxies in the early universe have higher gas-fractions (Daddi et al. 2010; Tacconi et al. 2010, 2013; Genzel et al. 2015), star formation rates (Genzel et al. 2006; Förster Schreiber et al. 2006; Genzel et al. 2008) velocity dispersions (Elmegreen and Elmegreen 2005; Förster Schreiber et al. 2006) and a clumpy morphology (Genzel et al. 2008; Förster Schreiber et al. 2011; Guo et al. 2015) compared to their counterparts at $z = 0$.

Observationally these clumps are mostly identified in the rest-frame UV, optical or H_α maps (Elmegreen et al. 2007, 2009; Genzel et al. 2011; Förster Schreiber et al. 2011; Guo et al. 2012; Wuyts et al. 2012; Tadaki et al. 2014; Murata et al. 2014), although sometimes they are also found in the CO line emission of lensed galaxies (Jones et al. 2010; Swinbank et al. 2010). They have sizes of about $\sim$ 1kpc with inferred masses between $10^7 M_\odot - 10^9 M_\odot$. The overall fraction of star-forming galaxies with observed clumps shows significant evolution with redshift (Guo et al. 2015; Shibuya et al. 2016) and increases up to ~50%. However, the number of galaxies with observed clumps shows a large uncertainty among different measurements.

Wuyts et al. (2012) found that the clumpy fraction depends sensitively on the selected wavelength to define clumps. They find that the clumpy fraction decreases from ~75% for clumps selected in 2800 Å images to ~40% in the V-band. This suggests a connection between the presence of luminous clumps and recent star formation episodes, as also indicated by the observation that some clumps are seen to be the launching spots of outflows from the disc (Genzel et al. 2011). However, carefully constructed stellar mass maps of galaxies show no signs of prominent clumps (Wuyts et al. 2012).

Several theoretical studies have focused on an explanation for the formation of these giant star-forming clumps either analytically (Dekel et al. 2009b), in isolated disc galaxy simulations (Bournaud et al. 2007, 2008; Bournaud and Elmegreen 2009; Inoue and Saitoh 2014; Bournaud et al. 2014; Tamburello et al. 2015; Mayer et al. 2016) or in cosmological simulations of galaxy formation (Ceverino et al. 2010, 2012; Genel et al. 2012; Hopkins et al. 2012; Mandelker et al. 2014; Moody et al. 2014; Mandelker et al. 2017).

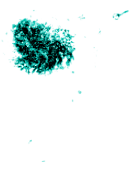
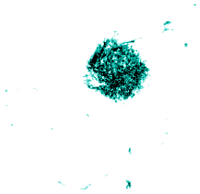


Table 2.1: Properties of the high mass end ($M_{\rm star} > 10^9$ M$_\odot$) of NIHAO galaxies at $z \sim 1.5$. From left to right I present the name of the galaxy, the number of particles within R_{200} (all species, dark matter and stars), the total mass within R_{200}, the stellar mass measured within $0.2R_{200}$, the value of R_{200}, the gas mass within $0.2R_{200}$, the fraction of cold gas (< 30000 K) and the the SFR measured within $0.2R_{200}$.

Name	N_{200}	$N_{\rm dark}$	$N_{\rm star}$	M_{200} [M$_\odot$]	$M_{\rm star}$ [M$_\odot$]	R_{200} [kpc]	$M_{\rm gas}$ [M$_\odot$]	$f_{\rm coldgas}$	SFR [M$_\odot$/yr]
g2.04e11	1,122,554	635,540	110,861	1.53×10^{11}	9.01×10^{8}	62.74	5.03×10^{9}	0.77	0.61
g2.41e11	814,971	467,054	55,838	1.13×10^{11}	4.64×10^{8}	57.18	3.35×10^{9}	0.84	0.22
g2.42e11	1,282,787	663,987	219,824	1.61×10^{11}	1.92×10^{9}	64.32	7.48×10^{9}	0.75	1.08
g2.57e11	1,408,427	714,783	314,763	1.71×10^{11}	2.81×10^{9}	64.89	6.16×10^{9}	0.61	1.99
g3.06e11	1,077,199	556,033	139,713	1.36×10^{11}	1.22×10^{9}	60.28	5.08×10^{9}	0.73	0.56
g3.49e11	1,219,383	693,736	118,777	1.67×10^{11}	1.00×10^{9}	64.48	4.12×10^{9}	0.70	0.60
g3.71e11	591,465	334,290	58,670	8.06×10^{10}	4.99×10^{8}	51.19	2.95×10^{9}	0.80	0.21
g4.90e11	824,643	454,348	92,880	1.10×10^{11}	8.16×10^{8}	56.47	4.39×10^{9}	0.76	0.68
g5.02e11	1,478,107	793,862	56,186	1.97×10^{11}	4.13×10^{8}	70.73	7.18×10^{9}	0.89	0.23
g5.38e11	1,920,057	1,123,330	121,085	2.75×10^{11}	3.25×10^{9}	76.13	0.98×10^{10}	0.72	2.24
g5.46e11	808,030	454,991	84,139	1.10×10^{11}	7.40×10^{8}	56.17	4.08×10^{9}	0.77	0.54
g5.55e11	814,019	446,562	81,263	1.08×10^{11}	6.81×10^{8}	55.99	3.82×10^{9}	0.74	0.74
g7.55e11	345,668	171,936	53,240	3.38×10^{11}	3.73×10^{9}	81.78	1.71×10^{10}	0.76	2.09
g7.66e11	357,279	180,174	31,052	3.60×10^{11}	1.35×10^{9}	83.61	1.17×10^{10}	0.78	1.93
g8.13e11	836,211	277,144	404,458	5.52×10^{11}	2.93×10^{10}	95.69	1.36×10^{10}	0.27	17.54
g8.26e11	662,237	226,691	307,793	4.49×10^{11}	2.20×10^{10}	89.60	1.47×10^{10}	0.35	10.22
g1.12e12	766,034	294,512	267,954	5.87×10^{11}	1.96×10^{10}	97.76	1.95×10^{10}	0.42	17.64
g1.92e12	2,081,091	752,770	906,338	1.49×10^{12}	6.46×10^{10}	133.25	2.24×10^{10}	0.22	38.21
g2.79e12	2,207,915	806,995	853,758	1.62×10^{12}	6.10×10^{10}	137.89	4.76×10^{10}	0.37	40.42

While some clumpy galaxies might be the result of an ongoing merger (Somerville et al. 2001), their overall high fraction can not be explained by the expected merger rate at these redshifts (Dekel et al. 2009a; Stewart et al. 2009; Hopkins et al. 2010, 2012). Another explanation for the origin of clumps, given the high gas fractions and high gas surface densities in $z > 0$ galaxies, is disc fragmentation via gravitational (disc) instabilities (Toomre 1964). Indeed, clumps are mainly observed to reside in gravitationally unstable regions (Genzel et al. 2011). The formation scenario invoked for clumps is the same as for local giant molecular clouds: local collapse and fragmentation happens in regions where the self-gravity of gas and stars is stronger than the internal support by pressure and turbulent motions.

As already mentioned, several groups have studied the dynamics and stability of discs with the aid of high resolution numerical simulations (Noguchi 1998, 1999; Dekel et al. 2009b; Agertz et al. 2009; Cacciato et al. 2012; Ceverino et al. 2015; Genel et al. 2012; Inoue and Saitoh 2012; Perez et al. 2013; Tamburello et al. 2015). In most of these studies discs do fragment and break up into large clumps, however there are two different possible scenarios for the fate of the clumps and their subsequent impact on the global evolution of the host galaxy. If clump collapse is very efficient, it could lead to the formation of gravitationally self-bound, long-lived giant star clusters. These clusters will then lose angular momentum within the disc via gravitational torques



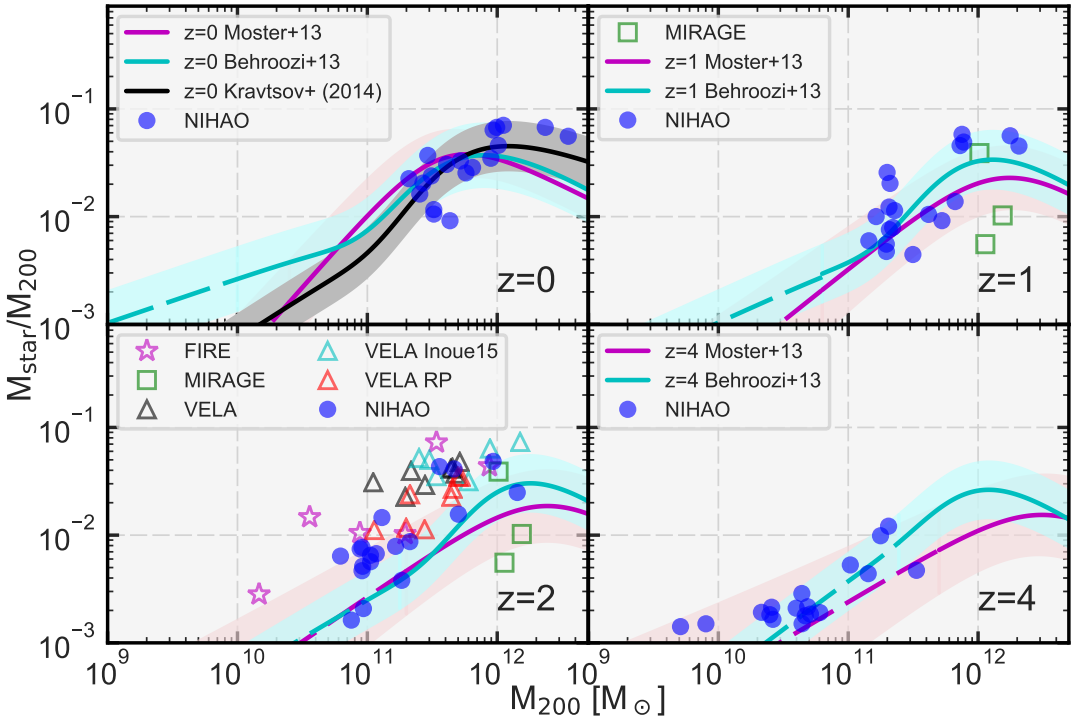
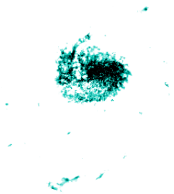


Figure 2.1: Evolution of the stellar mass vs. halo mass relation for the selection of hosts. Redshift z = 0 (top left), z = 1 (top right), z = 2 (bottom left), and z = 4 (bottom right). For all redshifts shown the simulations agree well with constraints from halo abundance matching (Moster et al. 2013; Behroozi et al. 2013; Kravtsov et al. 2014). Where the relations are extrapolated into mass scales without observational constraints the lines are shown in dashed line style.

and dynamical friction and migrate inwards on timescales of about 10^8yr to build up the central bulge (e.g. Bournaud et al. 2014). This picture seems to be supported by observed color gradients of the clumps within the disc. Clumps closer to the center of a galaxy show redder colors (Förster Schreiber et al. 2011; Guo et al. 2012; Shibuya et al. 2016) although this trend appears to be weak and might be caused by underlying evolved structures like e.g. bulges (van Dokkum et al. 2010; Patel et al. 2013; Morishita et al. 2015; Nelson et al. 2016a).

Conversely if gas cooling is suppressed, as for example in the presence of substantial stellar feedback, the resulting stellar clumps will not be self-bound and will then be quickly dispersed within the disc before experiencing any drag to the center.

Recent numerical work (Mayer et al. 2016; Oklopčić et al. 2017) has somehow suggested that when robust feedback (needed to reproduce observed galaxy properties at redshift $z = 0$) is invoked, clumps are either short lived transient features or do not form at all. Thus a treatment of feedback, that is able to prevent overcooling seems to



be crucial to understand the origin of clumpy galaxies at high redshift. On the other hand these studies were either based on a single simulated galaxy (Oklopčić et al. 2017) or they were lacking cosmological gas inflow (Mayer et al. 2016) and hence more work on the simulation side is needed.

In this chapter I revise the issue of the formation and evolution of luminous clumps in cosmological simulations of disc galaxies at $z = 0.5 - 3$ using the NIHAO simulation suite. I first compare the "clumpiness" of the galaxies with real galaxies using an observational motivated clump selection procedure based on the UV luminosity of our objects. For this purpose I have post processed all the galaxies with the radiative transfer code GRASIL-3D. (Domínguez-Tenreiro et al. 2014). Subsequently I look at the evolution of these luminous clumps and their relation with the underlying stellar mass distribution to assess their final fate and their overall impact on galaxy evolution.

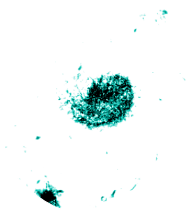
2.2. The Galaxy Sample

In order to match the stellar range of the observed galaxies at high redshift I have selected from the NIHAO sample all the galaxies with stellar masses larger than $M_{\rm star} > 10^9 M_\odot$ at redshift $z = 1.5$, obtaining a final sample of 19 galaxies. A full list of parameters of the 19 NIHAO galaxies is given in Table 2.1. From these galaxies I use all the snapshots in the redshift range $3 > z > 0.25$ where the stellar mass of the galaxy is larger than the above threshold mass. This selection criteria results 203 snapshots in the redshift range $3 > z > 1$, 155 in the redshift range $1 > z > 0.5$ and 130 in the redshift range $0.5 > z > 0.25$.

2.2.1. Stellar Mass-Halo Mass Relation

Fig. 2.1 shows the evolution of the stellar mass vs. halo mass relation since redshift z = 4 (a look back time of ~12 Gyr); NIHAO simulations (blue circles) show a very good agreement with the abundance matching relations from Behroozi et al. (2013) and Moster et al. (2013). At redshift 2 and 1 some of the higher mass galaxies show about a factor of 2 to many stars but this is consistent with e.g. the FIRE simulation Hopkins et al. (2014). Some of this discrepancy w.r.t abundance matching results might be due to systematic uncertainties in the form of the stellar Initial Mass Function (IMF, e.g. Conroy and van Dokkum (2012); Dutton et al. (2013b,a)). Thus for massive galaxies ($M_\star \gtrsim 10^{11} \mathrm{M}_\odot$) the stellar masses may be underestimated by a factor of ~ 2 when assuming a Milky Way IMF.

Comparison to the VELA galaxies (Ceverino et al. 2015; Inoue et al. 2016; Moody et al. 2014) (colored triangles in Fig. 2.1) shows these galaxies tend to substantially overproduce stellar masses at redshift 2. Inclusion of radiation pressure as an additional



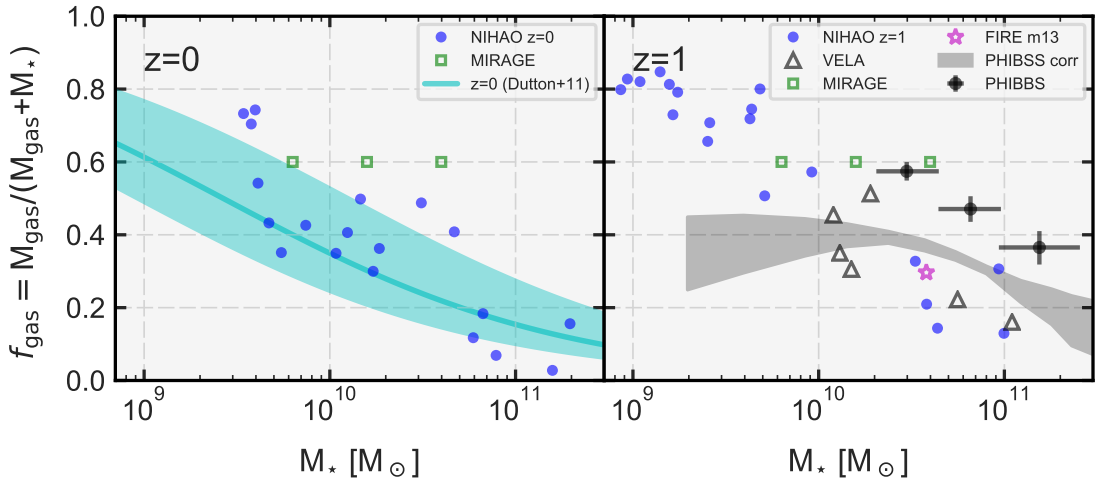


Figure 2.2: The galaxy gas fraction as a function of stellar mass at redshift $z = 0$ (left panel) and $z = 1$ (right panel). The selected NIHAO galaxies are shown with blue points and the relation from Dutton et al. (2011) for redshift 0 galaxies is shown with a cyan line with a shaded region indicating the scatter. At redshift ~ 1.5 the PHIBBS survey data (Tacconi et al. 2013) is shown as black dots. The incompleteness corrected relation from the PHIBBS survey is shown as the grey shaded area.

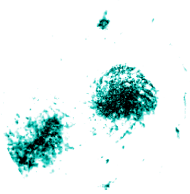
source of feedback in these galaxies (VELARP) brings them in better agreement with the abundance matching relation. This in comparison to the results from the FIRE simulation and from NIHAO indicates that inclusion of some sort of feedback prior to supernova (Ceverino: radiation pressure; Hopkins: radiation pressure, stellar winds, and photoionization; NIHAO: strong photoionization included as thermal energy) is needed to reproduce the stellar mass-halo mass relation at high redshifts.

It is worth noticing that the VELA galaxies were not run down to redshift 0 so there is no information whether these simulations do or do not provide realistic present day galaxies. For reference we also include the isolated simulations by Perret et al. (2014) taken from the MIRAGE sample.

2.2.2. Gas Fractions

Together with the total stellar mass, another important quantity in determining the stability of a disc in a galaxy is the fraction of cold gas.

In Fig. 2.2 I show the gas fraction defined as $f_{gas} = M_{gas}/(M_\star + M_{gas})$ as a function of stellar mass compared to observations at redshift 0 from Dutton et al. (2011) (left panel) and observations from the PHIBBS survey (Tacconi et al. 2013) for galaxies at redshift 1-1.5 (right panel). The selected NIHAO galaxies follow nicely the trend observed by Dutton et al. (2011).



The discrepancy at these lower masses might be due to different measurement methods in the simulations and the observations. In the simulations I use all the gas with a temperature smaller than 3×10^4 K in a sphere of radius $r_{\rm gal} = 0.2R_{200}$ while the observations measure atomic and molecular gas with a correction factor for helium (Dutton et al. 2011).

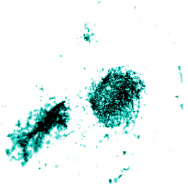
As was shown in Stinson et al. (2015) a simple temperature cut overestimates the amount of neutral gas, especially at lower masses. The galaxies are also broadly in agreement with the incompleteness corrected measurements from the PHIBBS survey (gray band) for galaxies in the redshift range $z = 1 - 1.5$. For reference I also show the gas fractions of the VELA galaxies (Ceverino et al. 2015; Inoue et al. 2016; Moody et al. 2014), the FIRE galaxy from Oklopčić et al. (2017) and the MIRAGE sample (Perret et al. 2014). The VELA sample and the FIRE galaxy are well in agreement with the NIHAO sample as well as the observed gas fractions. The two higher mass MIRAGE galaxies show very high gas fractions of 60% in slight tension with the completeness corrected PHIBBS observations. Although galaxies with such high gas fractions are observed they are likely not typical.

2.3. Radiative Transfer

In order to compare the fraction of galaxies with clumps in the simulations and in the CANDELS galaxy sample I post-process the simulations with the radiative transfer code `GRASIL-3D` (Domínguez-Tenreiro et al. 2014). The post-processing step insures that the effects of dust attenuation and cosmological redshift are accounted for, thus allowing for a meaningful comparison between simulations and observations.

`GRASIL-3D` is a three-dimensional radiative transfer code designed to be used with the outputs of hydrodynamical simulations. The code solves the radiative transfer equation for dusty media on a regular grid. The treatment of dust is based on the formalism of the `GRASIL` model (Silva et al. 1998; Granato et al. 2000), which has been successfully used with semi-analytical models of galaxy formation. The key feature of this dust model is that it does a detailed non-equilibrium calculation for polycyclic aromatic hydrocarbons molecules and dust grains smaller than 150Å, thus allowing for a proper description of the cirrus emission in mid-infrared (Guhathakurta and Draine 1989).

An important point to remember is that any RT post-processing of simulated galaxies introduces a few more sub-grid parameters on top of those already included in the hydrodynamic codes. In the case of `GRASIL-3D`, these parameters are particularly related to the properties of the molecular clouds (MCs). Since short-lived massive stars are spatially associated with MCs, it is well established that much of the dust reprocessing of stellar light occurs inside MCs. In the case of most cosmological



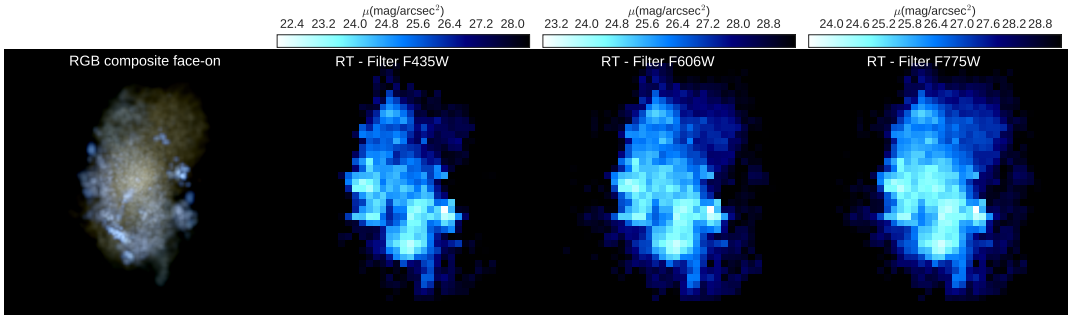


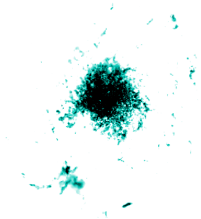
Figure 2.3: RGB image (left panel) and radiative transfer (RT) maps in different filters. The second panel shows the map of the F435W filter, the third panel shows the F606W image and the most right panel shows the F775W filter. Image sizes are 20 x 20 kpc.

simulations these small scales are not resolved, and as such, dust reprocessing has to be modeled. In GRASIL-3D, the interstellar medium is split into MCs and diffuse cirrus, by assuming the densities of unit hydrodynamical gas masses to follow a lognormal probability distribution function with a mean equal to the local gas density. The dispersion of the distribution is a free parameter. In this manner, the fraction of the gas mass above a certain density threshold gives the MC contribution, while the rest is considered cirrus. Thus, the first two parameters GRASIL-3D needs are the MC density threshold and the dispersion of the density distribution function.

In GRASIL-3D the dust reprocessing of stellar populations is age-dependent, similar to the implementation in GRASIL which was the first model to take age into account. Practically, stars younger than a certain age, t_0, radiate all their energy inside MCs, while stars older than $2t_0$ have already dispersed their MC cocoons. In the intermediate age regime, the fraction of energy dumped inside the MC is a decreasing function of stellar age. The last parameter the code needs is the spatial extent of molecular clouds. Once these sub-grid parameters are set, GRASIL-3D solves the RT equation by treating separately the light reprocessing in the dense and diffuse interstellar medium.

Finally, the stellar particles luminosities are computed according to the simple stellar population models of Bruzual and Charlot (2003) (which is the only option available in the current version of GRASIL-3D) assuming a Chabrier IMF (Chabrier 2003).

The code has already been used to study the star formation main sequence of simulated galaxies (Obreja et al. 2014), the properties of high redshift clusters and proto-clusters in sub-mm and IR (Granato et al. 2015), and the correlations between IR fluxes of $z = 0$ simulated galaxies and their baryonic content (Goz et al. 2016). These



studies have shown that GRASIL-3D reproduces observables (e.g. broad band fluxes, spectral energy distributions) when used with realistic galaxy simulations.

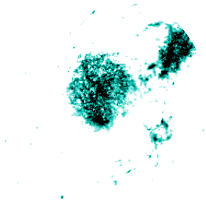
In order to run GRASIL-3D on the simulated NIHAO galaxies, the four parameters discussed above need to be specified. For this work I chose the fiducial values for disc galaxies of Domínguez-Tenreiro et al. (2014): 14 pc for the molecular cloud radius, 5 Myr for the molecular cloud destruction time-scale, $3.3\times10^{9}\mathrm{M}_{\odot}\mathrm{kpc}^{-3}$ for the molecular clouds threshold density, and a dispersion of the log-normal gas density probability distribution function of 3. I do not perform any GRASIL-3D parameter study in this work, given both the high computational cost implied and the fact that the above mentioned values have been shown to reproduce normal star forming galaxies (e.g. Silva et al. 1998; Goz et al. 2016). Finally, I chose pixel sizes corresponding to the resolution of the Hubble Space Telescope (HST) at the given redshift of the snapshots (0.06").

After running GRASIL-3D on all the snapshots of the galaxy sample in the redshift range $\sim 0.25-3$, I apply the same HST filter selection with the same magnitude cuts and surface brightness limits as chosen in Guo et al. (2015). For snapshots in the redshift range $3>z>2$ we select the F775W filter, for $2>z>1$ we select the F606W filter and for $z<1$ I select the F435W filter to detect clumps. The outcome of the radiative transfer calculations results in mock observations of the simulations closely matching the ones of the CANDELS galaxies used by Guo et al. (2015). A selection of images for the galaxy g7.55e11 at redshift $z\sim1.3$ in all three filters used are shown in Fig. 2.3 in comparison to an RGB map of the stellar luminosity (left panel). For the RGB map I calculate the stellar luminosity of a star particle given its age and metallicity in three different bands (see next section for a more detailed description). The radiative transfer images show the luminosity maps of the same galaxy in the three filters used for the analysis (from left to right: F435W, F606W, F775W). As described above, for the given snapshot time of $z\sim1.3$ I would use for the clump analysis the F606W image, while for higher redshifts I would use the F435W filter and for lower redshifts the F775W one.

2.4. Clump Detection

In this study I perform an observationally motivated clump selection, while other theoretical works on this subject focused on identifying clumps as regions of high surface density of gas or stars (Genel et al. 2012; Ceverino et al. 2015; Tamburello et al. 2015; Mayer et al. 2016; Inoue et al. 2016; Oklopčić et al. 2017)

Observed clumps are mostly detected as UV bright or H_{α} bright clumps and I thus decided to select clumps in the luminosity maps of our galaxies with and without radiative transfer post-processing. I refer to clumps detected in non dust-attenuated



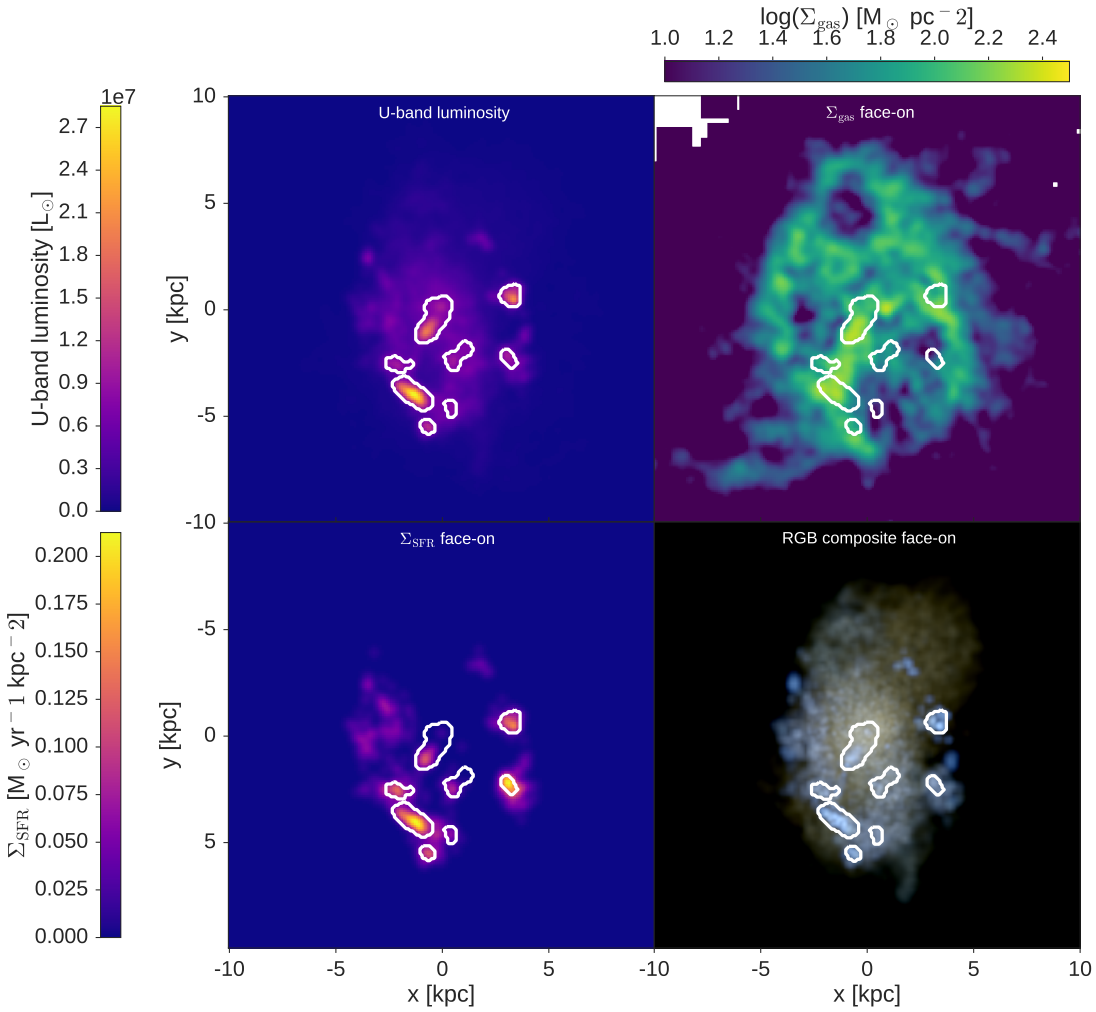
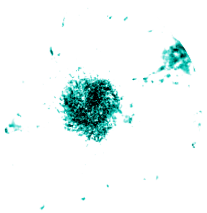


Figure 2.4: Face-on maps of intrinsic u-band luminosity (upper left), SFR surface density (lower left), cold gas surface density (upper right), and RGB stellar composite (lower right). The white contours show the clumps selected in the intrinsic u-band luminosity map.

images as *intrinsic* clumps, while I call clumps in the RT-processed images *observed* clumps. This allows to do a proper comparison with both observations and previous theoretical studies.

2.4.1. INTRINSIC CLUMP SELECTION

For every galaxy and every snapshot in the redshift range $z = 0.25 - 3$ I create UV-light images by calculating the UV luminosity of every star particle given its age, metallicity and its IMF under the assumption that these particles represent simple stellar



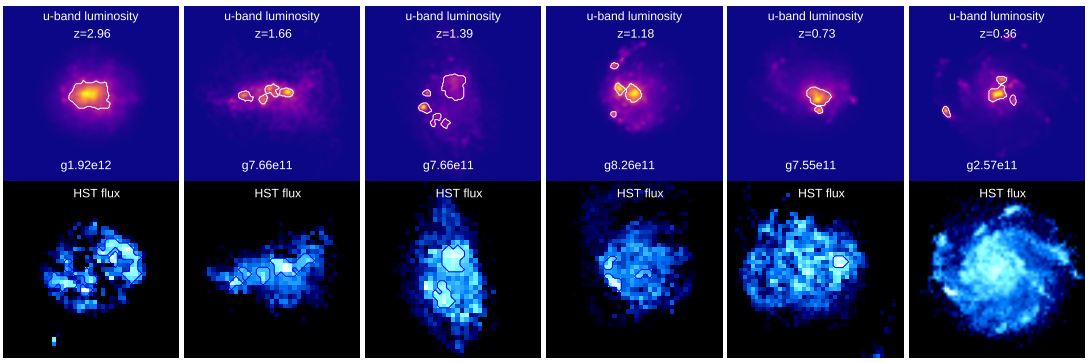


Figure 2.5: Comparison between clumps in the rest frame u-band luminosity maps (upper panels) and clumps in the radiative transfer (RT) images (lower panels). For the RT images the galaxies were redshifted to the proper redshift of the snapshot and observed in the same filter bands as the observations by Guo et al. (2015) accounting for dust absorption, scattering and cosmological redshift. For galaxies in the redshift range $3 < z < 2$ I selected the F775W filter, for $2 < z < 1$ I selected F606W and for $z < 1$ I selected F435W, where the redshift of each panel is indicated in the u-band maps.

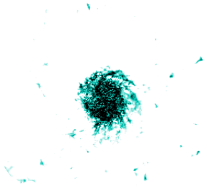
populations (SSPs). I use the PYNBODY-package[1] to perform these calculations. This package includes a grid of SSP luminosities for different stellar ages and metallicities in several bandpasses. The grids are calculated using Padova Simple stellar populations from Girardi[2] (Marigo et al. 2008; Girardi et al. 2010).

The clump finding procedure is similar to the one used by Oklopčić et al. (2017) and I will briefly describe it here. For all snapshots I first rotate the galaxies face-on, using the total angular momentum of the stars within a sphere of 10 kpc around the center of the halo. I then select all star particles in a cylinder of radius 10 kpc and height of 6 kpc centered on the galaxy and then construct the luminosity maps by binning the particle positions onto a 2d-grid of bin size 100 pc.

I sum up all luminosities of the star particles in one cell to get its total luminosity. After that I smooth the luminosity map by convolving it with a Gaussian filter of 200pc standard deviation (FWHM ~470pc) to account for the particle's softening. I checked that taking the softening into account before binning the data onto the grid does not make a significant difference in terms of clump detection.

Using the procedure described above the creation of maps of different quantities is also possible. E.g. the surface density maps of gas can be calculated by summing up all the mass in one bin and then dividing the result by the surface area of the bin. Figure 2.4 shows the u-band luminosity map (upper left), the SFR surface density map (lower left) with the SFR calculated as the stellar mass formed over the last 500 Myr, surface density of cold gas (upper right) and a RGB stellar composite image

[1]https://pynbody.github.io/pynbody/
[2]http://stev.oapd.inaf.it/cgi-bin/cmd



of the stars (lower right), where RGB stands for the colors used to render the stars (old stars are rendered with a Red color, intermediate aged stars with Green and young stars Blue). As expected, intrinsic clumps found in the u-band luminosity agree very well with clumps in the SFR surface density. Once a map of a given quantity is created I can further calculate the mean value of all non-empty bins and the according standard deviation. I then use the `python` package astrodendro[3] to find over-densities in these maps. The astrodendro package calculates hierarchical trees of structures so called dendrograms in the maps. There are three parameters needed by the package to calculate the tree. i) A threshold value to define the clump which is set to three standard deviations above the mean value (I checked that our results are robust if this value is altered, ii) The minimum difference between two close structures to count them as separate clumps; I set this to 10% following Oklopčić et al. (2017). iii) The minimum number of pixels within a clump which is set to be 30 pixels resulting in an effective radius of ~300 pc which is consistent with the gravitational softening of the gas and star particles of our simulations. An example of the outcome of this clump finding algorithm is shown in Figure 2.4 where u-band selected clumps are over-plotted on all four face-on images with white contours.

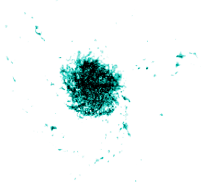
The astrodendro package already comes with tools to measure the size (surface area) of each clump in the plane of the disc (x-y-plane). Given the surface area, A, of each clump I can calculate an effective radius for the clumps, $R^2 = A/\pi$. I follow the assumption by Oklopčić et al. (2017) and take the extent of each clump perpendicular to the plane of the disc as equal to $2R$ centered on the densest part of the clump. All stellar and gas particles falling into this volume of space are counted as belonging to the clump and clump properties such as luminosity, mass, etc. can be calculated from these particles. I have checked that the enclosed mass does not depend strongly on the exact choice of the clump's vertical extent, as long as it is on the order of the disc scale height. Most of the snapshots show one large clump in the center of the galaxy which can be matched to the bulge component. Thus, I exclude from the search area the innermost 1 kpc around the center of the galaxy.

2.4.2. CLUMP SELECTION IN RADIATIVE TRANSFER IMAGES

While the above clump selection is useful to study physical properties of clumps, a comparison to observed galaxies is difficult due to missing dust attenuation and cosmological redshift. Therefore I further look for clumps directly in the dust attenuated radiative transfer (RT) maps computed as explained in section 4.

On the RT images I adjust the clump finder to better match the observational clump selection as described in Guo et al. (2015) (section 3). I first calculate the background mean after applying a 3σ clipping and then select clumps as local maxima

[3] http://www.dendrograms.org/



which are at least 3σ above the mean. Again I checked how results change if this threshold is changed to 2 or 4σ. Because I adjusted the pixel size of the RT images to match the resolution of HST I now set the minimum number of pixels to 5 per clump following (Guo et al. 2015) and I neglect clumps within the inner 1 kpc around the galaxy center.

Fig. 2.5 shows that the RT images recover some of the clumps found in the U-band images but not all. Sometimes the dust attenuation and the cosmological redshift dim down clumps such that they fall below the detection threshold of 3σ above the mean (e.g. fourth panel of Fig. 2.5). On the other hand a non-clumpy galaxy in the U-band shows clumps in the RT image due to a non-uniform gas distribution (e.g. first and fifth panel of Fig. 2.5). This underlines the importance of using radiative transfer images to compare simulation and observations quantitatively.

2.5. RESULTS

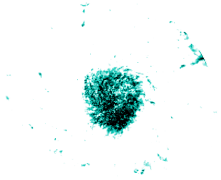
2.5.1. THE *OBSERVED* CLUMPY FRACTION OF NIHAO

As first test I check how the clumpiness of the NIHAO galaxies compares with observed galaxies in order to assess if the galaxies have a realistic number of structures in their light distribution.

In order to compare the simulations with observations used by Guo et al. (2015), I construct HST mock images with `GRASIL-3D` (Domínguez-Tenreiro et al. 2014) for all snapshots in the redshift range $0.3 < z < 3$ of the 19 NIHAO galaxies as explained above. I apply the same filters (F435W, F606W and F775W) and surface brightness cuts used by Guo et al. (2015) to the mock images and look for clumps as described in section 2.4.2.

Fig. 2.6 compares the fraction of simulated galaxies with at least one off-center clump with that of observations. The left panel shows the comparison between the complete simulation sample (blue) and different observations. Overall the clumpy fraction in NIHAO galaxies follows quite well the clumpy fraction derived by Shibuya et al. (2016) (purple dotted line) and agrees within the error bars with the results of of Guo et al. (2015) (black short-long dashed line). The right panel shows the results when galaxies are separated into three stellar mass bins $\log(M_\star/M_\odot) < 9.8$, blue; $9.8 < \log(M_\star/M_\odot) < 10.6$, green; $\log(M_\star/M_\odot) > 10.6$, red.

There is a peak in the clumpy fraction of about $60\% - 70\%$ at $z = 1.5 - 2$ in both simulations and observations. At higher and lower redshifts the clumpy fraction goes down to 50% at $z \sim 3$ and to 40% at $z \sim 0.5$, dropping even further in the simulations to 20% at $z \sim 0.25$, thus matching observations by Murata et al. (2014).



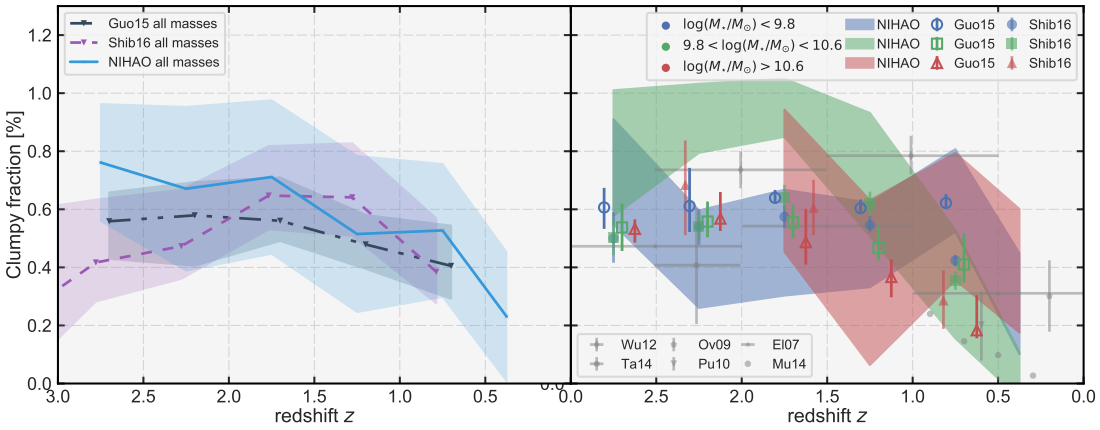
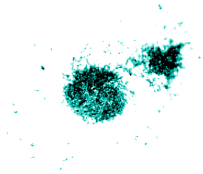


Figure 2.6: Evolution of the fraction of galaxies with at least one *observed* off-center clump. *The left panel* shows the evolution of the clumpy fraction for the whole NIHAO sample (blue line) compared to observations from Guo et al. (2015) (black dash-dotted line) and Shibuya et al. (2016) (purple dotted line). The shaded band shows the 1σ scatter. *The right panel* shows the evolution of the clumpy fraction for different mass bins. Colored bands show the result for the simulations, colored open symbols show values from Guo et al. (2015) and colored filled symbols from Shibuya et al. (2016). Grey open symbols show results from other observational studies: diamonds from Wuyts et al. (2012), squares from Tadaki et al. (2014), pentagons from Overzier et al. (2009), inverse triangles from Puech (2010), stars from Elmegreen et al. (2007) and dots from Murata et al. (2014).

When inspecting the different mass bins separately I still find a quite good agreement between simulations and observations. Specifically at low redshifts the two less massive bins (blue and green bands and points) agree very well with observed clumpy fractions for the same mass ranges. However, the highest mass galaxies (red band) in NIHAO show a clumpy fraction slightly too high but still in agreement with the observations within their error bars. At intermediate redshifts the high and low mass bins agree again well with the observations but the intermediate mass bin (green band) shows a too high clumpy fraction although in agreement with measurements from Wuyts et al. (2012). Finally due to the selection function of the NIHAO galaxies, no data for the highest mass bin are available. However, the other two mass bins agree well with the observed clumpy fraction.

Another observable to which the RT calculations can be compared is the fractional contribution of the clump's UV flux to the total galaxy UV flux. Following Guo et al. (2015) I call this quantity $C_{\rm UV}$. In Figures 2.7 and 2.8 I show $C_{\rm UV}$ as a function of the clump size and of the galaxy mass, respectively. Clump sizes found in the RT calculations of the NIHAO sample are in agreement with observed clump sizes from Förster Schreiber et al. (2011) and with intrinsic clump sizes if the pixel scale is matched to the HST pixel scale.



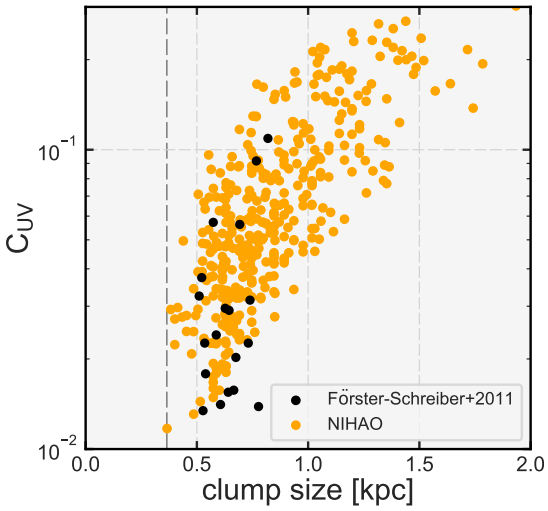
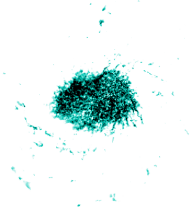


Figure 2.7: Clump contribution to the rest-frame dust attenuated UV light of galaxies as a function of clump size for the NIHAO sample (orange dots) and observations from Förster Schreiber et al. (2011) (black dots). The gray dashed line indicates the lower limit on clump sizes set by our clump finding procedure.

Figure 2.8 shows the comparison between the observed $C_{\rm UV}$ as a function of stellar mass and the NIHAO one in three different redshift bins $0.5 < z < 1$, $1 < z < 2$ and $2 < z < 3$. As in Guo et al. (2015) the clump contribution to the total UV flux of the galaxy is calculated for all galaxies not only the clumpy ones. In the two lower redshift bins simulations (orange points) agree well with observations (black squares) within their error bars, while the contribution of UV light from clumps of intermediate mass galaxies in the highest redshift bin is too high in NIHAO. A partial explanation of this excess could be related to the difference in the sample size in this redshift bin: ~ 70 simulation snapshots vs several thousand galaxies in CANDELS. Furthermore I did not add noise to the images which might lead to recovering more clumps than the observers would do. Despite this discrepancy NIHAO recovers quite well the observed UV light fraction of clumps.

Mock observations of simulated clumpy galaxies have already been studied before using different methods (see e.g. Genel et al. (2012); Moody et al. (2014); Tamburello et al. (2016)) and similar results to the ones presented here were found. Genel et al. (2012) converted the SFR of one of their zoom-in cosmological galaxy (s224) to H_α flux, convolving it with a Gaussian of FWHM=0."17 and putting it at redshift $z = 2.2$ to mimick SINFONI observations. They found that their short lived clumps are consistent with the SINFONI observations of galaxies at redshift $z = 2.2$. Moody et al. (2014) run the radiative transfer code `SUNRISE` (Jonsson 2006; Jonsson et al. 2010; Jonsson and Primack 2010) on their sample of 8 cosmological zoom-in simulated clumpy galaxies producing mock HST observations in four different filters. Unlike this work these authors additionally add noise to their images. They find qualitatively very similar results to the ones found here; a clump selection in longer wavelength maps results in lower clump counts compared to shorter wavelength maps. Furthermore these authors



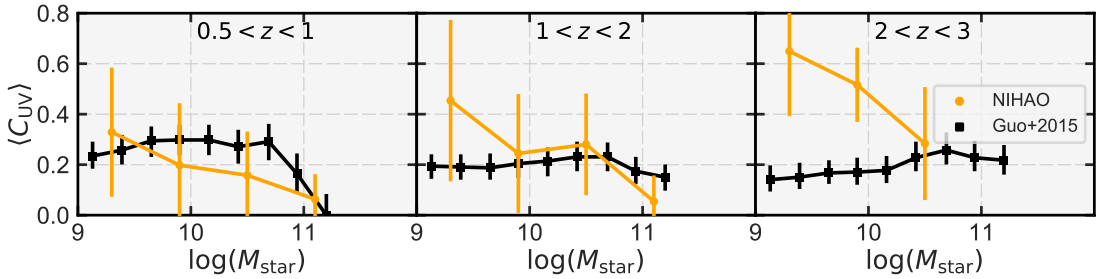


Figure 2.8: Average intrinsic clump contribution to the rest-frame dust attenuated UV light of galaxies as a function of stellar mass in three different mass bins. The observations from Guo et al. (2015) are shown as black squares and the results from NIHAO are shown with orange dots.

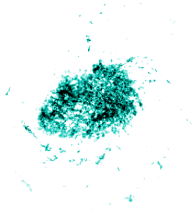
find that if clumps are selected in mock observations, stellar mass maps or gas surface density maps the outcome shows vastly different clumps (see e.g. their figure 5). There is only a minority of clumps showing up simultaneously in two or more maps. This is also confirmed by Tamburello et al. (2016) who used the radiative transfer code TRAPHIC (Pawlik and Schaye 2008, 2011) to create H_α maps of ionizing radiation of their non-cosmological simulations of galaxies. These authors add different levels of noise to their mock images and convolve the images with Gaussians with different values of FWHM to mimick different spatial resolutions. They find that the recovered properties of clumps strongly depend on the noise level and the spatial resolution. Clump sizes and masses can change by more than a factor of 2 depending on the sensitivity and the spatial resolution.

However, the focus of this study is the evolution of the clumpy fraction. This is the first time that such an observational motivated comparison of the clumpy fraction in the light distribution between observations and simulations has been carried out. The results show that the NIHAO galaxies have a realistic light distribution suggesting that they are a good testbeds for a better understanding of the origin and fate of these luminous clumps. Therefore, in the next sections I analyse the physical properties of the intrinsic clumps.

2.5.2. PROPERTIES OF THE *INTRINSIC* CLUMPS IN NIHAO

In order to better understand the physical properties of the clumps, I analyse in detail the *intrinsic* clumps. Selecting u-band luminous clumps results in a variety of clumps with different properties for every galaxy and over a vast redshift range ($0 < z < 3$). In total I find 682 u-band clumps in 488 snapshots in the selected redshift range (203 snapshots within $3 > z > 1$, 155 within $1 > z > 0.5$ and 130 within $0.5 > z > 0.25$).

In Fig. 2.9 I show some of the properties of NIHAO UV *intrinsic* clumps. The mass (gas+stars) distributions is shown in the top left panel of the figure. Independently of



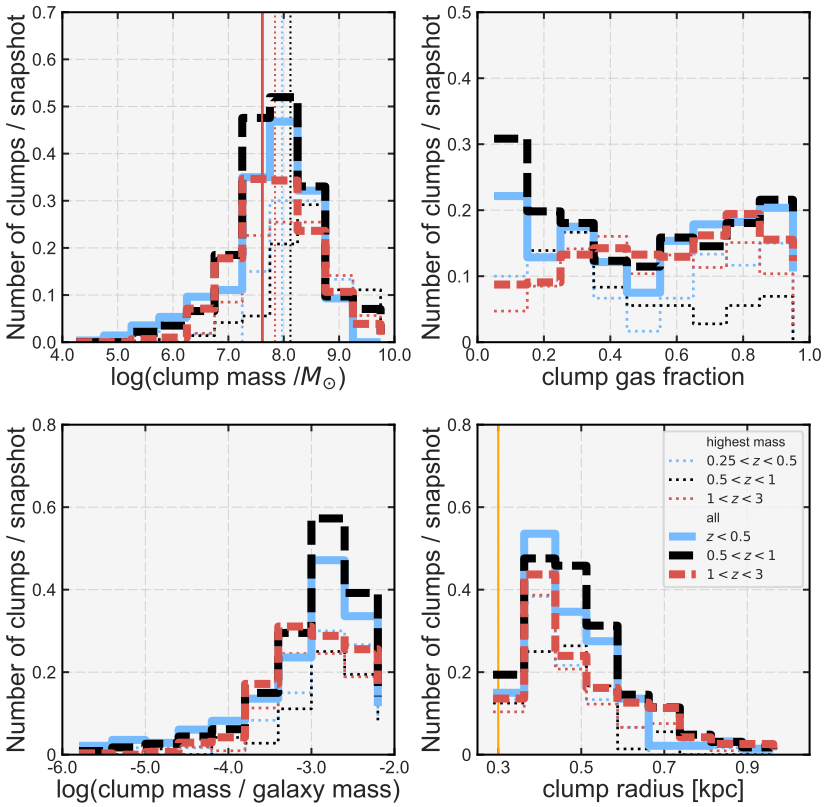
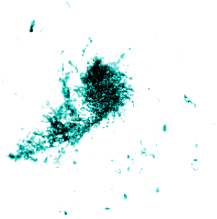


Figure 2.9: Clump properties for three different redshift bins ($z < 0.5$, $0.5 < z < 1$, $1 < z < 3$) for u-band selected clumps. *The top left* panel shows the total clump mass, *the top right* shows the clump gas fraction, *the bottom left* panel shows the clump mass as a fraction of galaxy mass and the *bottom right* panel shows the clumps effective radii with the solid vertical orange line indicating the lower limit of clump sizes set by our selection criteria. Thick dashed lines show the results for the whole galaxy sample while thin dotted lines show only the 6 most massive galaxies. The colored solid lines in the top left panel show the median mass of clumps in the whole sample and dotted lines show the median mass of clumps for the most massive galaxies.

redshift the mass of clumps in U-band maps always peaks at $\sim 10^8 M_\odot$ with a maximum clump mass around $\sim 10^{9.5} M_\odot$ and a minimum around $\sim 10^{6.5} M_\odot$. This minimum value is mainly due to the resolution of the simulation which fixes the minimum pixel size of the maps (see section 2.4.1). These results do not change if only the 6 most massive galaxies which most closely resemble the observed galaxies are considered as can be seen by comparing the thick dashed lines with the thin dotted lines in fig. 2.9.

The upper right panel shows the distribution of the clump gas fraction defined as $f_g = M_{gas}/\left(M_{gas} + M_{star}\right)$. The clump finding algorithm has no specific lower mass limit. The lower limit on the clump mass is set by the size limit (300 pc) and the surface density of the selected clump. The lowest clump masses found in the redshift bins are as



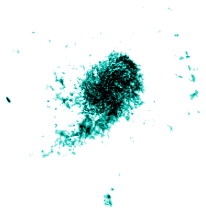
follows: $0.25 < z < 0.5 : 2.7 \times 10^4 M_\odot$, $0.5 < z < 1 : 7 \times 10^3 M_\odot$, $1 < z < 3 : 1.3 \times 10^5 M_\odot$ The clump gas fraction shows a slight trend to higher gas fractions at higher redshifts ($1 < z < 3$) and a more flat distribution at lower redshifts ($0.5 < z$). For intermediate redshifts a slight bimodality with clumps showing either very low gas fractions or very high ones close to $f_g = 1$ is found. This is in contrast with Oklopčić et al. (2017) who find a peaked distribution of clump gas fraction with the maximum around gas fractions of $f_g = 0.3$. This discrepancy comes from the difference in the selection method. Here u-band bright clumps are selected while Oklopčić et al. (2017) select clumps in gas surface density.

Despite the fact that I find giant clumps of masses greater than $10^8 M_\odot$ the contribution of these clumps to the total baryonic mass of the galaxy disc is less than 1% as shown in the lower left panel of figure 2.9. The sizes of the clumps found in the NIHAO galaxies range from ~ 300 pc to ~ 900 pc with a median value of 450 pc for every redshift bin. The lower bound is given again by the resolution (the minimum effective radius is set to 300 pc). Finally most of the clumps found are round(ish) in shape and sometimes slightly elongated (see. e.g. Fig. 2.4).

The next question to address is what determines if a galaxy has one or more luminous clumps. Fig. 2.10 shows the correlation between stellar mass, SFR, cold gas fraction (f_g) and the mean surface density within the half mass radius (Σ_{Re}) and color code each galaxy according to the "morphology" of the light distribution (clumpy=orange, non-clumpy=green). In the lower triangle of the plot every galaxy is shown at every snapshot in the redshift range $0 < z < 3$ as a point while in the upper right triangle a kernel density estimation of the point distribution is displayed. On the diagonal the marginal histograms of the property in the according column for clumpy/non-clumpy galaxies is plotted.

Clumpy and non-clumpy galaxies mostly separate in two distinct populations in these parameter spaces. Clumpy galaxies show high cold gas fractions, are less centrally concentrated (lower value of Σ_{Re}) and show low and average SFRs and stellar masses. In contrast non-clumpy galaxies are more centrally concentrated, have low gas fractions and are among the highest mass galaxies with high SFR. Qualitative similar correlations are found by Tadaki et al. (2014) (e.g. their Fig. 1) for galaxies from the SXDF-UDS-CANDELS field and by Shibuya et al. (2016) (e.g. their Fig. 7, 8, 9) for HST photo-z and Lyman break galaxies.

There is one notable difference between simulations and observations. From observations one would expect the highest mass, highest star forming galaxies to be clumpy. Here I find that the lower mass, lower star forming galaxies are preferentially clumpy. This can be explained by the fact that the simulations are more centrally concentrated than observed galaxies, and as a consequence the gas in the simulated discs is less prone to gravitational instabilities (Martig et al. 2009). Furthermore, I use non dust-attenuated properties for this plot and as was shown in Fig. 2.5, the degree of



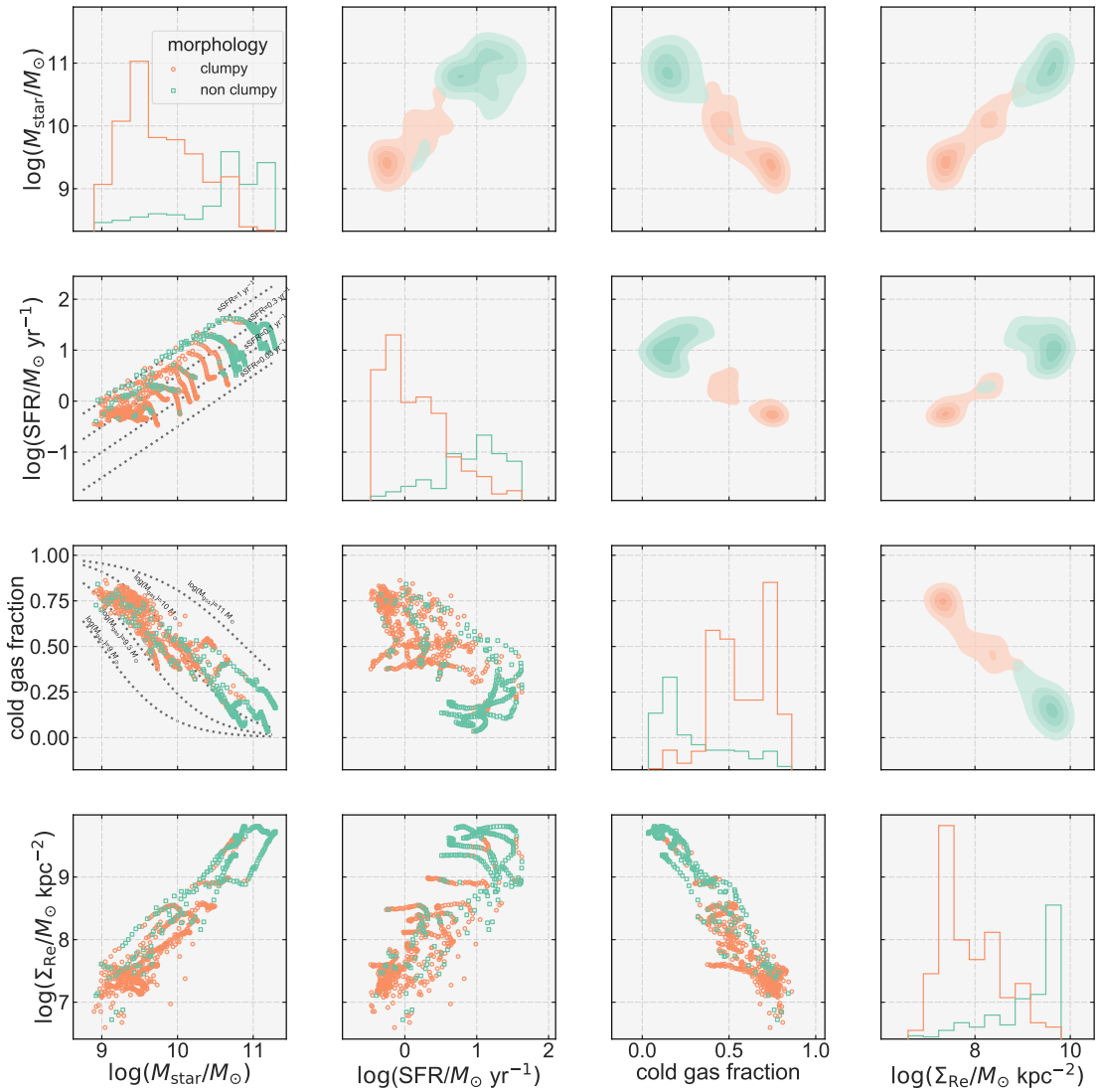
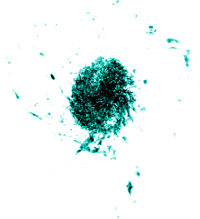


Figure 2.10: The correlation of host galaxy properties with clumpy morphology for all galaxies and all redshifts in the sample. Correlations of stellar mass (left column), SFR (second column), cold gas fraction (third column) and the mean surface density within the half mass radius (right column) with each of the other quantities are shown where I distinguish clumpy (red colored points and lines) from non-clumpy galaxies (green squares/lines). The lower left triangle shows all snapshots for all galaxies with single dots while the upper right triangle shows a kernel-density estimation of the point distribution. The diagonal shows the marginal histogram of the property of the given column.

clumpiness in non-dust attenuated images can be different from that of dust-attenuated ones. Some of the most massive galaxies in particular, are not clumpy in the non-dust attenuated maps, but clumpy in the mock radiative transfer images. However, other



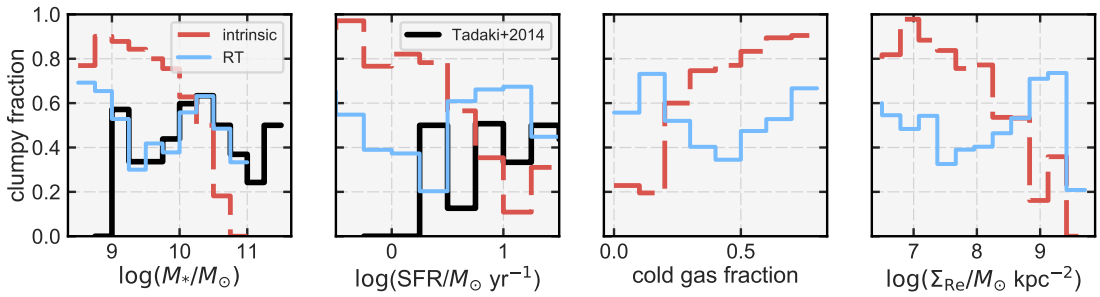


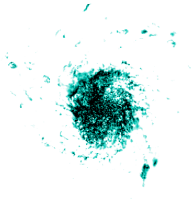
Figure 2.11: The fraction of clumpy galaxies as a function of host galaxy parameters for *intrinsic* and *observed* clumps in comparison to observations from Tadaki et al. (2014). From left to right: the clumpy fraction as a function of stellar mass $M_{\rm star}$, SFR, cold gas fraction and the mean surface density within the half mass radius.

galaxies show the opposite behaviour; they are clumpy in the non-dust attenuated maps and not clumpy in the mock images. Therefore in figure 2.11 I give the clumpy fraction as a function of stellar mass, SFR, cold gas fraction and mean surface density within the half mass radius for both *intrinsic* and *observed* clumps, as well as the observational data from Tadaki et al. (2014). For the *intrinsic* clumps I find an anti-correlation between clumpy fraction and stellar mass, SFR and mean central surface density and a correlation of clumpy fraction with the cold gas fraction of the galaxies. While *intrinsic* clumps show a strong evolution with all four galaxy parameters (anticorrelation with the galaxie's stellar mass, SFR and central surface density and correlation with the cold gas fraction) I do not find such an evolution for the *observed* clumps. This is due to the beforehand mentioned dust attenuation. The *observed* clumps, however, show very good agreement with the observational data, which also shows no strong correlation between the clumpy fraction and galaxy parameters. This result further supports the need for a careful modeling of dust obscuration when comparing galaxy morphologies between simulations and observations.

2.5.3. Clumps in Light or Clumps in Mass?

A lot of discussion is going on whether the observed clumps in high-redshift galaxies represent self-bound clumps of stars orbiting within the disc or if they are simply a concentration of luminous young stars with practically non dynamical influence on the disc.

To start to answer this questions in the upper panel of figure 2.12 the clumpiness of stars in different wavelength bands (u, v, i, h) is compared. It is clear from the plot that moving to longer wavelength the disc clumpiness tend to disappear, and practically no clumps are detected in the h band. This seems to suggest that observed and simulated clumps in the non-dust attenuated u-band are not actually bound



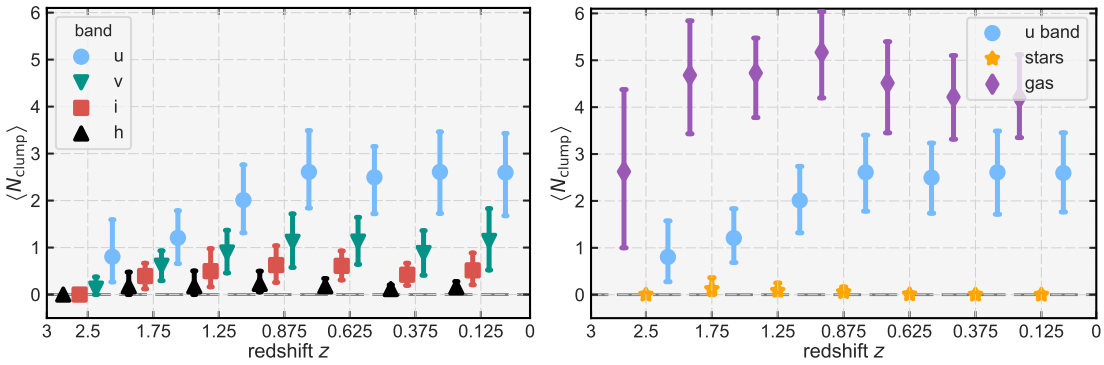
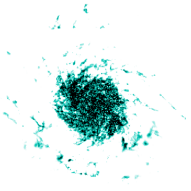


Figure 2.12: Mean number of clumps per galaxy for clumps selected in different wavelength bands. The left panel shows the mean number of clumps for clump selected in the u-band (blue dots), the v-band (green lower triangles), the i-band (red squares) and the h-band (black upper triangles). The right panel shows a comparison of the mean number of clumps selected in the u-band (blue dots) with clumps selected in the gas surface density maps (purple diamonds) and the stellar surface density maps (orange stars). The points are slightly offset to avoid overlap.

structures of stars. This result is even more clear in the lower panel of figure 2.12 where I look at the presence (or lack thereof) of clumps in maps constructed for different quantities: u-band luminosity, gas and stellar masses. As already noted in figure 2.4 clumps in the u-band match clumps in the gas surface density, but when the stellar mass maps are investigated these are found to be extremely smooth and no clumps can be detected by the algorithm in practically any of the simulated galaxies.

This is confirmed by a visual inspection of one of the NIHAO galaxies (same already shown in fig 2.4) in figure 2.13, where there is clearly a lack of any substructure in the stellar mass map. This is maybe the most important result of this study. Despite having galaxies as clumpy as the observed ones in *light* maps, I find no evidence of any self-bound stellar structures in the *mass* maps of the same galaxies. What we are facing here are luminous clumps and not dynamical ones. The good match between clumps in the u-band and the gas surface density maps suggests that observed clumps are simply a manifestation of localised (clumpy) star formation regions, as also observed in redshift zero galaxies.

This is also confirmed by the life-time of the these luminous clumps: most of the clumps disappear between two consecutive simulation snapshots in NIHAO, setting an upper limit to their dissolution time of about 200 Myr, less than one dynamical time of the galaxy. Figure 2.14 shows the fraction of clump stars still close together in consecutive snapshots (~ 200 Myr). I track the star particles of every clump identified in a given snapshot via their particle IDs. In this manner, I evaluate how many stellar particles are still within a region of $1R_{\rm eff}$ or $2R_{\rm eff}$ around the clump's center of mass in the next snapshots. I show the median fraction of clump stars still within a region



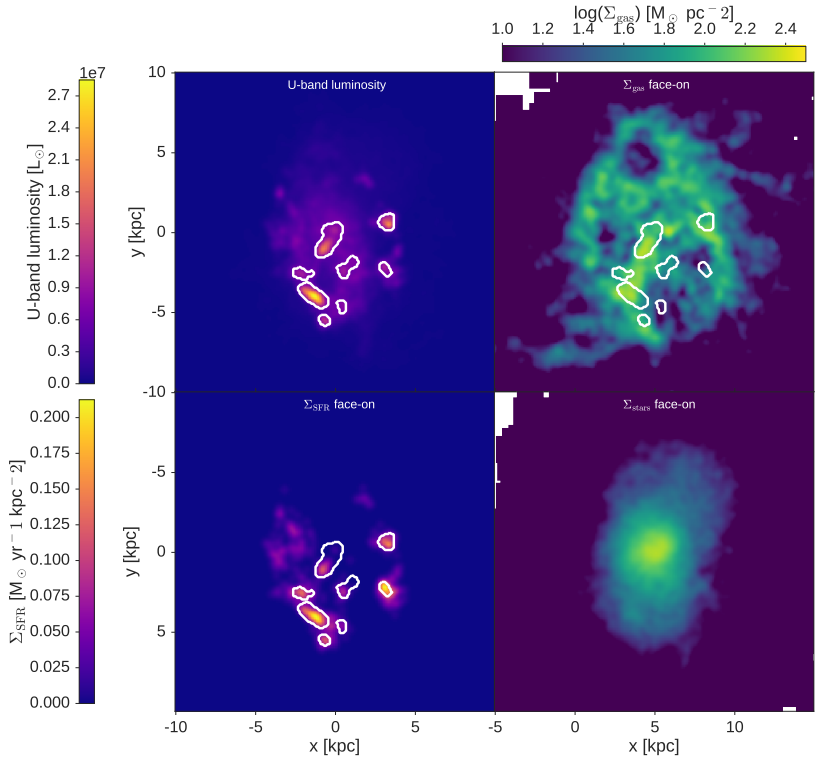
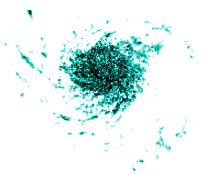


Figure 2.13: Face-on maps of u-band luminosity (upper left), SFR surface density (lower left), cold gas surface density (upper right) and stellar mass surface density maps (lower right). The stellar mass surface density map is extremely smooth. White contours show again the clumps selected in the u-band luminosity map.

of $1R_{\rm eff}$ with a blue line and the according 16th and 84th percentile as a blue shaded region. The yellow line and yellow shaded region give the the median fraction of clump stars still within a region of $2R_{\rm eff}$. With the exception of a few of the most massive clumps, I find that all clumps lose more than 90% of their mass between two consecutive snapshots.

These results are at odds with previous works (Dekel et al. 2009b; Bournaud and Elmegreen 2009; Bournaud et al. 2014; Ceverino et al. 2010, 2015; Mandelker et al. 2014), which suggested that clumps are gravitationally bound structures that migrate towards the center under the influence of dynamical friction. In support of this picture there is the observation of a color gradient of clumps as a function of distance from the galaxy center (Förster Schreiber et al. 2011; Shibuya et al. 2016), with clumps closer to the center being redder than outskirt clumps. The color gradient is supposed to be a proxy for the clump age. On the other hand it has already been suggested that such a gradient could simply be due to the underlying stellar disc population (Oklopčić et al. 2017; Nelson et al. 2016b; Genel et al. 2012).



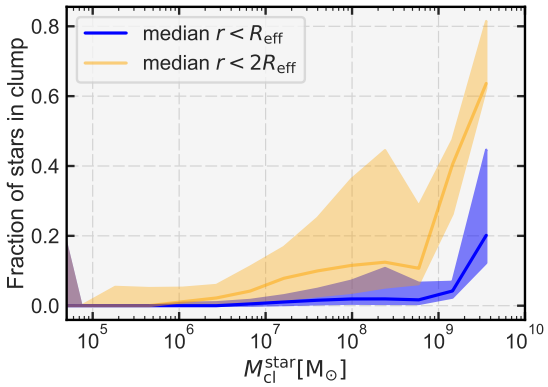
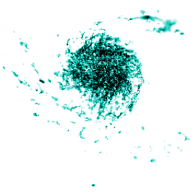


Figure 2.14: Fraction of clump stars still close together after 200 Myr. For every identified clump we show the fraction of clump stars still close together in the following snapshot. The blue line shows the median fraction of clump stars still within a region of $1R_{\rm eff}$ around the clump's center of mass while the yellow line shows the median fraction of clumps stars still within $2R_{\rm eff}$.

In figure 2.15 I show the average age of simulated clumps as a function of their distance from the center. The stellar age of a clump is the (mass weighted) average age of *all* stars within the clump, which of course is a mix of stars actually formed in the clump and the underlying stellar population. As reference, I show in the same figure the mean stellar age of the global stellar disc population as a function of distance from the galactic center. The gradient is quite weak with a slight increase of stellar ages in the outskirts of the disc, consistent with expectations from stellar migration El-Badry et al. (2016).

I find that most clumps are in the central parts of the galaxy within 5 kpc from the center, (but keep in mind that we excluded the innermost 1 kpc from our analysis). In NIHAO I find a wide range of clump stellar ages from ~200 Myr up to about 2 Gyr in the lowest redshift snapshots in agreement with observed ages of stellar populations in high redshift clumps (Elmegreen and Elmegreen 2005; Elmegreen et al. 2009; Förster Schreiber et al. 2011; Genzel et al. 2011; Guo et al. 2012; Wuyts et al. 2012). Stellar ages of clumps are generally slightly younger than the underlying mean age of the disc stars, consistent with the picture of clumps being sites of intense star formation

Interestingly I recover the observed trend of clumps in the outskirts being younger than clumps in the central parts of the galaxies. Contrary of what was suggested by some authors, who ascribe this gradient to a migration of clumps, I find that this effect is strongly due to a selection bias. Clumps in the central parts of the galaxy include more underlying disc stars which increases the mean stellar age while in the outskirts the density of the stellar disc decreases and clumps are less polluted by disc stars and thus appear younger. Although I recover the observed trend of clump ages as a function of radius, this is not a signature of clumps spiraling inwards and moving to the center as I will show in the next section.



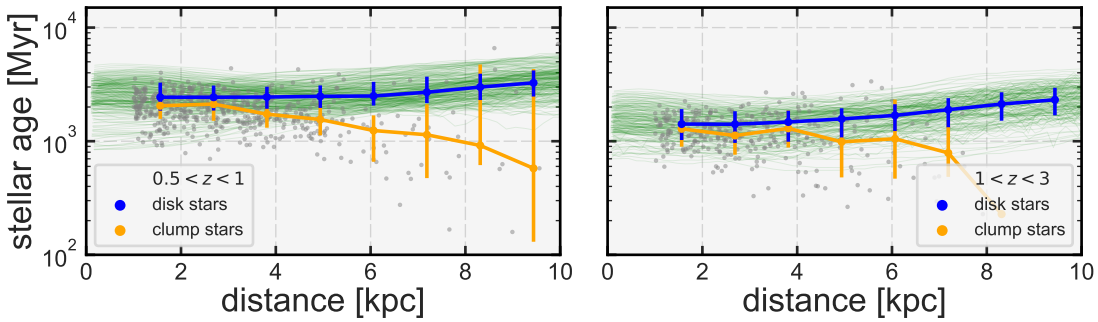


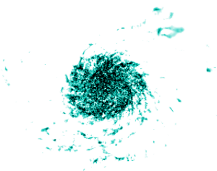
Figure 2.15: Mean mass weighted stellar ages of individual clumps (grey dots) and the underlying disc stars (green lines) as a function of radius in two different redshift bins. The left panel shows the mean mass weighted stellar ages in the redshift range $0.5 < z < 1$ and the right panel shows the stellar ages for the redshift range $1 < z < 3$. The yellow dots show the median stellar age of individual clumps as a function of distance from the galaxy center and the blue dots show the median age of stars in the disc. The error bars show the 16th and 84th percentile.

2.5.4. The Evolution and final Fate of Light Clumps

If light clumps were self bound structures of stars it would be natural to expect them to spiral in under the influence of dynamical friction. Previous studies have indeed argued that high redshift clumps can be responsible for the building of bulges at high redshift (Ceverino et al. 2010; Bournaud et al. 2014).

As discussed in the previous section our simulations suggest a quite different scenario, and hence it is interesting to ask what is the evolution of our luminous (but not bound) clumps. For every clump in every galaxy I track its evolution by calculating the mean galacto-centric distance of all its stars at later times ($r(z)$), and I normalise this number by the distance at the time the clump was firstly detected ($r(z_{\rm form})$). For stars moving inwards the expectation for the ratio $r(z)/r(z_{\rm form})$ is to be below one and the opposite for particles moving outwards.

Figure 2.16 shows the evolution of the ratio $r(z)/r(z_{\rm form})$ as a function of redshift for all our NIHAO galaxies. In the plot I also show the same quantity for a "control sample" of disc stars; for each clump with a given amount of stars, I select an identical number of disc stars at the same galacto-centric distance as the clump of interest at the time of its first detection. The shaded region shows the 16th and 84th percentile. The orange dots in Fig. 2.16 show that there is no preferential inwards migration for clump stars. If anything there is a slight trend for clump stars to migrate outwards. When compared to the control sample of disc stars, clump stars do not show any particular difference, they behave in a very similar manner. Similar results for the lack of inward migration of clumps are found by Oklopčić et al. (2017) who looked at the angular momentum change between the final and initial snapshot in which a clump



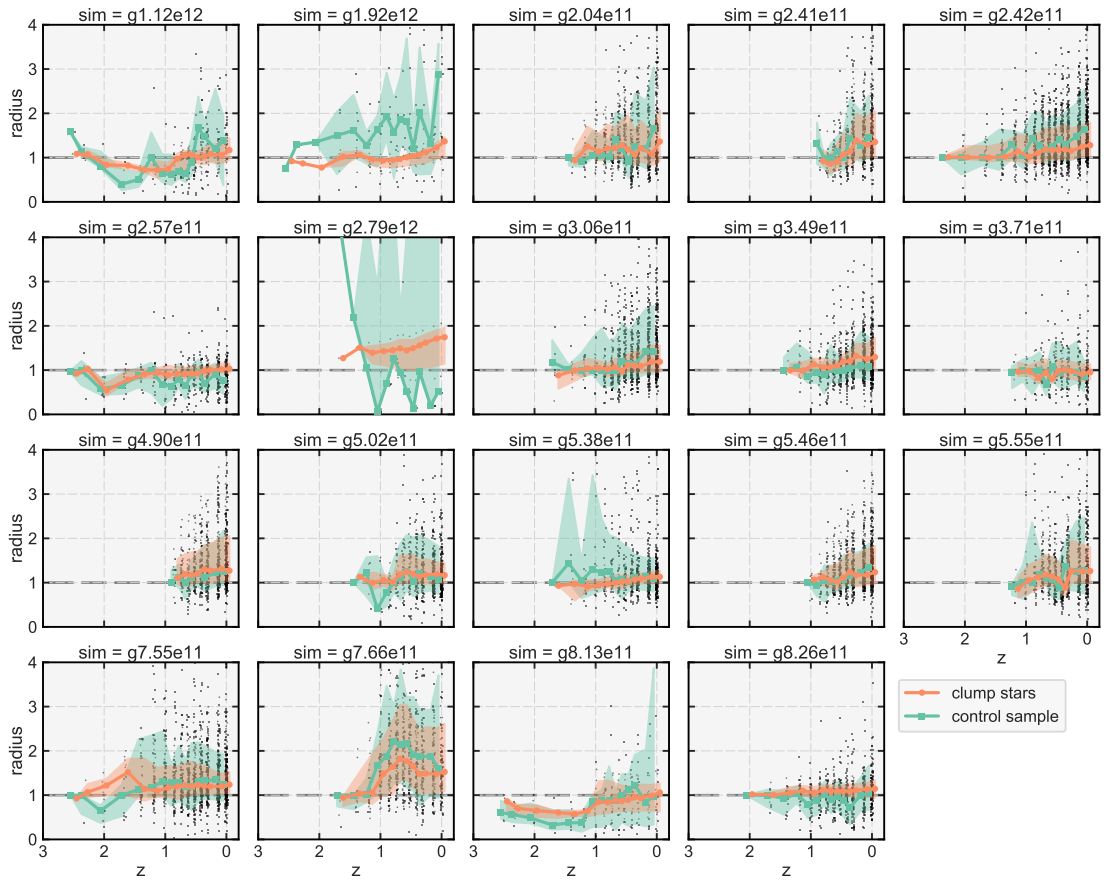
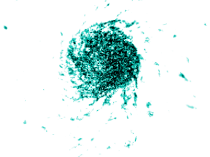


Figure 2.16: Median distance of clump stars (red dots) and control stars (green squares) as a function of redshift. For every galaxy and for every clump we track the stars found to be in one clump at a given time and calculate their mean galacto-centric distance at later times. Shown is the median value of all clump radii normalized to the initial clump radius. The same procedure is done for a control sample of stars of same number and same average radius as the clump stars. The shaded region shows the 16th and 84th percentile.

is visible. Theses authors do find a roughly equal likelihood for clumps to lose and to gain angular momentum. Thus these results indicate that clump migration is not governed by dynamical friction but rather by gravitational torquing or tidal forces.

Since I plot the average distance, it could still be possible that a substantial migration of stars inward is compensated by a same amount of stars moving outwards. Therefore, in Fig. 2.17 I look at the mass contribution from clump stars to the galaxy bulge at $z = 0$. I first decompose each galaxy at redshift zero into a disc and spheroidal component using the same procedure described in Obreja et al. (2016). All stars marked



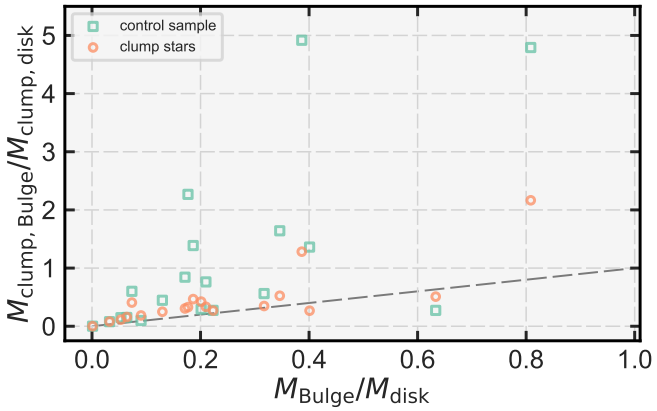


Figure 2.17: Contribution of clump stars to the bulge and to the disc at redshift 0. Shown is the ratio of stellar mass from clumps in the bulge and in the disc as a function of bulge to disc ratio. The red dots show the result for stellar mass from clumps while the green squares show a control sample of disc stars chosen to have the same size and radius as the clumps stars.

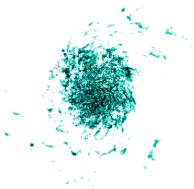
as belonging to the spheroid and having a galacto-centric distance smaller than 1 kpc are regarded as bulge stars.

We then calculate the fraction of disc and bulge mass due to stars that have been found in clumps at some earlier point in time. In figure 2.17 I plot the ratio of mass from clumps in the bulge $M_{\mathrm{clump,Bulge}}$ to mass from clumps in the disc $M_{\mathrm{clump,disc}}$ as a function of bulge to disc ratio $M_{\mathrm{Bulge}}/M_{\mathrm{disc}}$ of the galaxy. Similar to the previous plot I show clump stars as orange dots and our control sample as green squares. The dashed grey line shows the 1:1 relation. Overall clump stars seem to be equally distributed between the bulge and the disc at $z = 0$. Furthermore when compared to the control sample clump stars seems to have the same final fate as any other stars in the disc.

One can then conclude that, consistently with not being gravitational bound, light clumps in high redshift galaxies do not preferentially move inwards as time goes by and, do not preferentially contribute to the bulge growth.

2.6. SUMMARY

In this study I used 19 galaxies from the high mass end ($M_\star > 10^9$ $M_\odot$ at $z \sim 1.5$) of the NIHAO sample to analyse them in detail for their clumpy morphology and quantify the clumpy fraction of this simulation suite in the redshift range $0.25 < z < 3$. The NIHAO sample is a suite of high-resolution cosmological hydrodynamical simulations of galaxies in the mass range $10^9 M_\odot < M_{200} < 4 \times 10^{12} M_\odot$ which reproduces realistic galaxy properties over this huge range of galaxy masses. Unlike most other theoretical studies which looked for giant clumps in galaxies I do not select clumps in gas or stellar mass maps but I select clumps in luminosity maps. I apply two different selection methods: *intrinsic clumps* are selected in the non dust attenuated rest frame u-band images closely matching the observational selection method, while for *observed clumps*



I run the radiative transfer code GRASIL-3D (Domínguez-Tenreiro et al. 2014) on the 488 snapshots of our sample to create realistic mock HST observations of the galaxies. In this way I am able to directly compare the clumpy fraction of the NIHAO suite to the observed clumpy fraction from Guo et al. (2015) and Shibuya et al. (2016).

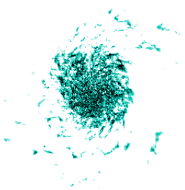
The main findings of this chapter can be summarised as follows:

- Comparing the observed clumpy fraction, the number of galaxies/snapshots with at least one off-center clump, of our RT images to the observed clumpy fraction of Guo et al. (2015); Shibuya et al. (2016) I find very good agreement between our simulations and the observations (see figure 2.6). The NIHAO sample can well reproduce the observed number of clumpy galaxies and their evolution with redshift and perfectly matches the correlation of the clumpy fraction of galaxies with stellar mass (compare figure 2.11). Sizes of clumps found in the NIHAO sample agree well with observed clump sizes (Fig. 2.7) Furthermore, I recover the observed UV-light contribution of clumps to the total UV-light of the galaxy with $\sim 30\%$ of the light coming from clumps.

- Selecting *intrinsic* clumps in the rest frame u-band images results in clump masses of few times $10^6 M_\odot$ to $10^9 M_\odot$, sizes of about 300 pc to 900 pc and gas fractions spanning a wide range from 0.1 to 0.9. These findings agree well with observed sizes and masses of giant clumps. However, although clumps are prominent in u-band luminosity maps they contribute only a small fraction of less than 1% to the disc mass (compare figure 2.9).

- For this work *intrinsic* clumps are selected in stellar light and can only be found in young stars showing up in the the u-band. Selecting clumps in longer wavelength bands like the v-, h- or i-band the number of clumps found drops to zero (see figure 2.12) and no clumps can be found in stellar mass at all. This recovers the findings of Wuyts et al. (2012) that clumps are only present in short wavelength images but not in the inferred stellar mass maps (compare also figure 2.13). Thus, I find clumpy star formation but no clumpy stellar discs in the NIHAO galaxies.

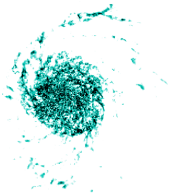
- Comparing the properties of *intrinsic* clumpy and non-clumpy galaxies in figure 2.10 I find a bimodality between these two. Clumpy galaxies show high cold gas fractions, are less centrally concentrated and show low and average SFRs and stellar masses. In contrast non-clumpy galaxies are more centrally concentrated, have low gas fractions and are among the highest mass galaxies with high SFR. These correlations for *intrinsic* clumps are strongly altered if I use *observed* clumps to divide our galaxy sample into clumpy and non-clumpy galaxies as was shown in figure 2.11. Especially the clumpy fraction as a function of stellar mass for the *observed* clumps is in very good agreement with the observed relation.



Thus, I conclude that a careful modelling of dust obscuration has to be taken into account for a direct comparison of galaxy morphologies between simulations and observations.

- The mean mass weighted stellar ages of clumps in the simulations show the same trend as observed color gradients of clumps (e.g. Shibuya et al. (2016)). Clumps in the outskirts of the galaxies are younger and clumps in the center are almost as old as the underlying mean mass weighted stellar age of the disc stars (see figure 2.15). This trend can be attributed to the fact, that the stellar density of disc stars is lower in the outskirts and higher in the center, thus when selecting clumps in images the contribution/pollution of disc stars to the clump is higher in the center than in the outskirts. That is why the mean mass weighted stellar ages of clumps and stellar disc are more similar in the galaxy center than in the outskirts.

- I find that clumps in the NIHAO sample do not spiral inwards and do not contribute much mass to the bulge. Clumps get quickly disrupted and disperse. They lose about 90% of their mass in less than 200 Myr (see fig. 2.14). Tracing the stars of the clumps through time down to redshift zero and following their mean galacto-centric radius I do not find any net inward migration of clump stars. Indeed, I find that clump stars and disc stars behave the same way, both do not show signs of a net inward migration as I have shown in figure 2.16 and 2.17. Furthermore, I quantify how much mass these stars contribute to the bulge and to the disc of the galaxies. Clump stars and randomly selected disc stars contribute the same mass to the bulge. Thus there are no indications that clumps in NIHAO would contribute to preferentially build up the bulge.



Chapter 3

The Milky Way's Central Region I - Matching the Milky Way's Peanut Bulge with Simulations

There is a theory which states that if ever anyone discovers exactly what the Universe is for and why it is here, it will instantly disappear and be replaced by something even more bizarre and inexplicable.

— Douglas Adams, The Restaurant at the End of the Universe

The results presented in this chapter are accepted for publication in the *Astrophysical Journal* and the final version of this paper can be accessed online as an arXiv preprint (Buck et al. 2018c). All the research presented in that paper and in this chapter has been conducted by myself and the simulation used as well as its analysis has been performed by me as well.

This chapter together with the next one presents a study of the properties and the formation of a peanut shaped bulge in a fully cosmological simulation. In this chapter I focus on a detailed comparison between the properties of the bulge in the simulation and the MW's peanut bulge. While the next chapter focusses on the formation scenario of such a peanut bulge in a cosmological context.

The high resolution simulation presented here matches the profile and kinematics of the MW's boxy/peanut-shaped bulge, and can hence be used to reconstruct and understand the bulge assembly. In particular, the age dependence of the X-shape morphology of the simulated bulge parallels the observed metallicity dependent split in the red clump stars of the inner Galaxy. This feature is used to *propose* an observational metric that might allow to quantify when the bulge formed from the disc. Most

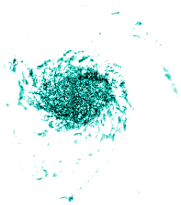
importantly, the proposed metric can be employed with upcoming survey data to constrain the age of the MW's bar. From the split in stellar counts along sight-lines going through the center of the model galaxy a formation time of the bar, $t_{\rm form}^{\rm bar} \sim 8^{+2}_{-2}$ Gyr ago, can be inferred. I further test the prospects for observationally differentiating the stars that belong to the bulge/bar compared to the surrounding disc, and find that the inner disc and the bulge are practically indistinguishable in both chemistry and ages. Therefore, other measures to distinguish disc and bulge stars need to be explored. This is the subject of the next chapter where kinematical properties of the stars are investigated in order to discriminate between bulge and disc populations.

3.1. CONTEXT

Almost 50 percent of all nearby galaxies show signs of a boxy or peanut shaped bulge (Lütticke et al. 2004) and similarly our Galaxy, the MW, is observed to host a boxy/peanut shaped bulge and a galactic bar (Okuda et al. 1977; Blitz and Spergel 1991; Weiland et al. 1994; Dwek et al. 1995) as well. The major axis of the MW's Galactic bar is inclined by about 27° with respect to the line-of-sight and it reaches out to about 3.5 kpc (Gerhard 2002; Wegg et al. 2015) with the bar extending in the plane up to about 5 kpc (Portail et al. 2017a).

The formation scenario of boxy/peanut-shaped bulges from the galactic disc is well studied in idealised simulations and several mechanisms have been identified where by stars of the disc become the boxy bulge. Isolated N-body simulations of galaxies have shown that boxy/peanut bulges can form in-situ via disc instabilities (Bureau and Freeman 1999; Athanassoula and Martinez-Valpuesta 2009), where flat discs develop a bar after only a few revolutions. This bar then puffs up into a boxy/peanut bulge structure (Raha et al. 1991; Merritt and Sellwood 1994; Bureau and Athanassoula 2005; Debattista et al. 2006) via a vertical instability, the so called buckling instability. The formation of boxy/peanut bulges has also been explained by orbit trapping, into a vertical Lindblad resonance during bar growth (Combes and Sanders 1981; Quillen 2002; Quillen et al. 2014) and via orbits associated with vertical resonances (Combes et al. 1990; Pfenniger and Friedli 1991). However, there is no overall agreement as to what specific orbits and in what relative fraction actually make up the boxy/peanut bulge of the Galactic bulge of the MW (see e.g. Portail et al. 2015a,b).

The observational evidence suggests that the MW's boxy/peanut bulge has, in large part, formed from the disc (e.g. Ness et al. 2012). However, the time of formation and the details of the subsequent evolution are uncertain. Additionally, the fraction of any underlying component that is not associated with the disc and whether this is a classical bulge or part of the inner halo, is under debate.



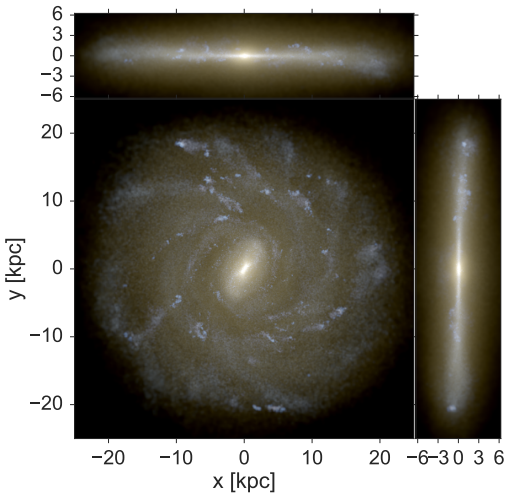
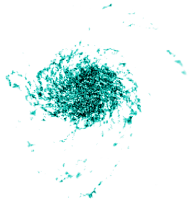


Figure 3.1: Stellar composite image of the galaxy in face-on and edge-on projections. We use i, v, u-band fluxes to create the r,g,b maps. The colors are based on luminosities found using Padova Simple Stellar populations from Girardi and Marigo (Girardi et al. 2010; Marigo et al. 2008). We did not run a radiative transfer code to account for dust attenuation.

The bulge is not only observed to be boxy in photometric images, but the red clump stars in the center of our Galaxy are split into two components well separated along the line of sight (Nataf et al. 2010; McWilliam and Zoccali 2010). The interpretation of this phenomenon is an underlying X-shaped structure in the bulge (Li and Shen 2012; Saito et al. 2011; Ness et al. 2012), a clear signature of formation from the disc. This split shows different properties for different metallicity populations; the metal rich populations show the strongest split, the metal poor stars a weaker split, with no split seen below [Fe/H] < -0.5 (e.g. Ness et al. 2012; Uttenthaler et al. 2012; Rojas-Arriagada et al. 2014a).

Many N-body models of bulge formation starting from a pure thin disc with evolving disc instabilities can alone explain the *overall* observed characteristics of the MW's bulge (Martinez-Valpuesta and Gerhard 2013b; Vásquez et al. 2013; Gardner et al. 2014; Zoccali et al. 2014). Data from the BRAVA (Howard et al. 2008), ARGOS (Freeman et al. 2013) and APOGEE surveys (Majewski et al. 2015) have revealed cylindrical rotation in the bulge of the MW (Howard et al. 2009; Ness et al. 2013b, 2016b) which is characteristic of an in-situ boxy/peanut bulge. Moreover, using BRAVA kinematics (Kunder et al. 2012), Shen et al. (2010a) constrained any merger-generated component of the bulge to be less than 8 percent.

However, the stars in the MW's bulge show not only different morphology as a function of metallicity (Dékány et al. 2013; Portail 2016, e.g.) but also different kinematics. This is most dramatic for the small fraction ($\sim 5\%$) of most metal poor stars in the bulge, [Fe/H] ≤ -1 dex (Kunder et al. 2016; Ness et al. 2013a), but is seen across the full metallicity distribution function, which extends from $-3 <$ [Fe/H] < 0.6 dex. These differences have been explained as being a consequence of composite



populations in the inner MW. Several studies (e.g. Clarkson et al. 2008; Hill et al. 2011; Gonzalez et al. 2011) have decomposed the MDF of the bulge into two stellar populations, which have different kinematics. These authors associate the metal-rich, rapidly rotating and dynamically cold population they find with a boxy/peanut bulge with disc origin. The metal-poor component, dynamically hotter, more slowly rotating population has been associated to be an old classical bulge component (e.g. Rojas-Arriagada et al. 2017) although no final agreement about this interpretation exists (e.g. Zoccali and Valenti 2016).

Using the ARGOS survey, Ness et al. (2013a) showed that the metallicity distributions of stars in the inner Galaxy can be represented by five different components, which these authors associated with the thin disc, the thick disc, the boxy peanut bulge, and also a very small population at the lowest metallicities, of metal weak thick disc and halo. Debattista et al. (2017) has explained these composite populations, where by the stars have different properties as a function of metallicity, using idealised N-body simulations and isolated hydrodynamical simulations of galaxy formation, largely in initial radial velocity dispersion, which leads to separation in evolution. They show that a bar is able to separate initially co-spatial populations of stars if only their initial radial velocity dispersion is different. Portail et al. (2017a) have used these observational data to constrain the density distribution and morphology of stars in the inner region with their associated properties and find distinct separation in morphology are associated with the different observed kinematics as a function of metallicity. Di Matteo et al. (2015) use the observational data with their N-body simulation to determine that both thin and thick disc are necessary to explain the observed kinematic behaviour in the MW.

While isolated simulations and controlled N-body experiments (e.g. Di Matteo 2016; Athanassoula et al. 2017; Fragkoudi et al. 2017) are ideal to study the mechanisms at play in shaping the bulge and are able to well explain the observed kinematics, they ultimately exclude the chemical enrichment history of star formation and are not able to properly model different temporal or chemical populations. Isolated hydrodynamical simulations of galaxy formation, which include star formation and feedback do alleviate the problem of self-consistent chemical enrichment and can well explain (compare) metallicity trends. Nonetheless, even these simulations miss one key ingredient to study the build-up of the bulge in a realistic environment. Galaxies grow in a cosmological environment by accreting gas, forming stars, getting disturbed and bombarded with satellite galaxies and self enrich the gas with metals by stellar feedback. Including all these phenomena is absolutely necessary in order to study the different components of galactic bulges and explain their origin. Furthermore we need to consistently be able to reproduce properties of the universe on the smallest and largest scales.

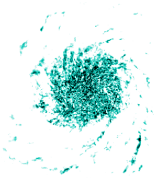


Table 3.1: Properties of the g2.79e12 galaxy: virial mass, M_{200}, virial radius, R_{200}, dark matter mass, $M_{\rm dark}$, stellar mass within $0.1R_{200}$, $M_{\rm star}$, total gas mass, $M_{\rm gas}$, mass of gas within $0.1R_{200}$, $M_{\rm gas}^{\rm gal}$, disc scale length, $R_{\rm d}$, disc scale height, $H_{\rm z}$, circular velocity at 8 kpc, $V_{\rm circ}$ and radial extension of the bar, $L_{\rm bar}$.

M_{200} [10^{12}M$_\odot$]	R_{200} [kpc]	$M_{\rm dark}$ [10^{12}M$_\odot$]	$M_{\rm star}$ [10^{10}M$_\odot$]	$M_{\rm gas}$ [10^{10}M$_\odot$]	$M_{\rm gas}^{\rm gal}$ [10^{10}M$_\odot$]	$R_{\rm d}$ [kpc]	$H_{\rm z}$ [kpc]	$V_{\rm circ}$ [km/s]	$L_{\rm bar}$ [kpc]
3.13	306	2.78	15.9	18.5	4.93	5.0	0.5	326.0	4.0

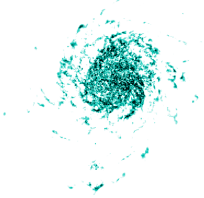
Cosmological simulations are the means to link and understand the far and near universe, but have typically had a hard time reproducing realistic bulges observed in spiral galaxies. Due to its inherent hierarchical nature, ΛCDM simulations of galaxy formation predict that galactic spheroids are primarily built up through hierarchical mergers (e.g. Kauffmann et al. 1993; Abadi et al. 2003; Kobayashi and Nakasato 2011; Guedes et al. 2013) which produce an old classical bulge, incompatible with a boxy/peanut shaped bulge, as is observed in our Galaxy (Weiland et al. 1994; Dwek et al. 1995).

In this chapter I use, for the first time in the literature, a fully cosmological hydrodynamical simulation of galaxy formation to study the inner region of a galaxy showing a bulge that is like that of the MW. I will establish the similarity of the simulated bulge with the observed features of the MW bulge - and critically - I can make predictions for the properties of the bulge, the bar and the surrounding disc in age, chemistry and dynamics. By comparing the properties of bulge stars to properties of other components of this galaxy (thin, thick disc or halo) and by tracing the stars from the inner region through time I can understand the mass assembly of the bulge and disentangle the effects of secular evolution from accretion.

3.1.1. Galaxy Properties

The simulation analysed in this chapter, the galaxy g2.79e12, is one of the higher-resolution versions of the NIHAO galaxies introduced in sub-section 1.4.3. The main properties of this galaxy can be found in table 3.1 and the numerical resolution for this galaxy is specified in table 1.1 in sub-section 1.4.3. The final total mass within the virial radius ($R_{\rm vir} \sim 300$ kpc) is $M_{\rm tot} = 3.13 \times 10^{12} M_\odot$ and the stellar mass of the galaxy (measured within $0.1\times R_{\rm vir}$) is $M_{\rm star} = 1.59 \times 10^{11} M_\odot$. The galaxy's stellar disc has a scale length of $R_{\rm d} \sim 5$ kpc and a total scale height of $H_z \sim 500$ pc within the innermost 5 kpc and $H_z \sim 1$ kpc in the outskirts at $R > 10$ kpc.

Similar to the MW, g2.79e12 contains a bar. It is important to have a good description of this bar because there is some confusion in the literature as to what we call the bulge of the MW. Some authors use the terminology pseudobulge some



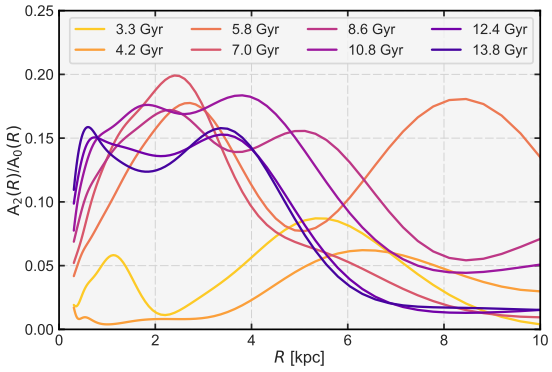


Figure 3.2: Bar strength as a function of radius as calculated from the ratio of the fourier components A_2/A_0 for different times in the simulation. A prominent bar forms around ~ 7 Gyr after the big bang at a redshift $z \sim 1$.

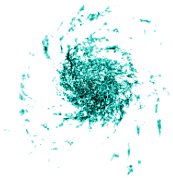
use boxy/peanut bulge but all of them mean the same thing. The structure seen in the center of our MW is the bar, and this is the same as the bulge (when viewed edge on, which appears to be boxy/peanut shaped. Therefore, throughout the rest of this chapter I will use (boxy/peanut) bulge or bar for referring to the same thing. If I take all stars in the inner region, including the disc surrounding the bar, I refer to the inner most region of the MW. At redshift zero the bar in the simulation extends out to about 4 kpc from the galaxy center. I characterise the bar in the simulation using the $m = 2$ Fourier modes of the galaxy:

$$A_2 = \sum_j \exp\left(i2\varphi_j\right) m_j \tag{3.1}$$

where m_j and φ_j are mass and azimuth angle of the stars. The sum extends over all stars in the considered region (spherical bins) of the galaxy. This $m = 2$ mode encodes the bar strength defined as

$$A_2/A_0 = \frac{|A_2|}{\sum_j m_j} \tag{3.2}$$

I use this quantity to estimate the formation time of the bar as a function of radius which is shown in Fig. 3.2 at several redshifts. After an initial strong fluctuation of the bar strength due to a violent merger dominated phase before redshift $z = 2$, the bar strength grows continuously from redshift $z = 2$ onwards. Before $z = 1$ the value of A_2/A_0 in the innermost 4 kpc is relatively low, while after that time it shows a larger value of $A_2/A_0 \sim 0.17$. This is the signature of a bar extending up to ~ 4 kpc. The bar in this simulation is first visible in surface density images at redshift $z = 1.3$ or ~ 8 Gyr ago, and from then onwards it grows in strength and size. At redshift $z \sim 0.75$ or equivalently ~ 6.5 Gyr ago, the bar buckles and forms the boxy/peanut bulge. This process causes a reduction in bar strength and an increase in vertical velocity dispersion. Thus I conclude that the bar in this simulation formed between ~ 10 and 8 Gyr ago at a redshift of $z \sim 2 - 1$ as can be confirmed by visual inspection.



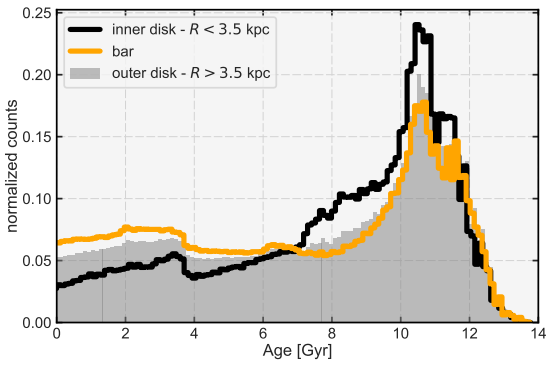


Figure 3.3: Age distribution of stars in the bar (orange histogram), the inner disc ($R < 3.5$ kpc, black histogram) and the outer disc ($R > 3.5$ kpc, gray filled histogram) in the galaxy at redshift $z = 0$. Stars belonging to the bar meet the following spatial selection criteria: $-3.5 < x/\mathrm{kpc} < 3.5$, $-1.25 < y/\mathrm{kpc} < 1.25$ and $-1.0 < z/\mathrm{kpc} < 1.0$ while the inner disc is defined as the inner most 3.5 kpc of this galaxy excluding the bar.

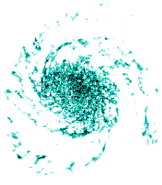
3.2. Comparing Bulge Properties in the MW and the Simulation

In this section I compare the properties of the bulge region of the simulation to key observations from our own Galaxy to establish the similarity between the simulation and the MW. In the following analysis I place the Sun at $(x, y, z) = (8, 0, 0)$ kpc and rotate the simulation such that the bar is inclined at 27° with respect to the line-of-sight to match the Sun's position in the MW (Wegg and Gerhard 2013). I then transform all coordinates to galactic longitude and latitude (l, b).

In observations the metallicity of individual stars has been used to infer the temporal evolution of the bulge structure (i.e. metal poor stars are mostly old, metal rich stars are mostly young). Ages for small samples of individual stars have been measured using microlensing events (see Bensby et al. 2017). For several reasons, I use in this work the stellar ages of the star particles directly and not their metallicity. First, I find for this particular simulation that stellar populations show a large scatter in ages for single metallicity bins, similar to the results of Minchev et al. (2017). This prevents a clean investigation of the temporal build up of structures in the simulation using stellar metallicity. Second, the fundamental variable to measure galactic formation and evolution is age, and it is straightforward to obtain this in simulations. Furthermore, observationally, stellar ages are now being measured from spectra of bright red giant stars in the bulge (Ness et al. 2016a; Martig et al. 2016). Therefore, our choice for stellar ages allows for a direct link to new generations of spectroscopic surveys [e.g. MOONS (Cirasuolo et al. 2012), APOGEE-2 (Zasowski et al. 2017) and Sloan V (Kollmeier et al. 2017)].

3.2.1. The Age Distribution of Bulge Stars

Fig. 3.3 shows the age distribution of the stars in the model galaxy, for stars of the disc within 25 kpc from the galactic centre and a height smaller than 6 kpc from the



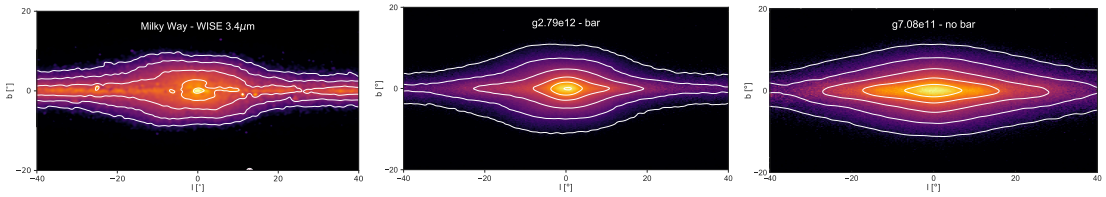
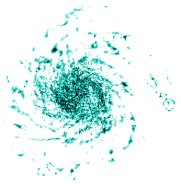


Figure 3.4: *Left panel:* MW 3.4μm image of the WISE satellite (Ness and Lang 2016). *Middle panel:* K-band image of the boxy/peanut bulge of the g2.79e12 simulation in galactic coordinates. *Right panel:* K-band image of the bulge of the non-barred simulation g7.08e11 (Buck et al. 2018a). The two left most panels show clearly the boxy/peanut shape of the bulge region with a qualitative visual similarity between the MW and the simulation analysed here. In contrast, the right most panel shows one of our non-barred galaxies clearly showing morphological differences with respect to the other two panels.

mid plane. Three spatial bins are shown, (i) stars in the inner galaxy, < 3.5 kpc of the galactic center but excluding the bar, (ii) stars in the bar selected to meet the spatial selection criteria $-3.5 < x/\mathrm{kpc} < 3.5$, $-1.25 < y/\mathrm{kpc} < 1.25$ and $-1.0 < z/\mathrm{kpc} < 1.0$, (for the bar aligned with the x-axis) and (iii) stars of the disc outside of the inner 3.5 kpc. The model galaxy shows a wide distribution of stellar ages ranging from 0 to ~ 14 Gyr with a peak around $10 - 11$ Gyr and a tail towards lower ages with a slight peak for very young stars (< 3 Gyr). The distribution of stellar ages in the outer disc and in the bar is very similar. However, the inner disc excluding the bar shows a lower (larger) proportion of young (old) stars. This points towards a preferential origin of bar stars from the outer disc which I study in much more detail in the next chapter and I will come back to the similarity of ages in the inner disc region and those trapped in the bulge in section 3.3.3, when I discuss the origin of stars in the bar.

Comparing these results to observed age distributions for stars in the MW and its bulge I find very good agreement. The total age distribution of stars in this model galaxy is very similar the reconstructed one of the MW by Snaith et al. (2015) using spectroscopic data from Adibekyan et al. (2012). Their age distribution shows a strong peak at ~ 11 Gyr and a tail towards lower ages with indications of a secondary peak at ~ 3 Gyr well in agreement with this simulation.

Using the APOGEE data set (Majewski et al. 2015), Zhou et al. (2017) find a wide distribution of ages in the bulge region of the MW. Their high metallicity population shows ages ranging from 2 to 14 Gyr while their metal poor population is slightly older with ages between 6 and 14 Gyr. This is consistent with the findings of Bensby et al. (2013) and Bensby et al. (2017). The age-metallicity relation reconstructed from the APOGEE data is quite flat for stars in the bulge region, indicating a wide range of stellar age populations at similar metallicities. This suggests the existence of multiple stellar populations in the bugle region, ranging from young to old, which is in very good agreement with the results obtained from the simulation.



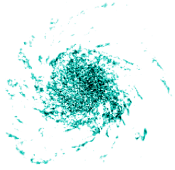
On the contrary, using ages derived from proper motion cleaned color magnitude diagrams the fraction of young stars in the bulge region of the MW is found to be less than 3.5% (Clarkson et al. 2008, 2011; Gennaro et al. 2015). This discrepancy with the results of e.g. Bensby et al. (2013) lead Haywood et al. (2016) to suggest that an age-metallicity degeneracies might make a young population undetectable using color magnitude diagrams (see recent review by Barbuy et al. 2018, for a more detailed discussion).

3.2.2. The X-Shape and the Split in Stellar Counts

The MW contains a boxy/peanut shaped bulge with a strong X-shaped structure clearly visible in photometric imaging. In Ness and Lang (2016) the X-shape of the bulge is readily seen from the WISE satellite photometry, which penetrates the dust obscured inner-most region. This X-shape and the overall boxy/peanut bulge morphology are not uncommon in extragalactic spirals (Bureau et al. 2006; Gonzalez et al. 2017).

In Fig. 3.4 I show a K-band image of the simulation side-by-side to the WISE 3.4μm image with data taken from Ness and Lang (2016) to show the remarkable qualitative similarity between the morphology in the simulation and in our own Galaxy. A feature of the presence of a peanut-shaped bulge is the X-shaped structure which can often be seen if viewed side-on. In Fig. 3.5 I show this feature for the different stellar populations of the simulation. This figure shows the surface density of stars in a thin slice of 1 kpc thickness centered around the peanut bulge mid-plane. Starting from the youngest stars the strength of the X-shape gets stronger with age. Only the oldest stars do not show this feature. The X-shaped morphology gets less prominent and more boxy, or thicker (stars reach larger heights above the galactic mid-plane) for increasingly older populations. The X-shaped morphology is strongest for the intermediate age population ($2.5 < t_{\rm star}/{\rm Gyr} < 6.0$), where the stars extend in the arms of the X to the highest latitudes and trace orbits down to the lowest latitudes at the very center. The respective mass fractions in the innermost 4 kpc in the four different age bins in terms of total stellar mass of this simulated galaxy are: 10%, 12%, 18% and 18% for stellar particles in the age bins $t_{\rm star}/{\rm Gyr} < 2.5$, $2.5 < t_{\rm star}/{\rm Gyr} < 6.0$, $6.0 < t_{\rm star}/{\rm Gyr} < 10.0$ and $t_{\rm star}/{\rm Gyr} > 10.0$.

The bulge of our own Galaxy can only be observed from within the Galaxy. Thus to reconstruct the structure of the bulge one has to rely on line-of-sight counts of stars. The X-shaped structure of the bulge thus translates into a double peaked distribution of stars as a function of distance. This feature was first observed in our own Galaxy from photometry in the star counts along the line of sight (McWilliam and Zoccali 2010; Nataf et al. 2010) and found from spectroscopy to be metallicity dependent e.g. (Ness et al. 2012; Uttenthaler et al. 2012; Rojas-Arriagada et al. 2014b). For the MW there have been published various studies of star counts for sight-lines



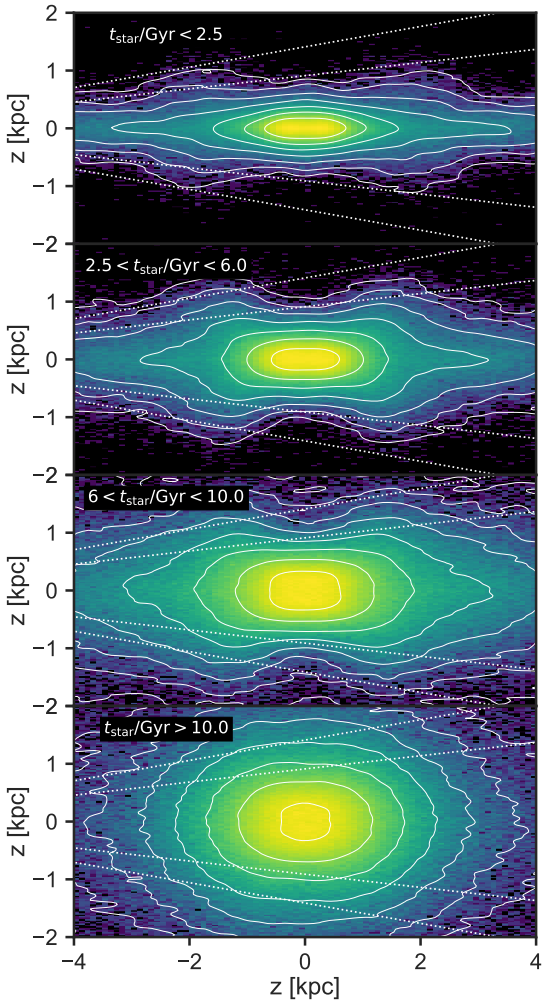
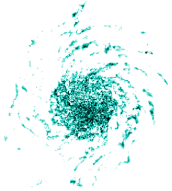


Figure 3.5: Side on surface density plots of a thin slice of thickness 1 kpc centered on $y = 0$ kpc of the X-shaped bulge in our simulation. The sun's position is assumed to be at $(x, y, z) = (8, 0, 0)$ kpc. The white dashed lines indicate the cones in which I count stars along the line of sight for Fig. 3.6. From top to bottom I show the different age populations used in Fig. 3.6 from the youngest stars (age< 2.5 Gyr) to the oldest stars (age> 10.0 Gyr).

going through the center of the Galaxy ($-2.0° < l < 2.0°$ at $6.5° < |b| < 10°$ above the galactic plane, e.g. Ness et al. 2013a,b). We use the same sight-lines in this simulation which are indicated by the dashed white lines in Fig. 3.5. From this one can see that the anisotropic distribution of stars in the X-shaped structure lead to a double peaked distribution of star counts. In Fig. 3.6 I show the radial distribution of star counts in the bulge region of our simulation. Similarly to the observations of the MW bulge I count the number of stars as a function of distance in the above mentioned sight lines. I restrict myself to distances ranging from 5-11 kpc from the Sun's assumed position (thus ± 3 kpc from the galactic center) and divide the stars into four different age bins.

The resulting split in the stellar line-of-sight counts of stars in the simulation looks qualitatively very similar to the observations of the ARGOS survey (Ness et al.



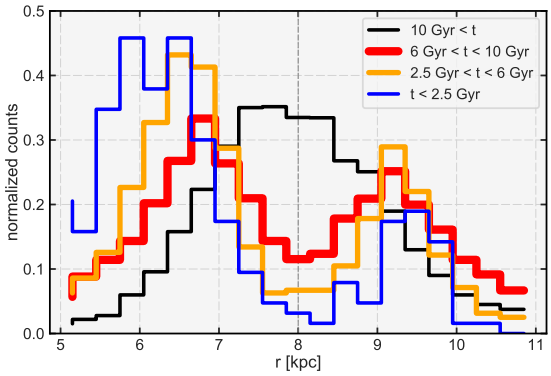
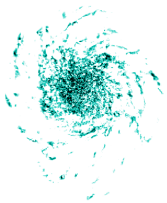


Figure 3.6: Star counts as a function of distance from the sun in different age bins for line-of-sights going through the center of the galaxy ($-2.0° < l < 2.0°$) at a height of $6.5° < |b| < 10°$ above the galactic plane similar to ARGOS observations of our MW (Ness et al. 2013a,b). The Galactic center position is indicated by the vertical dashed gray line at $r = 8$ kpc.

2013a,b). Up to a stellar age of 10 Gyr a split in the radial distribution of stars is visible and I checked that for any age bins older than 10 Gyr there is no such a split. Therefore I conclude that this population older than 10 Gyr is not part of the boxy/peanut structure. In Fig. 3.6 it is clearly visible that the peak separation becomes smaller for progressively older stellar populations. This is similar to what is observed for the MW – as a function of stellar metallicity – where the metal poor population is less separated compared to the metal rich population. This is confirmed by the surface-density maps shown in Fig. 3.5. The slight asymmetry of the line-of-sight counts for the younger stellar populations visible in Fig. 3.6 can be explained by the inclination of the cones use to count the stars (see white dashed lines in Fig. 3.5). On the near side the cones are close enough to the mid-plane to cut right through the X-shape while on the far side the cones are to far from the mid-plane and the X-shape does not extend high enough above the mid-plane to fully intersect with the cones.

The question of the origin of such a spatial separation of different populations of stars was recently addressed by Debattista et al. (2017) using pure N-body simulations and an isolated simulation of galaxy formation. These authors find that initially co-spatial stellar populations with different in-plane random motions separate when a bar forms. In their simulations the stellar population with higher radial velocity dispersion becomes a vertically thicker box while the radially cooler population stays thinner and forms a peanut-shaped bulge. These authors termed this mechanism *kinematic fractionation*. One important prediction of this mechanism is that even after the buckling instability of the bar, the disc stars can be scattered by the bar to large heights above the disc. As explained in Debattista et al. (2017, section 2): *as long as the bar is slowing down, therefore, the disc will continue to thicken at different rates for different radial dispersion populations, allowing the separation of populations to persist in subsequent evolution.* This mechanism is important in this simulation as the bar forms around 8 Gyr ago. I also observe a strong X-shape in the stars with ages between 2.5 and 6 Gyr as can be seen in Fig. 3.5. This however points towards further dynamical



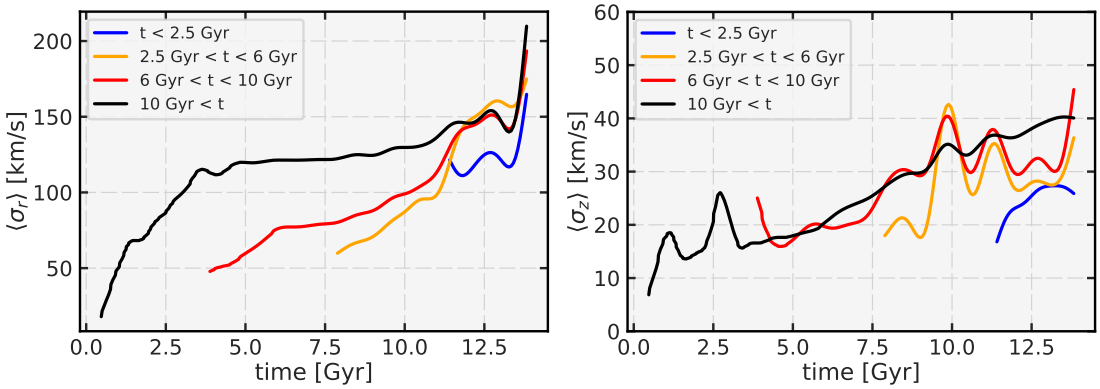
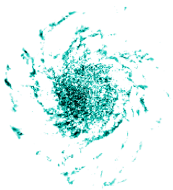


Figure 3.7: Evolution of the radial (left panel) and vertical (right panel) velocity dispersion of stars in the inner region ($R < 3.5$ kpc). Color coding is the same as in Fig. 3.6 with blue lines showing stars younger than 2.5 Gyr, orange lines showing stars with $2.5 <$ age/Gyr < 6, red lines $6 <$ age/Gyr < 10 and black showing the oldest stars with age > 10 Gyr.

influences after bar formation acting on the redistribution and star formation in the already barred galaxy. E.g. Fragkoudi et al. (2017) have shown that thin disc stars get trapped more easily in the bar compared to thick disc stars which explains the enhanced contribution of young stars to the bar compared to the inner disc seen in Fig. 3.3.

I confirm with this fully cosmological simulation that indeed the radial velocity dispersion is higher for older stellar populations over the whole cosmic time of evolution which agrees with the picture presented in Debattista et al. (2017). It is reassuring that the same mechanism is at work in pure N-body simulations and idealised, isolated simulations of galaxy formation as well as in the fully cosmological context. These mechanisms thus also seem to shape the galaxy in an environment where there are many additional perturbations, from incoming satellites and minor mergers, as per this work.

In Fig. 3.7 I show the evolution of the radial (left panel) and vertical velocity dispersion (right panel) of the four different stellar age populations as a function of time. The color-coding of the lines is the same as for Fig. 3.6. For both panels I trace back all the stars within a sphere of 3.5 kpc at redshift $z = 0$ and calculate the velocity dispersion in cylindrical bins aligned with the stellar disc and then average over all bins, as in Debattista et al. (2017). The lowest radial dispersion is found in the youngest stars (blue line), and the radial velocity dispersion increases with increasing stellar age. The vertical velocity dispersion of the stars is much more similar among different sub-populations as can be seen from the right panel of Fig. 3.7. The increase in vertical velocity dispersion around 7.5 Gyr is due to the buckling instability of the bar, and the spike in vertical velocity dispersion at $t \sim 10$ Gyr is due to a massive satellite passing



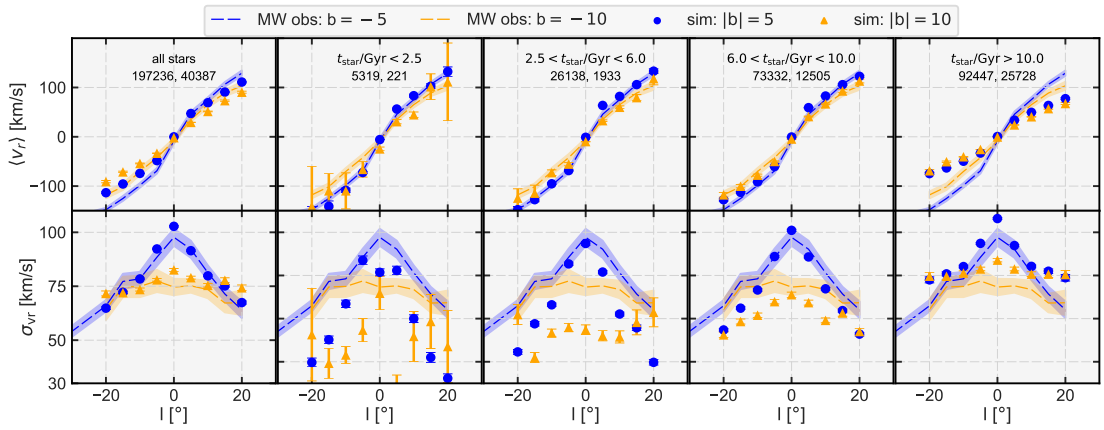


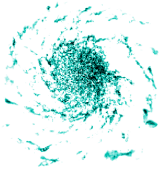
Figure 3.8: Rotation (top) and dispersion (bottom) profiles for stars of different ages for two different latitudes $|b| = 5°$ (blue) and $|b| = 10°$ (yellow). Rotation is the mean radial velocity for stars at distances 5 to 11 kpc along the line-of-sight, as a function of galactic longitude l. The dispersion profile is the velocity dispersion along the line-of-sight as a function of galactic longitude l. Lines show the measurements from ARGOS (Ness et al. 2013a,b) for the whole sample of MW stars and dots/triangles show the result obtained for the simulation. From left to right, the panels show the profiles for: all stars, young stars (age < 2.5 Gyr), stars with ages 2.5 < age/Gyr < 6, stars with ages 6 < age/Gyr < 10 and the oldest stars with age > 10 Gyr. The numbers in each panel indicate the amount of stellar particles in each sample, the first for sight lines with $|b| = 5°$, the second for $|b| = 10°$.

through the stellar disc of our simulated galaxy causing almost equal extra heating of the stellar populations. Interestingly the radial velocity dispersion is less affected by the disc passage of the satellite.

As a last remark, gradual kinematical heating of all stellar populations in the simulation can be observed. With cosmic time the radial and vertical velocity dispersion of the stars increases, although the relative increase is stronger for the vertical velocity dispersion.

3.2.3. Kinematics: Rotation and Dispersion Profiles

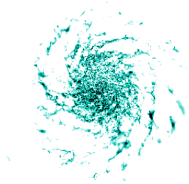
The stars in the inner MW ($R < 3.5$ kpc) show a distinct rotation and dispersion profile (Kunder et al. 2012; Ness et al. 2013a; Zasowski et al. 2016). The rotation is the mean radial velocity for stars at distances 5 to 11 kpc along the line-of-sight, as a function of galactic longitude l and the dispersion profile is the velocity dispersion along the line-of-sight as a function of galactic longitude l. In Fig. 3.8 I compare the rotation and dispersion profiles of the bulge stars in the simulation (for all stars and for our four different age populations) with observed profiles for the MW calculated from ARGOS data – for all stars, across all [Fe/H]: this helps to guide the eye to compare how the trends in the simulation change with age.



In the left panels of Fig. 3.8 I compare the rotation curves (upper panel) and the dispersion profiles (lower panel) for all stars in the observational sample and all stars in the simulation. Following the observations, I calculate rotation and dispersion in 2° sized bins in (l, b). Due to the higher mass of the model galaxy compared to estimated values of the MW, the rotation and dispersion values obtained from the simulation are slightly too high compare to the observed values. Thus, I rescale the rotation and dispersion values by a constant factor of ~ 0.45 to match the observed dispersion value at $(l, b) = (0^\circ, -5^\circ)$ of the observations. This rescaling is valid since the interesting feature of the observations is not the absolute value of rotation or dispersion but the particular shape of the profiles. After the rescaling, the dispersion profile of all stars show excellent agreement with the observed profiles (colored shaded bands) for both latitude bins ($b = -5^\circ$ blue dots and $b = -10^\circ$ yellow triangles). The simulation is able to recover the flat dispersion profile for large heights above the plane and the triangular peaked shape of the dispersion profile closer to the disc mid-plane. The rotation profile of the simulation shows the same qualitative behaviour as the observations but somewhat smaller maximum values of rotation for the smallest and largest l-bins. The reason for this is most likely a slight miss match in size of the simulation and the MW.

The other eight panels of Fig. 3.8 show the rotation and dispersion profiles for stars of the simulation in the different age bins (chosen to be the same as in Fig. 3.6), together with the profiles of all stars in the observations to guide the eye (a closer, more direct comparison between simulation and MW is performed in the next chapter). I do not see large differences in the rotation profiles of different age populations. Note however that the rotation is slowest for the oldest stars (the far right panel). This is in qualitative agreement with the observations given that metal-poor stars are generally younger than metal-rich stars. Observationally, the rotation profile shows only a very slight variation for different metallicity populations in our MW for stars [Fe/H] > -1.0. (see e.g. Ness et al. 2013b). However, for the most metal-poor stars observed in the bulge, that is the 5% of stars with [Fe/H] < -1.0, which have the highest dispersions, the rotation is far slower than the more metal rich stars (on the order of 50% of the more metal rich population, as measured by ARGOS). The RR Lyrae population, which peaks at [Fe/H]$= -1.0$ in the bulge, shows no rotation at all, in the observations of Kunder et al. (2016).

I now turn to examine the dispersion profiles which for the MW bulge stars show a strong variation for different metallicity populations (Ness et al. 2013a, 2016a; Zasowski et al. 2016; Babusiaux 2016). The simulation shows that with increasing age of the stars, the velocity dispersion increases for both b-bins. This is in qualitative agreement with what is seen in the ARGOS survey for stars of decreasing [Fe/H], down to [Fe/H]> -0.5 (see e.g. Ness et al. 2013b, Fig. 6). Observations show that the most metal-rich stars ([Fe/H]> 0) are, overall, the kinematically coolest and show a



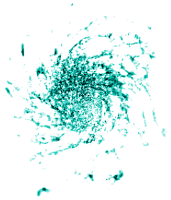
triangularly peaked dispersion profile at low latitudes ($b = 5°$) and a flatter dispersion profile at high latitudes ($b = 10°$), across longitude (see e.g. Fig. 3.8).

Furthermore, the shape of the dispersion profile for the low latitude value $|b| = 5°$ changes in the simulation. The dispersion profile for the lowest age bin shows a flatter dispersion profile at $b = 5°$ than the older stars and at $b = 10°$ it shows structure in the dispersion profile as a function of longitude. From a visual inspection, I find that this structure at $b = 10°$ is due to the line-of-sight selection of stars that are crossing the arms of the X, and comprises the stars confined to the X-shape orbits. Lower dispersion is indicative of stars that most strongly trace out the X which are on coherent orbits. The triangular shape that is seen in the simulation at low latitudes of $b = 5°$, is due to an intermediate and old stellar population (this peaked morphology is not present for the youngest stars in the second panel from the left).

This simulation does not reproduce two of the MW properties: 1) the almost latitude independent dispersion of old stars as seen in the MW for stars with $-0.5 >$[Fe/H]> -1.0, and 2) the presence of a very dynamically hot population with [Fe/H]< -1.0 (Ness et al. 2013b). That the model does not reproduce the kinematics of the most metal poor stars indicates that there is some population missing from the model (similar to Debattista et al. 2017). I conclude that this model galaxy is able to qualitatively well reproduce the overall rotation and dispersion profiles seen for the MW, but there might be a population that is missing in this division by age that matches the kinematics of the most metal poor stars. In the ARGOS survey these show a latitude independent hot dispersion and the RR Lyrae stars in the MW show negligible rotation and significantly hotter dispersion than the more metal rich stars. I will further elaborate on the different components building up these profiles and the differences to the observed profiles in the next chapter.

3.2.4. Rotation and Dispersion Maps

Observational surveys, particularly those that target distant stars in the bulge [e.g. APOGEE (Majewski et al. 2015), ARGOS (Freeman et al. 2013), Gaia-ESO (Gilmore et al. 2012), GIBS (Zoccali et al. 2014)] typically adopt a pencil beam survey approach as completeness in coverage is expensive. In Fig. 3.9 I complement the rotation and dispersion measurements of Fig. 3.8 done in only 18 bins in (l, b) by all-sky maps in (l, b) of the same measurements. The left column shows the surface density maps, the middle column shows the mass-weighted rotation maps and the right panel shows the mass-weighted dispersion maps for all stars within $R = 25$ kpc from the center of our simulated galaxy. Again I divide the simulation into different age bins. The upper row shows the maps for all stars, the second row shows only the youngest stars (< 2.5 Gyr), the third row shows stars with ages $2.5 < t_{\rm star} < 6.0$ Gyr, the fourth row stars with $6.0 < t_{\rm star} < 10.0$ Gyr and the bottom row shows only the oldest stars with $t_{\rm star} > 10.0$ Gyr.



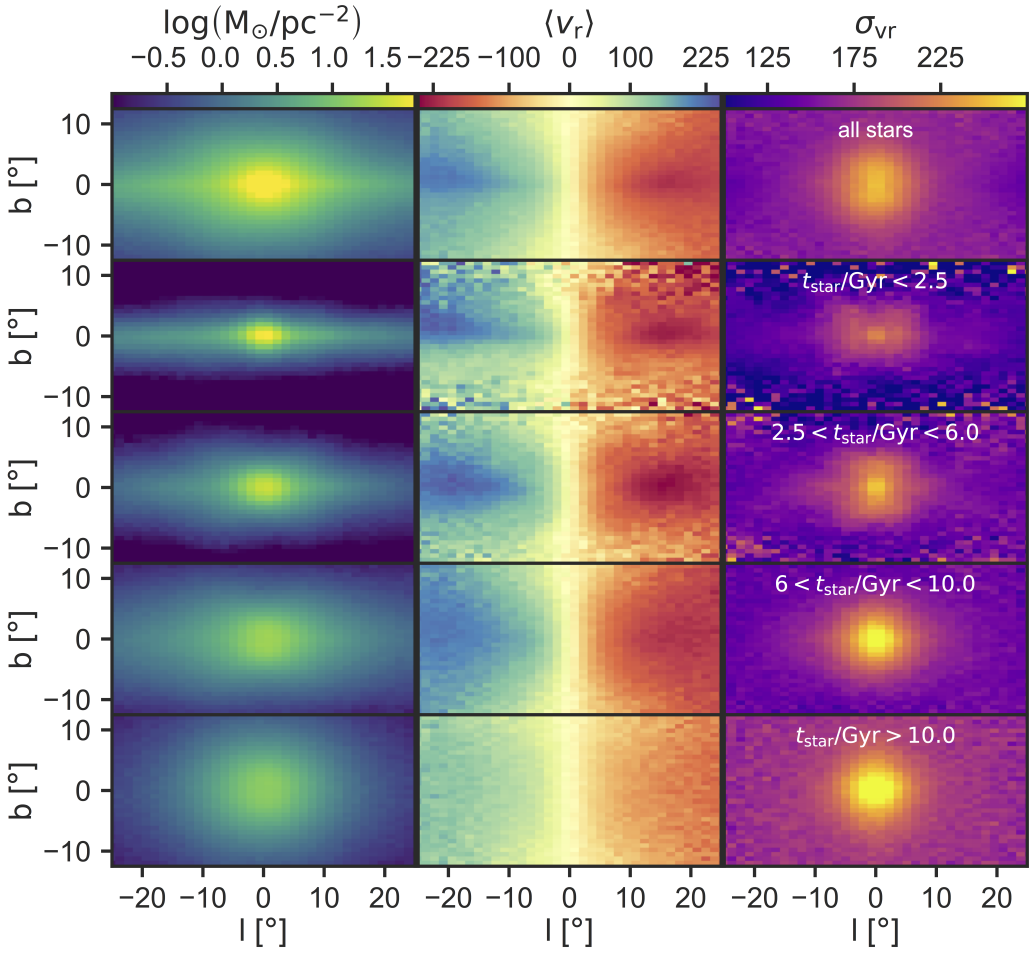
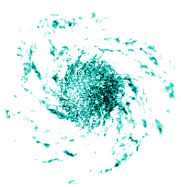


Figure 3.9: Surface density (left column), mass-weighted rotation (middle column) and dispersion maps (right column) for different stellar age populations in (l, b)-projection for stars within $R = 25$ kpc from the center of the simulated galaxy. The *first row* shows all the stars, the *second row* stars younger than 2.5 Gyr , the *third row* stars in the age range 2.5 Gyr up to 6 Gyr, the *fourth row* stars in the age range 6 Gyr up to 10 Gyr and the *bottom row* stars older than 10 Gyr.

The surface density plots in the left column reveal that the scale height of the disc increases for increasingly older populations while the scale length decreases (see e.g. Stinson et al. 2013a; Haywood et al. 2013; Marinacci et al. 2014; Bovy et al. 2016; Ma et al. 2017). The surface density map of all stars clearly show the peanut-shaped (X-shaped) structure of the bulge and by comparing the surface density maps of different age populations I find that this structure is most prominent in the two intermediate age bins. The youngest stars are too concentrated to the mid-plane to exhibit the strong features high above the plane while the oldest population is too spherically symmetric.

Turning to the rotation maps, I find the highest values of rotation close to the galaxy mid-plane and in the l-range of $\sim 5^\circ < |l| < 25^\circ$. Furthermore, with decreasing



age of the stars the rotation velocity increases across all (l, b). The old stars show a more spherically symmetric, slowly rotating configuration at all (l,b), from the bulge into the disc.

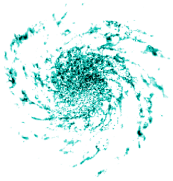
The dispersion maps are most interesting and show different structures as a function of stellar age. For all populations (including for the oldest stars) the lowest dispersion values are found in the disc mid-plane and far away from the galactic center ($-10° < l < 10°$), while there is a peak in velocity dispersion in the galactic center. For the younger stars (see second panel from top in Fig. 8) the velocity dispersion peak in the center itself shows a X-shaped substructure while for the older stars it is more spherically symmetric. In agreement with the findings from the rotation maps, the dispersion maps show the lowest dispersion values for the young stars and increasingly higher values for older stars.

3.3. Key Predictions for Observables

Having established the overall agreement of the simulation with observations of the MW bulge, I will now use this simulation to understand the formation scenario of the bar/bulge in the simulation – and make predictions for upcoming surveys. I will focus in the next subsections on the age of the bar structure and the differences between stars in the bar and the surrounding disc and I will then investigate the formation of the bulge in detail.

3.3.1. Measuring the Age of the Bar from the Split in Stellar Counts

Fig. 3.2 shows that the bar in the simulation forms around 8 Gyr ago at redshift $z \sim 1$. This agrees well with the results from Fig. 3.6 where I found that the split in the stellar counts is visible only for the stellar populations younger than 10 Gyr. Combining this with previous findings, that the complex dynamics of stars under the influence of the bar causes the X-shaped structure (see e.g. Di Matteo 2016; Debattista et al. 2017; Fragkoudi et al. 2017), I propose that the split in the stellar counts might be used to determine the formation time of the bar of the MW. I do this by linking the X-shape distribution as a function of stellar age to the time of formation in the simulation. The underlying assumption of this method is: (a) that the effect of an evolving bar on disc stars is different for stellar populations of different (radial) velocity dispersion, and (b) there is significant evolution of the (radial) stellar velocity dispersion with cosmic time, and thus with stellar age. I present here a first idea how such a measurement could be performed. I caution however, that more simulations of barred disc galaxies and more detailed studies on the dependence of the X-shaped structure on time of



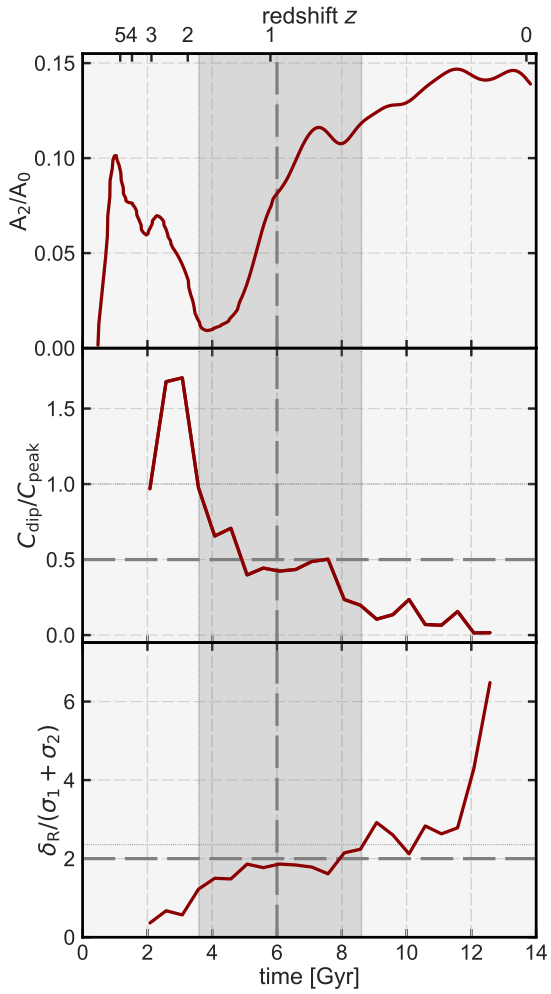
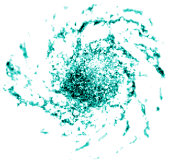


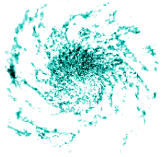
Figure 3.10: *Upper panel*: Bar strength as a function of time measured within 2 kpc from the center of the galaxy. *Middle panel*: Ratio of the dip height to peak height of the double peaked radial distribution of stars for stars in different age bins of width 500 Myr. *Bottom panel*: Ratio of peak separation to the sum of the widths of the two peaks of the radial distribution of stars as a function of radius for stars in different age bins of width 500 Myr. The vertical dashed line indicates where for the first time a strong bar can be visually detected in the simulation. Faint dotted lines indicate lower and upper bounds for the point in time when the bar forms as measured by our method and the shaded area indicates the resulting uncertainty (see main text for detailed description).

formation and the specific mechanisms at play are needed to result in a robust age estimate of the bar. However, this is outside the scope of this thesis and I proceed by laying out the principals of the idea: The peak heights and peak separation of the double-peaked distribution of stars decreases with increasing stellar ages until the double-peaked feature finally disappears for the oldest stellar bins and transitions into a single-peaked distribution. *Kinematic fractionation*, as described in Debattista et al. (2017), has differentiating effects on different stellar populations. Given this, and that I know the formation of the bar precisely in the simulation, I might be able to calibrate the time of formation to the distribution of stars as a function of their age, and apply it to galaxies like the MW.

In the simulation the procedure is as follows: I divide the stars in the simulation into different age bins separated by 500 Myr and fit a double Gaussian to the two peaks



in the stellar counts as a function of distance. From this I first determine, for every age bin, the height $C_1(t)$ and $C_2(t)$ of the two Gaussians and average them to a mean peak height $C_{\rm peak}(t)$. I define the dip height $C_{\rm dip}$ as the value of the double-Gaussian in the center at $R = 8$ kpc. From the ratio of the central dip height to the average peak height $C_{\rm dip}/C_{\rm peak}$, I can determine the time when the double-peaked distribution transits into a single-peaked distribution. A similar measure can be obtained from the ratio of the peak separation $\delta_{\rm R}$ to the sum of the widths of the two Gaussians $\sigma_1 + \sigma_2$. The former ratio as a function of time is shown in the middle panel of Fig. 3.10, while the latter ratio is shown in the lower panel of Fig. 3.10. If I compare the evolution of these two curves to the evolution of the bar strength, either a value of $C_{\rm dip}/C_{\rm peak} \sim 0.5$ or a value of $\delta_{\rm R}/(\sigma_1 + \sigma_2) \sim 2$ marks the formation of the bar in the simulation (indicated by gray dashed lines in Fig. 3.10). This agrees well with the expectation that a value of $C_{\rm dip}/C_{\rm peak} \sim 0.5$ would correspond to a clear visual separation of two equal Gaussians with roughly a separation of 3.33σ (full width at a quarter of a maximum). And a value of $\delta_{\rm R}/(\sigma_1 + \sigma_2) \sim 2$ corresponds well to the fact that for a separation of 2.355σ (FWHM) two equal Gaussians can well be distinguished from a single peak distribution (in this case $C_{\rm dip}/C_{\rm peak} \sim 1$). Clearly the agreement between the two different ways of measuring the separation of the two Gaussians is not perfect. But this is due to the fact that I do not deal with two identical Gaussians, but with asymmetric Gaussians where the Gaussian peak on the near side of the bulge is higher than the one on the far side. Needless to say that the assumption of Gaussian peaks is already a simplification. I therefore indicate in the figure the extreme case of $C_{\rm dip}/C_{\rm peak} \sim 1$ and correspondingly $\delta_{\rm R}/(\sigma_1 + \sigma_2) \sim 2.355$ with thin dotted lines. Taking these into account and given the fact that the bar forms around $t^{\rm bar}_{\rm form} \sim 8^{+2}_{-2}$ Gyr ago I am able to calibrate the values of $C_{\rm dip}/C_{\rm peak}$ and/or $\delta_{\rm R}/(\sigma_1 + \sigma_2)$ to ~ 0.5 and/or ~ 2. However, I caution that this method is used on only a single galaxy here. Calibration against more simulations of barred spiral galaxies would be needed in order to account for possible degeneracies between actual formation time of the bar and its effects on the stellar populations of the underlying disc. Further calibrations would also enable a more robustly determination of the values of $C_{\rm dip}/C_{\rm peak}$ and $\delta_{\rm R}/(\sigma_1 + \sigma_2)$, which correspond to the formation of the bar. As I detailed above, I expect the bar to influence all stars present in the inner disc. Thus the formation of the bar does not coincide with the transition from a single peak to a double peaked distribution and there can be stars of all ages be found in the bar. I do not investigate the role of diffusion over time of the stars in the bulge, where the bulge stars lose the dynamical information linked to their interaction with the bar. However, the observations which show a strong correlation between the morphology of stars in the bulge and their kinematics as a function of [Fe/H] (and in the simulation as a function of their age) is a strong indicator that this information is preserved. This holds promise for the use of a metric as I propose to age date the bar's formation.



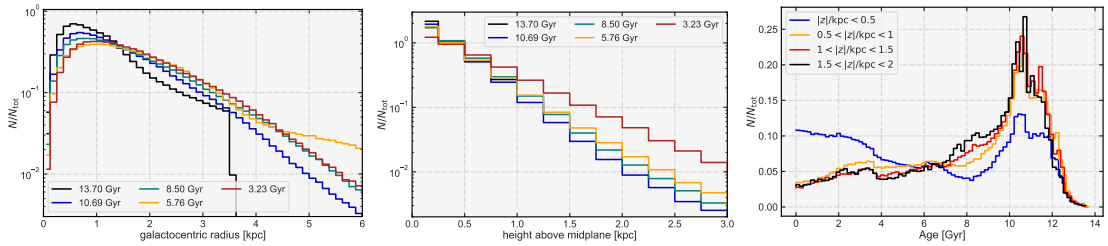


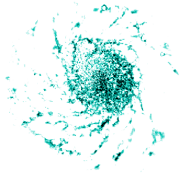
Figure 3.11: Evolution of the radial and vertical distribution of stars in the bar at redshift $z = 0$. I select stars at redshift $z = 0$ which belong to the bar with the following spatial selection criteria: $-3.5 < x/\mathrm{kpc} < 3.5$, $-1.25 < y/\mathrm{kpc} < 1.25$ and $-1.0 < z/\mathrm{kpc} < 1.0$. *Left panel*: Radial distribution of stars in the bar at redshift $z = 0$ (black line) and for different snapshots at earlier times. *Middle panel*: Vertical distribution of the same selection of stars for the same selection of snapshots. *Right panel*:Age distribution of stars in the innermost 3.5 kpc from the galaxy center for different heights above the stellar mid-plane. The *blue histogram* shows the age distribution for stars with $|z| < 0.5$ kpc from the mid-plane, the *orange one* shows stars with $0.5 < |z|/\mathrm{kpc} < 1.0$ kpc, the *red histogram* shows stars with $1.0 < |z|/\mathrm{kpc} < 1.5$ kpc and the *black histogram* shows stars with $1.5 < |z|/\mathrm{kpc} < 2.0$ kpc.

3.3.2. Origin of the Stars in the Bar

The bar (and the boxy-peanut bulge) of the simulated galaxy formed around 8 Gyr ago, and as such two questions arise naturally: (1) what triggers the bar formation, and (2) where do the stars that currently belong to the bar came from? I have checked visually that no merger is responsible for triggering the bar instability in this simulation. However, at redshift $z = 1$ when a strong bar forms, I can identify two close encounters between satellites and the main galaxy after which the bar is established. This might just be a coincidence, but investigating the connection between close encounters and bar formation is outside the scope of this thesis and is left for future work (see Zana et al. 2017, for a detailed discussion).

To address the second question, I trace the stellar particles of the $z = 0$ bar backwards in time via their unique particle IDs and analyse their spatial distributions at each timestep. The procedure is as follows: I select stars at redshift $z = 0$ in the center of the galaxy in a bar-like structure. First I rotate the simulation such that the stellar disc of the simulation lies in the $x - y$ plane and the long axis of the bar coincides with the x-axis. I then select all the stars in the region $-3.5 < x/\mathrm{kpc} < 3.5$, $-1.25 < y/\mathrm{kpc} < 1.25$ and $-1.0 < z/\mathrm{kpc} < 1.0$. These spatial cuts agree well with a visual identification of the bar in surface density images and also agree with the assumptions of Portail et al. (2015b) for the bulge region of the MW.

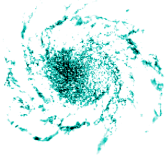
Having selected these stars, I plot in Fig. 3.11 the histograms of their radial distributions (left panel) and their vertical distance from the mid-plane of the stellar disc (middle panel) for increasingly earlier times (only for those stars already born at that given time). Most of the stars which are at present day in the bar (black line) were



born at small galacto-centric radii (the sharp cut in the black histogram at $R \sim 3.5$ kpc marks the selection of the bar at $z = 0$). The histograms of the radial distribution stay peaked around $R \sim 1$ kpc for all previous times shown. Only a few stars migrated inwards. As a sanity check I tracked the position of stars which have been in the bar already at redshift $z = 1$ down to redshift $z = 0$ and find similar results. Almost all stars already in the bar at $z = 1$ stay there and only few are migrating outwards. These findings suggest that stars in the bar region at the present day have a pure disc origin as already suggested by Di Matteo (2016) and Fragkoudi et al. (2017). The left panel of Fig. 3.11 shows that there is a contribution of stars from outside 4 kpc to the present day bar. This in combination with the findings from Fig. 3.3 suggests that there exists a mechanism which preferentially adds younger stars (thin disc stars) to the bar but less so the inner disc (see also Fragkoudi et al. 2017).

The same result is found for the vertical height of stars above the stellar mid-plane. Stars at earlier times in the simulation show the same height distribution as stars at redshift $z = 0$. The height distribution for the whole sample stays almost unaffected. These findings might indicate that the fractionation of of the early disc into the boxy/peanut bulge was not purely kinematical but also depends on the initial structure of the thick disc as suggested by Di Matteo (2016) and Fragkoudi et al. (2017). The scale height is slowly decreasing with cosmic time. About 3 Gyr after the big bang I find scale heights of almost 1 kpc which reduce to a scale height of about 470 pc at redshift $z = 0.25$, or about 11 Gyr after the big bang. These scale heights are almost twice as large as the gravitational softenings of the stellar and gaseous particles (~ 260 pc) in this simulation and thus the disc is at all times well resolved. Observations of stellar discs at higher redshifts $z \gtrsim 1$ (e.g. Elmegreen and Elmegreen 2006; Elmegreen et al. 2017) show that scale heights at these redshifts are of the order of ~ 1 kpc which is in good agreement with the scale heights in the simulation.

The result obtained from Fig. 3.9, that younger stars show a thinner configuration and are found closer to the stellar mid-plane is analysed in more detail in the right panel of Fig. 3.11 where the age distribution of stars as a function of height above the stellar mid-plane at redshift $z = 0$ is investigated. For simplicity I have selected all stars with galacto-centric radius $r < 3.5$ kpc and grouped them into 4 different bins in height ($|z|/\mathrm{kpc} < 0.5$, $0.5 < |z|/\mathrm{kpc} < 1.0$, $1.0 < |z|/\mathrm{kpc} < 1.5$ and $1.5 < |z|/\mathrm{kpc} < 2.0$). I then plot the distribution of stellar ages for every slice of height above the mid-plane. In general, I see a double peaked distribution with one old peak around stellar ages of $\sim 9 - 10$ Gyr and a younger peak with stellar ages around ~ 2 Gyr. Comparing the younger peak with the older peak I find that there is a slight overabundance of young stars close to the disc mid-plane (blue line) while older stars are more abundant at larger heights from the disc (red and black lines). This is in concordance with the results from Fig. 3.9 where I have seen that young stars are concentrated close to the disc mid-plane while older stars can also be found at larger heights from the disc. These



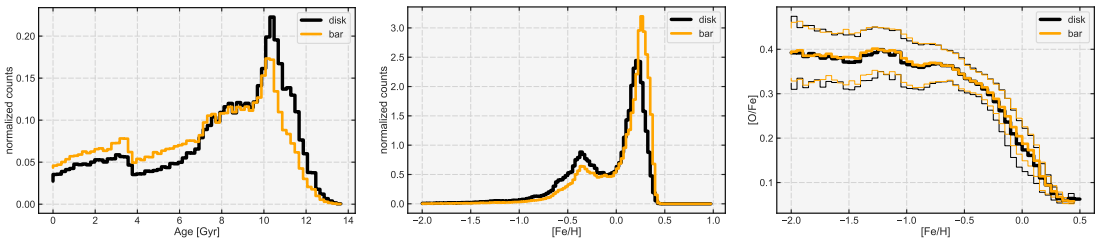


Figure 3.12: Properties of bar (orange histogram) and "disc" stars (black histogram). The *left panel* shows the age distribution function, the *middle panel* the metallicity distribution function and the *right panel* the oxygen abundance [O/Fe] as a proxy for α-elements vs. metallicity. The thin lines show the 1σ scatter in [O/Fe] while for the other two panels the scatter is much smaller than the line thickness.

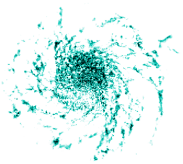
findings are further consistent with the results from Ness et al. (2014) who studied the bulge region in an isolated simulation of galaxy formation and the results from Di Matteo et al. (2014) who studied in detail the formation of boxy/peanut bulges by means of idealised N-body simulation. These authors find that all stellar populations within the outer Lindblad resonance of the bar get mapped into this structure which points towards a pure disc origin of the MW bulge. A consequence of this is that that bulge and disc populations show very similar properties.

Combining the results from Fig. 3.11 and Fig. 3.9 I conclude that the bar/bulge region in this simulation is formed in-situ from the disc. For the whole population I do not see considerable evolution in the thickness nor in the radial component. However, I do see that there are different sub-components present in the bar/bulge region showing different spatial distributions with younger stars being found closer to the disc mid-plane in agreement with observational findings from Bensby et al. (2013) and theoretical results from Ness et al. (2014).

3.3.3. Differentiating Stars in the Bar and the Disc

Following the result that most stars in the bar were locked up in this structure since they were born, or at least shortly after their birth, I now try to answer the question if bar membership comes with a distinct imprint on this stellar population, thus enabling disc and bar to be distinguished.[1] To test this, I select two samples of stars: A) The bar sample, for which I select all the stars which have a distance from the galaxy center in the range $2 < R/\mathrm{kpc} < 3.5$ and which intersect with the previous bar selection of $-3.5 < x/\mathrm{kpc} < 3.5$, $-1.25 < y/\mathrm{kpc} < 1.25$ and $-1.0 < z/\mathrm{kpc} < 1.0$ for the bar lying

[1] That is, other than via their orbits, which are not a direct observable. (Even with Gaia, observing the bulge is problematic due to both reddening and crowing and the precision of proper motions for stars that are observed at the distance of the bulge is too low over the 5-year baseline of the mission to determine orbits for stars in much of the bulge region).



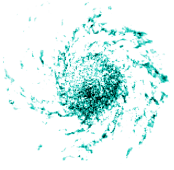
in the $x-y$-plane aligned with the x-axis. B) The disc sample, for which I select stars in the stellar disc with the same radial distance from the galaxy center but instead of being located in the barred structure, I select them to belong to a barred structure 90° offset from the bar. For these two samples of stars I plot in Fig. 3.12 the distribution of stellar ages (left panel), stellar metallicities [Fe/H] (middle panel) and the mean value of [O/Fe] for every metallicity bin (right panel).

The age distribution of bar stars and disc stars looks almost the same, except for a slight shift to younger ages for the bar population, maybe indicating ongoing star formation at the tips of the bar. Similar results are found for the metallicity distribution of bar and disc stars shown in the middle panel of Fig. 3.12. Bar stars and disc stars show very similar distributions with the bar stars offset to slightly higher metallicities. In the [O/Fe] vs. [Fe/H] plot I do not see any differences between bar and disc stars at all. The only subtle differences between bar and disc stars fit in the picture of an in-situ formation of the bar/bulge region from the disc, as laid out previously. The slight distinctions can be explained by the different densities of stars in the bar and the surrounding disc, which differ for each population, e.g. the oldest stars do not show a barred structure but a more spherically symmetric distribution, while for increasingly younger stars the bar is more and more pronounced. Thus, one finds in the same volume slightly more young stars in the bar region than outside it. This explains the similarity, but also the very slight differences in age and metallicity. In the simulation there is continued star formation in the center and maybe even in the bar such that new, young stars are continuously added to the bar. The near identical properties of the disc and bar populations that I find in the simulation is aligned with observational results (e.g. Alves-Brito et al. 2010; Bensby et al. 2017). That the inner disc and bulge are practically indistinguishable is not an unexpected result given that the bar formed from the disc at early times. In the simulation, the differences in the overall distributions are simply a consequence of the different spatial profiles of these structures.

3.4. Summary and Conclusion

In this chapter I presented a high resolution cosmological hydrodynamical simulation of a galaxy, whose bulge properties are in remarkable good agreement with MW observations. I used this simulation to study in detail the different stellar constituents of the bulge and bar region, their kinematical and chemical properties and their origin, and to make predictions for up-coming spectroscopic surveys like MOONS (Cirasuolo et al. 2012), 4-MOST (de Jong and Consortium 2015), APOGEE-2 (Zasowski et al. 2017) and Sloan V (Kollmeier et al. 2017). My main results can be summarised as follows:

- I compare stellar counts in the simulation to the key observations of a double-peaked distribution in the line-of-sight star counts towards the Galactic center,



and find an excellent qualitative agreement between the two. All stars younger than 10 Gyr in the simulation show a split in the line-of-sight counts with increasing peak separation for younger stars (see Fig. 3.6).

- In the simulation the bar leads to a fractionation of the boxy/peanut bulge. By tracing the different stellar populations of the bulge region back in time, I find that their kinematic properties are in agreement with the idea of *kinematical fractionation* (Debattista et al. 2017). I also find a significant contribution from young stars to the bar which implies further dynamical effects present in the already barred galaxy.

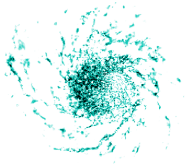
- The secular evolution under the influence of the bar separates initially co-spatial populations of stars into different orbit families, thus resulting in a different strength of the X-shaped structure for different stellar populations (see also Di Matteo 2016; Fragkoudi et al. 2017, for the dependence of fractionation in boxy/peanut bulge on the initial structure of the early thick disc).

- In Fig. 3.8 I compare the kinematics of the stars in the bulge region of the simulation with observed kinematics of the MW bulge stars taken from ARGOS, and find excellent qualitative agreement. The shape of the rotation and dispersion profiles agree very well, although the rescaled (absolute) values for rotation and dispersion of this simulation are lower (higher) than those observed for the MW due to a stellar mass difference. In the same figure I show the rotation and dispersion profiles for different age populations of stars in the simulation predicting what one would see if ages were available for MW stars.

- The peak separation in the split of line-of-sight star counts and the age of the stellar population correlate (Fig. 3.6). Younger stars show larger peak separation. Further, I find, in agreement with results from Debattista et al. (2017), that the split is due to the bar separating different stellar populations. I propose that this might be used to measure the age of the bar in the MW. Using a Fourier analysis of the simulation (Fig. 3.2) I find an age of ~ 8 Gyr for the bar and calibrate a measurement involving stellar line-of-sight counts of stars in the bulge.

- Most of the bar stars at $z = 0$ were born at small radii (Fig. 10). Furthermore, the simulation suggests that once stars are in the bar they are locked-up there.

- I compare the properties of stars in the bar (with radii between 2 and 3.5 kpc) and the inner disc (same radii but 90° offset from the bar). I find almost indistinguishable age, metallicity and oxygen abundance distributions, (compare Fig. 3.12). I conclude that simple cuts in age, metallicity or oxygen abundance are not sufficient to discriminate stars that reside in the disc from those in the bar.



Chapter 4

The Milky Way's Central Region II - A Formation Scenario for the Milky Way's Peanut Bulge

There is another theory which states that this has already happened.

— Douglas Adams, The Restaurant at the End of the Universe

This chapter presents the second part of the analysis of the peanut shaped bulge in one of the high-resolution NIHAO galaxies. The content of this chapter has been submitted to the *Astrophysical Journal* is currently under review. A preprint version is available on the arXiv (Buck et al. 2018b). All the research done for this chapter has been conducted by myself.

While the last chapter presented a detailed comparison of the properties of the MW's bulge and the simulated bulge of the galaxy g2.79e12, this chapter employs a kinematical decomposition technique on the exact same galaxy in order to study stellar populations defined to be on distinct orbits. In order to do so I use a clustering algorithm on stellar kinematics to identify a number of discrete kinematic components: a thin and thick disc, a stellar halo and two bulge components; one fast rotating and one non-rotating. I then focus on the two bulge components and show that the slow rotating one is spherically symmetric while the fast rotating component shows a boxy/peanut morphology. Although the two bulge components are kinematically discrete populations, they are *both* mostly formed over similar time scales, from disc material. The key finding of this chapter is that stellar particles with lower initial birth angular momentum end up in the non-rotating spherical bulge, while stars with higher birth angular momentum are found in the peanut bulge. This has the

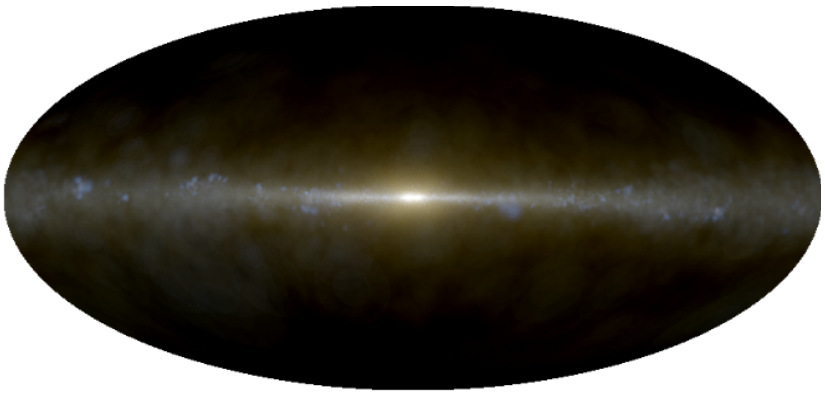


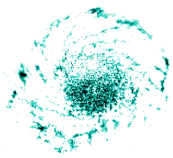
Figure 4.1: RGB all sky projection of the simulated galaxy. The camera position is chosen to be 8 kpc from the Galactic center imitating the earth's position in the MW. Stellar particles are rendered using their luminosity in the wavelength bands i, v, u in order to create the r, g and b channels.

important consequence that a bulge population with a spheroidal morphology does not necessarily indicate a merger origin. In fact, I do find that only $\sim 2.3\%$ of the bulge stars components are ex-situ stars brought in by accreted dwarf galaxies early on.

4.1. CONTEXT

The structure and dynamics of stars in the inner region of disc galaxies carries important information about the formation and subsequent evolution processes shaping them. While the inner parts of disc galaxies can have a boxy or spheroidal morphology, several stellar constituents can co-exist, including halo, disc, bulge and cluster populations. Some galaxies, like M31, show evidence for multiple bulge populations, of both a spherical and boxy component (Blaña Díaz et al. 2017). Typically, boxy bulges are attributed to internal evolution processes, formed from the disc (e.g. Combes and Sanders 1981; Raha et al. 1991; Bureau and Freeman 1999). These processes are driven by the influence of non-axisymmetric components, such as the bar (e.g. Herpich et al. 2017; Fragkoudi et al. 2018). Conversely, large spheroidal bulge components are typically attributed to turbulent, external formation processes, such as mergers.

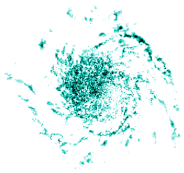
Over the last two decades, a large number of studies have explored the structure of the MW's bulge, revealing the presence of rich substructures within the inner region (e.g. Zoccali et al. 2008; Lecureur et al. 2007; Babusiaux et al. 2010; Gonzalez et al. 2013; Bensby et al. 2013; Zasowski et al. 2016). The BRAVA (Howard et al. 2008), ARGOS (Freeman et al. 2013) and APOGEE survey data (Majewski et al. 2015) show that the stars in the bulge of the MW are cylindrically rotating (Howard et al. 2009; Kunder et al. 2012; Ness et al. 2013a). This is indicative of formation from the disc via internal



evolution (Ness and Lang 2016; Fragkoudi et al. 2017; Buck et al. 2018c). However, the kinematic character of the bulge changes as a function of the stellar metallicity (e.g. Portail 2016). More metal rich stars show lower velocity dispersions (Ness et al. 2013b) and the most metal-poor stars (< -1.0) are nearly non-rotating (Kunder et al. 2016). The origin of the metallicity dependent kinematics for stars that are in the boxy/peanut bulge population has been interpreted as a consequence of kinematic fractionation in the disc from which it has formed (Debattista et al. 2017). The metal-poorer stars that are very slowly rotating have been associated with a population that is not part of the boxy bulge structure. These metal poor stars are possibly (a combination of) thick disc (e.g. Di Matteo et al. 2014, 2015), stellar halo (Howes et al. 2016) and/or classical bulge, with an origin distinct from the disc (e.g. Rojas-Arriagada et al. 2017). However, the detailed formation of the metal-poor, slowly rotating population that is seen in the inner region of the MW and its formation timescale in relation to the boxy/peanut structure is not yet understood.

Only cosmological simulations are able to self-consistently capture the effects of a cosmological environment, namely gas accretion, star formation, close encounters with satellite galaxies and effects of stellar feedback. Including these processes in addition to the internally driven evolution is necessary in order to study the different components of galactic bulges and explain their origin. However, for a long time cosmological simulations were not able to reproduce realistic bulges due to numerical resolution and the inherent hierarchical nature of galaxy formation. Cosmological simulations commonly predict that galactic spheroids are primarily built up through hierarchical mergers (e.g. Kauffmann et al. 1993; Abadi et al. 2003; Kobayashi and Nakasato 2011; Guedes et al. 2013, but see also Obreja et al. (2018a)). This formation scenario produces old classical bulges in contrast to a boxy/peanut shaped bulge such as is observed in the MW (Weiland et al. 1994; Dwek et al. 1995; Ciambur et al. 2017). In the last chapter I have presented one of the first cosmological simulations able to reproduce several of the key characteristics of the MW central region (Buck et al. 2018c) including a realistic boxy/peanut bulge morphology (see also Debattista et al. 2018).

Given I can now reproduce MW type bulges in cosmological simulations, I have the opportunity to test the orbital structure of these objects in fully cosmological simulations (see e.g. Portail et al. 2015a,b). For the MW, we have the expectation that several stellar constituents co-exist in the inner region. Using an orbital decomposition of stars is a promising framework to understand bulge substructure and its formation origin, particularly in the Gaia era. From a dynamical point of view, stellar orbit classification provides the most robust way to disentangle different galactic stellar structures (Binney 2013). Observationally, this approach can be applied to the MW, thanks to recent large scale surveys (e.g. Steinmetz et al. 2006; Gaia Collaboration et al. 2016a; Majewski et al. 2017). Stellar orbit classification has also been recently applied



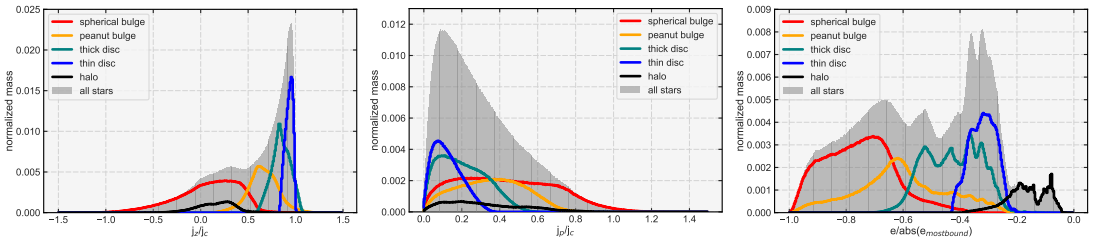


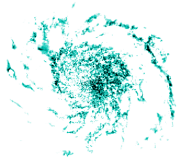
Figure 4.2: The result of the GMM decomposition shown as normalised stellar mass in each component (colored histograms) as function of dynamical features: j_z/j_c (left panel), j_p/j_c (middle panel), $e/|e_{\mathrm{mostbound}}|$ (right panel). The gray histograms show the normalised stellar mass distribution for the whole stellar population of the galaxy.

to extragalactic observations (Zhu et al. 2017b,a; Gonzalez et al. 2016, 2017) of CALIFA galaxies (Sánchez et al. 2012b).

In this chapter I use an unsupervised Gaussian mixtures algorithm in a particular stellar kinematic space (Obreja et al. 2016, 2018b) in order to understand the orbital composition of the MW-like bulge in the high resolution galaxy, which has a clear boxy-peanut morphology and a cylindrical kinematic profile. Standard analysis of abundance patterns and line-of-sight velocities in the central regions of this galaxy suggest that large parts of the bulge and its central bar are formed from disc material (Buck et al. 2018c). Using the decomposition technique, I find that the stellar particles of this simulated galaxy decompose into a thin and thick disc, a peanut bulge, a spherical bulge and a stellar halo population. In this chapter I focus on the two bulge components and study in detail their properties and formation scenarios in order to investigate the driving mechanisms in separating stellar particles into different orbit families.

4.2. Stellar Kinematical Decomposition

The current standard kinematic decomposition of simulated galaxies was first introduced by Abadi et al. (2003) and relies on analysing the distribution of stellar circularities, $\epsilon(E) = J_z/Jc(E)$, which is computed from the azimuthal angular momentum of a particle, J_z, and the angular momentum of a circular orbit, $J_c(E)$, having the same binding energy, E (e.g. Brook et al. 2004; Brooks 2008; Tissera et al. 2012). This decomposition method has widely been used to study discs and bulges in galaxy formation (see e.g. Scannapieco et al. 2010, 2011; Martig et al. 2012; Marinacci et al. 2014; Kannan et al. 2015; Zavala et al. 2016). However, this classical method makes ambiguous classifications of stars with intermediate values of circularities. In order to circumvent this ambiguity Doménech-Moral et al. (2012) suggested adding the binding energy, E, and the angular momentum component perpendicular to the disc, J_p, to the



parameter set. Furthermore, instead of adopting fixed values in the various parameters to discriminate between disc and bulge, Doménech-Moral et al. (2012) used a cluster finding algorithms (e.g. *k-means* Schölkopf et al. 1998) to arrive at data driven cuts.

Obreja et al. (2016, 2018b) used the method outlined by Doménech-Moral et al. (2012), but with the *Gaussian Mixture Models* (GMM) of the machine learning code scikit-learn (Pedregosa et al. 2011) as clustering algorithm instead of *k-means*. The main reason for using GMM instead of *k-means* is that the latter algorithm naturally results in clusters of roughly equal sizes which is not optimal for finding sub-dominant structures like stellar halos. The more recent method operates on a similar parameter space as suggested by Doménech-Moral et al. (2012). However, to factor out the galaxy/halo mass dependence and to remove the dimensionality of the energy, Obreja et al. (2016) switched to specific values of angular momentum and binding energy, $(j_z/j_c, j_p/j_c, e/\max(|e|))$. Additionally, the binding energies of stellar particles are scaled to fall within -1 to 0, such that -1 represents the most bound star particle.

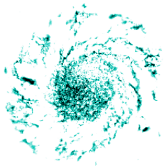
One advantage of using data-driven decomposition techniques such as GMM, is the flexibility in being able to define the number of components. Using GMM, the only input-parameter to be provided is the number of components that represent the data. Further one can also determine, by iterating over the number of components, how many components best fit the data. For this study I started with a 2 component specification (disc- and spheroidal-component) and increased the number of components successively. I found that a total of 5 different components best represents the data in our simulation. Fig. 4.2 gives the normalised stellar mass distributions of all 5 components in the input kinematic space of $(j_z/j_c, j_p/j_c, e/\max(|e|))$. For more details on how the algorithm works to determine the optimal number of components that represent the data, see Obreja et al. (2018b).

4.2.1. Morphology and Angular Momentum

Figure 4.3 shows the surface density maps in edge-on and face-on projections for all the stars in the galaxy (left most column) and for the five different components identified in the subsequent columns. I like to stress here that I define these five components **solely** via their kinematics and not their morphological properties (see also Fig. 4.2 for the distributions of j_z/j_c, j_p/j_c, and e/max(|e|) for each component).

I name the components returned by the algorithm based on their morphology (which is **not** part of the separation process) as follows: a spherical bulge component, a boxy-peanut shaped bulge[1], a thick disc, a thin disc and a spheroidal stellar halo component (from left to right in Fig 4.3). I caution that these names are inspired by

[1]There is some confusion in the literature about the usage of boxy/peanut bulge and bar. Here I use both terms as synonyms for the same component as the boxy/peanut bulge is essentially the buckled bar.



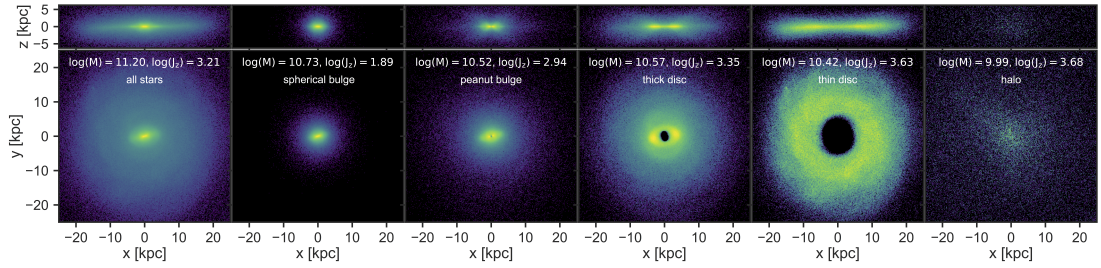


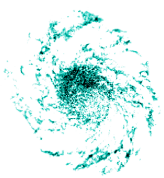
Figure 4.3: Surface density maps in edge-on (upper panels) and face-on (lower panels) view of all stars in the simulated galaxy (left most panels) and in the different kinematic components identified using the method of Obreja et al. (2018b). From left to right: all stars, spherical bulge, boxy-peanut bulge, thick disc, thin disc and stellar halo. Each panel indicates the total mass in $M_\odot$ and the total specific angular momentum of each component in kpc km s^{-1}.

the overall morphology of these components and I do not claim that these necessarily reflect the specific individual populations in the MW. Each panel indicates the stellar mass in each component and its specific angular momentum. Except for the stellar halo component, all others contribute nearly an equal amount of stellar mass to the whole stellar budget of the galaxy. Interestingly, the two disc components reveal holes in the central region. This implies that all stellar particles in this region are on hot orbits and are thus assigned to the other three components - the two bulge components and the halo (see also Portail et al. 2017a).

The spherical bulge component shows, as the name suggests, a spherical symmetric morphology. The peanut bulge component is barred in face-on view and shows signs of an X-shaped morphology in edge-on view, with a very thin component extending out to ~ 10 kpc in the disc mid-plane. The spherical bulge component shows the lowest value of total angular momentum, indicating almost no net rotation. The boxy bulge component has a much larger total angular momentum. The thick disc component is short and extends up to heights of ~ 4 kpc above the disc mid-plane. The thin disc component is much more extended, and appears thinner in the edge-on view. The thick disc component shows a lower value of total angular momentum than the thin disc, but a larger value compared to the peanut bulge. The largest value of total angular momentum is found for the stellar halo component. This halo component is by far the smallest component in terms of mass. We attribute the high angular momentum amplitude to its much more extended morphology.

4.2.2. STELLAR AGES

The left panel of Fig. 4.4 shows the mass-weighted distribution of stellar ages in each component (colored lines) as well as in the whole galaxy (gray filled histogram). All components differ in their median age, although stars are distributed across a broad



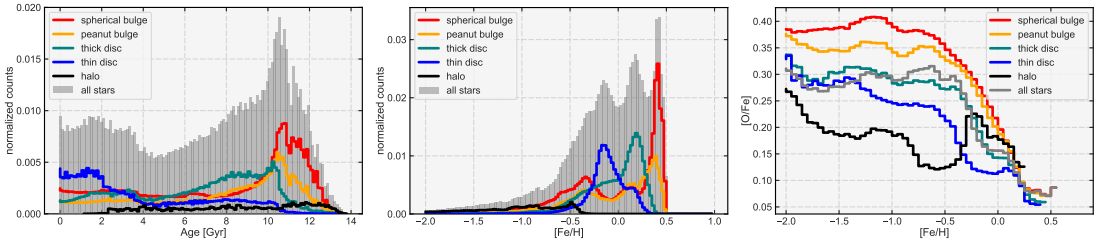
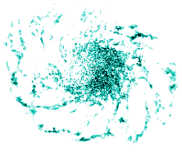


Figure 4.4: Properties of the kinematically decomposed populations of stars. From left to right the mass-weighted age distribution, the metallicity distribution and the oxygen abundance [O/Fe] as a proxy for α-elements vs. metallicity are shown. Colored lines indicate the different components as labeled in the legend and the gray filled histogram or the gray thick line (right panel) shows the distribution for the whole stellar population of the galaxy. The scatter around the mean is much smaller than the line thickness for the two left most panels and about Δ[O/Fe]~ 0.05 at low metallicities and Δ[O/Fe]~ 0.025 at the high metallicity end.

age range for all of them. The spherical bulge (red line) has the largest fraction of old stars. The age distribution peaks around 10-13 Gyr, at higher ages compared to all other components. The peanut bulge (yellow line) is the second-oldest component overall, with the peak shifted to slightly lower stellar ages, of around 10 Gyr. Interestingly, both bulge components show tails down to the youngest stellar ages. I will come back to this point in the discussion of this chapter. The thick disc (green line) shows a broad peak around stellar ages of ~8 Gyr, and the thin disc (blue line), by far the youngest of the five, shows a clear peak at stellar ages of about 1 Gyr, with a tail towards older stellar ages. The stellar halo has a far flatter age distribution and exhibits stars of all ages down to 2.5 Gyr (there are no very young stars in the halo with ages < 2.5 Gyr).

4.2.3. Stellar Metallicities

The components also separate out in the median and peak of their metallicity distributions, as shown in the middle panel of Fig. 4.4. The spherical bulge, seen to be the oldest component in the left panel of figure 4.4, shows a strong peak at the highest metallicities, of values above solar (~ 0.4) and smaller peaks at around solar metallicity and ~ -0.4 and below (red line). The peanut bulge (yellow line), the second oldest component, has a similar metallicity distribution to the spherical bulge, but shifted to slightly lower metallicities. The thick disc (green line), shows a strong and broad peak around metallicities of about 0 to 0.2 dex with a tail down to -0.5 dex. The thin disc (blue line) shows a well defined single peak around solar metallicity. Finally, the stellar halo (gray line) is made up of stars of the lowest metallicities and shows (only) a broad distribution below metallicities of -0.4 dex. The total metallicity distribution function (black line) shows three distinct peaks at slightly sub-solar (~ -0.2 dex),



slightly super-solar values (~ 0.2 dex) and 0.4 dex. Comparing the single components to the total metallicity distribution, one finds that these peaks are made up of primarily the thin disc, thick disc and bulge stars.

4.2.3.1. [O/Fe] vs. [Fe/H]

In the right panel of Fig. 4.4, I show the average [O/Fe] vs. [Fe/H] distribution for all five sub-components (thick colored lines) with the same line colors as before. This figure recovers the expected trend in oxygen enrichment as a function of metallicity. The spherical bulge is the most α-enhanced population, followed by the peanut bulge. Thick and thin disc separate in the metallicity range of -1.0 dex to 0.0 dex, with the thin disc being offset to lower values of [O/Fe] (interestingly, these show similar α-enhancement at very low, < -1.0 dex, and very high, > 0 dex, metallicities). By far the lowest values of [O/Fe] are found for the stellar particles in the halo component. In this panel, the gray thick line shows the result using all stellar particles in the disc.

The MW shows two alpha sequences, a low and a high sequence (e.g. see Hayden et al. 2015) that have been associated with a thin and thick disc component (see e.g. Gilmore and Reid 1983). I highlight here again that I recover a difference in the α-enhancement of the thin and thick disc star particles, using a decomposition solely based on stellar kinematics. This result is worth investigating in more detail in subsequent work, but is beyond the scope of this thesis.

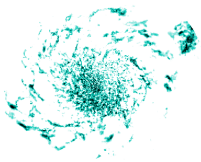
4.3. Properties of the Spherical Bulge and the Peanut Bulge

In order to compare properties of the two bulge components with observations of the MW, I rotate the model galaxy to a heliocentric frame of reference where the stellar disc is in the $x-y$ plane and the bar inclined at $27°$ with respect to the line-of-sight. I then observe the bulge from the sun's position at a distance of 8 kpc from the galactic center (see also the last chapter for more details).

4.3.1. Rotation and Dispersion Maps

Fig.4.5 shows maps of the stellar surface density (left column), rotation (middle column) and dispersion values (right column) of the spherical and the peanut bulge in l, b. Fig. 4.6 shows similar maps for all kinematically identified components.

The surface density maps clearly reveal the different morphologies for the spherical and the peanut bulges. They further show that the spherical bulge component shows only small to no rotation, while the peanut bulge component shows a fast rotation. The clear X-shaped structure in the rotation map is indicative of bar/box orbits viewed edge-on.



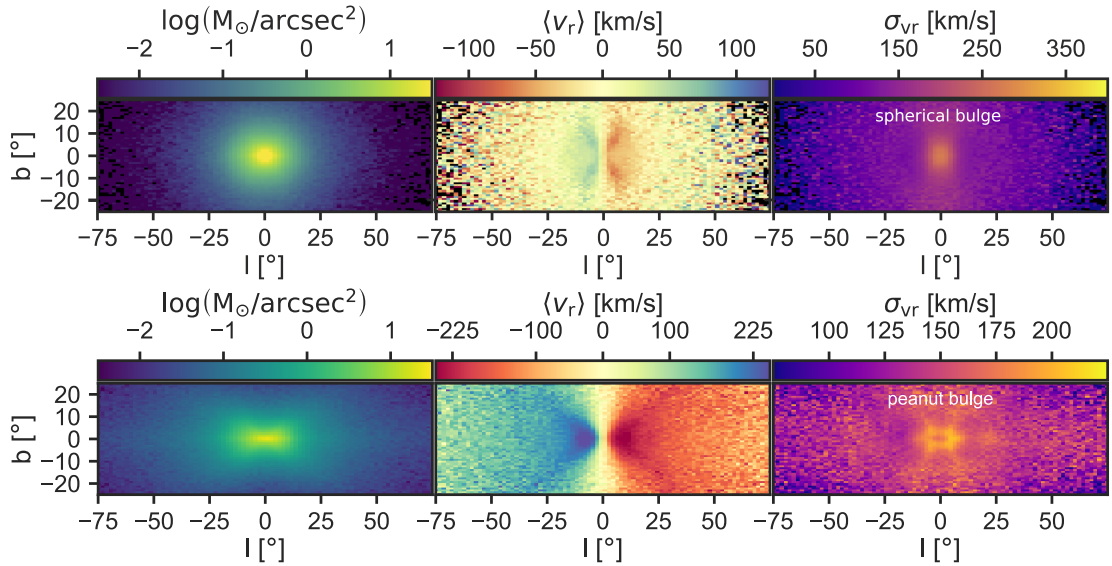
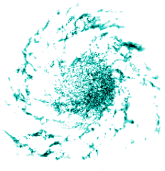


Figure 4.5: Surface density (left column), mass-weighted rotation (middle column) and dispersion maps (right column) in (l, b)-projection. The top row shows the results for the spherical bulge component and the bottom row for the peanut bulge component respectively.

The dispersion map of the spherical bulge component shows remarkable spherical symmetry with a strong peak in the center, and a very latitude dependent dispersion profile. On the contrary, the dispersion map of the peanut bulge component shows strong features due to the underlying morphology. The map shows a clear X-shaped dispersion signature in the center, resembling the morphology of the X in the surface density projections. Apart from this, the dispersion map is relatively flat and does not show an increase in dispersion towards the center, as seen for the spherical bulge component. Thus, dissimilarly to the spheroidal bulge component, the boxy bulge component has a fairly latitude independent dispersion.

4.3.2. Rotation and Dispersion Profiles

The rotation and dispersion maps for the two bulge components shown in figure 4.5 highlight the different signatures clearly seen when breaking up the stars by their orbital classes. Observationally, one can not discriminate orbital classes via line of sight velocities which have been measured for the bulge in pencil beam studies. It is therefore interesting to see how the kinematics of both bulge components individually and also their combination compare with the observations of bulge stars. Therefore Fig. 4.7 shows the rotation (mean velocity along the line-of-sight, top row) and dispersion (velocity dispersion along the line-of-sight, bottom row) profiles, as a function of longitude for two different latitudes. The left panels show the stars of the spherical



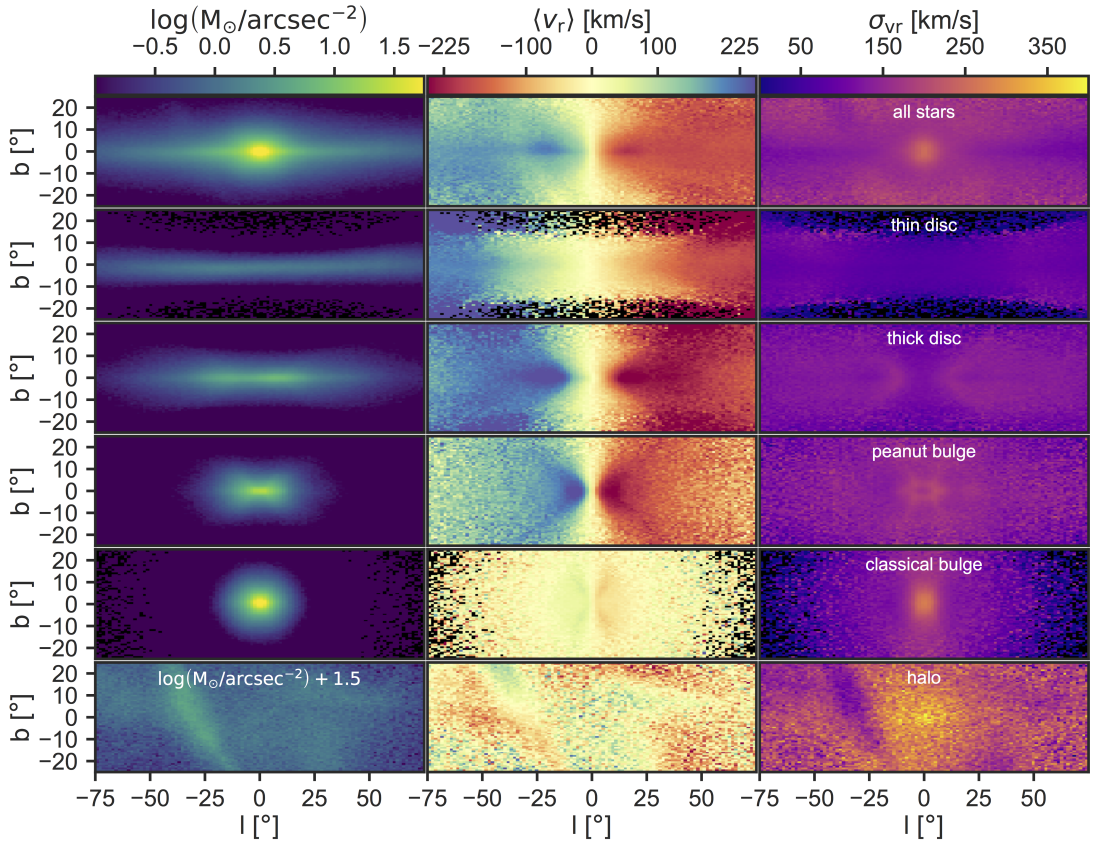
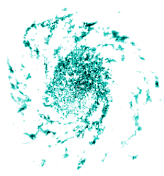


Figure 4.6: Surface density (left column), mass-weighted rotation (middle column) and dispersion maps (right column) for different kinematically defined stellar populations in (l, b)-projection for stars within $R = 25$ kpc from the center of our simulated galaxy. The *first row* shows the results for all stars, the *second row* shows thin disk stars, the *third row* shows thick disk stars, the *fourth row* shows stars in the peanut bulge and the *bottom row* shows stars of the spherical bulge.

bulge component, the middle panels the ones of the peanut bulge and the right panels the combination of both components in comparison to observational data from the ARGOS survey (colored dashed lines Ness et al. 2013a). Blue dots and yellow triangles dots show the profiles for latitudes of $b = 5°$ and $b = 10°$, respectively. In order to account for the stellar mass difference between the MW and the simulation the same rescaling of the velocities as in the previous chapter is applied.

I start the discussion of Fig 4.7 by first comparing the rotation and dispersion profiles of the two bulge components to each other and then turn to compare them in detail to the observations. I find that the spherical bulge shows at most slow (< 50 km/s) rotation, while the peanut bulge is rotating fast (~ 100 km/s) in a cylindrical manner. The rotation profile of the spherical bulge is latitude independent while the peanut bulge shows slower rotation at $|b| = 10°$ compared to the rotation speed at



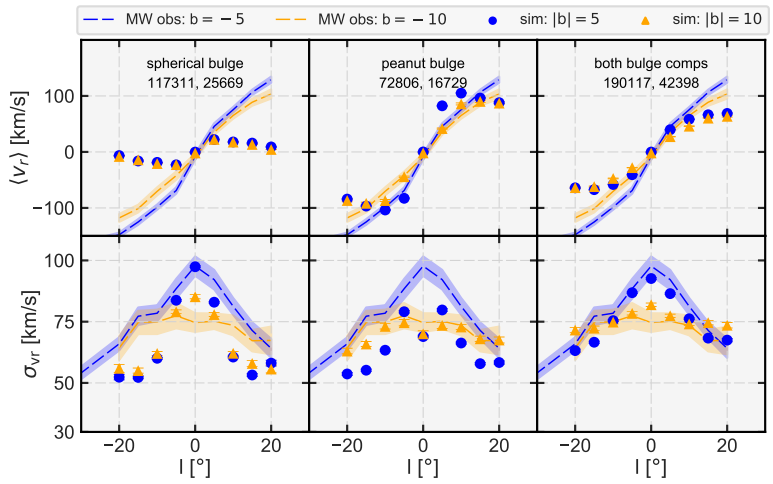


Figure 4.7: Rotation (upper row) and dispersion profiles (bottom row) for stars of the spherical (left panel), the peanut bulge (middle panel) and both components combined (right panel) for two different latitudes $|b| = 5°$ (blue) and $|b| = 10°$ (yellow). The rotation profile is the mean radial velocity and the dispersion profile the velocity dispersion along the line-of-sight as a function of galactic longitude l. Lines show the measurements for the MW from the ARGOS survey (Ness et al. 2013a,b) and dots/triangles show the result obtained for our simulation. The numbers in each panel indicate the amount of stellar particles in each sample, the first number refers to sight lines with $|b| = 5°$, the second to $|b| = 10°$.

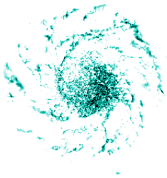
$|b| = 5°$. Its rotation profile is similar in shape and magnitude to the profile of the thick disc component. It rises quickly to its maximum value and then flattens, well in agreement with what is observed from the BRAVA survey (Howard et al. 2008).

The velocity dispersion profile of the spherical bulge (lower panels in Fig. 4.7) is triangular shaped for both latitudes shown and the peak at $l = 0°$ is stronger closer to the disc mid-plane at $|b| = 5°$ compared to $|b| = 10°$. The dispersion profile of the peanut bulge in turn is flatter and less triangularly shaped compared to the spherical bulge. There is still a small peak in velocity dispersion in the center close to the disc at $|b| = 5°$[2], while for larger heights from the disc at $|b| = 10°$ the velocity dispersion profile is flat. This shows that the the peanut bulge component is rotationally supported while the spherical bulge is dispersion dominated as already seen in Fig. 4.5.

I now compare the rotation and dispersion profiles of the simulation to observations from the ARGOS survey (dashed lines in Fig. 4.7). I caution that this comparison of simulation and observation is only of qualitative nature because I compare a subpopulation of stellar particles (spherical bulge or peanut bulge) to the full observational sample where such a distinction is not made. However, in doing so I can learn about the importance of an underlying spherical bulge component in the MW.

In comparison to the observed rotation profiles of the ARGOS survey, the spherical bulge component show much lower rotation, although for longitudes in between

[2]The dip in central velocity dispersion of the peanut bulge components is most likely due to the missing stars in the very center.



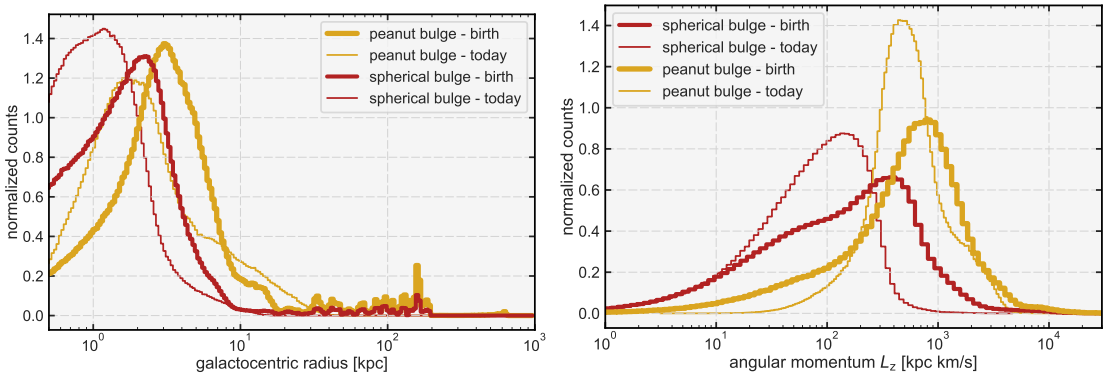
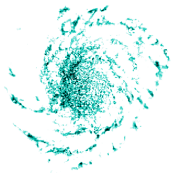


Figure 4.8: *Left Panel:* Comparison between the birth radius (thick lines) of stellar particles and their present day radius (thin lines) with respect to the galaxy center for stellar particles in the spherical bulge (red histogram) component and the peanut bulge component (orange histogram). *Right Panel:* Comparison between the birth angular momentum (thick lines) in z-direction and the present day angular momentum (thin lines) in z-direction (for the stellar disc in the $x-y$-plane) for stellar particles in the spherical bulge (red histogram) component and the peanut bulge component (orange histogram).

$-10^\circ < l < 10^\circ$ the profiles agree well. In contrast, the rotation profile of the peanut bulge is in agreement with the observed profile, however, with slightly too large values of rotation close to the disc ($b = 5^\circ$) at positive longitudes.

Comparing the dispersion profile of the spherical bulge component to the observed profile I find that for both latitudes the simulated profile is far too peaked to be in agreement with the observations. This is somehow not surprising since I compare a single "kinematically" selected sub-population in the simulation, the dispersion dominated population, to the full population in the observation with no further kinematical selection applied. The peanut bulge fits the observed dispersion profile of the MW much better. It shows a peaked dispersion profile close to the disc mid-plane (blue dots) while it is flat for larger latitude (yellow dots).

Finally, if I do not distinguish the two bulge components and analyse the rotation and dispersion profile of the combination of stellar particles of both components (right panel of Fig. 4.7) I find excellent agreement with the observations. Thus, no single profile of either the spherical bulge nor of the peanut bulge is able to reproduce the observed profile exactly while their joint profiles are. This makes me conclude, that the MW bulge can not be a pure peanut nor a pure spherical bulge but rather a mixture of both such components (see also Debattista et al. 2017). Since the distinction of the two bulge components in the simulation is purely based on stellar kinematics, I further predict that if with future surveys we are able to get orbital information for stars in the MW bulge we would be able to disentangle different kinematical components (e.g. spherical vs. peanut stellar distributions) in the bulge.



4.4. Origin of the Components

The close similarity in chemical abundances (and stellar ages) for the spherical and peanut bulges implies a common origin (birth time). Thus, it is surprising that I find vastly different morphologies and kinematics for stellar particles in the two sub-components. In order to investigate the reason for the separation of the two components, I trace back in time all stellar particles of each sub-component via their unique particle ID and record their birth radius and birth angular momentum.

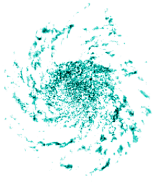
4.4.0.1. Birth Position

The left panel of Fig. 4.8 compares the birth galacto-centric radius (thick lines) to the present day galacto-centric radius (thin lines) for the spherical (red histogram) and the peanut bulge (orange histogram). The birth radius of the spheroidal component peaks at $\sim$ 2 kpc and for the boxy/peanut component at $\sim$ 3 kpc. There is only a slight difference between the overall birth radius distribution of stellar particles in the two components. Stellar particles belonging to the peanut bulge show on average slightly larger (by about 1 kpc) present-day and birth radii compared to those of the spherical bulge. The former result is not surprising, since already Fig. 4.3 indicates that the peanut bulge has a larger spatial extent. For both components, the birth radius distribution peaks at larger radii compared to the present-day distribution. This indicates that material has been accreted from the outer and moved to the inner region, which points towards a significant fraction of disc stars in these two components (e.g. Di Matteo et al. 2015; Di Matteo 2016). Both components show contributions from stars born outside 100 kpc which I refer to as ex-situ stars. In terms of total stellar mass these ex-situ stars contribute about 0.7%. I investigate if and how these ex-situ stars are different from the rest of the stars in the next section.

The left panel of Fig. 4.8 shows that populations of stellar particles selected to be on different orbits at the present day (low angular momentum, non-rotation for the spherical bulge and higher angular momentum and rotation for the peanut bulge) show distinct morphologies – but are indeed born at fairly similar radii and times. Thus, I conclude that their birth position is not the main cause for different present day orbits. These findings hint at a secular mechanism splitting stellar particles into different orbit families at present day. The next birth property to investigate to shed light on this finding is their birth angular momentum.

4.4.0.2. Birth Angular Momentum

In the right panel of Fig. 4.8 I show the total angular momentum in z-direction, L_z, at birth (thick lines) and at present day (thin lines), where the z-direction is defined as the direction of total angular momentum of the disc stellar particles. Again, the red histogram shows the spherical bulge and the orange histogram shows the peanut

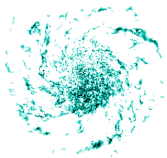


bulge component. As was already appreciated from Fig. 4.7, the peanut bulge shows strong rotation while the spherical bulge is dispersion dominated. Thus, this figure shows that the peanut bulge has higher angular momentum at present-day compared to the spherical bulge. Furthermore, stellar particles belonging to the peanut bulge are on average born with a higher angular momentum compared to stellar particles of the spherical bulge. I also compared the total angular momentum distribution and found that the z-component for the peanut bulge population is much more similar to the total angular momentum, while the spherical bulge component has already a significant angular momentum component perpendicular to the disc at birth.

In summary, I find that stellar particles of both the spherical and the peanut bulge show very similar age and birth radii distributions while their birth angular momenta differ. The angular momentum of stellar particles in the peanut bulge is on average higher than for the spherical bulge while other properties like the age distribution, birth positions or heights are fairly equal. This suggests that internal evolution e.g. via migration in the presence of the bar, leads to a separation of these populations. For this particular simulation a strong bar formed about 8 to 9 Gyr ago (see previous chapter). Stellar particles initially born with lower angular momentum in the z-direction (higher angular momentum perpendicular to the disc) get scattered inwards and out of the disc to become part of the spherical bulge. Stellar particles initially born with higher angular momentum get more efficiently trapped in the bar and will become part of the peanut bulge. I argue that the bar itself is able to separate the stars into different orbit families as suggested by Debattista et al. (2017). Especially for the younger and more metal-rich components, my analysis reveals a common disc origin of the bulge for both bulge components in agreement with recent studies (e.g. Di Matteo 2016; Fragkoudi et al. 2017; Portail et al. 2017a). Thus, although kinematically distinct at present day, I find a common origin of stellar particles in the two bulge components - from the disc material. I attribute the reason for a splitting into different orbit families at the present day to a difference in angular momentum at birth.

4.4.1. ORIGIN OF THE EX-SITU STARS IN THE BULGE

The ex-situ stellar particles (born at distances > 100 kpc from the galaxy center) in the two bulge components make up about 0.8% of the spherical bulge and about 2.3% of the peanut bulge and contribute a stellar mass of $\sim 0.7\%$ to the whole galaxy's stellar mass. Observationally, a contribution of a classical bulge component (created during the merger dominated early phase of the formation of the Galaxy) to the MW's bulge is constrained to be $< 8\%$ in stellar mass (Shen et al. 2010a). With this simulation I test the observational prospects to identify these ex-situ stars in the MW, if present. The ex-situ stars are preferentially found in the outskirts of the two bulge components with average galacto-centric radii of about 3 kpc (spherical bulge) up to 8 kpc (peanut



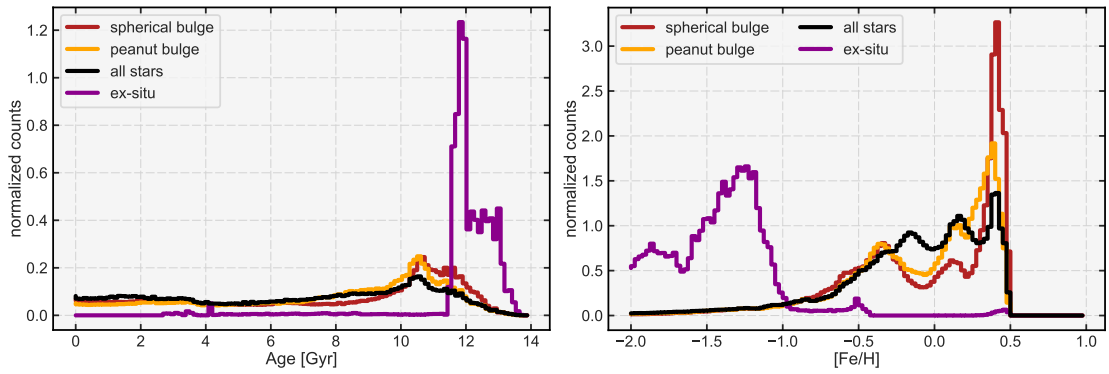


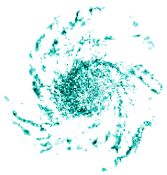
Figure 4.9: Comparison between the age (left) and the metallicity (right) distributions of all stellar particles in the galaxy (black histogram), the two bulge components (red, orange histograms) and the ex-situ stellar particles in the bulge (magenta histogram). Ex-situ stars are purely old and metal-poor.

bulge). Thus, these stars are among the highest angular momentum stars in the two bulge components today. The ex-situ stars can not be attributed to a single accretion event but originate from several accreted and disrupted satellites over a time span of ~ 5 Gyr previous to redshift $z \sim 0.75$. A recent study by El-Badry et al. (2018) looked at the spatial distribution of the oldest stars in MW like galaxies and found them to preferentially reside in halo like objects although their contribution in the very center of the galaxies can be significant, in very good agreement with the findings here.

In Fig. 4.9 I show the age and metallicity distributions of the whole galaxy (black histogram), the two bulge components (red - spherical bulge, orange - peanut bulge) in comparison to the distributions for the ex-situ stars (magenta histogram). This figure clearly shows that the ex-situ stars are exclusively old and metal poor. I further tested if these ex-situ stars are also identifiable through their kinematics but found that they essentially follow the kinematics of disc stars as they were accreted very early on ($z \gtrsim 2$) in the history of this galaxy.

4.5. Discussion

I have analysed in this chapter a simulation of a MW like galaxy that shows an overall boxy/peanut shaped morphology well in agreement with what is observed for the MW as I have established in the previous chapter. Here I focused on the different stellar populations present in the inner regions of the simulation where I separated the stellar particles of the galaxy into different orbit families. This decomposition enables to study and understand the different populations in our simulation separately. This particular galaxy has an equal mass fraction of stellar particles on spheroidal and boxy orbits, as it is shown in figure 4.3. Since it is widely assumed that different



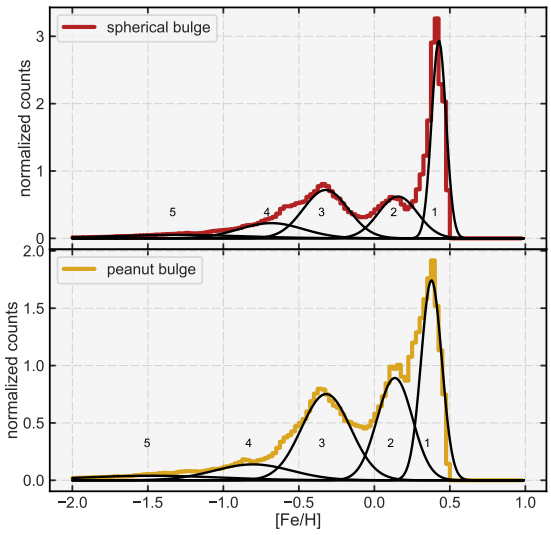


Figure 4.10: Chemical sub-components of the kinematically decomposed spherical bulge (top panel) and peanut bulge (bottom panel). The metallicity of the components spans the entire Metallicity Distribution Function of the bulge. Whilst I can identify 5 different sub-components 1 to 5 using GMM, as indicated, I do not associate these with the discrete populations as per Ness et al. (2013a). In Table 4.1 I show the mean, standard deviation and the weight of each metallicity component.

morphological/kinematical components of galaxies, like e.g. the peanut or the spherical bulge, follow from different formation scenarios (e.g. Kormendy 2013), I specifically focused on the origin of stars in the two bulge components. Note, I do not dispute that large spherical bulges in galaxies are a signature of mergers, I simply demonstrate that a spheroidal population in the bulge can be formed from disc material. While peanut shaped bulges are thought to be secular evolution driven, spherical bulges are associated with merger-built spheroids (Binney and Merrifield 1998; Elmegreen 1998; Kormendy 2013; Sellwood 2014). In this study I find that the two kinematically defined bulge components are mostly formed from disc material owing to a common secular origin as shown in the left panel of Fig. 4.8. Studying the cause of the separation of the two bulge components at present-day, I find that it is the initial angular momentum of stellar particles which influences their present-day orbits. As I have shown in the right panel of Fig. 4.8, the birth angular momentum for the peanut bulge is larger compared to the spherical bulge. Thus, I find that, except for their different orbital structure, the two bulge components share very similar properties (see Fig. 4.4) like e.g. their metallicity distribution or age distribution. Therefore, I propose that a kinematic decomposition technique offers a fresh and distinct framework to understand and quantify the MW's bulge in times where the Gaia satellite will delivering 5+1d phase space information for millions of MW stars. This will finally enable us to apply the same techniques to both observed stars and simulated stellar particles and thus, by combining simulations and observations, to understand the origins of the Bulge.

Already with the existing data sets, like e.g. the ARGOS survey, we are able to compare the different kinematic signatures of the two bulge components to observations of the MW. Comparing individual and combined rotation and dispersion profiles I find that only the combination of the two bulge components matches the observed

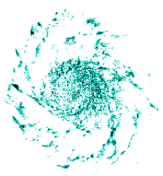


Table 4.1: Gaussian component fit to metallicity distribution.

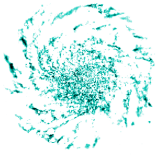
population	mean [Fe/H]	weight	σ
spherical bulge			
1	0.43	0.35	0.05
2	0.16	0.20	0.13
3	-0.32	0.27	0.15
4	-0.68	0.12	0.21
5	-1.31	0.06	0.44
peanut bulge			
1	0.38	0.30	0.07
2	0.13	0.26	0.12
3	-0.31	0.30	0.16
4	-0.79	0.09	0.25
5	-1.46	0.05	0.46

kinematics of bulge stars from the ARGOS survey (see Fig. 4.7). This finding makes me conclude that also for the MW we might find stars on both orbit families once we have access to stellar orbits through Gaia. Furthermore, I expect to find stars on both orbits across all metallicities as I have shown that the age and metallicity distributions for both bulge populations are broad (see Fig. 4.4). This feature is a direct result of the continuous star formation in the disc and the subsequent inclusion of further disc material into the bulge component by secular evolution. However, a broad metallicity distribution is also found for the stars included in the ARGOS survey (Ness et al. 2013a). In order to understand similarities and differences between the ARGOS survey and the simulation I briefly discuss the metallicity distributions in slightly more detail below.

4.5.1. Metallicity Distribution

The two left most panels of Fig. 4.4 indicate that the spherical and the peanut bulge populations show distinct substructures in their metallicity and age distributions. These features are similar to what is observed in the ARGOS data set (see Ness et al. 2013a) and observations from Clarkson et al. (2008); Hill et al. (2011); Gonzalez et al. (2011). Therefore, I examine the substructure in the metallicity distribution of the simulation following the approach by (Ness et al. 2013a) using a Gaussian mixture model. Similar to the results of Ness et al. (2013a) for the ARGOS data I am able to identify 5 different sub-components (1 to 5) in the simulation. The metallicity distribution function (MDF) of both bulge components together with the decomposition (black lines) are shown in Fig 4.10 and parameters for the metallicity decomposition are shown in Table 4.1.

The different components in the MDF of the MW bulge span each a small, overlapping part of the MDF. Ness et al. (2013a) associated the components each with different populations in the MW, including bulge, thick disc and halo stars. In contrast to that, I find that each of the bulge populations spans the entire range of the MDF which shows substructure and can itself be broken up into sub-populations. This highlights that metallicity itself in both observations and in simulations may in fact



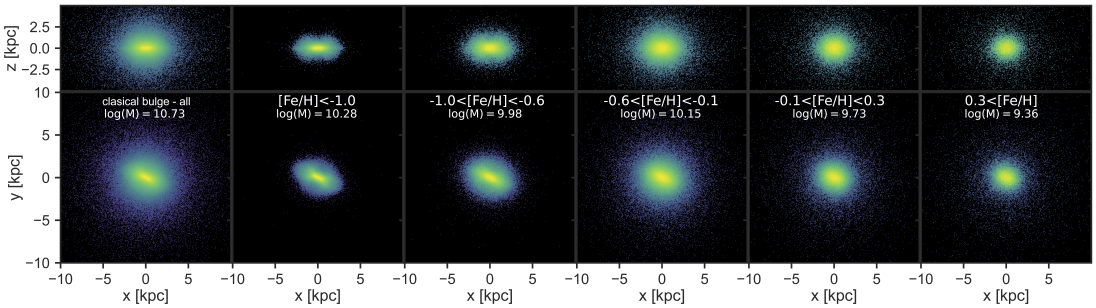


Figure 4.11: Surface density maps in edge-on (top row) and face-on (bottom row) projections for all stars (left most column) in the spherical bulge component and for stars in different metallicity bins (second column from the left to most right column) as indicated in the panels. Each panel indicates the amount of stellar mass in solar masses contained in the component.

be sub-optimal for understanding the evolution history of the bulge. In simulations, due to the uncertainty in recreating the chemical enrichment history as a function of time and in observations due to stars at a given metallicity reflecting a range of different times of formation – and not a direct tracer of history (Minchev et al. 2017). Nevertheless, since the morphology of the central regions of the MW is observed to be metallicity dependent I briefly discuss this for the simulation as well.

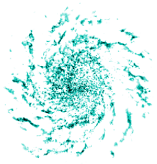
4.5.2. MORPHOLOGY

The substructure in abundance space directly relates to substructure in geometrical space. Recognising the different morphologies as a function of metallicity for stellar particles all on similar orbits is important in interpreting observational results. In Fig. 4.11 I show the different metallicity components of the spherical bulge and in Fig. 4.12 of the peanut bulge, respectively.

Across all metallicity bins, [Fe/H]> -1.0 dex to [Fe/H]< 0.3 dex, the spherical bulge (Fig. 4.11) is more spherically symmetric compared to the peanut bulge (Fig. 4.12) which has a distinct boxy- or bar-like morphology[3]. Furthermore, in edge-on view there is a clear X-shape morphology present across all metallicities.

The stars in the spheroidal bulge are most spherically symmetric for the most metal-poor (oldest) stars and show an elongation in the xy-plane, appearing increasingly ellipsoidal, following the bar outline, at higher metallicities (the youngest stars). In contrast, the most metal-rich (youngest) stars of the boxy/peanut bulge show the strongest signature of a thin bar-like feature close to the mid-plane which extends out to ~ 5 kpc. Interestingly, this is a similar extent to the long-bar proposed by Portail et al. (2015b). The thickness of the X-shape increases with decreasing metallicity, to

[3]The small hole in the center of the peanut bulge is due to our decomposition scheme where stars in the very center get assigned to the spherical bulge component



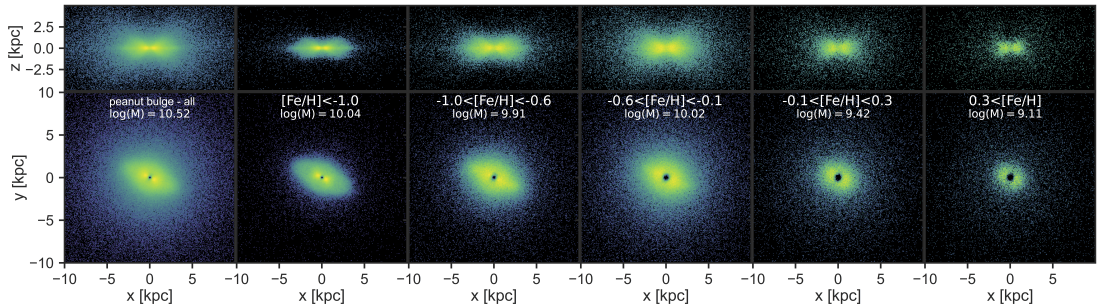


Figure 4.12: Same as Fig. 4.11 but for the peanut bulge component.

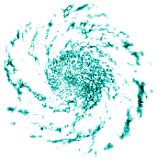
the intermediate metallicity bin, while the metal poorest stars are again more centrally concentrated. The bar signature diminishes with decreasing metallicity. This is similar to what is found by Portail et al. (2017b) for their model, and to what is observed for the old Mira population in the MW (López-Corredoira 2017).

Finally, if I compare the mass fraction of stars belonging to the two lowest metallicity, non-rotating components of the spherical bulge (which are also the oldest ones) to what is constrained for the MW, I find very good agreement. Components 4 and 5 of the spherical bulge account together for $\sim 6\%$ of the disc mass, while for the MW the mass fraction of an old merger-generated bulge component is constrained to be less than $\sim 8\%$ (Shen et al. 2010a).

4.6. Summary and Conclusion

In this chapter I analysed a fully cosmological hydrodynamical simulation of a MW like galaxy which shows bulge properties that agree well with the observed properties of the MW bulge as described in the last chapter (Buck et al. 2018c). I employ the kinematic decomposition of Obreja et al. (2018b) to separate the galaxy into its constituent (kinematically) distinct stellar populations. These include two bulge populations, two disc populations and a stellar halo. I use this kinematic decomposition to study, in detail, the different stellar components of the two bulge components, focusing on their kinematical, temporal, and chemical properties as well as their origin. I compare the kinematics of stellar particles in the bulge region of the simulation with observed kinematics of the MW bulge stars and find excellent qualitative agreement. My main results in this chapter can be summarised as follows:

- Applying the kinematical decomposition algorithm to the galaxy I find five different components: two bulges, a boxy/peanut bulge and a spherical symmetric bulge (see Fig. 4.3 and Fig. 4.4), a thick and a thin disc, and a stellar halo.



- I investigate the stellar kinematics in the two bulge components (Fig. 4.7) and compare it to observed kinematics of MW bulge stars. I find that the spherical bulge is mostly slow or non-rotating with a latitude dependent dispersion profile while the peanut bulge is fast rotating and shows only a very small latitude dependence — as is observed for the MW (Fig. 4.5).

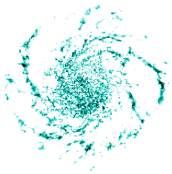
- I find that single components can not match the observed rotation and dispersion profiles. However, the kinematics of both bulge components together well matches the observations.

- I find remarkable similarity for the birth position of stars in the spherical and the peanut bulge (left panel of Fig. 4.8) despite their different morphologies at the present day. However, peanut bulge stars have higher birth angular momentum compared to the spherical bulge component (right panel of Fig. 4.8). I conclude that it is the secular evolution under the influence of the bar which separates initially co-spatial populations into different orbit families.

- I analyse the formation mechanism of the two bulge populations and find that these populations are almost entirely formed from the disc. Thus, the assumption that a spherical morphology originates via merger driven formation is not supported by the simulation. A boxy/peanut morphology is the signature of formation from the disc but a spheroidal morphology can also be formed from the disc. This also means that a group of stars on spherical orbits in the bulge have not necessarily formed via mergers.

- A small stellar population of the two bulges was formed via mergers at very early times. I can identify these stars in the simulation as I have the full galactic formation history in the cosmological context. These stars are characterised by being exclusively old and metal poor. They are preferentially found in the outskirts of the bulge, at galacto-centric radii of ~ 3 kpc.

- The two bulge populations show distinct substructure in their (overlapping) metallicity distributions and a metallicity dependent morphology. For both bulge components, the vertical thickness increases with decreasing metallicity, similar to what is reported in Ness et al. (2013a). I find that stellar metallicity alone can not be used as proxy for different kinematical components. This implies that full kinematical data from future surveys is needed in order to disentangle the different populations in the MW bulge.



Part III

The Dwarf Galaxy System of the Milky Way

Chapter 5

The Milky Way Dwarf Galaxies in high-resolution Simulations

Mál er dverga	*The race of the dwarfs*
í Dvalins liði	*in Dvalin's throng*
ljóna kindum	*Down to Lofar*
til Lofars telja,	*the list must I tell,*
þeir er sóttu	*The rocks they left*
frá salar steini	*and through wet lands*
Aurvanga sjöt	*They sought a home*
til Jöruvalla.	*in the fields of sand.*

From the epic poem Völuspá
(The Prophecy of the Seeress) Part of the Ljóþaedda,
a 13th century collection of Old Norse poems
Translated by Henry Adams Bellows

While the previous part of this thesis studied the properties and the formation of two major components of the galaxy itself, the bulge and the disc, in the next two chapters I investigate the cosmologically small scale environment surrounding the galaxy. The properties and the spatial distribution of dwarf galaxies surrounding the MW have long been difficult to reproduce in cosmological hydrodynamical simulations and a number of more or less severe problems (see sub-section 1.2.4) have been identified. As extensively discussed in sub-section 1.2.4, several analytical and/or idealised solutions to these small scale problems of ΛCDM have been suggested. In the next two chapters I will investigate two simulation suites specifically designed to explore possible solutions to these problems. This chapter deals with general properties of dwarf galaxies in fully hydrodynamic, cosmological simulations in a realistic environment while the next

chapter tackles the question of planes of satellites in dark matter only cosmological simulations.

In this chapter I utilise the high-resolution simulations introduced in sub-section 1.4.3 and study the properties of the dwarf galaxies and the environmental effect of the main galaxy on their properties. I extensively compare the properties of simulated dwarf galaxies to observed characteristics and verify that suggested solutions to the small scale problems indeed work in fully cosmological context. I further identify additional mechanisms aiding to bring simulations and observations in agreement.

The content of this chapter has been submitted to the journal *Monthly Notices of the Royal Astronomical Society* and a very positive referee report has been received. The submitted version of this paper is accessible as an arXiv preprint (Buck et al. 2018a). All the simulations used in this chapter have been run by myself and all the research presented here has been conducted by myself.

5.1. CONTEXT

As laid out in section 1.2.1 the standard cosmological model of Dark Energy (Λ, Riess et al. 1998; Perlmutter et al. 1999) and Cold Dark Matter (CDM, Peebles 1984), is in outstanding accordance with observations on large (>Mpc) scales (Tegmark et al. 2004; Springel et al. 2005) and provides a successful framework to describe the formation and evolution of dark matter haloes, which are the hosts of galaxies. Given a set of cosmological parameters (e.g. Planck Collaboration et al. 2014), it makes clear predictions for the structure and number densities of these haloes (Jenkins et al. 2001; Tinker et al. 2008; Angulo et al. 2012). For MW mass haloes and above, the predictions are in good agreement with observations, while for dwarf galaxies the theory nominally predicts too many luminous field and sub-haloes (e.g. Klypin et al. 1999; Moore et al. 1999b; Trujillo-Gomez et al. 2011; Papastergis et al. 2012). These small scale problems of ΛCDM have been introduced in detail in sub-section 1.2.4 and suggested solutions involve the suppression of gas cooling in low mass haloes (e.g. Bullock et al. 2000), and the disordered nature of dwarf galaxy kinematics (Macciò et al. 2016).

The theory of structure formation in the ΛCDM cosmology predicts hierarchical merging of small dark matter haloes and their galaxies. Thus a galaxy like our MW was formed by accreting a large number of small galaxies. Depending on the masses of the accreted dark matter haloes they either merge quickly with the main galaxy or they spend a long time orbiting around it (Chandrasekhar 1943; Binney and Tremaine 2008; Boylan-Kolchin et al. 2008; Jiang et al. 2008). While orbiting the main galaxy, these haloes and the galaxies they contain experience strong tidal forces eventually leading to (dark matter) mass loss (Mayer et al. 2001; Klimentowski et al. 2007; Peñarrubia et al. 2008; Kazantzidis et al. 2011; Chang et al. 2013; Frings et al. 2017). Additionally,

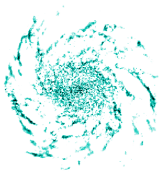


Table 5.1: Simulation properties of the main galaxies: The virial mass M_{200}, virial radius R_{200} and the total stellar mass, $M_{\rm star}$, as well as the total amount of gas, $M_{\rm gas}$, within the virial radius are given. The last column indicates the numbers of *satellites* (luminous sub-halos within R_{200}), *nearby dwarfs* (luminous halos within 1 to 2.5 virial radii) and *field dwarfs* (luminous halos outside 2.5 virial radii).

sim.	M_{200} $[10^{12}\mathrm{M}_\odot]$	R_{200} [kpc]	$M_{\rm star}$ $[10^{10}\mathrm{M}_\odot]$	$M_{\rm gas}$ $[10^{10}\mathrm{M}_\odot]$	$N_{\rm sat}$ $r < R_{200}$	$N_{\rm nearby}$ $1 < r/R_{200} < 2.5$	$N_{\rm field}$ $2.5R_{200} < r < 3$ Mpc
g2.79e12	3.13	306	15.9	18.48	20	16	26
g1.12e12	1.28	234	6.32	7.93	8	13	6
g8.26e11	0.91	206	3.40	6.09	7	7	13
g7.08e11	0.55	174	2.00	3.74	8	6	24

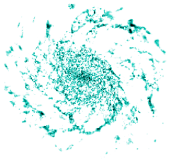
due to the hot gas halo of the host ram pressure stripping is acting on their gas content (Einasto et al. 1974; Faber and Lin 1983; Grebel et al. 2003) removing additional gaseous mass.

More and more observations have confirmed the scenario of tidal stripping which in simulations results in streams and complex stellar structures such as shells and cusps (see also Fig. 5.1 for some of these features). Indeed, such structures are observed in our own Galaxy (Ibata et al. 1994; Yanny et al. 2000; Newberg et al. 2002; Majewski et al. 2003; Martin et al. 2004; Martínez-Delgado et al. 2005; Belokurov et al. 2006), in the M31 galaxy (Ferguson et al. 2005; Kalirai et al. 2006; Ibata et al. 2007) and beyond the Local Group in more distant galaxies (Malin and Hadley 1997; Forbes et al. 2003; Pohlen et al. 2004; Martínez-Delgado et al. 2012, 2015). Furthermore, the origin of the stellar halo of galaxies such as our MW is thought to be the unbound stars from disrupted satellite galaxies (Bullock and Johnston 2005; Bell et al. 2008; Carollo et al. 2010; Cooper et al. 2010).

Several authors have studied the environmental effects on the properties of the local dwarf spheroidal galaxies and found severe effects (e.g. Kravtsov et al. 2004; Mayer et al. 2006, 2007; Klimentowski et al. 2009a,b; Hirschmann et al. 2014; Wetzel et al. 2015; Kazantzidis et al. 2017; Simpson et al. 2017; Frings et al. 2017). In the Local Group the dwarf galaxies within the virial radius of MW or M31 ($\sim$ 300 kpc) show a sharp evolution in their morphology and properties compared to dwarf galaxies outside that radius. Crossing the virial radius inwards, galaxies:

- decrease their molecular gas fraction (sometimes to zero)
- become more spheroidal (morphologically)
- become quiescent as a consequence of the drop in the molecular gas fraction

(e.g. McConnachie 2012). There are only a few exceptions to this behaviour. Outside the virial radii of MW and M31 there exist only few quiescent and gas-poor spheroidal galaxies like Cetus, Tucana, KKR 25, KKs 3 (Karachentsev et al. 2015) and M31 XVIII.



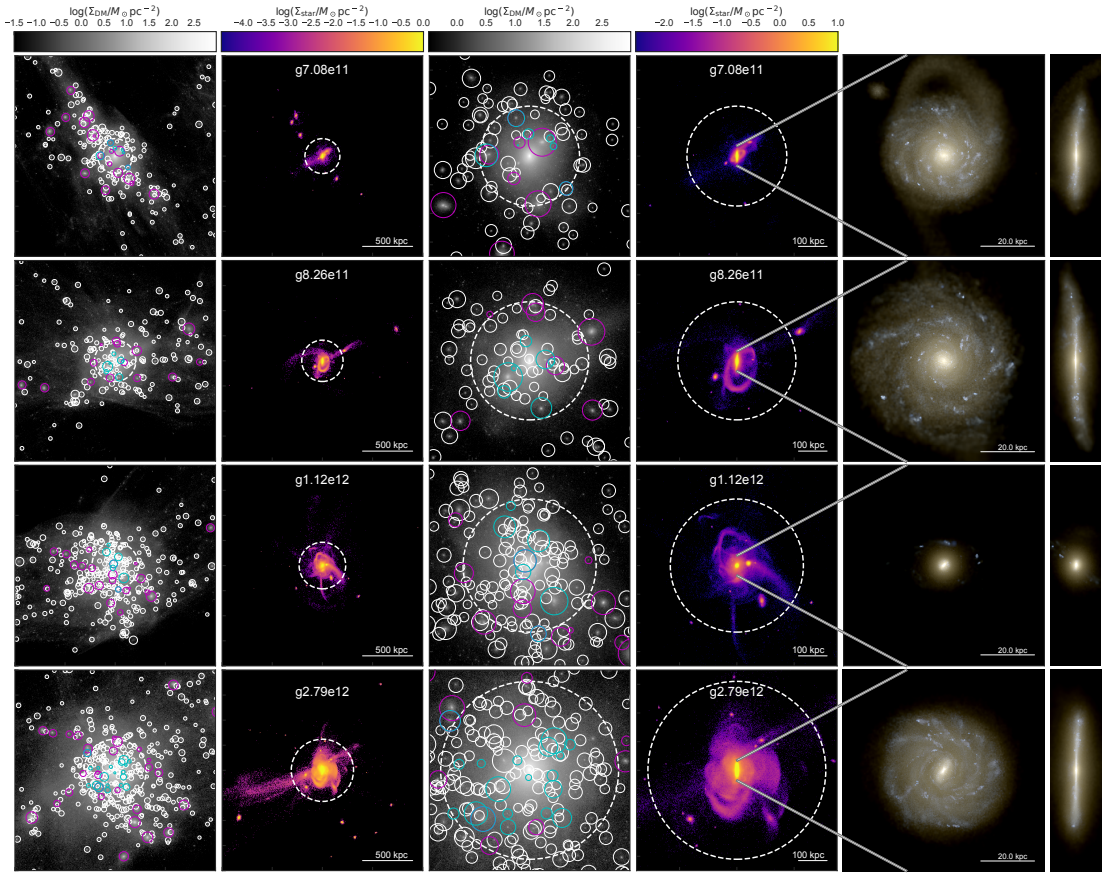
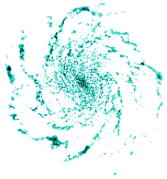


Figure 5.1: Projections of all four host haloes and their surrounding low mass haloes at redshift zero. The two left most columns show a view of 2 Mpc side length; the first column shows the dark matter surface density, the second column shows the corresponding stellar surface density. The third and fourth column show the same but for a close-in view that is 700 kpc across. The depth of each projection is equal to the width. In each panel, a white dashed circle shows the virial radius R_{200}. The projections are such that the disk of the host halo is viewed edge-on. Every subhalo with a total mass greater than $10^8 M_\odot$ is circled. Luminous subhaloes are circled in color: cyan for subhaloes within the host's virial radius, and magenta for subhaloes beyond that[1]. I chose the diameter of each subhalo circle to be proportional to the logarithm of the subhalo's mass. The dark matter surface density projections reveal that there is a large number of low mass haloes out to large distances ($\gtrsim 1$ Mpc) where many of these small haloes are completely devoid stars. The two right most panels show an RGB image of the main galaxy in face-on and edge-on views where we render the stellar particles using their luminosity in the wavelength bands i, v, u to create the r, g and b channels.

Teyssier et al. (2012) argued via the distance and radial velocities of Tucana and Cetus that they have been inside the virial radius of MW at earlier times. However, KKR 25 and KKs 3 are located much further away at ~ 2 Mpc and thus are not likely to have orbited inside the virial radius of any host. On the other hand, the only gas-rich, star



forming irregular galaxies within the virial radius of MW are LMC and SMC and of M31 are LGS 3 and IC 10 which are all most probably on their first infall (Besla et al. 2007).

Except for the above mentioned examples most local dwarf galaxies outside the virial radius of the MW or M31 are assumed to be similar to field objects, taken to be representative of unaffected objects. However, many others before (Moore et al. 2004; Gill et al. 2005; Warnick et al. 2008; Ludlow et al. 2009; Knebe et al. 2011; Wetzel et al. 2014; Behroozi et al. 2014; Diemer et al. 2017) have noted, that there exists a prominent population of dwarf galaxies, termed "backsplash" galaxies, that are located outside the virial radius of their host at the present day, but their orbits took them inside it at earlier times. More et al. (2015) showed that for dark matter haloes the region in which these "backsplash" galaxies can be found is $\sim 2.5R_{200}$. This finding renders the traditional virial radius meaningless as a physical boundary between satellite and field galaxies.

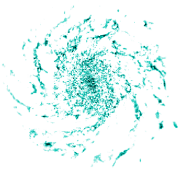
Since "backsplash" galaxies had, at one point in their lives, a close encounter with their host galaxy, the tidal influence of the host must have been stronger for them compared to field galaxies. What is the effect of this difference in tidal forces on the properties of the galaxies, and can we discriminate between the unaffected field objects and "backsplash" galaxies? Gill et al. (e.g. 2005) showed that "backsplash" galaxies lose about 40 per cent of their initial mass when brushing their host galaxy and Knebe et al. (2011) found that their total mass-to-light ratio is lower than for field galaxies, but higher than for bound satellites. This raises the question whether or not the observed sample of field galaxies consist (at least partly) of these "backsplash" galaxies and how one would distinguish them from unaffected dwarf galaxies.

In this chapter I elaborate on these previous efforts and investigate the effects of the host on its satellites and nearby dwarf galaxies. Quantifying the effects of tidal stripping of satellites and backsplash galaxies is crucial to understand galaxy evolution in general and observations of Local Group dwarf galaxies in particular. Thus, I will study how the dark and luminous components of the galaxies are effected, what influence can potentially be measured. Finally, I try to separate observed Local Group galaxies into unaffected galaxies and potentially disturbed ones.

5.2. Host Galaxies and their Sub-Haloes

Most notably for this work, as a result of dark halo expansion, the dwarf galaxies in the NIHAO sample have been shown to resolve the so-called Too-big-to-fail problem for

[1]The two luminous satellites of galaxy g7.08e11 and g1.12e12 not circled in cyan can not be identified by AHF in the redshift $z = 0$ snapshot. We include data for these two satellites from a snapshot 70 Myr earlier.



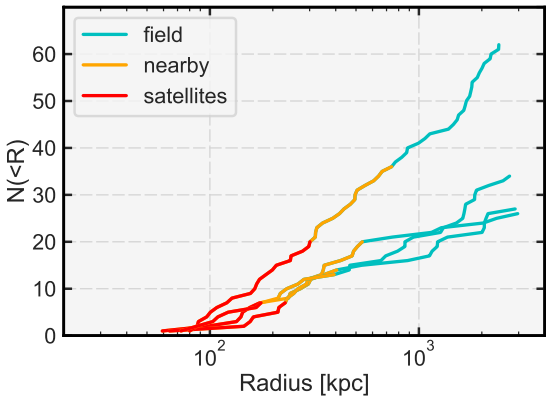


Figure 5.2: Radial profiles of *satellites* and *nearby* and *field* galaxies in the simulations. The colored lines show the profiles for the three simulations where red color denotes the *satellites* within the virial radius[2], orange color the *nearby* galaxies in the region $1R_{200} < R < 2.5R_{200}$ and cyan color marks the *field* galaxies with distances between $2.5R_{200} < R < 3$ Mpc from the host.

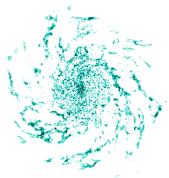
field dwarfs (Dutton et al. 2016), and successfully reproduce the diversity in rotation curves of observed dwarf galaxies (Santos-Santos et al. 2017). This means the employed feedback scheme of NIHAO has been proven to create realistic galaxies and high-resolution NIHAO galaxies are well suited to study satellite systems similar to the MW or M31. An impression of the galaxies and their surroundings used in this chapter is given in figure 5.1.

5.2.1. Host Galaxy Selection and Properties

The four galaxies used for this chapter are the higher-resolution versions of fiducial NIHAO galaxies introduced in sub-section 1.4.3 and numerical resolution parameters for these galaxies can be found in table 1.1. These galaxies have stellar masses between $2.0\times10^{10}M_\odot$ and $1.59\times10^{11}M_\odot$. Galaxy g2.79e12, g8.26e11 and g7.08e11 are disc galaxies as can be seen from the most right panels of figure 5.1. The stellar disc of galaxy g2.79e12 has a scale length of $R_d \sim 5$ kpc and a scale height of $H_z \sim 750$ pc. The corresponding parameters for galaxy g8.26e11 are $R_d \sim 5.5$ kpc and a scale height of $H_z \sim 500$ pc and galaxy g7.08e11 has a disc scale length of $R_d \sim 3.7$ kpc and a scale height of $H_z \sim 600$. Detailed parameters like the total virial mass, virial radius, gas and stellar mass as well as the number of satellites can be taken from table 5.1.

5.2.2. Sub Halo Selection

I am interested in the satellite system and the dwarf galaxies around the host galaxies. In order to keep a clean sample I only select dark matter halos with at least 10 stellar particles to belong to the luminous galaxy sample. Given the stellar particle masses this results in a lower galaxy stellar mass of $\sim 10^5 M_\odot$. I additionally require every dwarf galaxy outside the virial radius of the host to reside in a dark matter halo consisting of only high resolution particles. Figure 5.1 gives an impression of the large scale morphology (left two columns) as well as the closer environment inside R_{200} (column



3 and 4) and the host galaxies themselves (column 5 and 6). The first column shows the dark matter surface density of a cube of edge-size 2 Mpc where I highlight every luminous dark matter halo outside the virial radius with a purple circle and the ones inside it with a cyan circle[3]. All the galaxies highlighted that way reside in dark matter halos with masses larger than $\sim 10^8 M_\odot$. I thus indicate all other dark matter halos with masses above $\sim 10^8 M_\odot$ with white circles finding several completely dark halos. The second column shows the corresponding stellar surface density. The third and fourth column show the same for a smaller aperture of only 700 kpc aside. The right most column shows a multi-color RGB image of the main galaxies in the wavelength bands i, v, u in face-on and edge-on view.

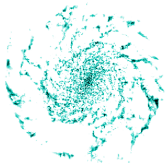
Having selected all (sub) halos meeting the selection criteria I distinguish between dwarf galaxies inside the host's virial radius at $z = 0$ (red squares in all plots) from now on named *satellites*, dwarf galaxies between one and 2.5 times the virial radii ($\sim 300 < r/\mathrm{kpc} <\sim 750$, orange triangles) named *nearby galaxies*, and *field galaxies* (outside 2.5 virial radii, cyan dots). This distinction seems to be ad-hoc but I find that $2.5R_{200}$ marks a boundary at which dwarf galaxy properties change significantly (see section 5.4 and e.g. Behroozi et al. 2014).

Figure 5.2 shows the radial distribution of luminous halos found in all four simulations. I apply the color-coding scheme outlined above where *satellites* are shown with a red line which changes to orange once the radial range where I denote galaxies as *nearby* galaxies is reached and then changing to cyan at radii larger than $2.5R_{200}$, the range of *field* galaxies. As one can see from this figure, at $z = 0$ there are no luminous satellites closer than 60 kpc to the host. However, at slightly earlier time steps I do find luminous satellites closer to the host than 60 kpc whose orbits take them further away from the host at $z = 0$ (compare also Figure 5.11 for the minimum radii of *satellites*).

In figure 5.3 I show the stellar mass function of the *satellites* from the four simulations in comparison to the ones of MW and M31 satellites calculated from the McConnachie (2012) data. In the observations I apply a stellar mass cut of $M_{star} > 10^5 M_\odot$ in order to match the resolution limit of the simulations. Comparing the resolution matched mass functions of simulations and observations in figure 5.3, one can see that the simulations match perfectly the observed mass functions of MW and M31. They only miss the most massive satellites LMC and SMC or Triangulum, NGC

[2]This figure is mainly to demonstrate the separation into the three populations thus we do not include the two satellites not appearing in the redshift $z = 0$ halo catalogue here.

[3]The two luminous satellites of galaxy g7.08e11 and g1.12e12 not circled in cyan can not be identified by AHF in the $z = 0$ snapshot. Due to the previous pericenter passage all particles (DM, gas and stars) of these satellites are removed by the unbinding procedure(see also van den Bosch et al. 2018; van den Bosch and Ogiya 2018). I include values for these satellites from the preceding snapshot 70 Myr earlier.



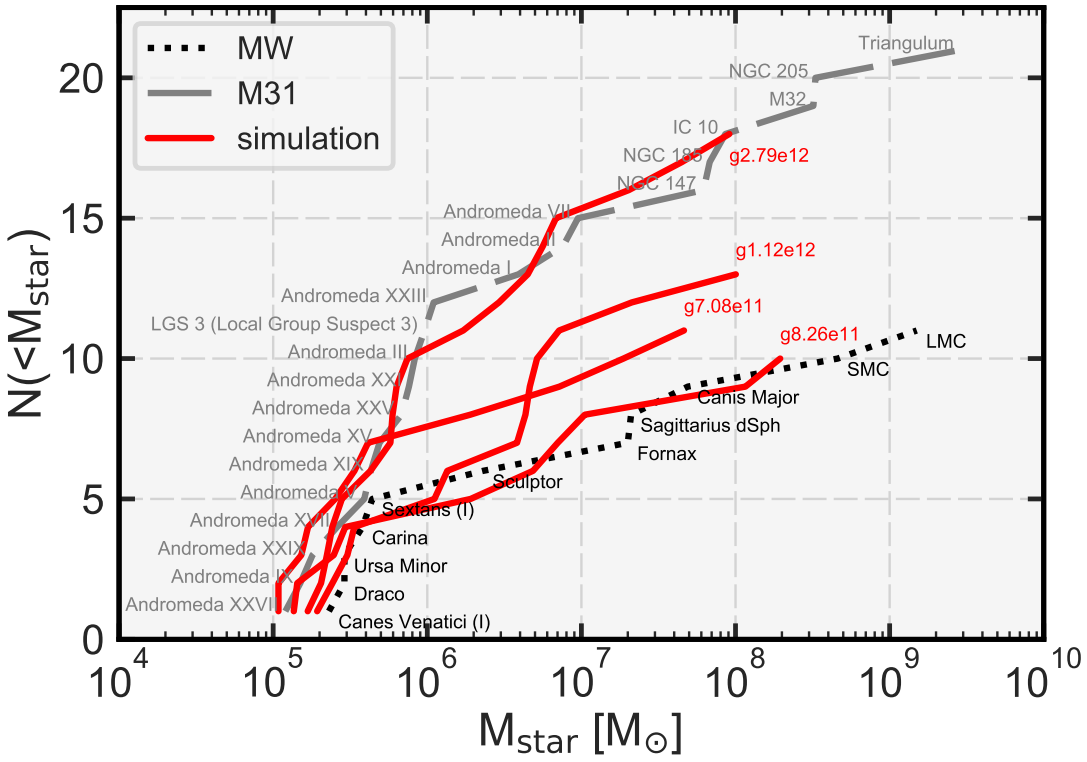
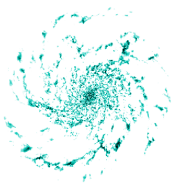


Figure 5.3: Satellite stellar mass function for the three simulations (thick red lines) and the observations of MW satellites (black dotted line) as well as M31 satellites (gray dashed line) within 300 kpc from the host. Two of the simulations perfectly match the observed mass function of MW and M31, except for the most massive satellites, like e.g. LMC, M32 or Triangulum which are known to be rare in cosmological simulations (Boylan-Kolchin et al. 2011).

205 and M32, which are known to be rare in cosmological simulations (Boylan-Kolchin et al. 2011). From visual inspection of the simulation movies I further see that a lot of low mass satellites get destroyed coming close to the stellar disc of the host. The debries of these satellites can still be seen in the $z = 0$ snapshots as stellar streams, e.g. in figure 5.1.

Finally, for all *satellites*, *nearby* and *field* galaxies I create merger trees in post processing. In order to link sub-haloes between two consecutive snapshots I trace their dark matter particles via their unique particle ID. For each luminous sub-halo I find the progenitor which shares the most dark matter particles with the sub-halo in question. From these merger trees I extract several evolutionary parameters like e.g. the infall time, the peak mass, defined as the maximum virial mass ever reached, and the peak $v_{\rm max}$, defined as the temporal maximum of the maximum of the circular velocity curve (e.g. Kravtsov et al. 2004).



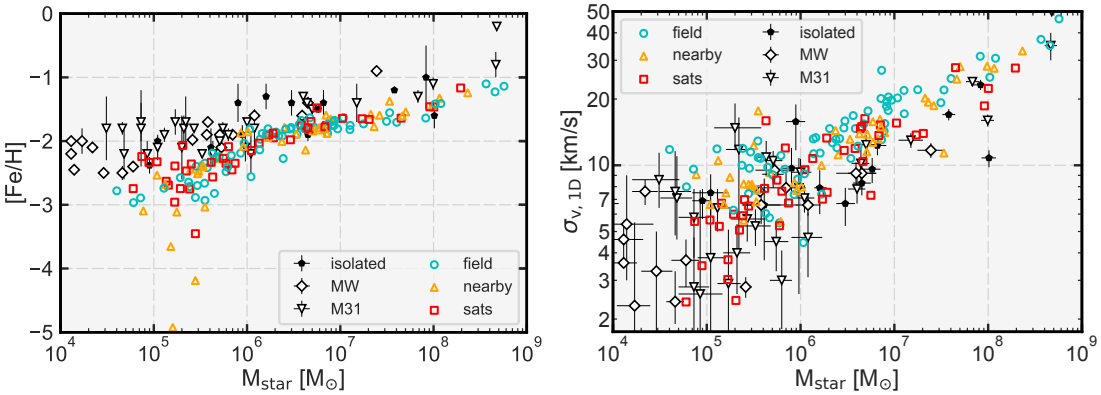


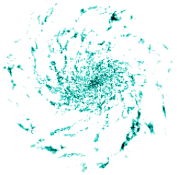
Figure 5.4: *Left:* Stellar mass vs. 1D velocity dispersion of stars within the half light radius. *Right:* Stellar mass vs. metallicity where the metallicity is calculated for all stars within $0.2 \times R_{200}$. Red squares show *satellites* within the virial radius (R_{200}), orange triangles show *nearby* galaxies within $R_{200} < R < 2.5R_{200}$ and cyan dots show all *field* within $2.5R_{200} < R < 3$ Mpc. Black and gray points show observations for satellites of the MW and M31 and isolated Local Group dwarfs taken from Fattahi et al. (2017) and references therein.

5.3. Dwarf Galaxy Properties

In this section I compare the properties of the simulated dwarf galaxies (inside and outside the virial radius) with observed properties of Local Group dwarfs. Observational data is taken from the compilation presented in Fattahi et al. (2017) (for further references see table 5.5). The velocity dispersion for Phoenix is taken from (Kacharov et al. 2017). Observational data for the star formation histories (SFH) are taken from Weisz et al. (2015). For the simulations I measure the 1D-velocity dispersion for all stars within the 3D half-light radius using a projection along the x-axis of the simulation cube. The metallicity is measured for all stars within $0.2R_{200}$.

5.3.1. Velocity Dispersion and Metal Abundance

Figure 5.4 compares the stellar mass-metallicity relation (left panel) and the one-dimensional velocity dispersion vs. stellar mass of our galaxies (right panel) to observational data. From the left panel of Fig. 5.4 one can see that the galaxy sample recovers the observed mass metallicity relation well, although with a slight offset to lower metallicities. This offset is no major issue and can be resolved by using a different/updated yield set for the chemical enrichment (Buck et al. in prep). For very low mass galaxies one sees an increasing deviation to lower metallicities from the observed relation. This is a result of the enrichment scheme which is not handling metal enrichment of single starburst galaxies properly. For future simulations I will employ a different enrichment scheme to reduce these shortcomings.



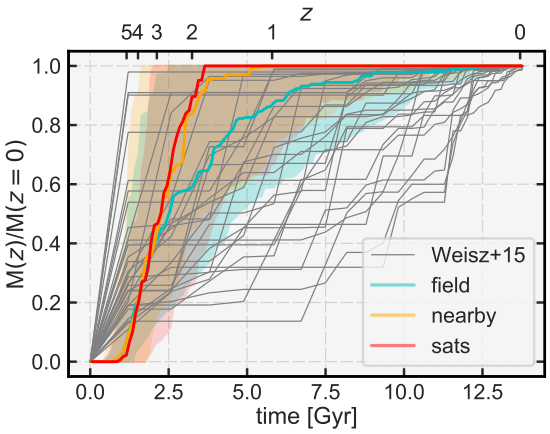


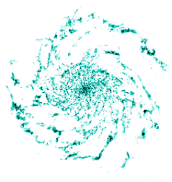
Figure 5.5: Median SFH of our simulated galaxies (colored lines) in comparison to observations of Local Group galaxies (gray lines) taken from Weisz et al. (2015). The red line shows the median SFH for *satellite galaxies*, the orange line for *nearby galaxies* and the cyan line for *field galaxies*. Shaded areas indicate the 16th and 84th percentile. Field galaxies show a much more extended SFH compared to satellites and dwarf galaxies.

Looking at the right panel of Fig. 5.4 one sees that the mass-velocity dispersion relations obtained from the simulated galaxies are in excellent agreement with the observed relations. Especially at low stellar mass ($M_{\rm star} < 10^6 {\rm M}_\odot$) the very low dispersion galaxies observed in the Local Group as well as the large scatter in the observed velocity dispersion values are recovered. At higher stellar masses ($\sim 10^8 {\rm M}_\odot$) there is some velocity dispersion excess in comparison to observed galaxies.

The most interesting result of the above two figures is however that galaxies from all three populations, *satellite*, *nearby* and *field galaxies*, mix well. It is hard to distinguish *satellite galaxies* from *nearby* or *field galaxies* just by measuring their velocity dispersion or metallicity as a function of stellar mass. Only at very low stellar masses one sees a slight separation between *satellite* and *nearby*/*field* galaxies. *Satellites* tend to have lower stellar velocity dispersions compared to equal mass *nearby* or *field* galaxies. As I will elaborate in section 5.4 this is the signature of tidal mass loss which reduces the stellar velocity dispersion of satellites (see e.g. Frings et al. 2017; Macciò et al. 2017).

5.3.2. Star Formation History and Gas Fraction

Figure 5.5 shows the cumulative SFH of simulated galaxies in comparison to observational data taken from Weisz et al. (2015, gray lines). The simulated galaxies cover the full range of observed SFH. Similar to the results from the last subsection, there is not much difference between *satellites* and *nearby galaxies* in their SFH. These two types of galaxies show an early stellar mass growth which then quickly stops at redshift $z \sim 2$ which is when *satellites* fell into their host halo and got stripped of their cold gas and thus rapidly quenched (see e.g. Wetzel et al. 2013; Fillingham et al. 2016). As I will show later, *nearby dwarfs* are biased towards early stellar mass growth by the *backsplash* galaxies belonging to this population. *Field galaxies* however show a more extended SFH and most are basically star forming up to today. These findings are in



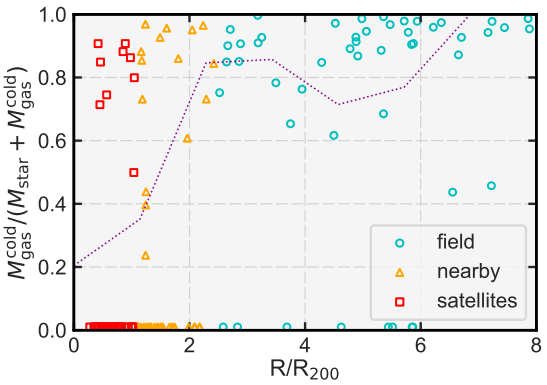


Figure 5.6: Cold gas fraction of *satellites* (red squares), *nearby galaxies* (orange triangles) and *field galaxies* (cyan dots) as a function of distance from the host. The purple dotted line indicates the fraction of galaxies which have cold gas as a function of radius. The closer one gets to the host the lower is the fraction of galaxies that still have a cold gas content.

broad agreement with the results obtained for Local Group galaxies by Weisz et al. (2015) and Brown et al. (2014) who find similar results for *satellites* and *field galaxies*.

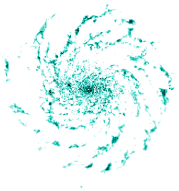
That indeed the dwarf galaxies closer to the host are more affected by stripping off the cold gas can be seen from Fig. 5.6. In this Figure I show the gas fraction of the simulated sample of galaxies as a function of distance from the host (colored dots). The purple dotted line shows the fraction of galaxies with cold gas as function of distance to the host. Here the *satellites*, with almost all of them being gas poor, the *nearby dwarfs*, which partly still have some cold gas left and the *field galaxies*, which almost all show very high gas fractions around unity, separate well. I ascribe these differences to ram pressure stripping which quickly removes the gas from the *satellites* and *nearby galaxies* (Wetzel et al. 2013; Fillingham et al. 2016; Simpson et al. 2017). Stripping off the cold gas from the *satellites* removes the fuel for star formation which shuts down late time star formation. Only *satellites* on their first infall still have some cold gas left. Overall the fraction of *satellites* and *nearby dwarfs* with a cold gas fraction larger than 0.1 quickly drops from ~ 0.8 at $R = 4R_{200}$ to ~ 0.3 at $R < R_{200}$ (purple dotted line in Fig. 5.6). I like to note here that the few *field galaxies* which do not have any cold gas still posses hot gas.

5.4. Environmental Effects

The last section revealed that *satellites* differ from *field galaxies* in the properties strongly affected by the host environment. In this section I quantify the mass loss via stripping for individual galaxies over their lifetime.

5.4.1. Abundance Matching - $M_\star$ vs. $M_{\rm halo}$

In ΛCDM there exists a well established relation for isolated galaxies between the mass of their dark matter halo $M_{\rm halo}$ and the amount of stellar mass $M_\star$ present in that halo

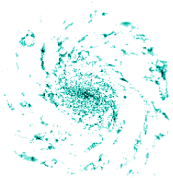


(Conroy and Wechsler 2009; Moster et al. 2010; More et al. 2011; Behroozi et al. 2013). This relation provides, as I will show below, a very good tool to tell environmentally affected and unaffected dwarf galaxies apart. In Fig. 5.7 I present the stellar mass of the simulated galaxies against their total gravitationally bound mass: for isolated galaxies this is M_{200} and for satellite galaxies this is the bound mass returned by `AHF`. I indicate the fiducial resolution limit of 10 stellar particles with the gray shaded region and show dark sub-haloes (sub-haloes without any stellar particle) with lower triangles at $M_\star \sim 10^3 \mathrm{M}_\odot$. Luminous galaxies follow the fiducial color scheme where *satellites* are shown with red squares, *nearby galaxies* with orange triangles and *field galaxies* with cyan dots. For comparison I show results from the fiducial NIHAO sample (Wang et al. 2015, open blue dots) as well as results from other simulation suites (open colored symbols) and measurements for three MW satellites and several observed field dwarfs taken from the literature in gray symbols. Finally, the black dashed line with the shaded dark gray area marks the abundance matching relation from Moster et al. (2013) and its corresponding scatter.

From Fig. 5.7 one can see that, as expected, the isolated *field galaxies* follow nicely the observed relation (black dashed line) and are well in agreement with the higher resolution versions taken from the NIHAO sample. The *satellite* galaxies strongly depart from the relation of isolated galaxies. For a given stellar mass these galaxies have a too low virial mass compared to isolated galaxies. This deviation is a signature of mass removal from the *satellites*. I have checked that almost all *satellites* retain their stellar mass after infall (see also Frings et al. 2017).

The *nearby galaxy* sample which is located in the radius range of R_{200} to 2.5 R_{200} from the host galaxy also shows signs of stripping. However, the galaxies of this sample deviate less from the main relation compared to the *satellite sample*. This can be explained by two effects: first, the environmental effect of striping is already present at these radii far away from the host although less pronounced due to a weaker tidal field. Second, most of the dwarf galaxies actually spent some time orbiting within the virial radius of the host (see next section).

In the left panel of Fig. 5.8 I compare the simulated galaxies to several abundance matching relations taken from the literature (colored lines). I turn the line style from solid to dashed where the relations are extrapolated. The purple dotted line (right y-axis) shows the fraction of dark haloes (e.g. haloes not able to form stars). At $\sim 10^9 \mathrm{M}_\odot$ I find a fraction of ~50% dark haloes in agreement with other simulations (e.g. Fattahi et al. 2016). In the range where galaxies are well resolved ($M_{\mathrm{halo}} \gtrsim 10^9 \mathrm{M}_\odot$) they follow the abundance matching relations of Moster et al. (2013) and Jethwa et al. (2016). Compared to the simulations, the relations from Behroozi et al. (2013) and Read et al. (2017) show a slightly too shallow slope while the relation from Brook et al. (2014) shows a slope slightly too steep. In general I find much larger scatter for



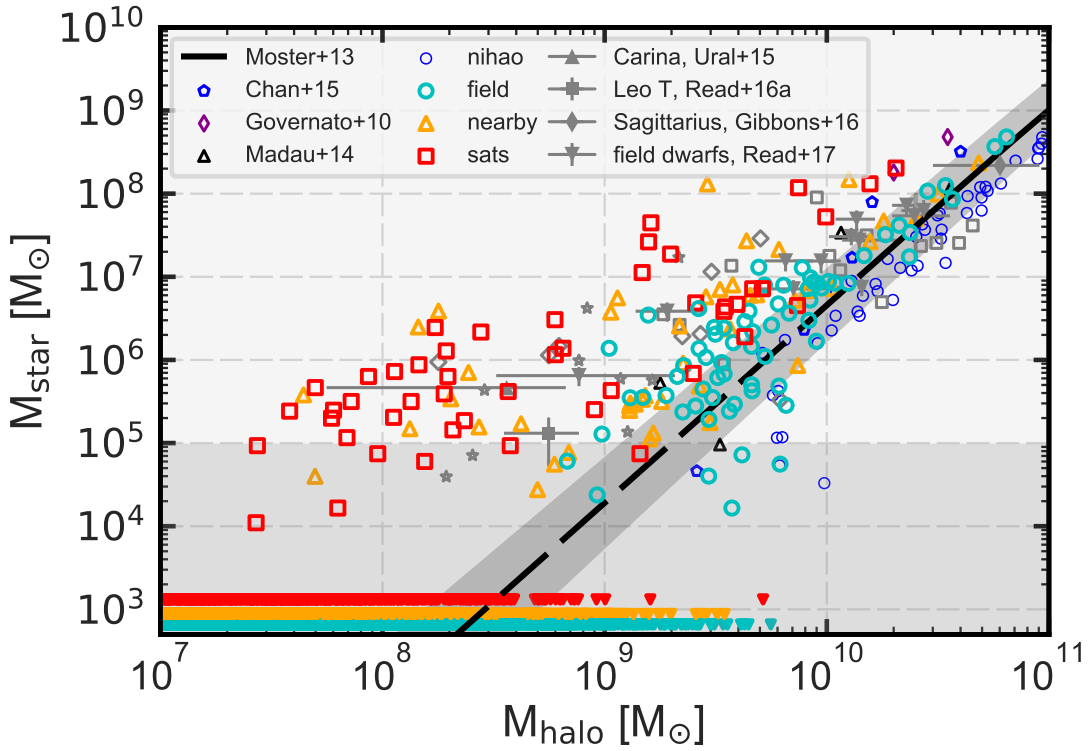
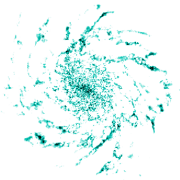


Figure 5.7: Stellar mass vs. the total halo mass M_{halo} for satellites, dwarfs and field galaxies. Colored points denote the satellites and dwarfs in the simulations with the same color coding convention as in previous plots and gray points show observational results for Local Group galaxies (Ural et al. 2015; Read et al. 2016; Gibbons et al. 2017; Read et al. 2017). Gray open symbol measurements are taken from Sawala et al. (2014) (and references therein), gray open stars show results for individual MW satellites, gray open diamonds for M31 satellites and gray open squares for dwarf irregulars. The black line shows the abundance matching result from Moster et al. (2013), where I turn the line style to dashed where the result is extrapolated. Open blue circles show the result from the whole NIHAO sample (Wang et al. 2015) and all other open colored symbols show results from other simulation suites (Chan et al. 2015; Governato et al. 2010; Madau et al. 2014). Lower triangles at the bottom of the plot indicate dark sub-haloes with no stellar particles at all. The gray shaded area marks the region where I have fewer than 10 stellar particles in the haloes.

the simulated galaxies than is predicted by the abundance matching relations (even excluding *satellite galaxies*).

One could argue that using the bound mass for satellites and the virial mass for isolated galaxies introduces a bias. Hence, in the right panel of Fig. 5.8 I use the maximum of the circular velocity curve V_{max} as a proxy for the total mass. This quantity is less effected by the host environment and the definition used to set the total mass. I convert the abundance matching relation from Moster et al. (2013) from being a function of



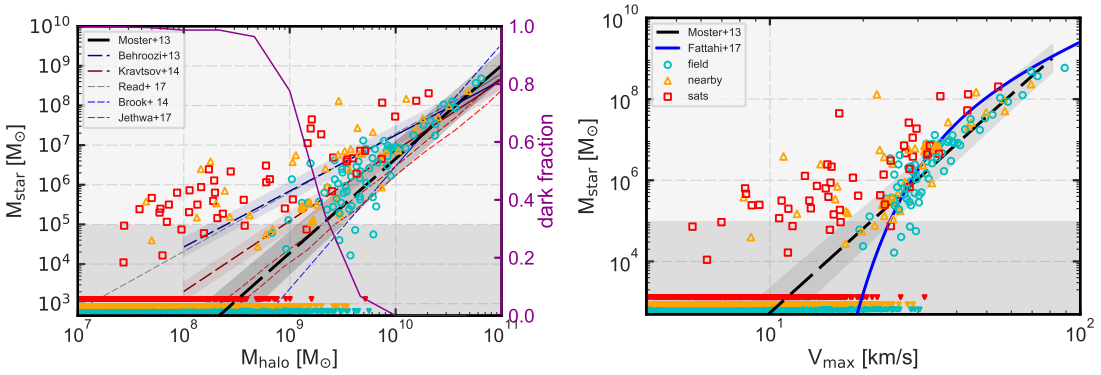
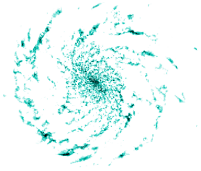


Figure 5.8: *Left panel*: Stellar mass vs. the total halo mass M_{halo}, the same data as in Fig. 5.7 is shown but this time in comparison to several abundance matching relations from the literature (Moster et al. 2013; Behroozi et al. 2013; Brook et al. 2014; Kravtsov et al. 2014; Read et al. 2017; Jethwa et al. 2016). The purple dotted line (right y-axis) shows the fraction of dark haloes with masses greater than $10^7 M_\odot$. *Right panel*: Stellar mass vs. maximum circular velocity. Colored points show again the simulation results with the same color coding convention as before. The black dashed line shows the result for the abundance matching relation from Moster et al. (2013) translated to a function of V_{max}. The gray shaded area around this line marks the uncertainty of this relation. The blue solid line shows the M_{star} vs. V_{max} relation obtained for central galaxies from the APOSTLE simulations (Fattahi et al. 2017). Again the gray shaded area at the bottom of the plot marks the region in which the galaxies contain fewer than 10 stellar particles. Lower triangles at the bottom of the plot indicate dark sub-haloes with no stellar particles at all.

virial mass to a function of V_{max} by assuming a NFW-profile (Navarro et al. 1997b) and using the concentration-mass relation from Dutton and Macciò (2014).

Again, I indicate the fiducial resolution limit of 10 stellar particles with the gray shaded region and I show dark sub-haloes with lower triangles at $M_\star \sim 10^3 M_\odot$. The solid blue line shows the scaling relation derived from isolated dwarf galaxies of the APOSTLE simulations (Fattahi et al. 2017). Although still in agreement with my findings, I do not see the bending behaviour in our $M_\star$ vs. V_{max} relation. The simulations are rather well in agreement with the transformed (linear) Moster relation. As one can see from this plot, I find no qualitative difference between the results obtained by using the total bound mass or the maximum circular velocity to derive the abundance matching relations. *Satellites* deviate in both versions from the expected abundance matching relation of isolated galaxies.

One could further argue that the deviation might be partly due to a resolution issue where I sample the abundance matching relation unequally (galaxies with stellar masses below $10^5 M_\odot$ are barely or not at all resolved). This issue would lead to preferentially sampling galaxies with stellar masses above the Moster relation for virial masses lower than $\sim 10^9 M_\odot$ and might explain the deviation from the abundance



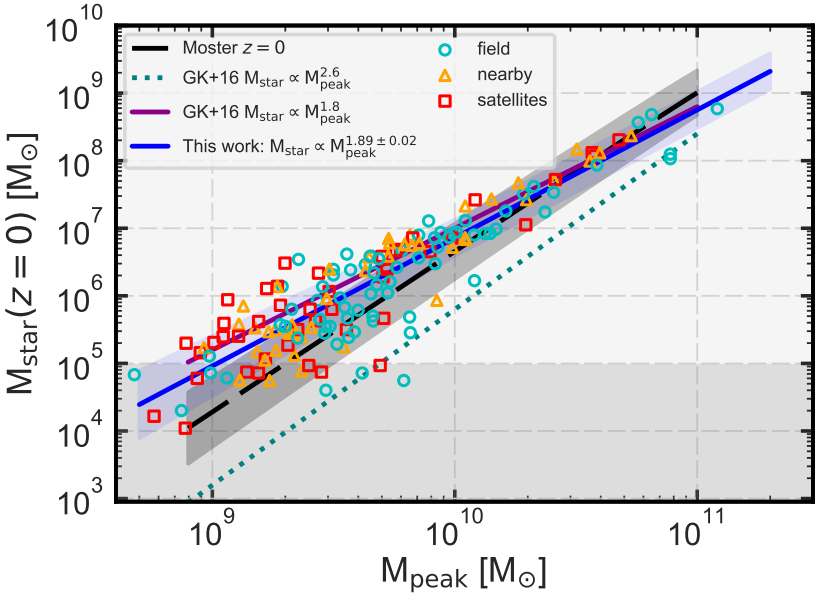


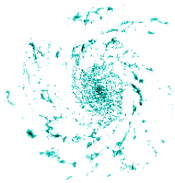
Figure 5.9: Present day stellar mass $M_\star$ vs. the maximum total mass ever reached (peak mass) $M_{\rm peak}$. Colored points show the results for simulated galaxies with the same color coding as applied to previous plots. The black dashed line shows the result from Moster et al. (2013) at redshift $z = 0$. The purple and turquoise lines are taken from Garrison-Kimmel et al. (2017). The blue solid line indicates a power law fit to the simulation data. The blue shaded area indicates the scatter of the simulation data around this fit and the gray shaded area at the bottom of the plot marks again the fiducial resolution limit of less than 10 stellar particles.

matching relation. However, this is not the case here as I will show in the next subsection.

5.4.2. The Peak Masses of Local Group Galaxies

It is well established that satellite galaxies loose mass while orbiting inside the potential of the host galaxies (e.g. Kravtsov et al. 2004; Frings et al. 2017; Fattahi et al. 2017). Especially using the peak mass $M_{\rm peak}$, the maximum mass of a galaxy ever reached, instead of the present day virial mass M_{200} brings *satellites* and *field galaxies* back onto the same relation. Here I use the merger trees to identify the peak mass for every dwarf galaxy in the sample and plot in Fig. 5.9 the stellar mass at redshift zero vs. the peak mass. [4] In order to guide the eye, in Fig. 5.9 I also show the abundance matching relation at redshift $z = 0$ taken from Moster et al. (2013) (black dashed line) and the results from Garrison-Kimmel et al. (2017) (purple solid line, green dashed line). I

[4] I like to add that for this analysis as well as for the following two subsections I had to exclude 8 dwarf galaxies. The reason for their exclusion is, either no progenitor could be found or the unique determination of the peak mass was not possible due to major merger.



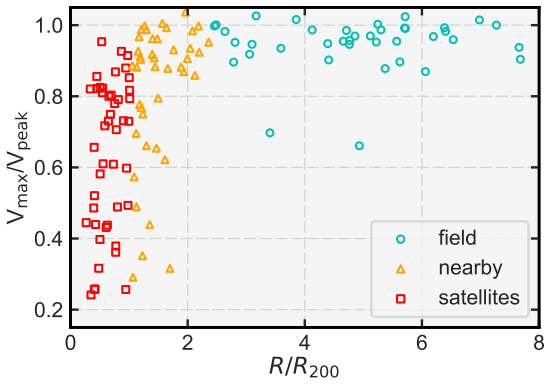


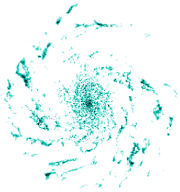
Figure 5.10: The ratio of the present day maximum of the rotation curve V_{max} and the maximum of the same ever reached during the lifetime of the galaxy V_{peak} as a function of the distance from the host at $z = 0$. This ratio is a proxy for the mass lost from the galaxies compared to their maximum mass reached. *Satellites* are shown with red squares, *nearby dwarfs* with orange triangles and *field galaxies* with cyan dots. The closer galaxies are to the host at present day the more severe is their mass loss.

use the same color-coding as in previous plots to distinguish *satellites, nearby dwarfs* and *field dwarfs*. The gray shaded area indicates again the fiducial resolution limit. I find that all dwarfs follow nicely the predicted abundance matching relation from Garrison-Kimmel et al. (2017) with an assumed scatter of zero dex and a slope of 1.8 (purple line). However, comparison to the Moster relation (with an approximate slope of 2.5) shows that the simulations deviate from this at lower peak masses. Similar behaviour was discussed by Sawala et al. (2014) in the APOSTLE simulations.

I fit a simple power law to the simulations in order to estimate the slope and the scatter of this relation. For the simulations used here I find a slope of $\alpha = 1.87 \pm 0.02$ fits the data best and the scatter around the main relation is 0.46 dex. In the simulations the stellar mass loss is negligible thus I can use the abundance matching relation of the simulations to estimate the peak masses of Local Group galaxies using their total stellar mass today (from Fattahi et al. (2017), derived from their total luminosity). The results are presented in table 5.5.

5.4.3. Deviations from the Abundance Matching Relations

Fig. 5.9 shows that *satellites*, *nearby dwarfs* and *field galaxies* can be brought in agreement with abundance matching relations when the peak mass is used instead of the present day virial mass. This shows that it is indeed mass-loss via stripping and thus a reduction in V_{max} which causes the *satellites* and *nearby dwarfs* to depart from the abundance matching relation. I investigate this further in Fig. 5.10 which shows the ratio of present day $V_{max}(z = 0)$ to its maximum over the whole cosmic time, V_{peak}, as a function of distance from the host galaxy. There is a sharp transition around $\sim 2R_{200}$ where most of the *satellites* and some of the *nearby dwarf galaxies* show a V_{max}/V_{peak} ratio of 0.8 while *field objects* on the other hand nearly retain their



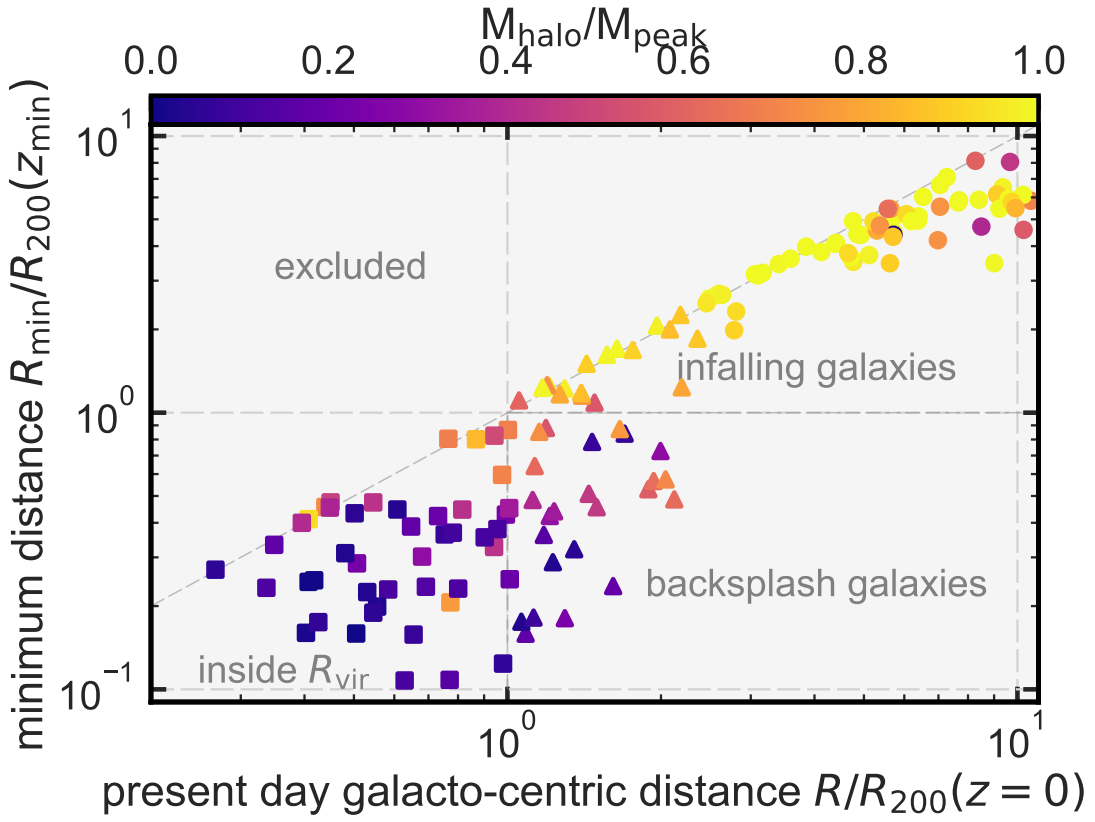
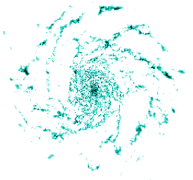


Figure 5.11: The minimum distance to the host galaxy in terms of the virial radius at the time this distance was reached vs. the present day distance in terms of the present day virial radius. Different symbols mark *satellites* (squares), *nearby dwarfs* (triangles) and *field galaxies* (dots). The color coding shows the fraction of present day virial mass in terms of the peak mass $M_{\rm halo}/M_{\rm peak}$. There is a clear color gradient in y-direction indicating a correlation of mass loss with minimum distance to the host. Gray dashed lines divide the plot into four different regimes, separating three different populations of galaxies, *satellites* (lower left), *backsplash galaxies* (lower right) and *infalling dwarfs* (upper right).

peak value. The small reduction in $V_{\rm max}$ for the *field* galaxies is mostly due to a loss of gas due to stellar feedback. The four *field* galaxies with $V_{\rm max}/V_{\rm peak}$ ratio around 70% are objects which had a major dwarf dwarf merger and their $V_{\rm peak}$ value is biased high and thus the ratio of $V_{\rm max}$ to $V_{\rm peak}$ is biased low.

The sharp transition between *field* galaxies and *nearby* galaxies is a hint that those *nearby* galaxies did experience some tidal stripping by being "backsplash" galaxies (e.g. they have spent some time inside the host halo). To test this hypothesis, in Fig. 5.11 I show the mimimum distance to the host against the present day distance from the host for *satellites*, *nearby dwarfs* and *field galaxies*. The same symbols as in previous plots are used to distinguish galaxies from different populations and the color-coding



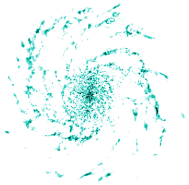
of the points shows the mass-loss quantified via the ratio of present day total mass $M_{\rm halo}$ to peak mass $M_{\rm peak}$. This plot can be divided into several distinct regions marked by gray dashed lines. The plot is cut into half by the diagonal dashed gray line. Every thing on the upper left side of that line is excluded because the minimum distance can not be greater than the present day distance. This line at the same time marks the position of galaxies that are today at their minimum distance and on their first infall. The lower right part of the plot is separated into three distinct regions:

1. Satellites: present day distance is smaller than the host's virial radius (lower left).
2. Infalling field: present day distance and the minimum distance are larger than the host's virial radius (upper right).
3. Backsplash field: present day distance is larger than the host's virial radius but the minimum distance was smaller than the host's virial radius at earlier times (lower right).

Part 1) is located on the lower left and is filled, by definition, with only *satellites*. Part 2) is located on the upper right part of the allowed region and inhabited only by *field objects*. Almost all of them line up on the first infall line. Part 3) is the region where I find the **backsplash galaxies** which have a minimum distance smaller than the present day distance. Indeed, this plot teaches us that about 75% of the dwarf galaxies are **backsplash galaxies** having spent some time within the virial radius.

Looking at the color-coding of this plot one can draw four conclusions for the mass loss of the galaxies:

1. There is only a color gradient in y-direction but not in x-direction. Thus, mass loss directly correlates with the minimum distance and not with the present day distance. This shows that close encounters with the host is the primary cause for mass-loss.
2. Looking only at the *nearby dwarf galaxy* population, one sees that only galaxies which entered the host's virial radius show strong mass-loss. This explains the fact that some *nearby dwarfs* show deviations from the Moster relation and some not. Their dependence of mass loss on the minimum distance shows that it is the pericenter distance which sets the amount of mass lost.
3. Almost all *field objects* are on first infall. Only at very large distances $R/R_{200} > 5$ there are some deviations from this behaviour. This suggests that a clear signal for being unaffected by the host is a positive radial velocity.
4. At very large distances from the host some field objects show mass-loss of about 20% to 30%. These objects were part of merging systems at earlier times which



leads to an artificially high peak mass and thus to higher values of mass-loss (see also Lee et al. 2017).

Fig. 5.10 together with Fig. 5.11 clearly shows that the deviation from the abundance matching relation observed in Fig. 5.7 is caused by (tidally) stripping dark matter mass from the galaxies which entered the virial radius of the host. Most remarkably the effects of mass loss are also strongly visible for the **backsplash galaxies** which only spent a short time (one pericenter passage) inside the host. I therefore advocate to carefully select the dwarf galaxies in the Local Group in order to be unaffected by the host and to be compared to ΛCDM predictions to test dark matter theories.

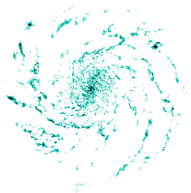
5.5. Implications for Local Group Galaxies

I have established and quantified the environmental influence of the host galaxy on its satellite and dwarf galaxies. I now turn to discuss the implications of these findings for the Local Group. Because of their proximity the small galaxies of the Local Group are among the most well studied systems we know. However, environmental effects of the MW or M31 on their small companions are mostly neglected, especially for dwarf galaxies outside the assumed virial radius of the hosts. The galaxies outside ~ 300 kpc of MW and M31 were long thought of as clean representatives of field dwarf galaxies. In this work however, I have shown that this zeroth order approximation breaks down for a significant fraction ($\sim 50 - 80\%$, see e.g. right axis of Fig. 5.13) of galaxies as close as $2.5R_{200} \sim 450$ kpc to their host. The dwarf galaxies in this region show similar properties to satellite galaxies with signs of significant mass loss (e.g. shown in Fig. 5.7 and Fig. 5.11), early quenching of their SFH (Fig. 5.5) and reduced gas fractions (Fig. 5.6) compared to the clean sample of field galaxies. In the following subsections I will discuss possible signatures to distinguish between *backsplash galaxies* and clean field galaxies.

5.5.1. Distinguishing *Backsplash Galaxies* from unaffected *Field Galaxies*

5.5.1.1. Reduction in Velocity Dispersion - One Way to identify *Backsplash Galaxies*?

How can we observationally separate *backsplash galaxies* from unaffected *field galaxies*? One possibility was pointed out by Knebe et al. (2011) who found that *backsplash galaxies* have lower mass-to-light ratios compared to *field galaxies*. However, getting firm estimates of the dynamical mass of dwarf galaxies is still worrisome and involves careful mass modeling and accounting for inclination effects (e.g. Oman et al. 2015).



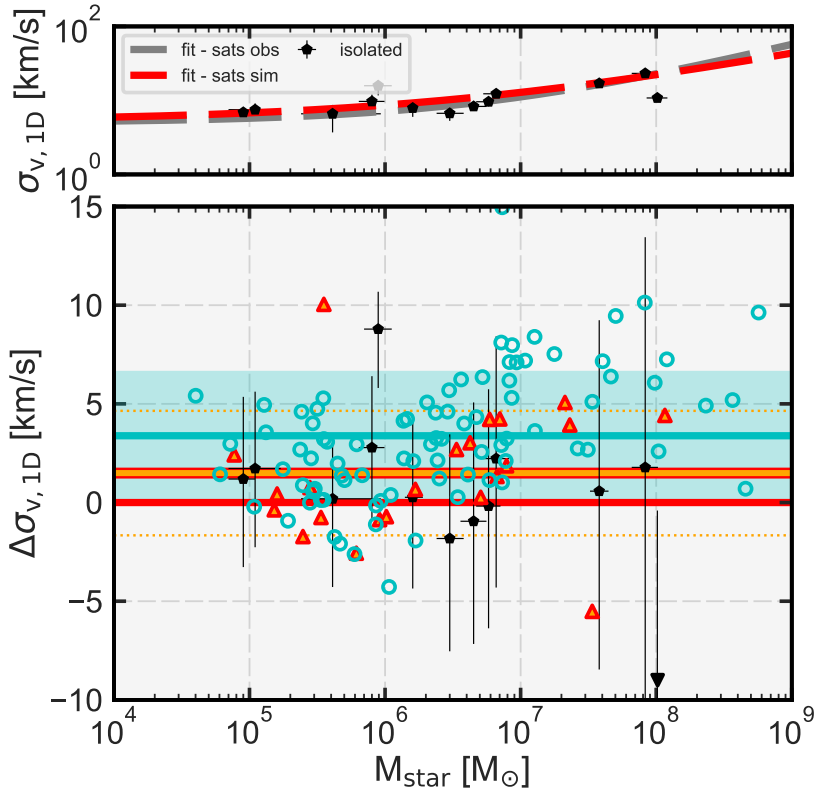
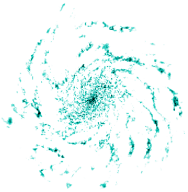


Figure 5.12: *Upper panel:* Stellar mass vs. 1D velocity dispersion for isolated Local Group galaxies similar to Fig. 5.4. Dashed lines show fits to the velocity dispersion of the (*satellites* in the simulations (red) and in the observations (gray). *Lower panel*: Deviations of the measured velocity dispersion of simulated dwarf galaxies from the relation of the simulated *satellite galaxies*. The red horizontal line at $\Delta\sigma_{v,1D} = 0$ shows the average relation for simulated *satellites*, the orange/red line for *backsplash* galaxies and the blue line for *field* galaxies. The blue shaded area indicates the scatter for the *field* population and the orange dotted lines for the *backsplash galaxies*. The deviation of observed isolated Local Group galaxies from the relation for observed satellites is shown by black pentagons. *Satellite galaxies* show at a given stellar mass lower velocity dispersions compared to the *field* sample which is indicative of having lost dark matter mass due to tidal forces. Individual galaxies from the *field sample* are shown with blue open circles. *Backsplash galaxies*, dwarf galaxies which have spent some time inside the virial radius of their host, are highlighted with orange triangles with red borders.

One rather easy way around this would be to use the line-of-sight velocity dispersion easily accessible by spectroscopic measurements.

In section 5.4.3 I showed that *backsplash galaxies* show significant mass loss due to their close encounter with their host and as was recently shown by Frings et al. (2017) mass loss results in a drop in stellar velocity dispersion. Thus one obvious choice of discriminating variable would be the stellar line-of-sight velocity dispersion which should on average be lower for *backsplash galaxies* compared to *field galaxies* at the



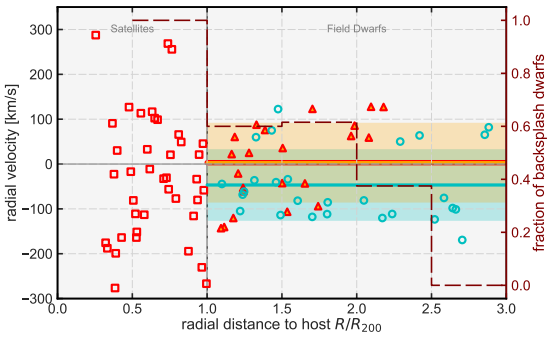
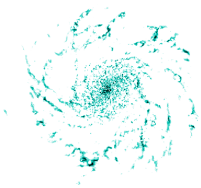


Figure 5.13: Radial velocity vs. distance from the host for simulated *satellites* (red squares), *backsplash galaxies* (orange/red triangles) and *field galaxies* (cyan dots). The red/orange line shows the mean radial velocity for *backsplash galaxies* and the cyan line for the *field population*. Qualitatively *backsplash galaxies* show more positive radial velocities compared to *field galaxies*. The maroon dotted line (right y-axis) shows the fraction of *backsplash galaxies* as a function of distance from the host.

same stellar mass, or equivalently higher compared to *satellites*. I test this assumption by fitting an exponential of the form

$$\sigma_{\rm v}\left(M_\star\right) = A + B\exp C\log\left(M_\star\right) \tag{5.1}$$

to the velocity dispersion-$M_\star$ relation obtained from our simulation in order to take out the mass dependence. In Fig. 5.12 I show the resulting fits (upper panel) for *satellite* galaxy populations in the simulation (red dashed line) and observations (gray dashed line) and the average deviation of populations from the fitted main relation (lower panel). The upper panel of this figure shows that the fits for the *satellite galaxies* in simulations and observations agree well. However, given the large scatter in velocity dispersion, the more robust test is the deviation from the fitted relation. In the lower panel I show the residuals if one subtracts the fitted main relation for satellites from the simulated dwarfs (colored symbols) and the observed dwarfs (black symbols). I find that the *backsplash galaxies* (orange triangles with red borders) scatter around zero while the *field galaxies* show on average positive residuals. This means at a given stellar mass *backsplash galaxies* have on average lower velocity dispersions compared to *field galaxies*, well in agreement with the findings of Frings et al. (2017). However, due to the large scatter *backsplash galaxies* overlap with low velocity dispersion *field galaxies* and there is no clear separation between *field galaxies* and *backsplash galaxies*. Thus, the velocity dispersion alone can not serve as a discriminating variable on an object by object basis. Having low velocity dispersion for a given stellar mass is only indicative for mass loss. Given the low number statistics of measurements for Local Group field galaxies (11) it is not possible to make a firm prediction for which galaxies might be *backsplash galaxies* based on the velocity dispersion alone.



5.5.1.2. DISTANCE VS. RADIAL VELOCITY - ANOTHER WAY TO SEPARATE *BACKSPLASH GALAXIES* FROM *FIELD OBJECTS*?

Teyssier et al. (2012) suggested, based on an analysis of the dark matter only simulation Via Lactea II (Kuhlen et al. 2009), that *backsplash haloes* and *field haloes* show, at a given distance from the host, different values of radial velocities. While *field haloes* in the vicinity of the host (300kpc up to 900 kpc) show on average negative radial velocities, *backsplash haloes* have positive velocities. These findings are then used to estimate which Local Group galaxy might be a *backsplash galaxy* (see also Pawlowski and McGaugh 2014). Here I test this behaviour for the set of **luminous** dwarf galaxies. In Fig. 5.13 I show the radial velocity as a function of distance from the host for the dwarf galaxy populations (*satellites* in red squares, *field dwarfs* cyan dots, *backsplash galaxies* orange/red triangles). On average *backsplash galaxies* show indeed a higher value of radial velocity compared to *field galaxies* but the scatter is large and our sample size small. Thus there is a large overlap of the two populations in this plot and again, these results are only suggestive of being a *backsplash galaxy*. This leaves the only firm measurement/test of being affected by the host through the total mass of the galaxies and their deviation from abundance matching relations. However, observations are far from being able to infer the total masses of observed field galaxies robustly.

Another result one can take away from Fig. 5.13 is the fact that the simulations predict a large fraction of *backsplash galaxies* in the vicinity of the MW or M31. In the simulations the fraction of *backsplash galaxies* between 1 and 2.5 virial radii is about 80 to 50 per cent. Therefore, in the next subsection I estimate the probability of Local Group dwarf galaxies to be a *backsplash* galaxy based on observable properties such as their radial velocity, distance and velocity dispersion.

5.5.2. PROBABILITY OF BEING A *BACKSPLASH GALAXY* FOR OBSERVED LOCAL GROUP DWARF GALAXIES

Having quantified the differences between *backsplash galaxies* and unaffected *field galaxies* in the parameters space distance from the host, radial velocity and velocity dispersion of the stars, I calculate the probability for the observed Local Group galaxies

Table 5.2: Mean and standard deviation for the velocity dispersion offset and the radial velocity of *backsplash* and *field* galaxies.

	μ_{BS} [km/s]	σ_{BS} [km/s]	μ_F [km/s]	σ_F [km/s]
$\Delta_{\sigma,1D}$	1.56	3.16	3.45	3.21
radial velocity	3.03	87.16	-46.74	78.06

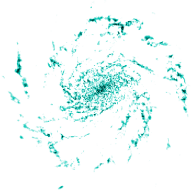


Table 5.3: Probabilities of being a *backsplash* galaxy for nearby Local Group galaxies. I derive probabilities based on distance ($P_{\rm d}$), radial velocity ($P_{\rm rv}$) and velocity dispersion (P_{σ}) as well as a combination of distance and radial velocity ($P_{\rm rv,d}$) and all three properties ($P_{\rm tot}$).

galaxy	$P_{\rm d}$	$P_{\rm rv}$	P_{σ}	$P_{\rm rv,d}$	$P_{\rm tot}$
Phoenix	0.56	0.36	0.51	0.41	0.43
NGC 6822	0.46	0.62	0.54	0.58	0.61
Leo T	0.54	0.43	0.54	0.48	0.51
And XXVIII	0.85	0.54	0.61	0.87	0.91
IC 1613	0.51	0.42	0.92	0.43	0.90
Cetus	0.15	0.62	0.66	0.23	0.36
Pegasus	0.61	0.69	0.52	0.78	0.79
WLM	0.0	0.52	0.59	0.0	0.0
And XVIII	0.35	0.54	0.49	0.39	0.38
EriII	0.65	0.67	0.56	0.79	0.83

to be a *backsplash galaxy* and thus being tidally affected by the host. For the velocity dispersion and radial velocity I assume a Gaussian distribution $\mathcal{G}(\mu, \sigma)$ around the mean relations derived for each population in the previous subsection. I compute the probability by a simple ratio of the distributions:

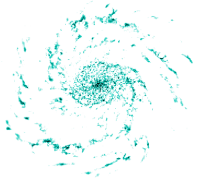
$$P_{\rm BS}(x_{\rm i}) = \frac{\mathcal{G}(x_{\rm i}, \mu_{\rm BS}, \sigma_{\rm BS})}{\mathcal{G}(x_{\rm i}, \mu_{\rm BS}, \sigma_{\rm BS}) + \mathcal{G}(x_{\rm i}, \mu_{\rm F}, \sigma_{\rm F})} \tag{5.2}$$

Here $\mathcal{G}(x_{\rm i}\mu_{\rm BS}, \sigma_{\rm BS})$ denotes the *backsplash galaxy* distribution and $\mathcal{G}(x_{\rm i}, \mu_{\rm F}, \sigma_{\rm F})$ the *field galaxy* distribution. $x_{\rm i}$ denotes either the velocity dispersion offset $\Delta\sigma_{\rm v,1D}$ or the radial velocity value of galaxies. All relevant values extracted from the simulations and needed to calculate these probabilities are given in table 5.2. I use the fraction of *backsplash* galaxies as a function of distance as shown in Fig. 5.13 in order to derive the probability of being a *backsplash* galaxy as a function of distance from the host. For simplicity I assume a linear decrease with distance, from 100% at the virial radius (here: 250 kpc for MW and 300 kpc for M31) to 0% at 2.5 virial radii.

The combined probabilities are calculated by multiplying single probabilities and re-normalising them in the following way:

$$P_{\rm BS}(x_{\rm i}, x_{\rm j}) = \frac{P_{\rm BS}(x_{\rm i}) P_{\rm BS}(x_{\rm j})}{P_{\rm BS}(x_{\rm i}) P_{\rm BS}(x_{\rm j}) + (1 - P_{\rm BS}(x_{\rm i}))\left(1 - P_{\rm BS}(x_{\rm j})\right)} \tag{5.3}$$

Numerical values for the derived probabilities can be found in table 5.3 and graphical representations are given in in Fig. 5.14, Fig. 5.15 and Fig. 5.16. In Fig. 5.14 I show the probability for the velocity dispersion offset. I color-code the $\Delta_{\sigma,\rm 1D}$ vs. $M_{\rm star}$ plane by the probability of being a *backsplash galaxy* which in my assumption only depends on the deviation from the *satellite* relation. Except for IC 1613 all observed *field galaxies* have about 50% probability to be a *backsplash galaxy* given only their



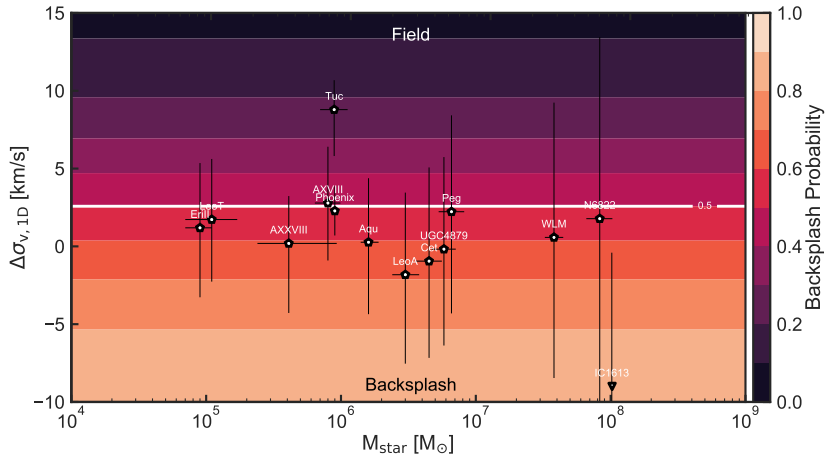
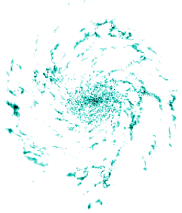


Figure 5.14: Same as the lower panel of Fig. 5.12 but this time I only show the observed isolated Local Group galaxies. The background color shows the estimated probability to be a *backsplash galaxy* based on the velocity dispersion offset $\Delta\sigma_{v,1D}$ as derived from the simulations.

velocity dispersion measurements. This reflects the fact that velocity dispersion alone is not able to discriminate between *backsplash* and *field galaxies*. In 5.15 I show the combined probability of being a *backsplash* galaxy in the radial velocity vs. distance plane. Every galaxy which is closer to the host than 1 virial radius is by definition a *satellite* and is excluded. I do not find any *backsplash galaxy* further away than 2.5 virial radii and thus the probability for galaxies with larger distances from the host than this is 0. In between I find that the probability of being a *backsplash galaxy* decreases with distance but increases with more positive radial velocity. I see that Leo I is basically a satellite given its distance and radial velocity. I find that Pegasus, Eri II, NGC 6822 and And XXVIII have a high probability of being a *backsplash galaxy*. Of particular interest is the result for the newly discovered dwarf Eri II. In the abstract of their paper about properties of Eri II Li et al. (2017) state: *The lack of gas and recent star formation in Eri II is surprising given its mass and distance from the MW*. Here however, I find that Eri II is most likely a *backsplash galaxy* and given that fact it is not surprising at all that this dwarf galaxy shows a lack of recent star formation and cold gas. Actually, given Eri II's radial velocity and distance I expect it to show a low cold gas content and a lack of recent star formation.

Finally, I compile the total probability of being a *backsplash galaxy* for Local Group galaxies in Fig. 5.16. Here I show a top-down view of the Local Group. I exclude all satellite galaxies of M31 and MW and indicate the virial radius with red filled circles ($\sim$ 250 kpc for MW and $\sim$ 300 kpc for M31). The region of 2.5 virial radii around MW and M31 is shown with gray filled circles and indicates the backsplash radius (More et al. 2015; Diemer et al. 2017; Mansfield et al. 2017). Colored stars show nearby dwarf galaxies with the color-coding indicating the total probability of being a *backsplash*



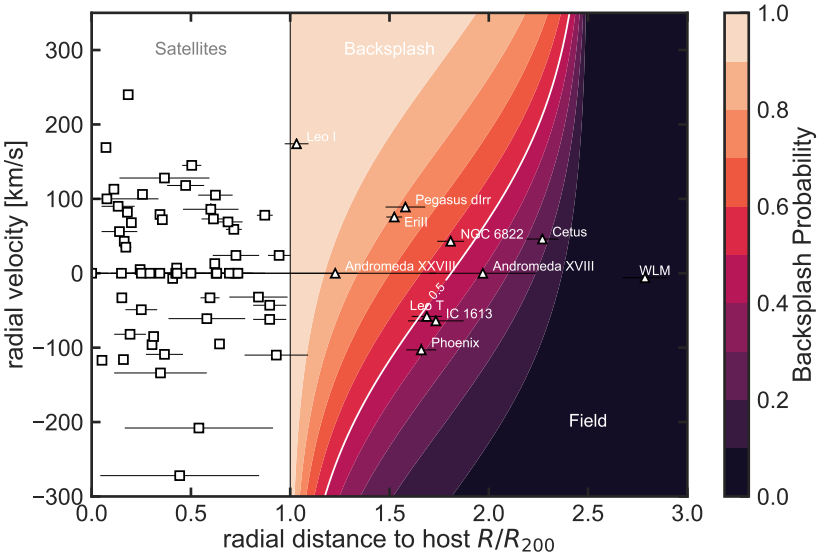
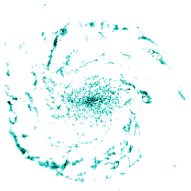


Figure 5.15: Radial velocity vs. distance from the host galaxy for Local Group observations (black open points). The background color shows the probability for given distance and radial velocity to be a *backsplash* galaxy as derived from the simulations. Especially the newly discovered MW dwarf galaxy EriII has a high probability to be a *backsplash* galaxy.

galaxy. Open black circle show all the dwarfs outside 2.5 virial radii which have by definition a probability of 0%.

5.6. Conclusion

In this chapter I explored the environmental effects of the host galaxy onto its satellites and dwarf galaxies. According to their distance to the host I distinguish *satellites* which are inside the virial radius at present day, *nearby dwarf galaxies* which are in between 1 and 2.5 virial radii (which is the expected backsplash radius of the host) and *field galaxies*, outside of 2.5 virial radii from the host. The reason for having three different populations of dwarf galaxies lies in the environmental effect of the host on its companions. While *satellite galaxies* and *field dwarf galaxies* share the same scaling relations, I verify that the former suffered stronger mass loss compared to the latter. *Field galaxies* are mostly on their first infall and almost unaffected by the host. *Nearby dwarf galaxies* make up an intermediate population well outside the virial radius at present day but with a large fraction of *backsplash galaxies*. The orbits of these galaxies took them inside the virial radius of the host at earlier cosmic times (see Fig. 5.11). I show that this population is strongly tidally affected and shows properties more similar to *satellite galaxies* than to *field objects*. Especially careful comparison shows that their velocity dispersion is on average lower compared to similar objects at the



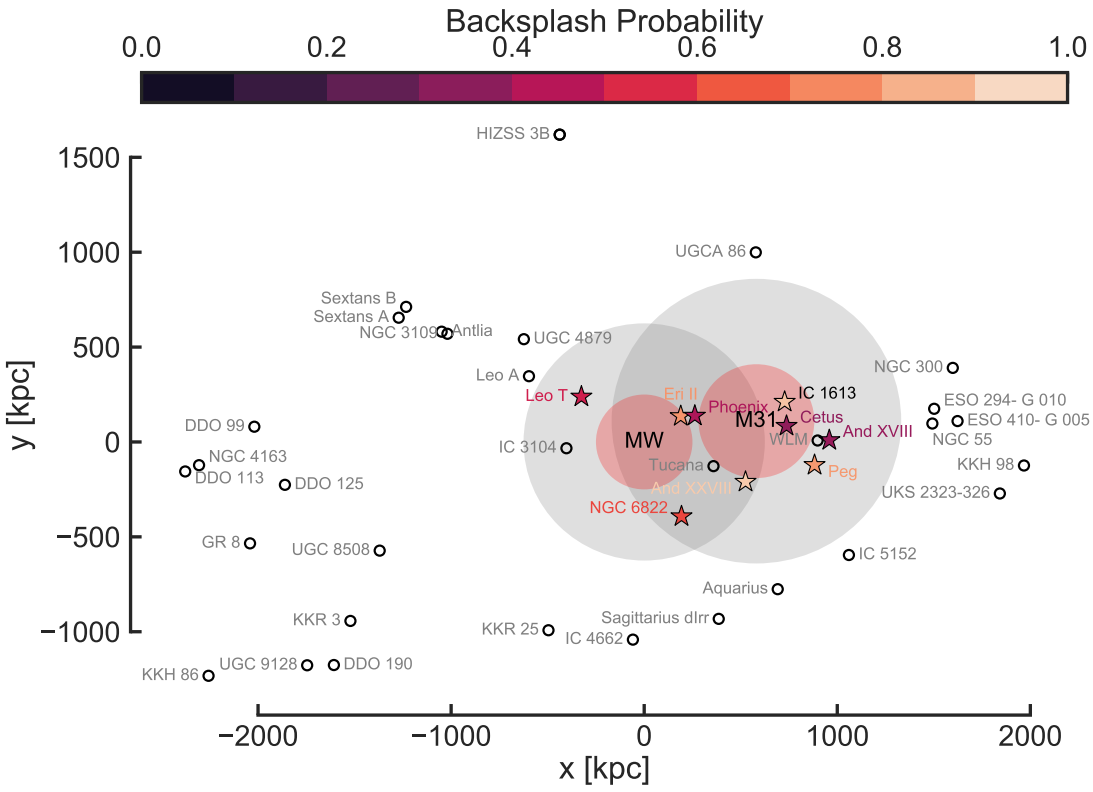
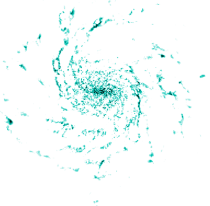


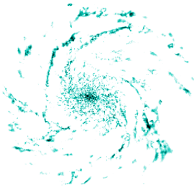
Figure 5.16: Top down view onto the Local Group such that MW's stellar disc lies in the x-y plane. Observations are taken from McConnachie (2012). Red circles show the virial radius of the MW (250 kpc) and M31 (300 kpc) and gray circles show their corresponding backsplash radii of $2.5 \times R_{200}$. Colored stars (with gray names) mark nearby Local Group galaxies (within $2.5 \times R_{200}$) where the color-coding shows the estimated probability to be a *backsplash galaxy*. Open black circles show Local Group galaxies which we quantify as clean field galaxies. I do not show satellite galaxies on this plot which would fall into the red circles.

same distance and mass. Such effects should be considered when selecting observed field objects to confront with ΛCDM predictions.
My main results are summarised as follows:

- The NIHAO simulation project, at very high resolution, is able to produce realistic host satellite galaxy systems. The simulations compare well with observed satellite stellar mass functions (Fig. 5.3) of MW or M31.
- The properties of *satellites*, *nearby dwarfs* and *field galaxies*, like e.g. the stellar mass-metallicity relation and the stellar mass-velocity dispersion relation (Fig. 5.4) or their star formation histories (see Fig. 5.5) agree well with observed properties of Local Group galaxies.



- Interestingly, *satellite galaxies* and *field galaxies* exhibit almost the same mass-metallicity and stellar mass-velocity dispersion relations. However, they differ in their SFH and cold gas fractions. *Satellite galaxies* show an early stellar mass build up compared to *field objects*, which show a more extended SFH. Furthermore, *field galaxies* are on average more gas rich compared to *nearby dwarf galaxies* or *satellites* (compare Fig. 5.6).
- *Field galaxies* almost perfectly line up with results from abundance matching while *satellite galaxies* and *nearby dwarfs* deviate from these results (compare Fig. 5.7, 5.8). In the simulations the reason for this is significant mass loss due to tidal stripping which results in a (strong) reduction of the maximum circular velocity of the dark matter haloes ($V_{\rm max}$, Fig. 5.10).
- Accounting for the mass loss by using the peak mass (the maximum mass ever reached) of the galaxies, all populations shift back onto the same abundance matching relation (see Fig. 5.9). For the dwarf galaxies I find a power law index of 1.89 ± 0.02 for the relation between halo mass $M_{\rm halo}$ and stellar mass $M_{\rm star}$ which is well in agreement with recent results from Garrison-Kimmel et al. (2017).
- I use this relation together with the fact that stellar mass loss is negligible in the simulations to estimate the peak masses of Local Group galaxies; my predicted peak masses are tabulated in table 5.5.
- Due to the mass loss, *backsplash galaxies* show on average lower stellar velocity dispersions compared to *field objects* (see Fig. 5.12). However, the differences are small and can not alone serve to judge if observed dwarf galaxies are stripped or not.
- *backsplash galaxies* differ from *field galaxies* in their position in the radial velocity-distance plot (5.13). *Backsplash galaxies* show on average positive radial velocities while *field objects* show negative radial velocities.
- Clean *field dwarfs* can only be found further away than 2.5 virial radii (~ 750 kpc) from any host in the Local Group.
- Given the distance from the host, the radial velocity and the velocity dispersion we derive a probability for Local Group dwarfs to belong to the *backsplash* population. My findings are compiled in table 5.3 and graphically represented in Fig. 5.16. The newly discovered dwarf Eri II has a probability of 83% to be a *backsplash* galaxy. This fits well to its observed properties which are unusual for its distance from the MW.



5.7. PROPERTIES OF SIMULATED DWARF GALAXIES

Table 5.4: Parameters of simulated dwarf galaxies

M_{200} ($10^9 M_\odot$)	$M_{\rm dark}$ ($10^9 M_\odot$)	$M_\star$ ($10^6 M_\odot$)	$M_{\rm gas}$ ($10^6 M_\odot$)	$V_{\rm max}$ (km/s)	$\sigma_V^{\rm 1D}$ (km/s)	R (kpc)	[Fe/H] (dex)	$z_{\rm infall}$	$z_{\rm peak}$	$M_{\rm peak}$ ($10^9 M_\odot$)	$V_{\rm peak}$ (km/s)	$R_{\rm min}$ (R/R_{200})
g7.08e11												
satellites												
4.28	4.25	1.90	18.64	28.2	10.8	156	−2.23	0.1	0.1	5.06	33.3	0.80
1.98	1.91	17.09	46.75	29.7	13.7	79	−1.74	0.0	0.1	2.74	30.2	0.46
0.90	0.90	0.25	0.0	23.5	7.9	176	−3.75	0.4	1.6	1.28	29.8	0.60
0.37	0.37	0.41	0.0	19.2	8.0	179	−3.21	0.1	0.6	1.55	28.3	0.43
0.15	0.15	0.06	0.0	15.6	2.5	117	−9.67	2.6	3.1	0.87	24.6	0.39
0.07	0.07	0.11	0.0	10.7	6.0	110	−5.45	0.2	2.1	1.65	27.7	0.45
0.06	0.06	0.17	0.0	9.2	3.7	90	−4.07	0.0	2.1	1.11	26.6	0.43
0.01	0.01	0.07	0.0	5.6	1.9	73	−2.87	0.0	3.4	1.55	30.9	0.24
backsplash												
0.27	0.27	0.15	0.0	17.8	6.8	212	−7.98	0.2	1.5	1.83	26.2	0.36
0.20	0.20	0.34	0.0	16.2	6.6	264	−3.46	0.5	1.8	2.56	31.1	0.78
fields												
57.10	54.75	3660.17	5917.68	72.9	37.0	790	−1.16	–	0.0	57.10	86.9	4.08
36.78	34.65	823.73	7778.83	58.5	32.5	468	−1.70	–	0.3	38.57	66.3	2.69
34.25	33.24	1198.20	2718.88	65.2	30.5	941	−1.54	–	1.5	77.46	91.4	4.51
28.45	27.72	1041.61	2018.22	55.2	25.2	658	−1.47	–	1.5	77.46	91.4	3.78
18.04	16.55	463.10	10247.41	49.8	26.6	282	−1.73	–	0.1	18.29	54.0	1.62
10.59	10.23	71.99	2239.76	34.1	17.7	217	−2.02	–	0.1	11.04	40.2	1.25
8.45	8.06	93.41	1894.82	37.8	19.6	1850	−2.15	–	0.6	14.79	44.6	4.58
8.30	8.28	29.70	168.21	38.3	15.9	464	−2.25	–	0.0	8.30	40.9	2.66
7.75	7.51	126.72	1899.00	38.8	21.9	1512	−1.95	–	0.1	7.80	48.6	5.88
7.40	7.35	8.58	236.12	33.3	8.5	393	−1.84	–	0.8	8.43	36.1	2.26
6.77	6.70	36.39	228.33	34.5	16.9	2528	−2.00	–	0.2	7.10	38.6	5.68
6.56	6.55	2.85	9.16	30.2	9.7	694	−5.11	–	0.0	6.56	34.3	3.98
4.64	4.57	21.80	280.48	28.4	12.7	857	−2.31	–	0.0	4.64	32.0	4.92
4.58	4.56	14.54	153.25	31.9	13.4	858	−2.16	–	0.7	4.77	39.9	3.51
4.15	4.15	0.72	0.61	28.3	9.6	1269	−3.01	–	0.0	4.15	30.5	6.66
3.80	3.77	16.15	194.62	28.9	11.4	1914	−1.96	–	0.2	5.41	34.5	5.83
3.84	3.83	2.93	50.59	28.1	11.5	1621	−6.24	–	0.1	3.86	32.8	3.47
3.45	3.41	6.78	7.99	25.7	9.6	1685	−2.94	–	0.0	3.52	29.1	6.53
2.95	2.95	1.92	0.0	26.1	6.3	1642	−2.97	–	0.4	3.27	30.2	6.15
2.94	2.92	0.40	9.13	26.5	11.8	1309	−9.43	–	0.0	2.94	29.8	7.10
2.66	2.65	13.67	50.44	29.6	12.8	2160	−3.12	–	0.3	2.85	37.5	8.31
2.25	2.25	2.36	0.0	25.3	9.4	2715	−7.95	–	0.0	2.25	28.2	8.64
2.12	2.12	6.17	26.61	27.1	10.4	1846	−6.17	–	0.0	2.12	33.0	6.13
1.60	1.60	1.08	0.0	24.9	6.7	233	−8.67	–	0.3	1.65	30.3	1.22
0.97	0.97	1.28	0.20	21.0	11.7	1659	−5.97	–	0.0	0.97	24.3	5.46
g8.26e11												
satellites												
20.48	19.37	194.99	593.41	54.4	27.6	117	−1.20	0.7	1.7	47.56	78.4	0.47
2.57	2.53	4.85	30.47	32.4	15.9	201	−1.88	0.4	1.7	5.97	44.9	0.33
1.47	1.46	10.53	0.0	28.9	15.7	161	−1.78	1.6	1.7	19.63	54.8	0.36
0.28	0.28	1.92	0.0	15.8	7.6	167	−2.30	1.5	1.5	2.74	30.6	0.37
0.21	0.21	0.14	0.0	16.1	5.1	108	−6.80	1.7	1.7	0.89	21.9	0.29
0.06	0.06	0.14	0.0	11.5	6.7	140	−6.89	0.4	1.5	0.78	21.8	0.16
0.04	0.04	0.09	0.0	8.7	3.6	148	−3.05	0.4	1.7	0.27	15.2	0.23
backsplash												
12.59	11.03	115.91	1104.73	46.2	27.5	240	−1.36	1.7	0.2	31.83	74.7	0.48
3.77	3.74	7.87	12.37	31.9	14.5	404	−1.73	0.3	0.4	6.54	38.0	0.53
3.31	3.25	7.02	41.36	31.5	15.8	242	−1.92	0.7	1.1	5.33	37.5	0.64
fields												
23.55	22.77	10.80	262.84	47.5	19.8	2056	−1.90	–	−0.0	23.55	49.0	5.92
9.04	9.00	8.29	27.48	40.3	20.2	2086	−1.76	–	0.6	9.83	43.4	5.78
6.39	6.24	7.89	75.03	33.5	18.4	1203	−1.80	–	0.9	7.10	42.5	3.47
6.05	5.98	4.72	26.24	35.9	13.5	883	−1.67	–	0.0	6.05	39.4	3.81
4.46	4.40	3.84	29.96	31.9	13.6	1095	−1.74	–	0.7	4.54	37.9	3.71
4.61	4.58	0.42	18.70	30.2	7.3	1224	−1.95	–	−0.0	4.61	31.3	4.49
4.28	4.25	2.89	19.63	32.0	13.7	1371	−1.82	–	−0.0	4.28	33.7	5.12
2.27	2.27	0.85	0.0	26.5	9.1	2121	−2.33	–	0.4	2.71	28.7	5.49
1.89	1.89	0.37	0.0	24.7	10.7	532	−4.44	–	0.1	1.91	41.9	2.58

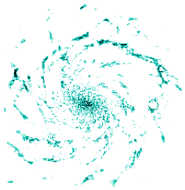


Table 5.4 – (continued)

M_{200} ($10^9 M_\odot$)	$M_{\rm dark}$ ($10^9 M_\odot$)	$M_\star$ ($10^6 M_\odot$)	$M_{\rm gas}$ ($10^6 M_\odot$)	$V_{\rm max}$ (km/s)	$\sigma_V^{\rm 1D}$ (km/s)	R (kpc)	[Fe/H] (dex)	$z_{\rm infall}$	$z_{\rm peak}$	$M_{\rm peak}$ ($10^9 M_\odot$)	$V_{\rm peak}$ (km/s)	$R_{\rm min}$ (R/R_{200})
1.81	1.80	0.32	0.0	25.4	11.3	351	−4.85	–	0.1	1.82	27.0	1.70
1.57	1.56	3.44	3.06	24.4	12.1	2887	−2.35	–	0.4	2.27	31.4	2.42
1.37	1.37	0.29	0.0	23.2	10.7	271	−2.55	–	1.0	1.71	24.0	1.16
1.30	1.30	0.25	0.0	23.0	7.6	317	−3.32	–	0.7	2.33	26.3	1.09
1.05	1.05	1.38	0.0	25.2	11.3	1990	−2.93	–	0.9	1.94	29.0	6.09
g1.12e12												
satellites												
15.64	14.25	100.47	981.23	43.5	22.4	199	−1.48	0.5	0.4	36.90	59.9	0.45
4.64	4.63	7.09	0.0	32.8	15.2	110	−2.07	0.5	0.9	9.74	48.3	0.47
3.95	3.91	4.63	18.57	27.3	10.4	245	−1.94	0.1	1.7	5.72	37.9	0.87
3.50	3.49	4.33	0.0	32.2	14.7	92	−1.95	0.7	0.6	9.35	42.7	0.29
3.44	3.44	3.82	0.0	28.9	11.9	187	−1.85	0.2	0.5	5.01	37.0	0.80
0.65	0.65	1.35	0.0	23.3	10.7	246	−2.19	0.7	2.7	1.86	32.7	0.45
0.60	0.60	1.11	0.0	18.5	9.5	178	−2.80	0.7	1.6	3.03	35.3	0.42
0.11	0.11	0.19	0.0	13.6	6.0	220	−7.62	0.5	3.0	1.02	29.0	0.35
backsplash												
6.09	6.06	21.23	6.63	43.6	20.2	290	−1.80	0.5	0.6	11.04	55.8	0.88
0.69	0.69	0.08	0.0	21.8	9.1	487	−14.44	0.4	2.0	2.33	27.8	0.73
0.42	0.42	0.16	0.0	17.6	7.5	352	−18.96	0.3	2.0	0.92	23.1	0.51
0.04	0.04	0.25	0.0	8.2	5.6	300	−4.49	0.3	3.1	1.29	29.4	0.29
fields												
25.23	23.86	50.30	981.03	57.2	28.1	479	−1.66	–	0.1	25.74	58.5	2.06
15.68	15.56	26.36	72.22	44.6	18.7	536	−1.79	–	0.5	19.77	60.1	1.23
8.74	8.32	8.59	256.96	38.9	17.8	1280	−2.04	–	−0.0	8.74	42.2	4.82
7.17	7.16	5.15	4.06	31.5	13.8	292	−2.03	–	0.3	9.78	41.1	1.26
4.94	4.88	12.75	43.61	34.0	17.1	2360	−1.96	–	0.9	11.05	47.8	8.06
4.84	4.65	5.89	76.90	29.4	12.7	349	−1.95	–	0.3	5.39	39.2	1.50
3.15	3.10	2.04	20.54	27.9	14.7	746	−2.14	–	0.0	3.16	34.6	3.16
3.12	3.09	2.44	2.65	26.0	12.0	2961	−2.63	–	0.1	3.16	37.0	7.93
3.06	3.03	0.35	2.32	27.6	7.8	1149	−7.48	–	−0.0	3.06	31.9	3.65
2.99	2.98	0.18	0.0	26.3	8.8	508	−5.76	–	0.3	3.48	31.2	2.00
2.67	2.67	0.48	0.0	25.9	9.3	422	−2.29	–	0.5	8.73	38.0	1.32
1.66	1.66	0.13	0.0	23.4	10.5	342	−5.94	–	0.3	2.18	26.5	1.15
1.48	1.48	0.34	0.0	24.1	7.7	286	−4.13	–	0.1	1.50	28.1	1.23
1.30	1.30	0.30	0.0	23.4	8.2	257	−3.42	–	0.6	2.15	28.3	1.11
0.68	0.68	0.06	0.0	19.4	8.0	2018	−10.93	–	0.7	1.15	25.3	8.14
g2.79e12												
satellites												
9.89	9.54	44.88	295.15	24.5	28.2	141	−1.79	0.7	0.7	26.01	29.9	0.45
7.46	7.21	91.17	117.44	16.9	18.5	317	−1.51	0.6	0.6	37.88	27.8	0.25
7.38	7.33	4.49	44.03	28.0	15.3	128	−2.21	0.1	0.2	7.90	60.1	0.41
5.13	5.13	6.83	0.0	16.7	13.7	243	−1.87	0.1	1.3	6.71	66.3	0.21
1.58	1.55	0.69	0.0	43.3	11.8	106	−4.81	1.0	1.5	12.13	64.0	0.23
1.07	1.07	20.36	0.0	15.1	14.0	124	−1.89	0.5	0.5	2.67	34.1	0.40
0.60	0.59	0.43	0.0	27.1	16.0	214	−3.23	1.7	2.1	1.99	40.1	0.30
0.20	0.20	0.65	0.0	14.2	8.4	308	−2.42	0.7	2.5	3.11	31.6	0.12
0.17	0.17	2.92	0.0	35.1	11.8	167	−2.63	2.2	2.7	5.25	40.2	0.22
0.19	0.19	1.71	0.0	24.5	8.8	183	−1.93	1.7	2.5	1.68	38.3	0.23
0.19	0.19	0.58	0.0	8.4	7.6	110	−4.89	1.0	2.7	1.12	46.7	0.33
0.15	0.14	0.28	0.0	15.3	6.7	251	−6.50	0.1	2.6	1.16	39.8	0.23
0.13	0.13	0.74	0.0	22.7	6.7	171	−2.58	1.2	1.7	2.25	30.5	0.19
0.11	0.11	0.24	0.0	13.0	6.5	84	−9.65	0.3	2.7	1.91	32.6	0.27
0.09	0.09	0.60	0.0	15.7	5.3	174	−2.71	0.5	2.2	2.53	31.4	0.20
0.07	0.07	0.20	0.0	15.4	2.4	126	−7.35	1.0	2.1	3.57	29.5	0.16
0.05	0.05	0.22	0.0	8.3	5.1	131	−2.60	2.1	3.0	5.09	35.8	0.25
backsplash												
8.13	8.03	6.70	18.58	34.9	13.1	363	−1.81	0.2	0.4	11.08	41.8	0.85
4.35	4.30	23.06	17.79	37.5	19.2	380	−2.04	0.9	1.3	14.16	53.1	0.42
4.52	4.51	5.91	0.0	34.2	16.0	608	−1.88	0.4	0.5	7.14	45.2	0.57
2.90	2.77	33.80	0.0	22.1	11.4	533	−1.45	0.7	1.0	39.63	76.3	0.84
2.86	2.85	4.24	0.0	28.0	13.9	470	−2.18	0.6	0.5	6.21	37.9	0.46
2.26	2.25	0.91	0.0	27.3	7.7	521	−3.50	0.3	0.5	2.97	35.3	0.87
1.52	1.52	0.35	0.0	24.8	17.2	641	−7.42	0.3	0.4	2.13	30.0	0.57
1.29	1.29	0.28	0.0	24.2	8.2	667	−9.63	0.4	0.4	2.07	32.4	0.49
1.14	1.14	5.08	0.0	22.6	11.5	341	−2.29	1.2	1.1	6.67	42.5	0.16
1.07	1.06	3.36	0.0	23.4	13.1	407	−2.06	1.1	1.4	4.43	39.8	0.18
0.24	0.24	0.61	0.0	16.5	6.1	506	−4.60	1.0	1.3	1.34	29.8	0.24
0.18	0.17	1.02	0.0	11.1	7.9	334	−1.90	1.9	2.4	5.32	44.5	0.18
0.14	0.14	1.67	0.0	14.6	9.5	424	−2.19	1.2	3.4	3.04	42.6	0.32
fields												
120.97	109.98	569.31	5768.46	9.2	46.4	1797	−1.23	–	−0.0	120.97	23.5	5.11
64.46	60.50	456.27	1736.70	23.7	35.6	1069	−1.27	–	0.2	64.85	38.9	3.45

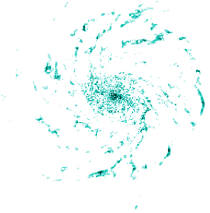
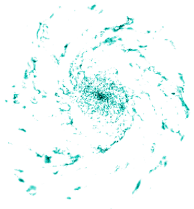


Table 5.4 – (continued)

M_{200} ($10^9 M_\odot$)	$M_{\rm dark}$ ($10^9 M_\odot$)	$M_\star$ ($10^6 M_\odot$)	$M_{\rm gas}$ ($10^6 M_\odot$)	$V_{\rm max}$ (km/s)	$\sigma_V^{\rm 1D}$ (km/s)	R (kpc)	[Fe/H] (dex)	$z_{\rm infall}$	$z_{\rm peak}$	$M_{\rm peak}$ ($10^9 M_\odot$)	$V_{\rm peak}$ (km/s)	$R_{\rm min}$ (R/R_{200})
48.26	45.61	232.43	1439.81	69.4	33.1	553	−1.31	–	0.4	53.41	82.3	1.69
31.76	30.62	97.55	536.17	56.7	28.2	741	−1.51	–	0.3	36.09	67.2	1.85
23.71	23.12	33.80	278.32	44.3	21.9	1462	−1.62	–	0.6	25.57	50.0	3.77
21.19	18.86	40.27	1425.28	69.4	24.8	1384	−1.86	–	−0.0	21.19	89.2	4.11
18.37	18.08	31.32	97.32	29.6	19.3	771	−1.76	–	0.3	19.24	32.9	2.49
14.73	14.57	17.74	102.41	25.0	22.0	874	−1.93	–	0.3	16.23	33.1	1.99
12.47	12.35	8.26	81.05	42.6	18.5	882	−2.40	–	0.4	13.33	50.6	2.32
10.88	10.42	7.30	138.73	52.2	12.8	1770	−1.72	–	0.3	13.99	53.2	5.46
10.17	9.74	8.66	154.29	13.3	20.4	1548	−2.36	–	0.1	10.18	32.2	4.39
9.48	8.79	7.32	519.79	49.4	27.0	1524	−1.96	–	−0.0	9.48	56.7	4.42
8.97	8.83	1.68	72.54	8.1	7.4	2214	−1.81	–	0.3	12.06	36.2	5.55
8.40	8.21	5.23	108.30	35.5	17.6	2412	−1.94	–	0.3	8.51	44.3	5.85
8.25	8.00	7.19	91.62	30.8	20.1	2052	−2.06	–	−0.0	8.25	36.6	6.03
6.09	5.92	0.47	62.87	29.7	5.8	1639	−2.95	–	0.8	6.51	35.0	4.91
5.64	5.57	2.61	52.13	34.0	13.2	828	−1.85	–	0.7	5.77	40.8	2.67
5.27	5.22	1.10	41.02	33.3	9.2	1945	−4.62	–	0.0	5.28	39.1	4.93
4.59	4.53	0.50	36.34	28.5	9.0	2405	−2.26	–	0.0	4.59	33.0	5.76
3.68	3.67	2.36	0.0	31.1	15.0	438	−2.83	–	0.4	4.28	37.0	1.18
3.65	3.64	0.24	0.19	27.2	11.9	2005	−9.24	–	0.0	3.65	31.5	4.95
3.45	3.35	2.38	56.66	26.2	13.1	1903	−2.57	–	0.5	3.72	35.1	5.22
3.36	3.33	0.93	11.79	36.4	8.7	995	−2.24	–	0.0	3.36	41.1	3.21
3.23	3.23	0.60	0.0	32.5	5.5	1665	−2.47	–	1.2	3.99	35.3	4.55
2.86	2.79	1.07	48.90	29.3	4.5	1749	−1.69	–	0.5	4.51	34.7	5.46
2.65	2.46	4.09	67.76	41.0	12.2	2192	−2.14	–	0.4	3.59	41.8	4.20
2.77	2.77	0.45	0.0	28.4	9.8	1128	−3.32	–	0.0	2.78	34.8	3.60
2.57	2.56	0.28	0.0	29.3	7.4	1791	−6.86	–	0.8	2.90	33.4	4.32
1.49	1.48	0.35	0.0	27.7	10.8	1687	−3.01	–	0.9	2.00	33.0	4.75

The minimum distance $R_{\rm min}$ is given in terms of the virial radius at the time this distance is reached $R/R_{200}(z)$



5.8. Predicted Peak Masses for Local Group galaxies

Table 5.5: Stellar mass and peak total mass of dwarf galaxies in the Local Group

Gal. Name	$M_\star$ ($10^5 M_\odot$)	M_{peak} ($10^9 M_\odot$)	references
MW satellites			
For	245^{+96}_{-69}	$19.10^{+12.39}_{-3.38}$	1
LeoI	45^{+19}_{-13}	$7.81^{+5.21}_{-1.36}$	1
Scl	39^{+25}_{-15}	$7.24^{+5.78}_{-1.03}$	1
LeoII	$12^{+4.4}_{-3}$	$3.89^{+2.46}_{-0.73}$	1
SexI	$7.0^{+4.3}_{-3}$	$2.93^{+2.29}_{-0.38}$	1
Car	$3.8^{+2.3}_{-1.4}$	$2.12^{+1.65}_{-0.31}$	1
Dra	$5.1^{+1.5}_{-1.2}$	$2.48^{+1.45}_{-0.48}$	1
Umi	$5.3^{+3.3}_{-2.0}$	$2.53^{+1.99}_{-0.37}$	23
CanVenI	$3.7^{+0.9}_{-0.8}$	$2.09^{+1.16}_{-0.42}$	1
CraII	$2.6^{+0.4}_{-0.3}$	$1.73^{+0.86}_{-0.41}$	2,3
Her	$0.60^{+0.23}_{-0.18}$	$0.80^{+0.51}_{-0.14}$	1
BooI	$0.46^{+0.11}_{-0.09}$	$0.70^{+0.38}_{-0.14}$	1
LeoIV	$0.29^{+0.14}_{-0.09}$	$0.55^{+0.38}_{-0.09}$	1
UMaI	$0.22^{+0.08}_{-0.06}$	$0.47^{+0.30}_{-0.08}$	1
LeoV	$0.17^{+0.08}_{-0.06}$	$0.41^{+0.29}_{-0.06}$	1
PisII	$0.14^{+0.13}_{-0.07}$	$0.37^{+0.36}_{-0.04}$	7
CanVenI	$0.13^{+0.08}_{-0.05}$	$0.36^{+0.28}_{-0.05}$	1
HydII	$0.13^{+0.05}_{-0.03}$	$0.36^{+0.23}_{-0.07}$	7
UMaII	$0.065^{+0.05}_{-0.03}$	$0.25^{+0.22}_{-0.03}$	1
ComBer	$0.060^{+0.04}_{-0.02}$	$0.24^{+0.19}_{-0.04}$	1
Tuc2	$0.045^{+0.012}_{-0.01}$	$0.20^{+0.12}_{-0.04}$	5
Hor1	$0.031^{+0.008}_{-0.006}$	$0.17^{+0.09}_{-0.03}$	4
Gru1	$0.031^{+0.013}_{-0.009}$	$0.17^{+0.11}_{-0.03}$	5
DraII	$0.020^{+0.025}_{-0.011}$	$0.13^{+0.15}_{-0.01}$	6
BooII	$0.016^{+0.021}_{-0.009}$	$0.12^{+0.14}_{-0.01}$	1
Ret2	$0.016^{+0.004}_{-0.003}$	$0.12^{+0.07}_{-0.02}$	4
Wil1	$0.016^{+0.018}_{-0.008}$	$0.12^{+0.13}_{-0.01}$	1
SegII	$0.014^{+0.005}_{-0.004}$	$0.11^{+0.07}_{-0.02}$	1
TriII	$0.0071^{+0.0045}_{-0.0027}$	$0.08^{+0.06}_{-0.01}$	8
SegI	$0.0054^{+0.0063}_{-0.0029}$	$0.07^{+0.07}_{-0.01}$	1
M31 satellites			
N205	4650^{+760}_{-650}	$90.29^{+45.13}_{-20.42}$	1
M32	4760^{+1260}_{-1010}	$91.41^{+51.86}_{-18.34}$	1
N185	680^{+118}_{-100}	$32.74^{+16.58}_{-7.32}$	1
N147	990^{+164}_{-150}	$39.91^{+20.01}_{-8.86}$	1
AVII	150^{+52}_{-39}	$14.74^{+9.14}_{-2.71}$	9
AII	$40.^{+9}_{-8}$	$7.34^{+3.97}_{-1.50}$	10,14
AI	$44.^{+10}_{-9}$	$7.72^{+4.19}_{-1.57}$	9,14
AVI	$50.^{+12}_{-10}$	$8.26^{+4.55}_{-1.69}$	11
AXXIII	$11.^{+3}_{-2}$	$3.71^{+2.13}_{-0.78}$	11,14
AIII	$10.^{+3}_{-2}$	$3.53^{+2.08}_{-0.72}$	9,14
LGS3	$9.6^{+1.6}_{-1}$	$3.46^{+1.73}_{-0.83}$	1
AXXI	$5.5^{+1.9}_{-1.4}$	$2.58^{+1.60}_{-0.48}$	11,14
AXXV	$6.3^{+1.8}_{-1.6}$	$2.77^{+1.61}_{-0.52}$	11,14
AV	$5.1^{+1.3}_{-1.0}$	$2.48^{+1.39}_{-0.51}$	9,14
AXV	$2.1^{+0.8}_{-0.6}$	$1.55^{+0.99}_{-0.27}$	9,14
AXIX	$12.^{+5}_{-4}$	$3.89^{+2.58}_{-0.62}$	11,14
AXIV	$3.3^{+1.5}_{-1.2}$	$1.97^{+1.35}_{-0.29}$	9,14
AXXIX	$2.7^{+1.5}_{-0.9}$	$1.77^{+1.32}_{-0.28}$	12
AIX	$4.3^{+1.5}_{-1.1}$	$2.26^{+1.41}_{-0.42}$	9,14
AXXX	$2.2^{+0.7}_{-0.6}$	$1.59^{+0.96}_{-0.29}$	11,14

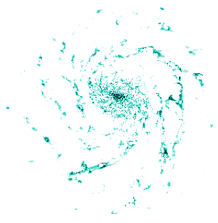
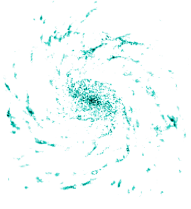


Table 5.5 – (continued)

Gal. Name	$M_\star$ ($10^5 M_\odot$)	$M_{\rm peak}$ ($10^9 M_\odot$)	references
AXXVII	$2.0^{+1.8}_{-0.8}$	$1.51^{+1.42}_{-0.21}$	11,14
AXVII	$1.7^{+0.6}_{-0.4}$	$1.39^{+0.87}_{-0.27}$	11,14
AX	$1.3^{+0.5}_{-0.3}$	$1.20^{+0.77}_{-0.23}$	9,14
AXVI	$1.1^{+0.5}_{-0.3}$	$1.10^{+0.76}_{-0.20}$	9,14
AXII	$0.85^{+0.62}_{-0.35}$	$0.96^{+0.82}_{-0.13}$	13,14
AXIII	$0.73^{+0.33}_{-0.23}$	$0.89^{+0.61}_{-0.15}$	9,14
AXXII	$0.73^{+0.33}_{-0.23}$	$0.89^{+0.61}_{-0.15}$	11,14
AXX	$0.48^{+0.22}_{-0.16}$	$0.71^{+0.49}_{-0.11}$	11,14
AXI	$0.46^{+0.22}_{-0.15}$	$0.70^{+0.49}_{-0.11}$	11,14
AXXVI	$0.31^{+0.20}_{-0.15}$	$0.56^{+0.45}_{-0.06}$	11,14
LG field dwarfs			
N6822	830^{+200}_{-170}	$36.37^{+20.06}_{-7.39}$	15,16
IC1613	1020^{+190}_{-170}	$40.55^{+20.89}_{-8.78}$	15,16
WLM	380^{+65}_{-55}	$24.08^{+12.16}_{-5.40}$	17
UGC4879	58^{+13}_{-11}	$8.93^{+4.83}_{-1.86}$	15,18
Peg	66^{+16}_{-13}	$9.56^{+5.28}_{-1.97}$	15,16
LeoA	30^{+8}_{-6}	$6.31^{+3.59}_{-1.29}$	19,16
Cet	45^{+11}_{-9}	$7.81^{+4.33}_{-1.60}$	20,16
Aqu	16^{+3}_{-2}	$4.53^{+2.34}_{-1.05}$	20,16
Tuc	$8.9^{+2.3}_{-1.9}$	$3.32^{+1.87}_{-0.66}$	1
AXVIII	$8.0^{+1.9}_{-1.6}$	$3.14^{+1.72}_{-0.64}$	9
AXXVIII	$4.1^{+5.2}_{-1.7}$	$2.21^{+2.50}_{-0.29}$	11
LeoT	$1.1^{+0.6}_{-0.4}$	$1.10^{+0.82}_{-0.16}$	1
EriII	$0.9^{+0.2}_{-0.2}$	$0.99^{+0.53}_{-0.20}$	21,22

References: The stellar masses are adopted from Fattahi et al. (2017) who derived these mostly from parameters taken from the updated (October 2015) version of the tables from McConnachie (2012) but also used parameters from other references, including the following: 1: McConnachie (2012), 2: Torrealba et al. (2016), 3: Caldwell et al. (2017), 4: Koposov et al. (2015b), 5:Walker et al. (2016), 6: Martin et al. (2016a), 7: Kirby et al. (2015), 8: Kirby et al. (2017a), 9: Tollerud et al. (2012), 10: Ho et al. (2012), 11: Collins et al. (2013), 12: Tollerud et al. (2013), 13: Collins et al. (2010), 14: Martin et al. (2016b), 15: Kirby et al. (2014), 16: Hunter and Elmegreen (2006), 17: Leaman et al. (2012), 18: Bellazzini et al. (2011), 19: Kirby et al. (2017b), 20: McConnachie and Irwin (2006a), 21: Crnojević et al. (2016), 22: Li et al. (2017).



Chapter 6

The Milky Way's Plane-of-Satellites

Hitherto we have explained the phenomena of the heavens and of our sea by the power of gravity, but have not yet assigned the cause of this power.

— Isaac Newton, Philosophiæ Naturalis Principia Mathematica

It has long been suggested that a large fraction of the dwarf satellite galaxies orbiting the MW (and also the M31 galaxy) are aligned in a thin, extended, and kinematically coherent planar structure. The presence of such a structure seems to challenge the current Cold Dark Matter paradigm of structure formation, which predicts a more uniform distribution of satellites around central objects. In this chapter I show that it is possible to obtain thin, extended, rotating plane of satellites in cosmological collisionless simulations based on the Cold Dark Matter model. I further investigate in detail their properties and their longevity. The main result of this chapter is that simulated planes of satellites resembling the one around MW or M31 are not long-lived and include a large fraction of chance aligned satellites which has recently be confirmed by the Gaia collaboration using proper motions of the classical MW satellites derived from Gaia DR2 data (Gaia Collaboration et al. 2018).

The results of this section have been published in a peer reviewed Journal (Buck et al. 2016). I am the first author of that paper and all relevant research and analysis has been performed by me.

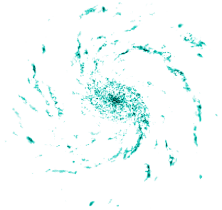
6.1. Context

Since Lynden-Bell (1976) found the first indication for a planar alignment of the classical dwarfs and stellar streams of our MW much progress in discovering further satellites and more planes of satellites has been made. Proper motion measurements showed that

many members of the MW plane share a common rotation direction and thus it has been concluded that this plane is rotationally stabilised (Metz et al. 2008; Pawlowski et al. 2013). Similarly recent observations of dwarf satellite galaxies around M31 (M31) revealed an anisotropic spatial distribution of the satellites around our neighboring galaxy (Koch and Grebel 2006; McConnachie and Irwin 2006b; Conn et al. 2013). These observations found roughly half of the satellites of M31 discovered in the PAndAS survey (McConnachie et al. 2009b) (15 out of 27) to align in a thin plane of thickness (12.6 ± 0.6) kpc with a projected diameter of ~280 kpc viewed nearly edge-on from Earth. Furthermore the analysis of the line-of-sight velocities of the satellites in the plane conducted by Ibata et al. (2013) showed that out of the 15 members in the plane 13 seem to share the same sense of rotation. Besides the plane around M31 there might be further observational indication for similar planes around other galaxies like Centaurus A (Tully et al. 2015) or M81 (Chiboucas et al. 2013) as well as NGC 3109 (Bellazzini et al. 2013) albeit much less convincing.

Many works have focussed on an explanation of the anisotropic distribution of satellites in ΛCDM (Libeskind et al. 2005; Zentner et al. 2005; Kang et al. 2005; Libeskind et al. 2009, 2011; Deason et al. 2011; Hammer et al. 2013; Wang et al. 2013; Smith et al. 2016) and found that this seems to be a common prediction. Flattened satellite distributions can arise from the filamentary accretion of substructure onto the main halo (Aubert et al. 2004; Libeskind et al. 2005) and the spatial information of the anisotropic accretion is retained in the distribution of the satellites in phase space (Libeskind et al. 2009; Lovell et al. 2011; Libeskind et al. 2011). Using the fact, that early forming haloes are more likely to reside at the nodes of intersections of dark matter filaments (Dekel et al. 2009a), Buck et al. (2015) could show that these haloes have a higher incidence of planes resembling the one around M31 with satellites in the plane being accreted onto the main halo via filaments from opposite directions.

Although anisotropies are predicted by ΛCDM due to the nature of the Cosmic Web and the presence of filaments, apparently rotating satellite distributions resembling the one around MW and M31 are not easily found in ΛCDM. An investigation by Wang et al. (2013) of the Aquarius and Millenium II simulations for satellite distributions consisting of 11 satellites similar to the one around our MW shows that 5-10% of the satellite distributions in their sample are as flat as the one around our MW. When demanding the same rotational coherence as for the MW satellites, with 8 out of 11 co-orbiting (Pawlowski et al. 2013), and using as well the Millennium II simulation, Pawlowski et al. (2014) found that only ~0.1% of the satellite systems show similar planes. The same result is found when searching for planes similar to the one around M31, consisting of 15 satellites in the plane with 13 co-rotating ones. Again using the Millennium II simulation, Ibata et al. (2014) and Pawlowski et al. (2014) found that only ~0.1% of all ΛCDM satellite systems show similar distributions as the one around M31. Recent work by Gillet et al. (2015) using hydrodynamical simulations of Local Group



analogues also found flattened satellite systems but not as rich in number as the one around M31. However, a work by Cautun et al. (2015) pointed out the large ambiguity in defining planes of satellites in terms of thickness vs. number of satellites in the plane. That work shows that, when accounting for this problem, ~10% of all ΛCDM haloes host more prominent planes compared to the Local Group.

While all of these studies focussed on either finding planes of satellites most similar to the ones observed, explaining the mechanism leading to planes of satellites or trying to quantify their occurrence, less work has been spend on investigating the actual kinematics of the planes produce by ΛCDM. The observations of the plane around M31 are so striking due to the high kinematical coherence of the satellites in the plane. The high degree of co-rotation inferred from the line-of-sight velocities makes the plane a challenge for ΛCDM. But, for the conclusion of kinematical coherence via the line-of-sight velocity, only one out of three velocity components is used. Therefore in this chapter I analyse in detail the kinematics of the satellite planes found in high-resolution cosmological "zoom-in" Dark Matter only (DMO) simulations of the ΛCDM model.

6.2. Simulations

For this work I used the suite of 21 high resolution "zoom-in" Dark Matter only simulations from Buck et al. (2015). These simulations include MW mass haloes in the mass range ($7.4 \times 10^{11} < M_{200}/[M_\odot] < 2.2 \times 10^{12}$). These values are in agreement with recent measurements of the mass of the MW or M31 from dynamical modelling the Local Group (Peñarrubia et al. 2014).

The Dark Matter haloes used in this chapter were selected from four cosmological boxes of side length 30, 45, 60 and 80 h^{-1}Mpc from Dutton and Macciò (2014), who used cosmological parameters from the Planck Collaboration (2014): $\Omega_\mathrm{m} = 0.3175$, $h = 0.671$, $\sigma_8 = 0.8344$, $n = 0.9624$. The simulations were then evolved to redshift $z = 0$ with the N-body code pkdgrav2 (Stadel 2001, 2013). Initial conditions for the "zoom-in" simulations were created using a modified version of the grafic2 package (Bertschinger 2001) as described in (Penzo et al. 2014). The refinement level was chosen to maintain a roughly constant relative resolution, e.g. $\sim 10^7$ dark matter particles per halo with particle masses of $\sim 10^5 h^{-1}\mathrm{M}_\odot$. This allows us to reliably resolve substructure down to $\sim 10^7 h^{-1}\mathrm{M}_\odot$, comparable to the expected dynamical masses of dwarf satellites in the local group (McConnachie 2012, Fig. 10). The force softening of the simulations ranges between $0.25\ h^{-1}$ kpc and $0.36\ h^{-1}$ kpc (see table: 6.1).

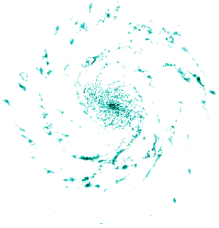


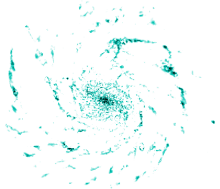
Table 6.1: Properties of the 21 high-resolution DMO simulations.

Halo	Box size [Mpc/h]	M_{200} [$10^{12} M_\odot/h$]	R_{200} [kpc/h]	c_{200}	N_{200} [10^6]	Force soft. [kpc/h]
(A)	30	0.736	146.82	13.62	8.3	0.25
(B)	80	1.003	162.78	12.03	7.6	0.29
(C)	30	1.321	178.44	11.29	10.2	0.25
(D)	60	0.890	156.45	7.65	7.3	0.25
(E)	60	0.570	134.85	8.19	6.4	0.27
(F)	60	0.831	152.88	8.69	9.4	0.25
(G)	60	0.637	139.93	4.18	7.2	0.25
(H)	60	0.813	151.78	7.19	9.2	0.25
(I)	60	0.535	132.02	17.19	6.01	0.25
(J)	60	0.907	157.41	6.93	7.5	0.27
(K)	60	0.654	141.20	5.63	7.4	0.25
(L)	60	0.872	155.37	11.63	7.2	0.28
(M)	60	0.661	141.65	7.65	7.5	0.25
(N)	60	0.626	139.12	13.30	7.1	0.25
(O)	60	0.760	148.44	9.14	8.6	0.25
(P)	60	0.864	154.90	13.93	9.8	0.25
(Q)	60	0.702	144.54	10.67	7.9	0.25
(R)	80	1.389	181.47	11.35	5.4	0.36
(S)	45	0.848	153.93	6.86	6.4	0.29
(T)	30	1.028	164.12	6.37	11.6	0.25
(U)	30	0.922	158.28	7.82	10.4	0.25

6.2.1. Halo Concentration and Formation Time

As established in Buck et al. (2015), aside from halo mass, the only other selection criteria for the haloes is the concentration, which is used as a proxy for halo formation time (Wechsler et al. 2002). The reasoning behind this correlation is, that at a fixed mass at the present time, early forming haloes are more likely to form at the nodes of intersections of a few filaments of the cosmic web, while typical haloes tend to reside inside such filaments (Dekel et al. 2009a). Therefore one then expects that, rare, early forming haloes would accrete their satellites from a few streams that are narrow compared to the halo size (see Buck et al. 2015, Figure 5), while later forming and thus more typical haloes accrete satellites from a wider angle in a less anisotropic manner (see also Libeskind et al. 2014, for redshift dependence of anisotropic accretion).

A roughly equal number of high, average and low concentration haloes is selected, where I aim at sampling the whole range of concentrations possible. Especially haloes with concentrations far offset from the main relation are selected (see left panel of Figure 1 Buck et al. 2015). The high concentration haloes have on average an offset



of about 2σ from the mean relation. This means these haloes are the rarest 2.3% of the whole population. For a random sampling of haloes, it would thus require ~ 40 simulations to recover one such rare halo. This helps to explain why previous high resolution simulations were unable to reproduce the observed properties of the planar satellite distribution: they simply did not sample enough haloes to find the rarer earliest forming ones.

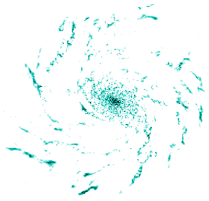
6.2.2. Satellite Selection

The substructure within the high-resolution region is identified using the AHF[1] (Knollmann and Knebe 2009), which is capable of finding sub-haloes as well as dealing with different particle masses. AHF identifies hundreds of resolved sub-haloes in the high-resolution simulations from which the actual luminous galaxies have to be chosen. Galaxy formation models robustly predict the luminous sub-haloes to be the ones most massive at infall times (Kravtsov et al. 2004; Conroy et al. 2006; Vale and Ostriker 2006). Thus, like in Buck et al. (2015), I select a sample of the 30 most massive sub-haloes at the time of the accretion via the maximum circular velocity $v_{\rm max}$. To find the maximum circular velocity at the time of accretion for every satellite in the simulations I use a fitting formula from Anderhalden et al. (2013, see their formula A.2). With this formula, the maximum circular velocity at the time of accretion can be estimated from the present day value and the orbital energy of the satellite.

For this analysis I decided to choose a more physical volume instead of modeling the PAndAS (McConnachie et al. 2009b) footprint, and thus restrict ourselves to sub-haloes within the virial radius of the host halo (~ 250 kpc) at the present time. Following the observations, I exclude satellites within the innermost 30 kpc. Selection of the 30 most massive satellites at the infall time results in present day satellite masses in the range ($4.4 \times 10^7 < M_{200}/[M_\odot] < 1.5 \times 10^{10}$). I select a number of 30 satellites instead of 27 like it is the case for the plane around M31 for two reasons: First, the number of 27 satellites around M31 results from the number of dwarf galaxies found only in the PAndAS footprint but there are 9 additional satellites of M31 known (Ibata et al. 2013, see their Fig. 1). Second, since the analysis of Ibata et al. (2013), there have been 3 more satellites found around M31 with the Pan-STARRS1 3π survey (Martin et al. 2014). So, to model the right number of satellites around M31 I would need to select either 36 or even 39 satellites, but to stay consistent with the amount of satellites used to find the plane I chose 30. I also identified planes for a number of 27 satellites and found that neither the thickness nor the number of satellites in the plane changes significantly.

Selecting host haloes of different concentrations might have an effect on the properties of the associated satellites. Namely leading to a more concentrated, more

[1] http://popia.ft.uam.es/AHF/Download.html



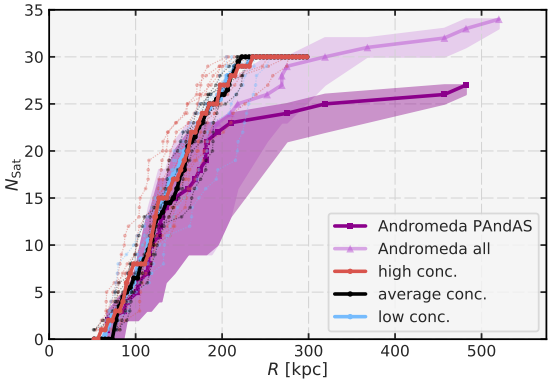
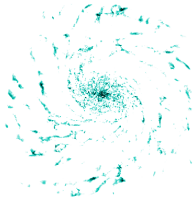


Figure 6.1: The present day cumulative radial distribution of the 30 most massive satellites at infall time. Colored lines show the median of the different concentration samples as indicated in the legend. The whole sample is shown as light colored lines. The dark purple line indicates the cumulative radial distribution of the satellites around M31 within the PAndAS footprint with the shaded area marking the measurement uncertainty. The light purple line plus shaded area shows the same when including several known satellites outside the PAndAS survey area.

compact radial distribution of satellites in high concentration haloes compared to the ones in low concentration haloes. However, this is not the case for the satellite samples. There is no indication that high concentration haloes have on average a different radial distribution, compared to low and average concentration haloes or the observed satellites of M31. In fact, the satellites of the haloes in the different samples show the same mean radius of ~ 130kpc. Figure 6.1 shows the present day cumulative radial distribution of the 21 satellite samples together with the observations plotted in yellow and green (Conn et al. 2012; McConnachie 2012). The yellow/green shaded area marks the measurement uncertainty by using the maximal and minimal radius of every satellite given by the measurement uncertainties of their distance. The red, black and blue lines show the median radial distribution of the three sub samples of high, average and low concentration haloes. This figure reveals that the selection of the 30 most massive satellites at infall time results in satellite samples occupying radii between ($75 \lesssim R/[\mathrm{kpc}] \lesssim 250$) in agreement with the observed radial distribution of the 27 satellites around M31 up to a radius of ~ 200 kpc. Inclusion of two satellites at radii of about $r \sim 400$kpc into the observational sample leads to the fact that the cumulative radial distribution extends far further out and deviates from the simulated distribution at large radii. Comparison to the green line which includes known satellites around M31 not falling within the PAndAS footprint (IC10, A7, A28, A29, A6, IC1613, LGS3) shows that the discrepancy between observations and simulations might be due to the PAndAS footprint not covering the whole virial radius of M31. A two sample Kolmogorov-Smirnov test on the median cumulative radial distribution of satellites of the different concentration samples shows with a p-value of 0.999 that the these samples are drawn from the same distribution. Thus there is no indication that high concentration haloes posses a more concentrated satellite distribution.



6.2.3. Plane Finding Algorithm

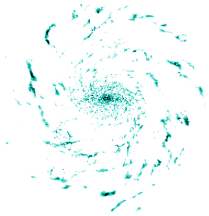
At $z = 0$, I apply a plane finding algorithm (as described in Buck et al. 2015; Gillet et al. 2015; Ibata et al. 2014; Conn et al. 2013) to the 30 most massive satellites at infall time, with the goal of identifying planes of satellites similar to the observed ones. In order to find planes in the distribution of sub-haloes I generate a random sample of planes defined by their normal vector. All planes include the center of the main halo but we exclude satellites closer to the main halo center than 30 kpc. To uniformly cover the whole volume I generate 100,000 random planes with a fixed thickness of $2\Delta = 30h^{-1}$ kpc. After specifying a plane I calculate the distance of every satellite to this plane. A satellite is considered to lie in the plane if its distance to the plane is smaller than Δ. For each plane I calculate the number of satellites in the plane and its thickness $\Delta_{\rm rms}$ as the root-mean-square value of the satellites distances to the plane's mid-plane. I then select for every number of satellites in the plane the one which is thinnest and richest to analyse for kinematics.

The plane of satellites around M31 can be characterized by 4 parameters including the number of satellites in the plane ($N_{\rm in}$), the number of co-rotating satellites ($N_{\rm corot}$), the thickness of the plane ($\Delta_{\rm rms}$, defined as the root-mean-square distance of satellites from the plane) and its extension on the plane of the sky ($\Delta_{\parallel}$). I define $\Delta_{\parallel}$ as the root-mean-square value of the distance of the satellites in the plane from the halo center when projected on the plane of the sky. For M31 these values are $N_{\rm in} = 15$, $N_{\rm corot} = 13$, $\Delta_{\rm rms} = 12.6 \pm 0.6$ kpc (Ibata et al. 2014) and $\Delta_{\parallel} = 91.2^{+6.2}_{-11.7}$, calculated from the data given by Conn et al. (2012); McConnachie (2012).

In the progress of this chapter I will investigate the number of co-rotating satellites. This will be done for two different measures of co-rotation. Assuming the plane of satellites lies in the $x - z$ plane (compare Figure 6.3), then when using the line-of-sight velocity as a proxy for co-rotation, like it is done in the observations, the number of co-rotating satellites is the maximum of counting all the satellites with x-position smaller than zero and line-of-sight velocity greater than zero and adding all the satellites with x-position greater than zero and line-of-sight velocity smaller than zero or doing the opposite. When co-rotation is inferred using the angular momentum vectors of the satellites the number of co-rotating satellites is the maximum of the number of satellites with positive z-component of the angular momentum vector or negative z-component.

6.2.4. Distribution of Plane Parameters

When applying the plane finding algorithm to the selected satellite samples from the simulations I obtain a variety of different planes characterised by different combinations of plane parameters. For example, it is possible to obtain different planes with the same number of satellites in them but with totally different thicknesses. This is shown



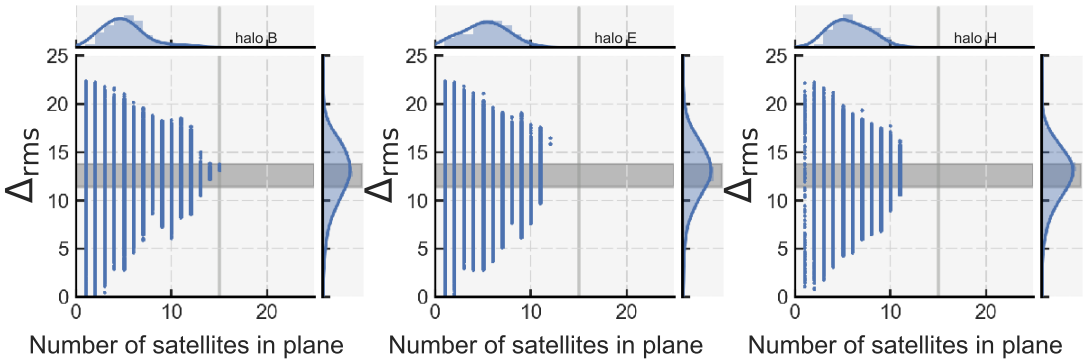
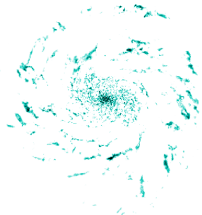


Figure 6.2: The distribution of plane parameters for a particular number of satellites in the plane N_{in} and the rms value, Δ_{rms}, of the associated plane. The *top marginal histogram* shows the cumulation along the y-axis, and the *right marginal histogram* shows the cumulation along the x-axis. The solid blue line in the marginal plots shows a kernel density estimation of the probability distribution function. The *grey line* shows a value of 15 satellites in the plane and the grey shaded area shows the measurement uncertainty of $\Delta_{\text{rms}} = 12.6 \pm 0.6$ kpc of the observed thickness of the plane around M31. The *left panel* shows a high concentration halo, the *middle panel* an average concentration halo and the *right panel* shows a low concentration halo.

in figure 6.2 for three examples haloes. This figure shows a scatter plot of the plane parameters obtained. For every number of satellites in the plane, N_{in}, the root-mean-square value for the plane thickness, Δ_{rms}, is plotted. Each halo in figure 6.2 shows a large diversity of planes. This plot is indicative of the fact that there is no uniquely defined plane. For a given number of satellites in the plane there exist a variety of possible thicknesses. And furthermore it is not clear if choosing one satellite less in the plane and thus decreasing its thickness is *better* than choosing a higher number of satellites in the plane. Therefore it is a priori difficult to decide or to define which ones of the planes should be taken as the *best* plane. I like to mention, that except for one low concentration halo only high concentration haloes host planes which contain more than 13 satellites. This problem was also investigated by Cautun et al. (2015), who introduced the *prominence* of a plane, the inverse probability of obtaining by chance a plane of given number of satellites with a thickness thinner than some predefined value. Cautun et al. (2015) used the *prominence* to decide which plane is the *best* to choose. However, for this work I decided to choose the *best* plane for a given halo by a slightly simpler criteria. I choose the plane with the highest number of satellites as the *best* plane. If there are two of such planes for a given halo I choose the thinner one of these planes as the *best* plane.

Figure 6.3 shows a visual impressions of some of the planes found by this algorithm. Satellites in the plane are shown as colored dots with the color indicating the sign of the line-of-sight velocity and arrows in each plot indicate the other two velocity



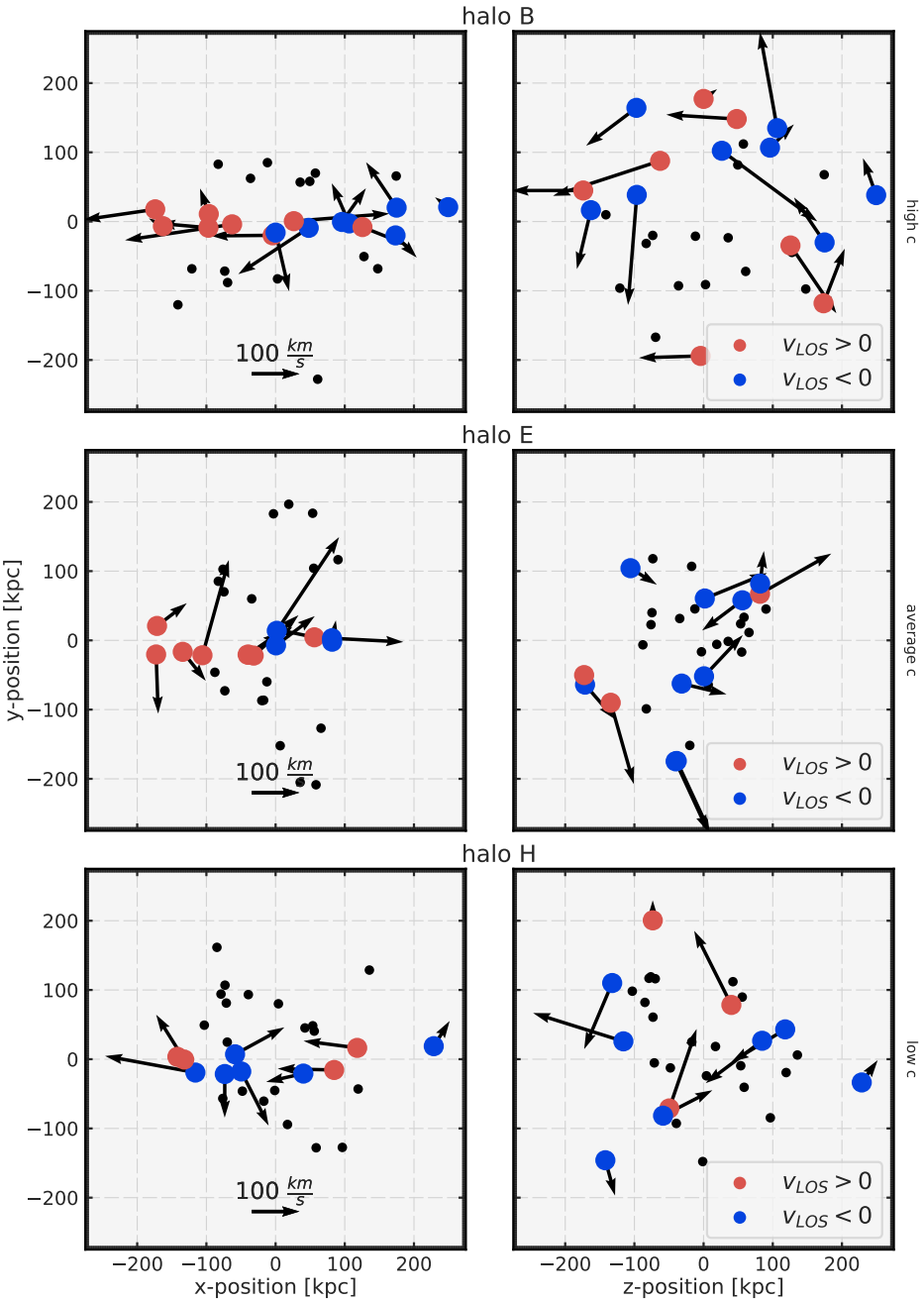
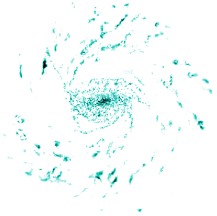


Figure 6.3: A visual impression of the planes. The *left panels* show the planes in edge-on view, while the *right panels* show the planes in face-on view. The colored dots show satellites in the plane with the color indicating the line-of-sight velocity (blue approaching, red receding), where the line-of-sight is chosen to be perpendicular to the plane of the plot (left panels: along the z-axis, right panels: x-axis). Black dots show the satellites that lie outside the plane. *Arrows* indicate the velocity perpendicular to the plane (left panels) and in the plane (right panels). The *top row* shows a high concentration halo (halo B), the *middle row* an average concentration halo (halo E) and the *bottom row* shows a low concentration halo (halo H).

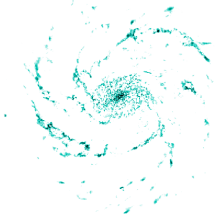


components. In this way, the kinematical coherence of the planes inferred from the line-of-sight velocity is immediately visible by eye. For example, the upper right panel clearly shows a plane which appears to be rotating to some degree, whereas a look at the edge-on view shows that at least 3 satellites (~20%) have a very high velocity component perpendicular to the plane. This means these satellites are likely to be chance alignments, which will quickly leave the plane. Nevertheless, this plane shows similar features compared to the M31 plane of satellites with 15 satellites in the plane and 13 co-rotating ones. Looking at the face-on view (right panel), it also shows a high degree of lopsidedness, with nearly all of the satellites on one side of the host center (more satellites on the upper half of the plot). The projected radial rms value parallel to the plane is ~ 127 kpc, higher than the calculated value for M31 (compare sect. 3.1). The other planes in this figure do not only have less satellites in the plane but also show less coherent spatial and kinematical planes. The two lower right panels do not show rotating planes, and the corresponding edge-on views in the left panels show a higher fraction of satellites with high velocity components perpendicular to the plane.

6.3. Spatial Analysis of Planes

6.3.1. Plane Thickness vs Halo Concentration

The most fundamental properties of the planes are its thickness, $\Delta_{\rm rms}$, its radial extension, $\Delta_{\parallel}$ and the number of its constituents, $N_{\rm in}$. As reported in Buck et al. (2015), the thickness of the plane correlates with the concentration of the host halo. High concentration haloes tend to have thinner planes. One could imagine that this might be due to a more concentrated satellite sample but as figure 6.1 shows the radial distribution of satellite samples of high concentration haloes is the same as for the other two samples and comparable to the observed one. The fact that high concentration haloes show similar planes compared to the observed one can also be seen as well in the left panel of figure 6.4, which shows a comparison of the root-mean-square thickness of the plane with its parallel root-mean-square value, calculated as the rms of the radial distances to the main halo center. The corresponding value for M31 calculated by Ibata et al. (2013) is indicated by a blue star. The value estimated by Pawlowski and Kroupa (2014) for the parallel rms of the M31 plane without the furthest satellite AndXXVII ($r > 400$kpc) is shown as a blue triangle to give an impression of the uncertainty of the parallel rms value. The grey shaded area indicates a nominal uncertainty range for the parallel and perpendicular rms value resulting from the two values given for the parallel rms value and the 1σ measurement uncertainty of 0.6 kpc for the perpendicular rms value. Values for the M31 analogue simulations of Gillet et al. (2015) are shown as green stars.



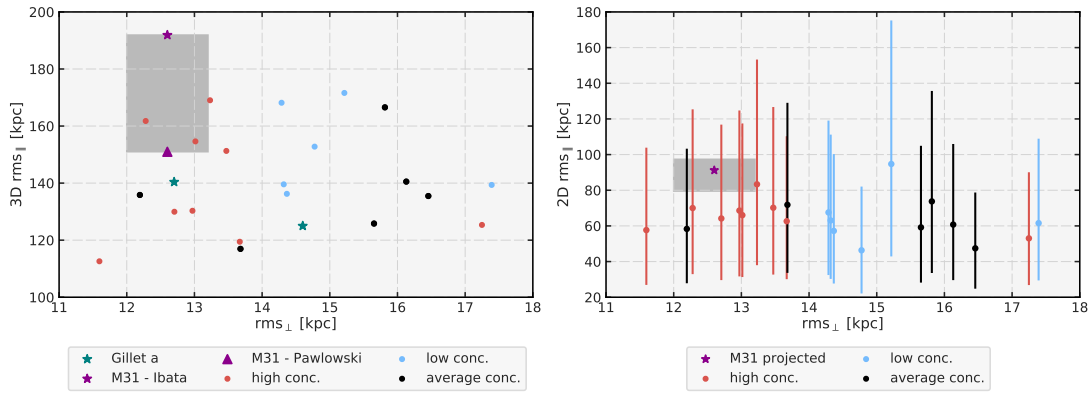
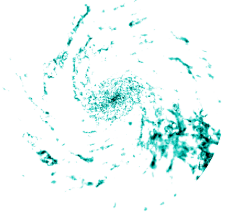


Figure 6.4: *Left panel*: The minimal root-mean-square thicknesses parallel and perpendicular to the richest planes found, color-coded by halo concentration. The values for M31 are indicated by the *purple triangle* (Pawlowski and Kroupa 2014) and the *purple star* (Ibata et al. 2013), with the grey shaded area indicating a nominal uncertainty of the perpendicular rms value of (12.6 ± 0.6) kpc and the parallel rms calculated by the difference of the two values given in the literature. The values obtained by Gillet et al. (2015) for their two M31 analogues are plotted in teal. *Right panel*: The projected 2 dimensional root-mean-square thickness parallel and perpendicular to the richest plane found, color-coded by halo concentration. The value for M31 is indicated by the *purple star* where the grey shaded area indicates the measurement uncertainties. For the perpendicular rms value this is given by (12.6 ± 0.6) kpc and for the parallel one the value is $\Delta_{\parallel} = 91.2^{+6.2}_{-11.7}$ kpc (this is the extension of the plane when projected on the plane of the sky), where the uncertainty is given by calculating the projected rms value with the upper and lower limit of the radial distance of each satellite from M31. The error bars of the simulated satellite planes indicate the range of possible values if different viewing angles for the projection of the edge-on plane are chosen.

The planes found in the simulations span a range from ∼ 12 kpc to ∼ 17 kpc in perpendicular rms and a range of ∼ 110 kpc to ∼ 170 kpc in parallel rms extension, comparable to the observed plane around M31 and the planes found by Gillet et al. (2015). However, the thinnest planes are only found to be associated with the highest concentration (red dots) haloes, and hence the earliest forming haloes, while low and average concentration haloes show slightly thicker planes compared to high concentration haloes and the observations.

One can clearly see that the planes in the simulations do not show the same high radial root-mean-square value as observed by Ibata et al. (2013) around M31. But this is no major problem since the root-mean-square value can be biased by outliers with very large radial distances from M31, such as the satellite AndXXVII with radial distance further away from the center of M31 than 400 kpc (larger than the virial radius of M31 and the simulated haloes). Excluding AndXXVII, the radial rms drops significantly from 191 kpc to 150 kpc. Therefore, it might be more meaningful to compare the



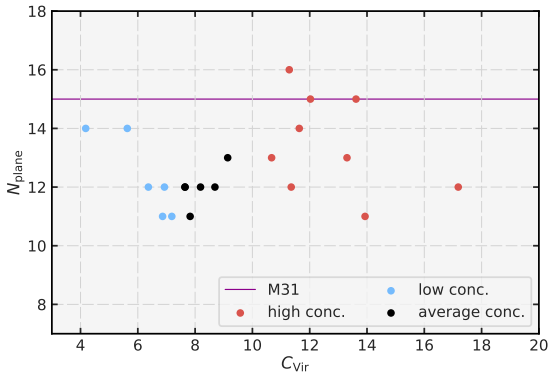


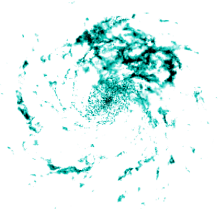
Figure 6.5: The maximum number of satellites in the plane as a function of the concentration. The color-coding divides the haloes into high (red), average (black) and low (blue) concentration haloes. The *purple line* shows the value of 15 satellites in the plane obtained for M31.

two-dimensional rms value of the radii of satellites in the plane as projected on the sky, as this is the actual observed value.

The right panel of figure 6.4 shows the 2-dimensional root-mean-square thickness parallel and perpendicular to the richest planes found when projected on the plane of the sky. The mean values of planes for individual haloes are shown as dots, color-coded by halo concentration. In comparison to the radial root-mean-square value shown in the left panel of figure 6.4 these values are in better agreement with the observed value and most of the high concentration haloes are consistent with the observed values. Furthermore when comparing the simulations to the observations one has to keep in mind that the observations include satellites obviously outside the virial radius of M31 which biases the 3-dimensional root-mean-square value of the observations high compared to the simulations where this selection was not applied. For example, the 3-dimensional root-mean-square extension of the plane including all 15 satellites is $\Delta_{\parallel} = 191.9$ kpc, excluding the 2 satellites outside the virial radius of M31 (AXVI, AXXVII) the value drops to $\Delta_{\parallel} = 129.6$ kpc. In contrast to that, the projected 2-dimensional rms extension of the plane is less effected by this selection ($\Delta_{\parallel 3d} = 96$ kpc vs. $\Delta_{\parallel 2d} = 97$ kpc)

6.3.2. NUMBER OF SATELLITES IN THE PLANE

As was shown in Buck et al. (2015) and can be seen from figure 6.4, for a given number of satellites in a plane, the thickness of the plane correlates with the concentration of the main halo. Furthermore from figure 2 of Buck et al. (2015) it is obvious that the thickness of the plane is also strongly dependent on the number of satellites in it. Together with the results from figure 6.4 in the previous section the question arises whether, for a given maximum root-mean-square thickness, the number of satellites in the plane correlates with the concentration as well. Figure 6.5 shows the maximum number of satellites in a plane as a function of the concentration which shows, that there is, if at all, only a weak trend with concentration with an overall maximum



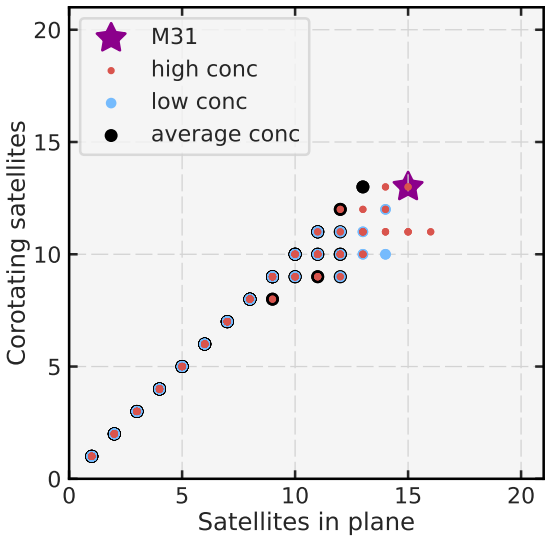


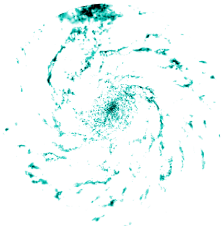
Figure 6.6: The maximum number of co-rotating satellites vs. the number of satellites in the plane, color-coded by halo concentration. The big purple star shows the observed values of M31's plane with 15 satellites in the plane and 13 co-rotating ones. Big black dots show values for planes found in average concentration haloes, middle blue dots show the same for low concentration haloes and small red dots show the results for high concentration haloes.

number of about 12 to 13 satellites in a plane, with just three high concentration haloes reaching a satellite count in the plane as high as that observed for M31. But most importantly by showing that high concentration haloes have the same or even higher numbers of satellites in their planes compared to the other planes, this plot confirms that high concentration haloes have indeed thin planes. The thinner planes in high concentration haloes compared to low or average concentration haloes are not due to a more concentrated satellite distribution (as discussed in section 2.2) nor to a lower number of satellites in the plane or to a smaller virial radius of the high concentration haloes. Rather, high concentration (and thus earlier forming) haloes seem to produce genuine thin planes.

6.4. Kinematic Analysis of Planes

6.4.1. Kinematics of the Planes from the line-of-sight Velocities

In order to investigate the co-rotation of the planes obtained from the plane finding algorithm, for every possible number of satellites in the planes, $N_{\rm in}$, I calculate the number of co-rotating satellites, $N_{\rm corot}$. For this purpose, like for the observations, I use the sign of the line-of-sight velocity in an edge-on view as a proxy for the co-rotation. Figure 6.6 presents the results for all main haloes in our sample. Many of the haloes give the same result leading to filling the same points in the diagram. Up to values of about 10 satellites in the plane, there are viewing angles from which the plane looks



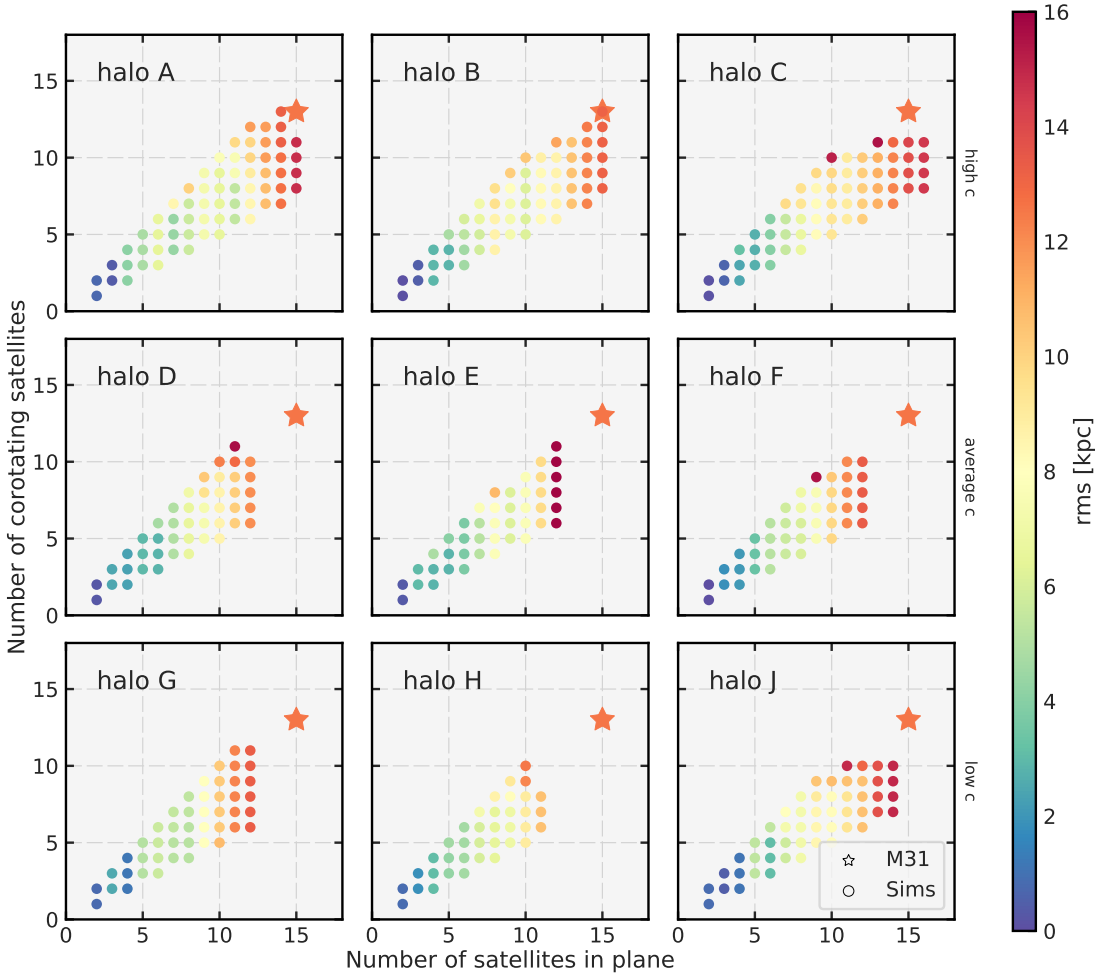
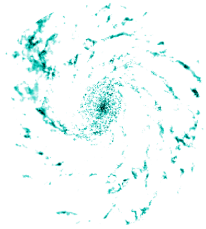


Figure 6.7: The number of co-rotating satellites vs. the number of satellites in the plane for a selection of haloes. The points are color coded by the rms thickness ($\Delta_{\rm rms}$) of each plane. The *star* marks the values observed for M31 (15 in the plane, 13 co-rotating). The *dots* show the values of different planes found per simulated halo. The *top row* shows the high concentration haloes, the *middle row* the average concentration haloes and the *bottom row* the low concentration haloes. The dashed grey lines show the physical limits of 100% and 50% co-rotation respectively.

like a fully rotating one (with 100% co-rotating). Interestingly, there is only a slight correlation between the number of co-rotating satellites and the halo concentration. And as was found before, there is no clear dependence of the absolute number of satellites on the halo concentration. There is quite wide scattering among haloes of the same concentration, but again, only high concentration haloes exhibit the highest numbers of satellites in their planes and the highest number of co-rotating satellites.



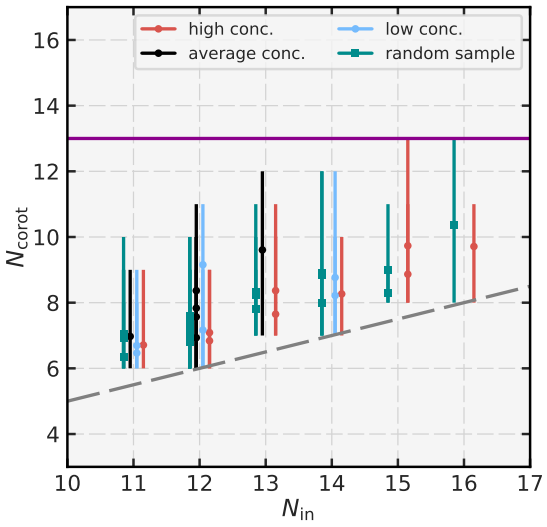
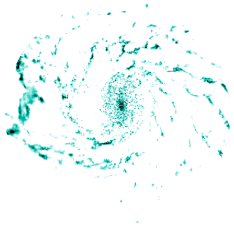


Figure 6.8: The number of co-rotating satellites counted via the los velocity vs. the number of satellites in the plane. I show the mean value averaged over the full range of viewing angles (180 steps in 1°) together with the minimum and maximum value (errorbars). Dots show the different haloes and teal squares show the result when randomising the velocities of the satellites. The points are slightly offset for better visibility. The *purple line* shows the value of 13 co-rotating satellites measured for M31. The gray dashed line shows the minimum co-rotation fraction of 50%.

Despite haloes with very high inferred co-rotation fractions the plane finding algorithm also returns planes which have a much lower inferred co-rotation fraction. To provide a better overview over the possible plane configurations, figure 6.7 shows the outcome of the plane finding algorithm for a selection of 9 haloes of different concentrations. For every value of the number of satellites in the plane $N_{\rm in}$, the plots show the number of co-rotating satellites, $N_{\rm corot}$. Every dot in the plot represents a different plane. The points are color-coded according to the thickness of the plane $\Delta_{\rm rms}$. This plot is summarising the key parameters of the planes ($N_{\rm in}$, $N_{\rm corot}$ and the thickness $\Delta_{\rm rms}$), and it shows again that there is some arbitrariness in selecting the best plane. In particular, it shows that for a given number of satellites in the plane, there is always a plane or viewing angle for which there is no kinematic coherence (50% co-rotating). As it was concluded from the previous plot, for all of the haloes one can find planes with up to about 10 members that have a 100% co-rotating fraction. As would be expected, planes consisting of more satellites tend to be thicker. The thickness of the plane, to first order, is also independent of the co-rotation fraction, except for at the highest values of co-rotation fractions.

A comparison between haloes of different concentrations reveals that only high concentration haloes show planes comparable to the observed ones (see also Figure 6.6), with 15 satellites in the plane and a comparable high co-rotation fraction while at the same time showing a similar low thickness. Haloes from the average or low concentration sample fall short in number of satellites in the plane with only about 12 satellites in the plane. Furthermore these haloes show at fixed number of satellites in the plane thicker planes compared to the high concentration sample.



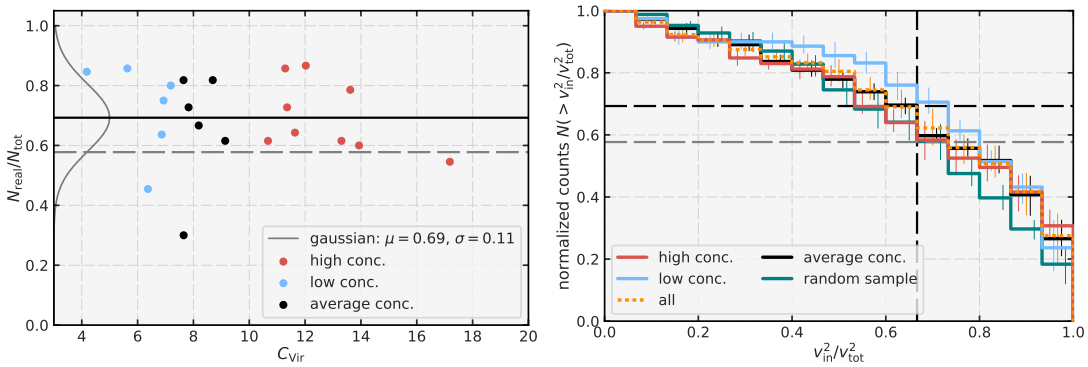
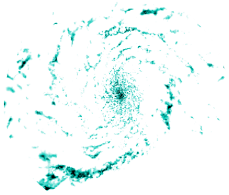


Figure 6.9: *Left panel*: The fraction of satellites kinematically bound to the plane, color-coded by concentration. The selection criteria for the satellites to be kinematically confined in the plane is the ratio of the velocity component in the plane to the total velocity: $v^2_{plane}/v^2_{tot} > \frac{2}{3}$. The solid black line indicates the mean value of $(69 \pm 11)\%$ bound satellites and the dashed gray line shows the expectation of 57.7% from a sample of satellites with randomised velocities. *Right panel*: Cumulative probability distribution of v^2_{plane}/v^2_{tot} for the high, average and low concentration sample (red, black, blue lines) as well as the whole sample of haloes (yellow line) and the same sample with randomised velocities (teal line). The black dashed lines show the expectation for $v^2_{plane}/v^2_{tot} > 2/3$ of $(69 \pm 11)\%$ and the gray dashed line shows the value of 57.7% expected for a random sample. The errorbars are slightly offset from each other for better visibility.

6.4.2. Number of co-rotating Satellites for different Viewing Angles

Once a plane is identified there are many possible line-of-sights view the plane edge-on. Thus I am interested in inferring the co-rotation for the same plane from different viewing angles by rotating it around its normal vector and measure the number of co-rotating satellites via the sign of the line-of-sight velocity. Since the line-of-sight velocity represents only one component of the three-dimensional velocity of the satellites on their orbit around the halo centre I expect a dependence on particular viewing angles. If the planes were fully co-rotating with satellites on circular orbits, there should be no dependence of the line-of-sight co-rotation fraction on the viewing direction. Thus, when rotating the plane around the normal vector, the line-of-sight count of co-rotating satellites should not vary. But the orbits of the satellites are not perfect circles and additionally there could be interlopers in the plane that only align with it by chance. Therefore the line-of-sight velocity count should depend on the exact viewing direction. Figure 6.8 shows the number of co-rotating satellites counted via the line-of-sight velocity as a function of the number of satellites in the plane. I show in this plot the mean value of co-rotating satellites together with the minimum and maximum value obtained. The first thing to notice is that there is quite a large variation in the number of co-rotating satellites as the viewing angle changes. The



mean number of co-rotating satellites is around 7 to 10 (60% co-rotation fraction) with a scatter of about 2 to 3. Really high co-rotation fractions are only reached at some peaks of special viewing angles and in only about 10% of all viewing angles a high value of co-rotating satellites is reached.

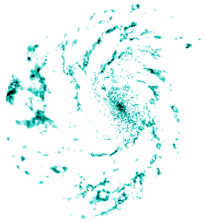
I recover that high concentration haloes have higher numbers of satellites in the plane and thus reach higher co-rotation fractions. But even these haloes do not exhibit fully rotating planes. The reason for the large variance in co-rotation fractions is that the planes seem to be not fully kinematically coherent structures but include a significant amount of interlopers, which have just joined the plane coincidentally. This can be concluded from doing the same analysis but randomising the velocities of satellites in the plane of the hosts. The line-of-sight counting of co-rotating satellites for a random sample exhibits the same features (mean number, scatter) as obtained for the simulated planes. Therefore I conclude that inferring the kinematical coherence of the plane from only a measurement of the line-of-sight velocity is not robust, even a sample of satellites with random velocities can appear as apparently rotating as figure 6.8 shows.

The conclusion of a significant fraction of interlopers in the plane is further supported if one compares the 2-dimensional velocity component in the plane $v_{\text{in plane}}$ to the total velocity v_{tot} of satellites. Assuming, the plane normal points in the z-direction, one obtains:

$$v_{\text{plane}} = \sqrt{v_x^2 + v_y^2} \qquad v_{\text{tot}} = \sqrt{v_x^2 + v_y^2 + v_z^2} \tag{6.1}$$

If the motion of satellites would be fully random and isotropic, one would expect every velocity component to have the same magnitude and the above comparison would result in $v^2_{\text{plane}}/v^2_{\text{tot}} = 2/3$. However this is obviously not the case for a ΛCDM cosmology where satellite orbits show some kind of ordered motion. Nevertheless, the isotropic case can be used to discriminate between ordered motion in a plane and unordered motion. Therefore I use this analysis to estimate the fraction of satellites rotating in the plane. If $v^2_{\text{plane}}/v^2_{\text{tot}} < 2/3$, the velocity component perpendicular to the plane is higher than in a random and isotropic case and the satellite can be regarded as not taking part in the motion in the plane. Vice versa, if $v^2_{\text{plane}}/v^2_{\text{tot}} > 2/3$, the 2-dimensional velocity component in the plane is higher than in the random and isotropic case, and the satellite‘s motion can be regarded as motion in the plane. For a sample of satellites with random velocities one would then expect that 57.7% would fulfil the above criteria. This can be estimated from the area of a spherical cap of height $(1/3)^{0.5}$ divided by the area of a hemisphere if one assumes the velocity components to be points on the surface of a sphere.

The left panel of figure 6.9 shows the fraction of satellites belonging to the plane if the above criteria is used to discriminate between kinematic members and

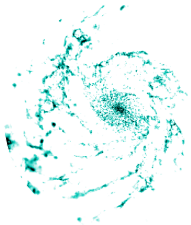


interlopers as a function of concentration. The simulations show a fraction of ~30% interlopers or vice versa a fraction ~70% of the satellites being kinematically bound to the plane according to the above criteria with no much difference between the high and low concentration haloes. This fraction is significantly higher then expected for a random sample and thus implies that ΛCDM produces some degree of motion in a plane although not all the satellites are necessarily confined to the plane. These results are in agreement with the findings of Gillet et al. (2015), who find a fraction of about 1/3 of the satellites to be interlopers. This conclusion is also supported by the analysis of the angular momentum vectors of the plane members presented in the next subsection as well as the analysis of the past orbits of the satellites making up the plane at the present time.

The right panel of figure 6.9 shows the cumulative probability distribution function for $v^2_{\rm plane}/v^2_{\rm tot}$ for both ΛCDM haloes (yellow line) and a random sample (green line). The random sample is created from the ΛCDM sample by randomising the velocities and keeping the other parameters of the satellites fixed. Comparison of both samples shows that there is a trend for ΛCDM to prefer rotation in a plane with slightly higher probabilities for values of $v^2_{\rm plane}/v^2_{\rm tot} > 0.5$ compared to the values for the random sample. Although for intermediate values of $v^2_{\rm plane}/v^2_{\rm tot}$ there is a difference apparent between the individual concentration samples, they are consistent within their error bars. The difference might be mainly due to a smaller number of satellites in the plane for low concentration haloes.

6.4.2.1. Angular Momentum Analysis

In the previous analysis of the planes we closely followed the methods used to quantify the co-rotation of the plane of satellites around M31. Thus, only a one-dimensional measure of the kinematical coherence of the plane, the line-of-sight velocity, has been used. In order to capture the motion of the satellites in the full 3-dimensional case, and not only as a projection by counting the number of co-rotating satellites by their line-of-sight velocity, I measure the angular momentum vector of each satellite in the plane and compare its direction to the direction of the plane normal and the mean angular momentum vector of all the satellites in the plane (mean orbital pole). For this analysis, the plane normal vector is set to $(\phi, \theta) = (0, 0)$ in spherical coordinates as seen from the halo center. The angular momentum vector of the satellites that are fully orbiting counter-clockwise in the plane should point in the same direction as the plane normal, while for clockwise orbiting satellites the angular momentum vector is pointing in the opposite direction, hence to $(\phi, \theta) = (-180, 0)$ or $(\phi, \theta) = (180, 0)$. Therefore, the main difference between the co- and counter-rotating satellites is the direction of their angular momentum vectors. Satellites that are not orbiting within the plane show a deviation in the directions of their orbital poles from the plane normal.



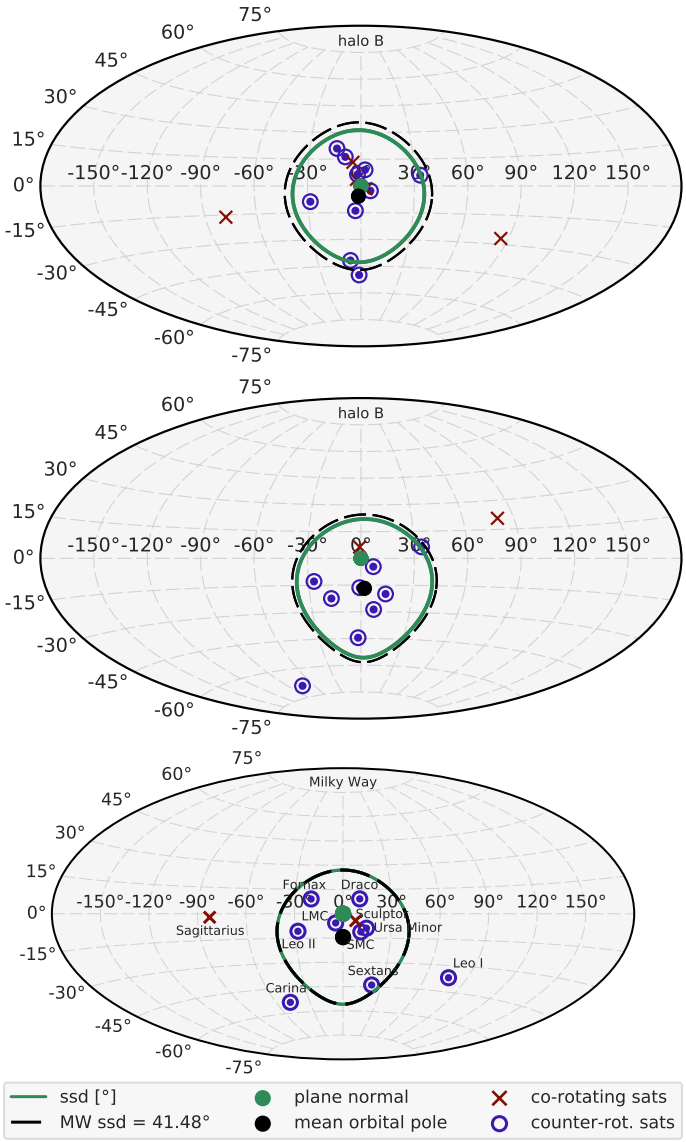
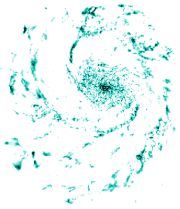


Figure 6.10: A Hammer-Aitoff projection of the orbital poles of the satellites. *The Upper panel* shows the satellites in the plane of halo B, the *middle panel* shows the 11 most massive satellites of halo B and the *lower panel* shows the 11 classical MW satellites with known proper motions (table 2, Pawlowski et al. (2013)). The *green dot* shows the direction of the plane normal and the color-coded symbols show the orbital poles of the co-rotating (red crosses) and counter-rotating (blue circles) satellites, respectively. Since angular momentum vectors are axial quantities, I invert the angular momentum vectors of clockwise orbiting satellites to scatter around $\phi = 0°$ rather than $\phi = \pm 180°$ and show them as blue circles with a dot in order to provide a better comparison of the clustering of orbital poles around the plane normal. The orbital poles for counter-clockwise rotating satellites are kept fixed and are shown as red crosses. The *green solid line* shows the spherical standard distance calculated from *all* the satellites in the plane with the *black dot* showing the average orbital pole of all of the satellites. For all the MW satellites I obtain a value of ssd=41.5° which is shown with a *black dashed line*.



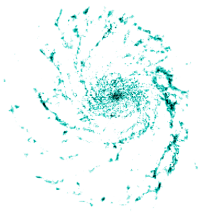
A similar study was done by Pawlowski et al. (2013) for the 11 classical MW satellites. This study revealed that the angular momentum vectors of 8 of these satellites are clustered. One measure of the clustering of orbital poles is given by the spherical standard distance of the orbital poles. The spherical standard distance is the scatter of the orbital poles in spherical coordinates (see Pawlowski et al. (2012) for a definition of their ssd). Pawlowski et al. (2013) obtained a value of ssd=29.3° for the 8 most clustered MW satellites. I decide to include all the 11 satellites into the analysis and use a slightly different definition of the ssd given by the following formula:

$$\mathrm{ssd} = \sqrt{\frac{\sum_{i=1}^{k} \left[\arccos\left(|\langle \boldsymbol{n} \rangle \cdot \boldsymbol{n}_i|\right)\right]^2}{k}}, \tag{6.2}$$

where $\boldsymbol{n}_i$ are the angular momenta vectors of the satellites and $\langle \boldsymbol{n} \rangle$ is the mean angular momentum vector of the satellites in the plane (calculated before inverting them). The difference to Pawlowski et al. (2013) is that I take the absolute value of $|\langle \boldsymbol{n} \rangle \cdot \boldsymbol{n}_i|$ and I choose to include all 11 satellites instead of only 8. I reproduce their figure 1 from the values given in table 2 of their paper and present it in the lower panel of figure 6.10 with my color coding convention. Calculation of the spherical standard distance for all 11 MW satellites with our formula gives a value of ssd=41.5°, somewhat higher than for the 8 most clustered ones with ssd=29.3°. The same figure also shows a visual comparison between the distribution of orbital poles of the satellites in the plane using my plane finding algorithm (upper panel) and using my plane finding algorithm only on a sample of the 11 most massive sub-haloes at infall time (middle panel). There is not much difference between the two different selection methods when comparing the distribution of orbital poles. The ssd is almost the same for both cases and compares well to the MW plane. Therefore I focus only on the planes discussed before.

There is a large degree of scattering in the angular momentum directions around the direction of the plane normal, indicating non-ordered motion. If the planes were indeed to some degree rotating structures as the line-of-sight velocity measurement would indicate, more or less all of the angular momentum directions would cluster near the plane normal direction at $(\phi, \theta) = (0, 0)$. This is indeed true for some of the satellites but a significant amount of satellites shows a large offset from the plane normal/mean orbital pole. To quantify this behaviour I show in figure 6.11 the distribution of the angle between the orbital poles of the satellites and the plane normal (left panel) and the mean orbital pole (middle panel) for all 21 hosts. In figure 6.12 I show the distribution of spherical standard distances for all of the host haloes in comparison to a sample with randomised velocity vectors.

The left panel of figure 6.11 shows that there is not much difference between the planes found in the haloes of different samples but a strong difference between the ΛCDM haloes and the random sample. All ΛCDM samples show a trend for the



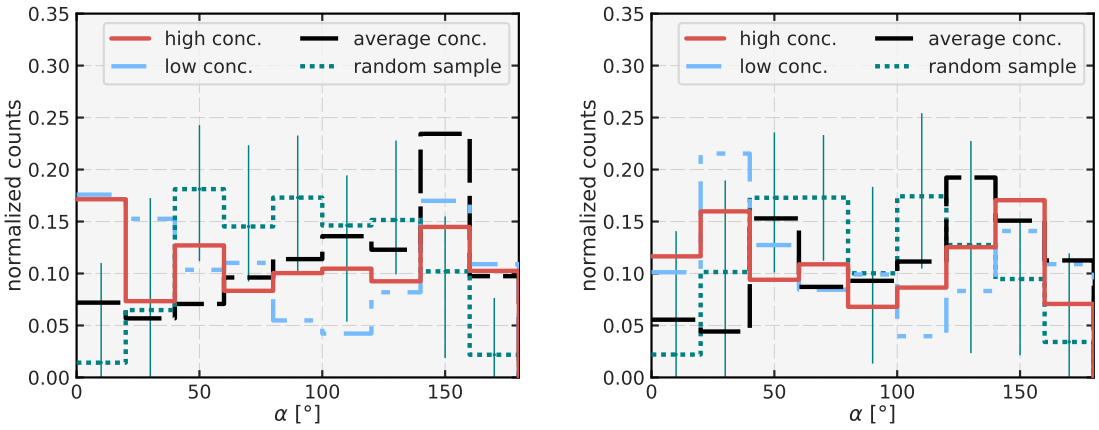
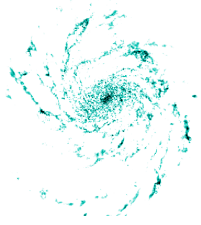


Figure 6.11: Distribution of the angles between the orbital poles of individual satellites and the plane normal (left panel) as well as the mean orbital pole (right panel) for the three different concentration samples. High concentration haloes are shown with a red solid line, average ones with a black dashed line and low concentration haloes with a blue dotted-dashed line. Additionally I show the same for the sample of hosts with randomised velocity vectors of the satellites as a teal dotted line. The scatter in the different samples is almost the same, therefore I only show the scatter for the random sample as a reference.

satellites to preferentially align with the plane normal. This is evident from a slight over-abundances of angles with values close to $\alpha \sim 0°$ (co-rotating) and close to $\alpha \sim 180°$ (counter-rotating). The random sample shows a more uniform distribution of angles with preferred values of α around $90°$. The nearly equal number of satellites with values close to 0 and $180°$ shows that the planes indeed show a spatial alignment but on average do not show a strong kinematical coherence. The same behaviour is found for the mean orbital pole which is calculated from the orbital poles of the satellites (right panel of Figure 6.11). Interestingly there is not much difference in the kinematics between the different concentration samples. All hosts show a fraction of about 30% of the satellites having values of $\alpha \sim 90°$ indicating that these satellites do not take part in a motion in the plane. This analysis reveals that although ΛCDM haloes show a higher degree of co-rotation compared to a random sample they do not exhibit fully kinematically coherent planes. This is further supported by analysing the distribution of spherical standard distance values for the different host haloes. All hosts in the sample show ssd values higher than $30°$ indicative of a large scatter in orbital poles. Although for most haloes, the calculated spherical standard distance is comparable to that of the MW of $\sim 41°$, the widespread distribution of orbital poles indicates a large fraction of interlopers. For the haloes with the most widespread distribution of angular momentum directions I expect that there is nearly no kinematical coherence in these haloes, mostly all satellites in the plane will have different orbital planes.



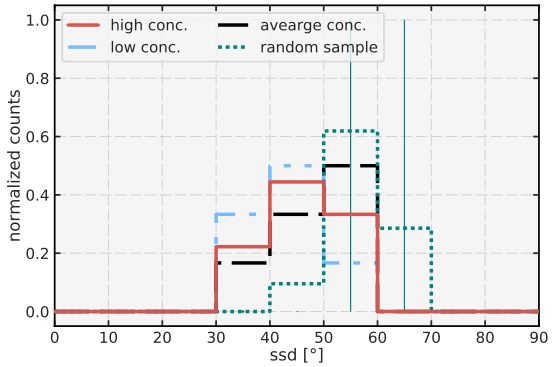


Figure 6.12: Distribution of values for the spherical standard distance for different concentration samples with the same color coding and line style convention used before. The teal bars show the distribution of ssd for the whole sample of hosts with randomised velocity vectors. Again I show only the scatter for the random sample as reference.

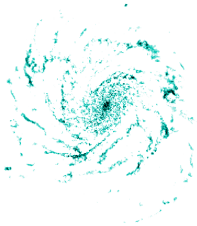
However, comparison to the random sample shows that the scatter is smaller than expected for a sample with randomised velocity vectors. This is in contrast to the result of figure 6.8 where no difference to a random sample was found. Therefore the analysis of orbital poles is better suited to measure the co-rotation of satellites in planes than simply count their line-of-sight velocity. The particular advantage of this measurement is that in contrast to the inference of co-rotation from line-of-sight velocity measurements this method is unique and is not dependent on specific viewing angles. Unfortunately it is hard to obtain proper motion information for most of the satellites in M31 to do this analysis (see also next section). It gets even worse if one would do this measurement for satellite planes further away from us than M31.

6.4.3. Plane Evolution and Plane Stability

With the finding, that the planes of satellites identified seem to contain a significant amount of satellites not taking part in coherent rotational motion it is interesting to estimate their proper motion. Given the average velocity component of the satellites perpendicular to the plane of ~100 km/s I can estimate their proper motion if they would orbit around M31. Given the distance of the sun to M31 of ~780 kpc (McConnachie 2012) I estimate the proper motion of the satellites to be ~ 0.03 mas/yr. This is at the edge of what is currently possible with the HST Promo project (Sohn et al. 2012). A more elaborate estimate of the plane's lifetime can be made by following the orbit of the satellites in the plane and tracing their positions back in time. This is done in the next subsection for two high concentration haloes that show evidence of kinematically coherent planes (halo A and B).

6.4.3.1. Satellite Orbits

The plane stability and the evolution of its thickness over the last 5 Gyr can be investigated by tracking the selected 30 satellites back in time and investigating their positions in the past. In order to investigate the plane coherence over time I rerun



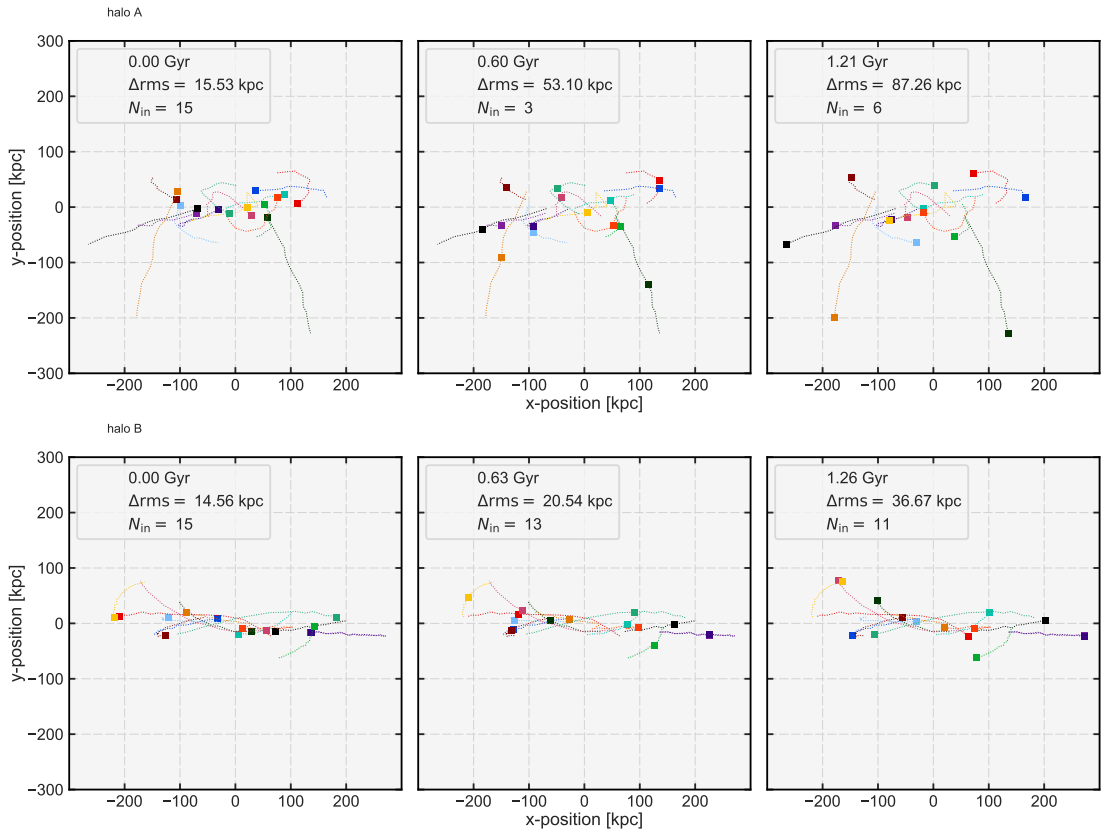
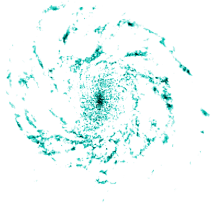


Figure 6.13: Visual impression of the orbits of the satellites in the planes of halo A (top panels) and halo B (bottom panels) with an edge-on view. *Dashed lines* show the trajectories of the satellites and *colored squares* show the positions of the satellites in the planes. From left to right, snapshots at increasingly earlier times are shown. *Left*: The present day configuration, *middle*: the configuration ~ 0.6 Gyr in the past ($\sim 2t_{\rm dyn}$) and *right*: ~ 1.2 Gyr ago ($\sim 4t_{\rm dyn}$). In each of the panels, the time, the rms value of the plane and the number of satellites still within the region of the plane at the present time is indicated.

the plane finding algorithm on the selected satellite samples of 30 satellites at an earlier time to find a new best fitted plane (see Fig. 6.14) probably consisting of a different subset of satellites compared to the $z = 0$ best plane to account for satellites presumably moving out of the plane and new satellites joining the plane.

A visual impression of the orbits of satellites (grey dotted lines) in the planes of halo A and B for the last 1.2 Gyr in the past is given in figure 6.13. The three panels of the figure also show the position of each of the satellites with colored squares at the present time (left panel), at ~ 0.6 Gyr (middle panel) and at ~ 1.2 Gyr (right panel) in the past. From a quick look at the orbits of halo A (upper panels), it is immediately clear that there is almost no motion in the plane, while halo B shows a more coherent motion of the satellites in the plane. For halo A the tracks of the satellites extend up



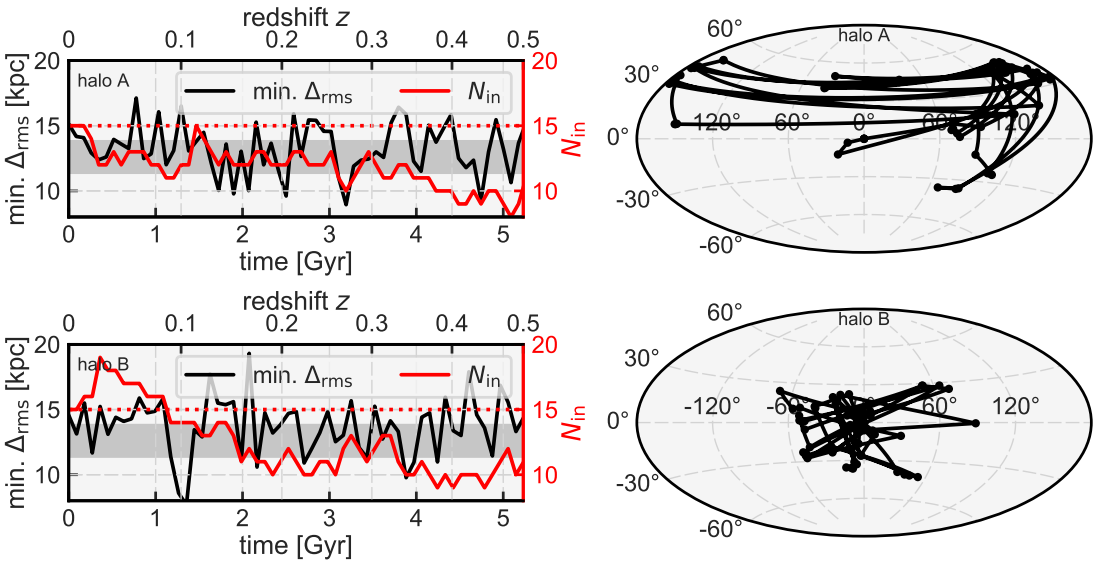
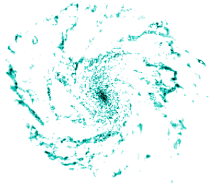


Figure 6.14: The planes at different time steps in the past. *Left panel*: The rms value perpendicular to the plane (black solid line) and the number of satellites in the plane (red solid line, right y-axis) for different time steps of the simulation down to 5 Gyr in the past. The grey shaded area shows the measurement uncertainty of $\Delta_{\rm rms} = 12.6 \pm 0.6$ kpc of the observed thickness of the plane around M31. The red dotted line shows the number of 15 observed satellites in the plane. *Right panel*: The evolution of the corresponding plane normal in spherical coordinates over the past 5 Gyr. The orientation of the plane was chosen such that at present time the plane normal points in the direction of $(\phi, \theta) = (0, 0)$. The *upper panels* show halo A and the *lower panels* show halo B.

to a height of about 75 kpc above the plane or are in some cases even perpendicular to the plane at the present time. Furthermore, after only 0.6 Gyr the positions of the satellites indicate a plane thickened up to about 50 kpc. For halo B (lower panels) most of the satellite orbits stay close to the plane, while for at least 3 satellites the orbits seem to be nearly perpendicular to the plane at present time. However, the plane of halo B does not show a thickening as pronounced as halo A. After 0.6 Gyr this plane only shows a thickening of a factor of 1.4, up to 20 kpc. After ~ 1.2 Gyr the plane of halo A is hardly visible, with an rms value of 87 kpc. At this time the plane of halo B is ~ 37 kpc thick and thus more than doubled its thickness and would by any criterion used for the observations not been regarded as a plane anymore.

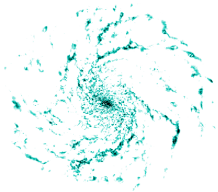
This result is confirmed by figure 6.14, where I show the plane thickness, the number of satellites in the plane and the orientation of the plane normal of halo A and B for many different time steps in the past. Here I restricted the rms value to be smaller than 22 kpc. This figure shows that while the rms value is strongly fluctuating around a value of ~ 14 kpc the number of satellites in the plane is continuously decreasing such that at redshift $z = 0.5$ the plane consists of only 10 satellites. At the same time



the right hand side of the plot shows that the orientation of the plane normal is far from constant and does not show a slow precession, which would be expected for a coherent plane. Rather the plane normal jumps around with only slight clustering behaviour. Halo A seems to show no temporal coherence of the plane normal, but a slight clustering point at $(\phi, \theta) \sim (130, 30)$. One has to keep in mind that the angular momentum vector is a axial quantity and thus the points on the left side of the plot at $(\phi, \theta) \sim (-180, 30)$ are basically the same plane as the clustering on the right side of the plot. For halo B the plane normal is somewhat more coherent with a scatter of $\sim 30°$ and clusters around $(\phi, \theta) \sim (0, 0)$ but still shows a significant scatter. However, both of these clustering points are not stable in time. The plane normal jumps from this point to several other points and back indicating that many different planes are found.

In more detail, these plots show that there is a possibility of finding planes with a comparably high number of satellites (~12 or even higher for halo B) with reasonably low rms values (~ 15 kpc) in the most recent ~ 1 Gyr. However, regarding the rms value and the number of satellites in the plane after this most recent phase, these planes are not stable. The rms value varies between 10 kpc and 18 kpc (upper panel) and between 9 kpc and 16 kpc (lower panel) for different time steps. The number of satellites varies for different time steps. For halo A (upper panel) the variation is only by about 1 satellite, and it stays nearly constant at 12 satellites for about 3 Gyr, and for halo B (lower panel) the plane gets richer in the past few time steps but then the number of satellites declines and fluctuates strongly around 12 satellites in the plane. As the right panel of the figure shows, the normal vector of halo A changes rapidly over the first Gyr (starting out from $(\phi, \theta) = (0, 0)$), and afterwards changes more slowly for a short time, implying some kind of temporal coherence of the plane during this time and then around 4 to 5 Gyr in the past it varies quite a lot. For halo B the variation in the orientation of the plane is equally strong over the whole time period indicating different planes at each time step although all plane orientations seem to cluster around $(\phi, \theta) \sim (0, 0)$.

If one only follows the satellites in the plane at redshift $z = 0$ back in time the behaviour is even worse. For both haloes shown, the planes found at earlier cosmic times have significantly higher values of the plane thickness. For halo A the plane thickness rises nearly constantly from ~ 15 kpc at redshift $z = 0$ to ~ 35 kpc at redshift $z = 0.5$, ~ 5 Gyr in the past. And for halo B the plane thickness rises from ~ 13 kpc at redshift $z = 0$ up to ~ 40 kpc at redshift $\sim 0.4 - 0.5$. At the same time the plane normal shows similar behaviour as before. There seems to be no strong temporal coherence of the plane orientation and only slight clustering of the plane orientations. This shows, in contrast to the previous plots where the plane thickness stays relatively constant over time with the number of satellites in the plane going down, that, when the number of satellites is fixed, the planes puff up their thickness fast. This leads to

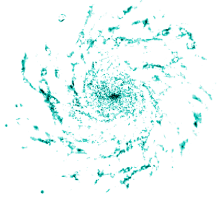


the conclusion that planes of satellites are only thin at present time and have been significantly thicker in the past. Furthermore the fluctuation of the plane orientation shows, that there seems to be no uniquely defined plane over a longer cosmic time period, leading to the impression that these planes are not stable. Thus, although I am able to find rich and thin planes with apparent co-rotation, this analysis indicates that they do not seem to be kinematically coherent in the sense, that they are stable over time. One distinct plane appears to be a short lived system containing a significant amount of chance aligned satellites.

6.5. Discussion

I have run 21 high-resolution, fully cosmological "zoom-in" Dark Matter only simulations of MW mass haloes to investigate planes of satellites resembling the one observed around our MW and its neighbouring galaxy M31. The sample of host haloes for this chapter is constructed such that I select main haloes with different concentrations aiming at haloes with high, average and low concentration compared to the mean relation found by Dutton and Macciò (2014). From these haloes I select the 30 most massive sub-haloes at infall time as the ones most likely to host the luminous satellites. As shown in figure 6.1, the radial distribution of the selected sub-haloes is similar to the observed radial distribution. Planes of satellites among these samples are then selected by a simple spatial selection criteria as the richest planes in number of members and if there are two planes of equal member numbers the thinner one is selected. For simplicity and because I do not have local group analogues, I select satellites from a spherical volume rather than modelling a non-spherical volume such as the PAndAS footprint. This seems to be no major issue since Gillet et al. (2015) showed that planes of satellites found in spherical and PAndAS like volumes reveal comparable properties. After specifying the best-fitting plane by this criteria, the kinematics of these planes is investigated.

I like to mention, that the simulations performed for this work are dark matter only ones, which do not capture the influence of baryonic physics. Therefore, the selection of the luminous satellites according to their mass at the infall time is one questionable point that could be alleviated by using hydrodynamical simulations which is beyond the scope of this chapter and is left for future work with the high-resolution NIHAO sample presented in previous chapters. However, the main influence of baryonic physics on the analysis is expected to be in the robust selection of luminous satellites as well as the influence of the galactic disc on the satellites in the inner region of the halo. Additionally hydrodynamical simulations would enable us to investigate the orientation of the plane of satellites compared to the disc of the galaxy.



Nevertheless, comparison to the work done by Gillet et al. (2015) shows that the planes compare well to the ones found in hydrodynamical simulations. Unfortunately, one draw back of hydrodynamical simulations is, up to now it is not possible to run a statistical sample of galaxies in high-resolution. E.g. Gillet et al. (2015) have only two local group analogues for their analysis, which means just one high-resolution simulation. Furthermore, they selected their galaxies to reside in a special environment, with a second massive galaxy close by. For this work I did not restrict the galaxies to have a companion, neither did I exclude such galaxies. Still the results are comparable to theirs which leaves the impression that a local group environment seems to play no major role (see also Pawlowski et al. 2014).

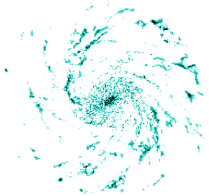
Another interesting point would be to investigate the effect of host halo mass on the occurrence of planes of satellites since previous studies as well as this work focussed only on MW mass like halos. Furthermore I focussed on a sample size of 30 satellites to mimic the case of M31. In general it would be interesting to also investigate sample sizes of $\sim 50 - 100$ sub-haloes to see wether planar structures are still visible at larger sample sizes accounting for ever more discovered satellites around MW and M31. This is however difficult since it is unclear which of the smaller satellites would actually form stars, if at all, or, if they form stars, which are then observable. These questions can be probably answered in future work.

6.5.1. Are the Planes in Simulations unique?

When selecting planes there is some ambiguity in defining the /textitbest plane. As Fig. 6.2 shows there is the possibility to select planes richer in number but with a larger thickness or planes less rich in number but significantly thinner. A priori there is no natural or obvious metric to select the *best* plane. This makes it hard to even define what a plane of satellites should look like to be regarded as a plane. Therefore, I decided to select always the plane richest in number and if there are two such planes consisting of the same number of satellites I select the thinner one. Recently this ambiguity of defining the best plane was investigated by Cautun et al. (2015). They also find that planes of satellites show a large diversity in their properties comparable to the findings in Fig. 6.2. They conclude that planes of satellites are common in ΛCDM ($\sim 10\%$ of the haloes host planes) in agreement with my findings.

6.5.2. Are simulated Planes of Satellites thin, extended and rich in number?

All the satellite planes show a thickness smaller than ~ 17 kpc and are more extended than ~ 120 kpc (see Fig. 6.4) while at the same time including a reasonable amount of satellites (12-16). The division of haloes into high, average and low concentration

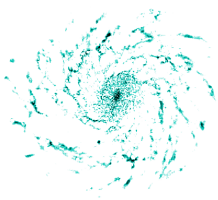


haloes demonstrates that there is a clear dependence of the plane thickness on halo concentration (see also Buck et al. 2015). A Kolmogorov-Smirnov test on the radial distribution of satellites of different concentration samples shows that the satellite distributions of the different concentration haloes are well comparable and high concentration haloes do not show a radially more concentrated distribution. As the left panel of Fig. 6.4 shows, the thinnest planes are only found in high concentration haloes, having the right thickness of ~ 15 kpc and also showing the right radial extension to be comparable to the plane around M31. However, comparing the three dimensional radial extension of planes is ambiguous since it can be biased by single satellites with a very high value of radius. The actual observable parameter is the two-dimensional extension of the plane on the sky. As I show in the right panel of figure 6.4 all of the planes are comparable to the value of M31. Furthermore, only high concentration haloes are able to come close to the observed plane, consisting of 15 satellites in a plane (compare Fig. 6.5) of thickness ~ 15 kpc with 13 co-rotating satellites. The reason why high concentration haloes are able to produce thinner and richer planes compared to average and low concentration haloes is their formation topology. High concentration haloes form at the nodes of the cosmic web and accrete matter along thin filaments, while average and low concentration haloes form later and accrete their matter less anisotropically. Thereby it is not the infall time of the satellites which makes the plane thinner but rather the infall direction along filaments.

Recently Pawlowski et al. (2015) published new results for the MW plane of satellites including more, newly discovered satellites. The new values for the plane are: $N_{\rm in} = 27$ and $\Delta_{\rm rms} = 29.3$ kpc or including new satellite objects these values are $N_{\rm in} = 38$ and $\Delta_{\rm rms} = 30.9$ kpc . These are nearly twice (three times) as much satellites in the plane than I find for my haloes. However, the rms value is also significantly higher. Looking at figure 2 of Buck et al. (2015) one sees, that it is easy to obtain planes with a thickness of ~ 30 kpc which include about 20 satellites when considering a sample of 30 satellites. Raising the sample size up to e.g. ~ 40 satellites to account for the new satellite objects in the MW, I expect to find a comparable number of satellites in the plane with a comparable thickness. This is also found by Gillet et al. (2015), which included sample sizes of 50 and 100 satellites in their analysis and found planes consisting of ~ 30 satellites with a rms thickness of about 15 kpc.

6.5.3. Is the Line-Of-Sight Velocity a stable Measure for Co-Rotation?

The kinematical information of the observed satellites around M31 and for most of the satellites of the MW is only 1-dimensional and consists of the line-of-sight velocity. The co-rotation of the plane is inferred by this information, lacking full 3-dimensional information. In this work I use the advantage of the simulations with access to full



3-dimensional velocity information to investigate in detail the co-rotation of planes of satellites within the frame of ΛCDM. If I infer the co-rotation of satellites in the same way as in the observations by using the line-of-sight velocity I find quite a good agreement between the planes and the observed ones (see e.g. Fig. 6.3 for a visual impression).

When counting the number of co-rotating satellites via the line-of-sight velocity the satellite samples show a quite high co-rotation fraction up to 100% for planes consisting of ∼10 satellites. As Fig. 6.7 shows, with 15 satellites in the plane and 13 co-rotating ones and a thickness smaller than 15 kpc, the high concentration haloes are able to resemble the plane of satellites observed around M31. However, the counting of the number of co-rotating satellites is done for one specific viewing angle and changes when looking at the edge-on plane from a different direction. As I show in figure 6.8 the line-of-sight co-rotation counting for different viewing angles shows a very high scatter of ∼2-3 satellites or ∼ 30%. Very high co-rotation fractions are only reached for special viewing angles. Furthermore a comparison to a sample with randomised velocity vectors shows that the line-of-sight counting of this sample is fully comparable to the simulations. Thus I conclude that the inference of co-rotation via the line-of-sight velocity is not a robust measure. This is in good agreement with the work of Phillips et al. (2015) in which they show that the inferred co-rotation of satellite planes in the Sloan Digital Sky Survey (York et al. 2000, SDSS) by opposite satellite pairs (Ibata et al. 2014) is comparable with random noise when carefully investigated (however, see also Ibata et al. 2015).

Satellite planes in the simulations which show a high degree of kinematical coherence measured in the 1-dimensional case using line-of-sight velocity information turn out to have a co-rotation fraction at most as high as 70% when using more robust measures like an analysis of the angular momentum vectors (compare Fig. 6.10). I thus conclude from the analysis of the simulations that a more reliable measure of the co-rotation is given by the analysis of the angular momentum vectors like done for the MW satellites, although it will be difficult to perform for M31 satellites.

6.5.4. The Kinematics of the Satellites in the Plane

The plane of satellites is just one snapshot in time. Disregarding the full three-dimensional velocity information can lead to incorrectly assigning satellites to the plane which only fly by. To quantify how many such interlopers or chance alignments of satellites occur, I come up with a simple measure of plane membership. By measuring the velocity of the satellites in the plane in terms of the total velocity and comparing it to the case of an isotropic velocity distribution I get a handle on the number of satellites fully orbiting in the plane. From this analysis I conclude that for the simulations about 30% of the satellites are just chance aligned with the plane (see

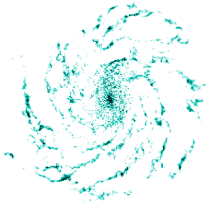
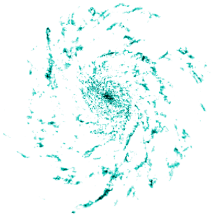


Fig. 6.9). This can also be concluded, when comparing the direction of the angular momentum vectors of the satellites with the plane normal done in Fig. 6.11. Satellites orbiting in a plane should show angular momentum vectors pointing in the same direction or opposite direction as the plane normal. Most planes show indeed a slight clustering of their angular momentum vectors around the direction of the plane normal but with quite a high scatter consistent with about 30% of interlopers. However, the planes found in the simulation compare well with the findings of Pawlowski et al. (2013) for the MW or show even a smaller scatter around the plane normal although the planes of this chapter are selected by a completely different, spatial selection criteria. A comparison to a sample with random velocities shows that the angular momentum analysis is better suited to measure the co-rotation fraction of satellites in the plane compared to the line-of-sight method.

6.5.5. PLANE EVOLUTION

The fact that the planes in the simulations contain a significant amount of interlopers leads to the question how this influences the stability of the planes over time. Planes in low concentration haloes thicken up by about a factor of 4 while in high and average concentration haloes the planes only thicken up by a factor of ~2. A detailed look at the movement of satellites in the planes of halo A and B over the last 5 Gyr indicates that the plane is either not a stable system (halo A) and just at present day resembles a thin extended plane or that the plane consists of a stable backbone including about 70% of the satellites in the plane (halo B) and a fraction of 30% of interlopers aligning at present time with the plane. This can be concluded from figure 6.13, where the orbits of the satellites in the plane for the last 1.2 Gyr are shown. However, this analysis includes only the satellites found to be in a plane at present day and does not account for plane precession. Applying the plane finding algorithm to the sample of the 30 most massive satellites at infall time at different time steps in the simulation shows, that at every time step one is able to find a different plane instead of a slightly precessing one. This is shown in the right panel of figure 6.14 where the orientation of the plane normal at different time steps is plotted. Accordingly, the left panel of figure 6.14 shows, that the root-mean-square thickness is varying much while the number of satellites in the plane is going down. Looking for planes with a fixed number of satellites in the plane at different time steps shows the same result. Going back in time the plane thickens up very fast and the orientation of the plane is changing a lot. Thus the planes of satellites in the simulations, thin and extended at present time, appear not to be a stable systems. At most, the planes arise out of a backbone of coherently rotating satellites plus a significant amount of chance aligned satellites. This may indicate that the plane of satellites around M31 might share the same properties as the planes found in our simulations, and thus might not be a stable system.



6.6. Conclusion

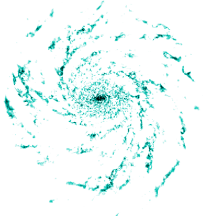
In this chapter I investigated the occurrence of planes of satellites in 21 high-resolution (10 million particles) dark matter only cosmological "zoom-in" simulations of MW mass dark matter haloes. I select dark matter haloes for re-simulation according to their formation times rather than selecting an unbiased sample. The planes found show similar properties as the one observed around our neighboring galaxy M31 (M31) regarding their spatial and kinematical properties, where the kinematic information is based on line-of-sight velocity measurements. Additionally, I do an angular momentum analysis of satellites in the plane using the full 3-dimensional velocity information similar to what Pawlowski et al. (2013) have done for the 11 classical MW satellites. I am able to find planes of satellites simultaneously showing similar properties to the plane around M31 and MW. My results are summarised as follows:

1. The samples of the 30 most massive satellites at infall time show similar spatial distributions of satellites as the one observed around M31, as figure 6.1 shows.

2. Using a simple plane finding algorithm, I obtain planes with a variety of different values for the characteristic values of number of satellites in the plane ($N_{\rm in}$), their thickness ($\Delta_{\rm rms}$), their extent ($\Delta_{\parallel}$) and the number of co-rotating satellites ($N_{\rm corot}$) (compare Fig. 6.2) in agreement with recent studies by Cautun et al. (2015). From the variety of planes I select the ones richest in number and with the smallest thickness.

3. When selecting the richest and thinnest planes, the simulations reproduce properties like the number of satellites in the plane, the thickness and the extent of the observed plane well (see Fig. 6.5 and left panel of Fig. 6.4). But caution has to be taken when comparing the simulations to the observations. The very large extent of the observed plane is biased high by ~ 40 kpc due to one satellite outside the virial radius. In the simulations I am not considering such satellites since I only select them within the virial radius. Therefore a better comparison is the projected extent of the plane on the sky (right panel of Fig. 6.4) for which simulations and observations agree well. Furthermore, the results obtained in this chapter, particularly those for the number of satellites in a plane and the number of interlopers, agree well with the results of other studies, like e.g. Gillet et al. (2015), who used hydrodynamical simulations of two local group analogues.

4. I further find that earlier forming haloes (high concentration) show thinner and slightly richer planes compared to average and late forming haloes (average, low concentration haloes) while there is no dependence of concentration on the extent of the planes.



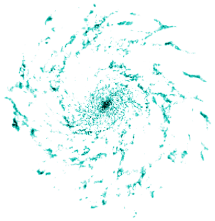
5. Including kinematical information obtained via the line-of-sight velocity of the satellites in the plane, I find planes similar to the observed one ($N_{\rm in} = 15$, $N_{\rm corot} = 13$, $\Delta_{\rm rms} = 12.6 \pm 0.6$ kpc). The planes do not only compare well in the number of satellites in the plane ($N_{\rm in}$), their thickness ($\Delta_{\rm rms}$) and their extent ($\Delta_{\parallel}$) with the observations but also in the number of co-rotating satellites ($N_{\rm corot}$) obtained via the line-of-sight velocity information (Fig. 6.7). However, the planes in the simulations are not kinematically coherent. Therefore, from ΛCDM simulations I predict a high perpendicular velocity (~100 km/s) for some of the satellites in the observed plane, which will be measurable as proper motion of the satellites perpendicular to the plane in future surveys. Indeed, for the MW plane of satellites Gaia Collaboration et al. (2018) recently showed that there exists no kinematical coherence.

6. Investigation of the dependence of the los velocity count of co-rotating satellites on the specific viewing angle onto the edge-on plane shows that this is not a robust measure of co-rotation (Fig. 6.8). This method uses just one component of the 3-dimensional velocity to infer co-rotation and thus appears to be erroneous. An analysis of the angular momentum vectors (Fig. 6.11) gives much better results on the inferred co-rotation fraction.

7. Combination of the angular momentum vector analysis and an additional investigation of the planes for interlopers reveals a significant fraction of about 30% chance aligned satellites (Fig. 6.9).

8. Tracking the satellites back in time and investigating earlier time steps of the simulations for planes of satellites shows that the planes are not a long-lived system (Fig. 6.14). They thicken up on short time scales and are hardly detectable after few hundred Myr. There is a strong dependence on halo concentration with lower concentration haloes thickening strongest. Investigation of the orbits of satellites in the plane (Fig. 6.13) shows that a significant fraction of the satellites in the simulations does not rotate in the plane.

Thus I conclude that the simulations of MW mass haloes in the framework of ΛCDM are able to reproduce planes of satellites similar to the one around M31 and around MW. However, the planes in the simulations in their present configuration turn out to be a rather transient occurrence with about 30% of chance aligned satellites. Which may indicate that also the observed planes may not be kinematically coherent structures. This prediction for satellite planes from ΛCDM could be tested by measuring the proper motion of the satellites in the plane.



Part IV

Discussion, Conclusion and Outlook

Chapter 7

Conclusion and Outlook

I may not have gone where I intended to go, but I think I have ended up where I needed to be.

— Douglas Adams, The Long Dark Tea-Time of the Soul

7.1. Conclusion

With this thesis, I set out to study the formation and evolution of the MW system in fully cosmological hydrodynamical simulations. Since the first attempts some twenty years ago, such simulations have improved significantly and various state-of-the-art simulation projects, like e.g. the big volume projects EAGLE (Crain et al. 2015) or Illustris (Vogelsberger et al. 2014) but also zoom-in projects such as AURIGA (Grand et al. 2017), APOSTLE (Sawala et al. 2015) or NIHAO (Wang et al. 2015), are now able to create realistic galaxies from only a handful of assumptions. Still, all these models lack the ability to model galaxy formation from first principles. Even worse, given the large dynamic ranges involved in galaxy formation, simulations will always need to rely on sub-grid models. Thus, having as many independent data sets as possible to compare and calibrate the simulations against is inevitable.

Using the MW as standard galaxy to compare with brings manyfold advantages, both on the theory side as well as on the observational side. Because we live inside the MW, it will always be the galaxy for which highest fidelity data is available. Already with ongoing surveys like, e.g. Gaia (Gaia Collaboration et al. 2016b), APOGEE (Majewski et al. 2015) or Galah (De Silva et al. 2015) we have a great wealth of data for the position, kinematics, abundances and ages of MW stars enabling us to study its present day structure in great detail. Furthermore, only for the dwarf galaxies of the Local Group it is possible to obtain resolved stellar observations to study their structure and SFH and eventually mass-model them to infer the underlying dark matter distribution. Thus, the wealth of Galactic surveys provides an unique data set to test and calibrate the sub-grid models used in simulations.

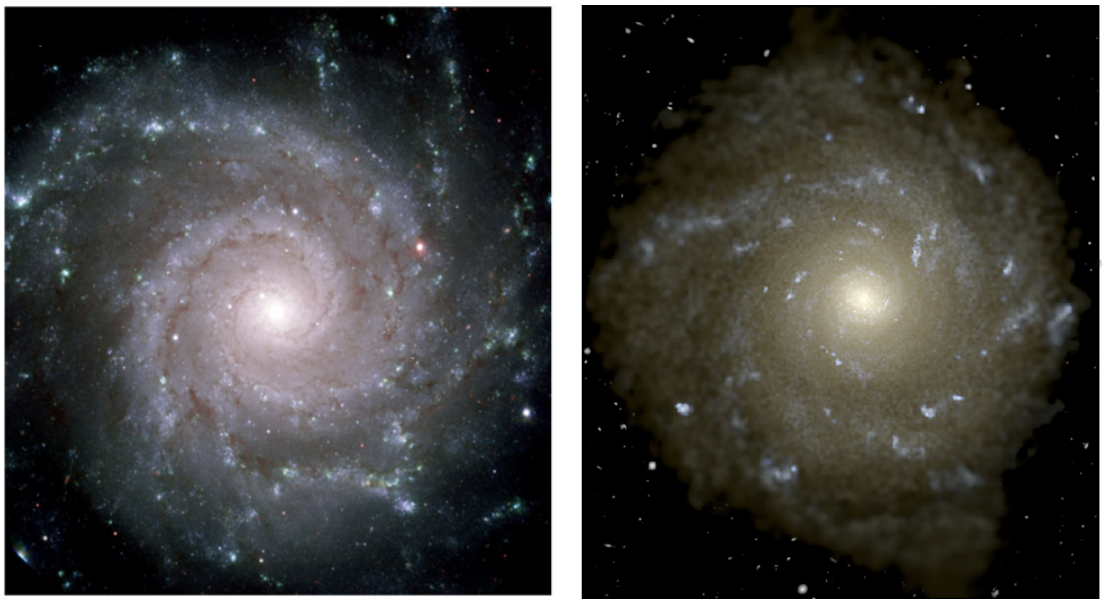
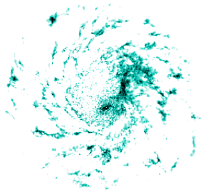


Figure 7.1: Comparison between the observed galaxy M74 (left panel) and a simulated disc galaxy from the high-resolution NIHAO sample (right panel, Buck et al. 2018a).

On the other hand, all Galactic surveys capture only the present-day configuration of the MW and inevitably need to rely on assumptions about its past history in order to unfold its formation. Galactic archaeology tries to use the stars of a galaxy, their ages, abundances, orbits etc., as fossil tracers to reconstruct its formation history. In order to be able to do so, the great question to answer is, how much evolutionary memory can be retained in galactic structures found at present day. Can imprints of past merger and accretion events still be seen in galactic structures at present day or are their signatures completely washed out by secular evolution?

Having arrived at a point where galaxy formation simulations result in realistic galaxies (see e.g. figure 7.1 and pages 42 and 43) showing the same properties as seen e.g. in the MW, we are able to solve the above stated question. By contrasting observations and simulations, identifying similarities (or differences) and tracing them back to particular events or mechanisms in the formation history of the galaxy we are able to quantify and single out their causes and directly connect them to observable features of the present-day MW. This is straight forward in simulations thanks to the accessibility of the full formation history. Hereby only cosmological simulations include at the same time the effects of a cosmological environment and internal evolution.

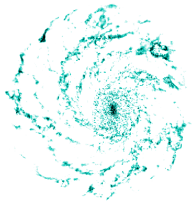
This thesis presents the first steps towards such a synergetic analysis of simulations and observations. While every chapter presents its own little piece of analysis, they all follow the strategy outlined above: Every chapter establishes the realism



of the suite of simulations and then uses them to learn and infer something about the formation history of the MW or its dwarf galaxies by connecting present-day observable features to particular formation events and/or internal mechanisms during its evolution. Below I summarise briefly the main conclusions of this work:

The Formation of MW's Stellar Components: In this first part of the thesis I studied the NIHAO suite of simulations to investigate the properties and build-up of the two major stellar components of the MW, the stellar disc and the bulge. In chapter 2 I use MW mass galaxies from the fiducial NIHAO set in combination with the radiative transfer code GRASIL-3D (Domínguez-Tenreiro et al. 2014) to create realistic mock HST observations for all the snapshots in the redshift range $0.25 < z < 3$. The simulated galaxy morphology is well in agreement with the observed clumpy morphology of disc galaxies in this redshift range. By careful comparison between mock images and *intrinsic* images of properties such as stellar mass, gas mass or star formation rate I determine the nature of such clumps. In contrast to previous analysis (e.g. Bournaud et al. 2014) but in agreement with more recent studies (Mayer et al. 2016; Oklopčić et al. 2017) I find that clumps are not self-bound entities. In the NIHAO simulations these clumps merely trace the clustered nature of star formation and get quickly disrupted by stellar feedback. Therefore I find that their dynamical impact on the formation of the stellar disc and the bulge is negligible. However, finding that the NIHAO galaxies are able to describe the clumpy morphology of stellar discs at higher redshifts is encouraging for the employed feedback model which was only tuned against the stellar mass at redshift zero. This shows that the basic principles of the model seem to work well over the whole cosmic time span.

Chapter 3 and 4 study one galaxy of the very high-resolution sample of NIHAO galaxies which shows a prominent stellar bar with properties well in agreement with the MW's bar. I compare this simulation in particular with the observational dataset of the ARGOS sample (Ness et al. 2013a,b) and recover the bi-modal distribution of stellar counts as a function of line-of-sight distance towards the galactic center. This bi-modality traces the X-shape structure of the bar. I find furthermore that the kinematics of stars in the simulated bar agree very well with the observations. Using this simulation, I test the observational prospects of disentangling inner disc and bulge stars by using easy accessible spectroscopic data such as stellar abundances or radial velocities. Because in the simulation the bar and the peanut shaped bulge form mostly by internal instabilities from disc stars I find that these basic observables are not able to separate the two populations. However, when applying a sophisticated kinematical decomposition technique (Obreja et al. 2018b) I find that with full 6D phase space information, as delivered by e.g. the Gaia satellite (Gaia Collaboration et al. 2016b), we would be able to separate stars into different orbit families such as thin and thick stellar disc, peanut and spherical bulge and stellar halo. Most importantly, I find

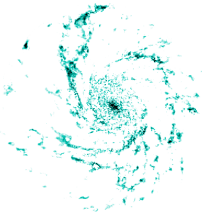


the presence of two different bulge components in the simulation, one boxy/barred population and one spherical symmetric one. Both populations are needed to describe the kinematics of observed bulge stars in the MW as also suggested by Debattista et al. (2017). Investigating the origin of the two components, I find that the star's birth properties cause the stars to end up in different orbit families. These findings positively point towards further usage of Galactic structures as tracers of the particular formation history of the MW such as e.g. the thin/thick disc dichotomy as recently suggested by Grand et al. (2018a).

The Dwarf Galaxy System of the MW: The second part of this thesis addresses the long-standing small scale problems of ΛCDM. With the new generation of high-resolution hydrodynamical cosmological simulations we are, for the first time, able to model and resolve the satellite system of MW mass galaxies in a fully cosmological context. Previous analysis (Moore et al. 1999a; Klypin et al. 1999; Garrison-Kimmel et al. 2014) had to rely on dark matter only simulations in order to study the satellite system of such galaxies and identified various discrepancies between the predictions from these simulations and the observed properties of MW satellites (see section 1.2.4 for a discussion of these issues).

The simulation suite performed and studied for this thesis shows that the properties of dwarf galaxies simulated in a realistic environment agree excellent with the observed properties of Local Group dwarfs. Thus, the initially posed problems of ΛCDM do not occur in these simulations. The reason why these simulations alleviate the long-standing issues are the effects of baryonic physics on the properties of dark matter halos. It has previously been shown, that e.g. stellar feedback driving outflows, is able to alter the dark matter density profile of dwarf galaxy haloes (Pontzen and Governato 2012; Tollet et al. 2016). Furthermore, inclusion of baryons in the simulations enhances tidal stripping of mass from dwarf galaxies orbiting inside the tidal field of a host halo (Garrison-Kimmel et al. 2017). Combining these effects with further suppression of star formation in low mass halos by the UV background leads to an almost perfect match in number counts and structure of the simulated dwarf galaxies with observations.

After the establishment of the realism of the simulated dwarf galaxy population, these simulations are used to quantify the environmental effect of the host galaxy on its dwarf galaxy inventory. The study presented in chapter 5 shows that satellites can loose up to 80% of their initial total mass orbiting inside the tidal field of the MW. It further shows that there exists a prominent population of dwarf galaxies far away from the host at present day but with significant mass loss due to a past close encounter. I test the observational prospects of identifying this population given observable properties such as distance, radial velocity and stellar velocity dispersion. Identifying tidally influenced dwarf galaxies is important since we need an observational clean sample



of unaffected dwarf galaxies in order to test the current cold dark matter model, i.e. to test if dark matter is indeed cold or if we need to invoke some form of warm dark matter to reconcile dwarf galaxy properties with the ΛCDM model.

Finally, chapter 6 discusses in detail the problem of planar alignments of satellite galaxies around the MW and Andromeda. By means of dark matter only simulations I test if the ΛCDM model is able to (a) produce thin planes of satellites and (b) if these planes are long-lived structures. In this chapter I am able to show that the ΛCDM model does indeed result in thin and extended planes of satellites very much resembling the observed ones. However, when analysing the longevity of these planes I find that they are not kinematically coherent structures as was suggested by observations. I trace this false conclusion back to the fact the one-dimensional radial velocity used in the case of the Andromeda plane is not sufficient to infer kinematical coherence. In the case of the MW plane, I find a significant fraction of satellite galaxies that only by chance align with the structure. Indeed, recent studies using the second data release of the Gaia satellite show that the plane of satellites around MW is not kinematically coherent (Gaia Collaboration et al. 2018).

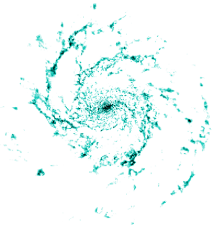
The discussion of the results of this thesis shows that a close comparison between simulations and observations can be very fruitful. The present simulations are able to recover and explain many observed Galactic properties and combining them with large scale Galactic surveys will lead to further insight into the formation of the MW and the scope of application of our model. In the next section I will discuss the future prospects of analysing the simulations and improving the model assumptions.

7.2. Future Prospects

In this thesis I presented a new suite of very high-resolution hydrodynamical simulations of the cosmological formation of MW mass haloes at the cutting edge of current computational possibilities. While I showed and discussed the opportunities such simulations offer in service with large scale Galactic surveys in studying the formation history of the MW much more work, both theoretically as well as observationally, is needed to arrive at a fully mature picture. In this section I will discuss the future prospects these simulations implicate as well as suggestions and ideas to improve currently used numerical galaxy formation models.

Predictions for Ongoing and Future Surveys:

The simulations introduced in this thesis have proven to lead to new insights into the formation and evolution of MW mass galaxies and especially showed that the sub-grid model of NIHAO is able to alleviate long-standing small-scale issues of the ΛCDM model. Having reached the point where simulations result in realistic disc galaxies, the



natural continuation of the present work is to use the simulation together with current and up-coming large scale Galactic surveys to further investigate the formation of the MW. The ideal way to proceed is to compare simulations and observations as close as possible, this is to post-process the simulations in such a manner that observational tools can be directly applied to them.

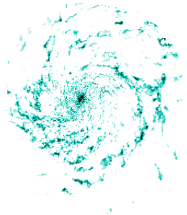
Recently Grand et al. (2018b) and Sanderson et al. (2018) introduced tools to create mock stellar catalogues from the stellar particles of a simulation by spawning single stars from the IMF of each star particle. Using these tools one is able to create a stellar catalogue of the simulation which can then be *observed* with any Galactic survey by applying its selection function and surface brightness limits. Thus, a star by star comparison of model and observations can be made and both can be compared on an equal footing. In times of Gaia and up-coming follow-up spectroscopic observations such as e.g. 4MOST this comparison will help to understand the information content of Galactic structures.

With the Gaia data release 2 we have access to 6 dimensional phase space information for billions of stars in the MW and are, for the first time, able to directly infer the gravitational potential of the MW from stellar kinematics. Combined with spectroscopic surveys such as e.g. APOGEE or Galah we have further access to stellar abundances and sometimes even stellar ages. This gives us essential the exact same information we obtain from simulated MW analogues enabling a direct comparison at present-day. The strength of the simulations is then, that structures can be followed back in time and the particular formation scenario can be inspected. Obviously, this is not possible for the observations. In this sense I am confident that the particular combination of observation and simulation will lead to further insights into the formation of major Galactic structures like e.g. the thin and thick disc and may help to clarify their chemical dichotomy as well as their formation scenario (if at all distinct).

Further application of the simulations introduced here exist in the study of the build-up of the stellar halo. As can be seen from figure 5.1 the simulations show pronounced stellar streams from accretion events of dwarf galaxies. Studying the accretion and disruption of dwarf galaxies in MW type galaxies and extracting their observational features might help to observationally identify disrupted dwarf galaxies via chemically or kinematically tagging stars from their progenitors.

Improved Numerical Models:

I highlighted the successes of the simulations and discussed the advantages of comparing the simulations as close as possible to observations. But like every model, the simulations are not perfect. While they are able to reproduce most galactic properties, there are several indications that the sub-grid model needs further improvements. One aspect which is currently not captured in full detail in the `Gasoline` code is the



chemical enrichment of ultra-faint dwarf galaxies. E.g. the left panel of figure 5.4 shows that the smallest dwarf galaxies systematically lie below the observed relation. During this study I could identify that short, single star bursts in these galaxies are not handled correctly and do not enrich the ISM properly. For this reason future work will implement a different chemical enrichment scheme in `Gasoline` on the basis of the `Chempy` package (Rybizki et al. 2017).

A further step in this direction would be to implement stochastic sampling of the stellar particle's IMF. The simulations used here have stellar particle resolutions of $\sim 9000 M_\odot$ which is still a valid representation of a SSP population. However, if future simulations further increase the resolution, we soon hit stellar particle masses which do not represent a SSP anymore and models have to account for this. Revaz et al. (2016) recently introduced and studied ways how to stochastically sample the IMF when particle masses drop below the mass limit where the assumption of a fully sampled IMF is still valid. Already with current simulations of dwarf galaxies we hit these mass limits and an implementation of IMF sampling in modern simulation codes is highly needed.

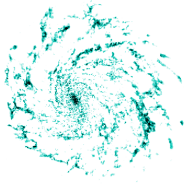
Clearly, such modifications will inevitably alter the stellar feedback returned to the ISM and detailed investigations of the ISM properties in nearby dwarfs and the MW itself will help to discriminate between different models. Due to the short lifetime of high-mass stars, most feedback events will be caused by supernovae type II. Studying the large scale properties of the ISM like e.g. its metal enrichment and turbulent properties will not only pin-down the model parameters but further establish the connection of small scale stellar physics and large scale ISM properties.

7.3. Concluding Remarks

With this thesis I show that state-of-the-art cosmological hydrodynamical simulations have arrived at a point where the models result in realistic MW type galaxies. With advanced computational power, simulations are now able to resolve the scale-height of MW's stellar disc and the half-light radius of classical satellite galaxies, both of the order of a few hundred parsec. This enables us to study the build-up of the stellar components of MW type galaxies in a realistic cosmological environment.

In this thesis I addressed the question of the formation of the MW system as a whole. In the first part I showed that observed clumpy stellar discs in the early phases of the formation of the Galaxy are dynamically unimportant for its further evolution. With this I confirmed observational results from e.g. Wuyts et al. (2011) who argued that unequal dust-attenuation might cause the stellar discs to appear clumpy.

Further studies of the bulge and bar region of one of the galaxies in my sample lead to the exploration of the formation mechanism of the MW's peanut bulge in

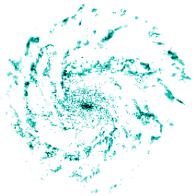


cosmological context. I was able to establish the agreement between model and observation and then use the simulation to study in detail the kinematical properties of the central stellar populations. Using a kinematical decomposition technique I found that the observed kinematic features of the MW bulge can only be explained if there is both a peanut bulge and a spherically symmetric bulge present in the MW. Observing and disentangling both components in the MW will soon be possible thanks to large scale Galactic surveys like e.g. Gaia.

In the second part of the thesis I studied the dwarf galaxy population of MW mass galaxies. The simulation presented there are among the first (see also Sawala et al. 2014; Wetzel et al. 2015) to be able to study the formation of dwarf satellite galaxies in a realistic cosmological environment. Indeed, the employed sub-grid model of the NIHAO simulations is able to reconcile simulated and observed Local Group satellite mass functions. Furthermore, the structure of the dwarf galaxies agrees with observed stellar velocity dispersion measurements of Local Group dwarfs. While these results are promising from a galaxy formation point of view, one has to keep in mind that a lot ad-hoc assumptions and calibration work of the sub-grid models went into these results. Nevertheless, having succeeded in simulating a population of dwarf galaxies with realistic properties, I test the observational prospects of identifying tidally effected dwarfs in the Local Group. I found that it is possible to identify these dwarf galaxies using three observables: their distance, their line-of-sight velocity and their velocity dispersion within the half-light radius.

Finally, using a set of high-resolution dark matter only simulations I investigated the formation and evolution of planes-of-satellites in the framework of ΛCDM. I was able to find planes resembling the ones observed around the MW and its companion Andromeda. Investigating how these planes evolve over time in a cosmological context I found that they quickly dissolve and are merely a result of chance alignment of satellites than tracing a physical mechanism aligning satellites in planar configuration. Recently, this result was confirmed using proper motions for the classical satellite galaxies of the MW derived from data of the Gaia satellite (Gaia Collaboration et al. 2018).

While the results of this thesis are very promising and show that we have understood galaxy formation in quite some detail, I identify a number of open questions. The detailed structure of the stellar disc of the MW will be revealed by on-going and future surveys and it is far from clear if current models are able to reproduce these structures. Furthermore, I pointed out the short-comings of the currently employed models and discussed model improvements. Both these tasks are sufficiently complex to fill more than another thesis on their own and will keep me busy for the next years.



Acronyms

ΛCDM Cold Dark Matter model with a cosmological constant

AGN Active Galactic Nuclei

APOGEE Apache Point Observatory Galactic Evolution Experiment

BH Black Hole

CDM Cold Dark Matter

DM dark matter

CMB Cosmic Microwave Background

DES Dark Energy Survey

GC Globular Cluster

GMC Giant Molecular Cloud

HI Neutral Hydrogen gas

H_2 Molecular Hydrogen gas

HII Ionized Hydrogen gas

IC Index Catalogue

IFU Integral Field Unit

IMF Initial Mass Function

IR Infrared

ISM interstellar medium

LG Local Group

LMC Large Magellanic Cloud

MW Milky Way

M31 Andromeda galaxy

NIHAO Numerical Investigations of Hundred Astrophysical Objects

NGC New General Catalogue of Nebulae and Clusters of Stars

PAndAS Pan-Andromeda Archaelogocal Survey

SDSS Sloan Digital Sky Survey

SED Spectral Energy Distribution

SF star formation

SFb stellar feedback

SFH Star formation history

SMBH super-massive black hole

SNIa Super Nova Ia

SPH Smoothed Particle Hydrodynamics

SSP Simple Stellar Population

UV Ultraviolet

First Author Publications of T. Buck

Buck, T., Ness, M., Obreja, A., Macciò, A. V., and Dutton, A. A. (2018c). Stars behind bars II: A cosmological formation scenario of the Milky Way's central stellar structure. *ArXiv e-prints*.
This publication was used in this thesis.

Buck, T., Macciò, A. V., Dutton, A. A., Obreja, A., and Frings, J. (2018b). NIHAO XV: The environmental impact of the host galaxy on galactic satellite and field dwarf galaxies. *ArXiv e-prints*.
This publication was used in this thesis.

Buck, T., Ness, M. K., Macciò, A. V., Obreja, A., and Dutton, A. A. (2018a). Stars behind bars I: The Milky Way's central stellar populations. *ApJ*, 861:88.
This publication was used in this thesis.

Buck, T., Macciò, A. V., Obreja, A., Dutton, A. A., Domínguez-Tenreiro, R., and Granato, G. L. (2017). NIHAO XIII: Clumpy discs or clumpy light in high-redshift galaxies? *MNRAS*, 468:3628–3649.
This publication was used in this thesis.

Buck, T., Dutton, A. A., and Macciò, A. V. (2016). Simulated ΛCDM analogues of the thin plane of satellites around the Andromeda galaxy are not kinematically coherent structures. *MNRAS*, 460:4348–4365.
This publication was used in this thesis.

Buck T., Dutton A. A., Macciò A. V., 2017, Formation and Evolution of Galaxy Outskirts, 40, IAUS..321

Buck T., Macciò A. V., Ness M., Obreja A., Dutton A. A., 2018, Rediscovering Our Galaxy, 209, IAUS..334

Buck, T., Macciò, A. V., and Dutton, A. A. (2015). Evidence for Early Filamentary Accretion from the Andromeda Galaxy's Thin Plane of Satellites. *ApJ*, 809:49.

Contributing Author Publications

Obreja, A., Macciò, A. V., Moster, B., Dutton, A. A., Buck, T., Stinson, G. S. and Wang, L. (2018a). Introducing galactic structure finder: the multiple stellar kinematic structures of a simulated Milky Way mass galaxy. *MNRAS*, 477:4915–4930.

Obreja, A., Dutton, A. A., Macciò, A. V., Moster, B., Buck, T., van den Ven, G., Wang, L., Stinson, G. S., and Zhu, L. (2018b). NIHAO XVI: The properties and evolution of kinematically selected discs, bulges and stellar haloes. *ArXiv e-prints*.

Arrigoni Battaia, F., Prochaska, J. X., Hennawi, J. F., Obreja, A., Buck, T., Cantalupo, S., Dutton, A. A. and Macciò, A. V. (2018). Inspiraling halo accretion mapped in Ly α emission around a z∼3 quasar. *MNRAS*, 473:3907–3940.

Macciò, A. V., Frings, J., Buck, T., Penzo, C., Dutton, A. A., Blank, M., and Obreja, A. (2017). The edge of galaxy formation - I. Formation and evolution of MW-satellite analogues before accretion. *MNRAS*, 472:2356–2366.

Frings, J., Macciò, A., Buck, T., Penzo, C., Dutton, A., Blank, M., and Obreja, A. (2017). The edge of galaxy formation - II. Evolution of Milky Way satellite analogues after infall. *MNRAS*, 472:3378–3389.

Dutton, A. A., Obreja, A., Wang, L., Gutcke, T. A., Buck, T., Udrescu, S. M., Frings, J., Stinson, G. S., Kang, X., and Macciò, A. V. (2017). NIHAO XII: Galactic uniformity in a ΛCDM universe. *MNRAS*, 467:4937–4950.

Dutton, A. A., Macciò, A. V., Dekel, A., Wang, L., Stinson, G., Obreja, A., Di Cintio, A., Brook, C., Buck, T. and Kang, Xi (2016). NIHAO IX: The role of gas inflows and outflows in driving the contraction and expansion of cold dark matter haloes. *MNRAS*, 461:2658–2675.

Tollet, E., Macciò, A. V., Dutton, A. A., Stinson, G. S., Wang, L., Penzo, C., Gutcke, T. A., Buck, T., Kang, X., Brook, C., Di Cintio, A., Keller, B. W., and Wadsley, J. (2016). NIHAO - IV: Core creation and destruction in dark matter density profiles across cosmic time. *MNRAS*, 456:3542–3552.

Dutton, A. A., Macciò, A. V., Stinson, G., Gutcke, T., Penzo, C. and Buck, T. (2015).

The response of dark matter haloes to elliptical galaxy formation: a new test for quenching scenarios. *MNRAS*, 453:2447–2464.

Bibliography

Abadi, M. G., Navarro, J. F., Fardal, M., Babul, A., and Steinmetz, M. (2010). Galaxy-induced transformation of dark matter haloes. *MNRAS*, 407:435–446.

Abadi, M. G., Navarro, J. F., and Steinmetz, M. (2006). Stars beyond galaxies: the origin of extended luminous haloes around galaxies. *MNRAS*, 365:747–758.

Abadi, M. G., Navarro, J. F., Steinmetz, M., and Eke, V. R. (2003). Simulations of Galaxy Formation in a Λ Cold Dark Matter Universe. I. Dynamical and Photometric Properties of a Simulated Disk Galaxy. *ApJ*, 591:499–514.

Adibekyan, V. Z., Sousa, S. G., Santos, N. C., Delgado Mena, E., González Hernández, J. I., Israelian, G., Mayor, M., and Khachatryan, G. (2012). Chemical abundances of 1111 FGK stars from the HARPS GTO planet search program. Galactic stellar populations and planets. *A&A*, 545:A32.

Agertz, O., Teyssier, R., and Moore, B. (2009). Disc formation and the origin of clumpy galaxies at high redshift. *MNRAS*, 397:L64–L68.

Ahmed, S. H., Brooks, A. M., and Christensen, C. R. (2017). The role of baryons in creating statistically significant planes of satellites around Milky Way-mass galaxies. *MNRAS*, 466:3119–3132.

Alam, S. M. K., Bullock, J. S., and Weinberg, D. H. (2002). Dark Matter Properties and Halo Central Densities. *ApJ*, 572:34–40.

Allgood, B., Flores, R. A., Primack, J. R., Kravtsov, A. V., Wechsler, R. H., Faltenbacher, A., and Bullock, J. S. (2006). The shape of dark matter haloes: dependence on mass, redshift, radius and formation. *MNRAS*, 367:1781–1796.

Alpher, R. A. and Herman, R. (1948). Evolution of the Universe. *Nature*, 162:774–775.

Alves-Brito, A., Meléndez, J., Asplund, M., Ramírez, I., and Yong, D. (2010). Chemical similarities between Galactic bulge and local thick disk red giants: O, Na, Mg, Al, Si, Ca, and Ti. *A&A*, 513:A35.

Anderhalden, D., Schneider, A., Macciò, A. V., Diemand, J., and Bertone, G. (2013). Hints on the nature of dark matter from the properties of Milky Way satellites. *J. Cosmology Astropart. Phys.*, 3:14.

Angulo, R. E., Springel, V., White, S. D. M., Jenkins, A., Baugh, C. M., and Frenk, C. S.

(2012). Scaling relations for galaxy clusters in the Millennium-XXL simulation. *MNRAS*, 426:2046–2062.

Arraki, K. S., Klypin, A., More, S., and Trujillo-Gomez, S. (2014). Effects of baryon removal on the structure of dwarf spheroidal galaxies. *MNRAS*, 438:1466–1482.

Astashenok, A. V., Nojiri, S., Odintsov, S. D., and Yurov, A. V. (2012). Phantom cosmology without Big Rip singularity. *Physics Letters B*, 709:396–403.

Astropy Collaboration, Robitaille, T. P., Tollerud, E. J., Greenfield, P., Droettboom, M., Bray, E., Aldcroft, T., Davis, M., Ginsburg, A., Price-Whelan, A. M., Kerzendorf, W. E., Conley, A., Crighton, N., Barbary, K., Muna, D., Ferguson, H., Grollier, F., Parikh, M. M., Nair, P. H., Unther, H. M., Deil, C., Woillez, J., Conseil, S., Kramer, R., Turner, J. E. H., Singer, L., Fox, R., Weaver, B. A., Zabalza, V., Edwards, Z. I., Azalee Bostroem, K., Burke, D. J., Casey, A. R., Crawford, S. M., Dencheva, N., Ely, J., Jenness, T., Labrie, K., Lim, P. L., Pierfederici, F., Pontzen, A., Ptak, A., Refsdal, B., Servillat, M., and Streicher, O. (2013). Astropy: A community Python package for astronomy. *A&A*, 558:A33.

Athanassoula, E. and Martinez-Valpuesta, I. (2009). Boxy/peanut bulges : formation, evolution and properties. *Astrophysics and Space Science Proceedings*, 8:77.

Athanassoula, E., Rodionov, S. A., and Prantzos, N. (2017). Metallicity-dependent kinematics and morphology of the Milky Way bulge. *MNRAS*, 467:L46–L50.

Aubert, D., Pichon, C., and Colombi, S. (2004). The origin and implications of dark matter anisotropic cosmic infall on ˜L$_*$ haloes. *MNRAS*, 352:376–398.

Babcock, H. W. (1939). The rotation of the Andromeda Nebula. *Lick Observatory Bulletin*, 19:41–51.

Babusiaux, C. (2016). Correlations between Kinematics and Metallicity in the Galactic Bulge: A Review. *PASA*, 33:e026.

Babusiaux, C., Gómez, A., Hill, V., Royer, F., Zoccali, M., Arenou, F., Fux, R., Lecureur, A., Schultheis, M., Barbuy, B., Minniti, D., and Ortolani, S. (2010). Insights on the Milky Way bulge formation from the correlations between kinematics and metallicity. *A&A*, 519:A77.

Bahl, H. and Baumgardt, H. (2014). A comparison of the distribution of satellite galaxies around Andromeda and the results of ΛCDM simulations. *MNRAS*, 438:2916–2923.

Baldry, I. K., Glazebrook, K., Brinkmann, J., Ivezić, Ž., Lupton, R. H., Nichol, R. C., and Szalay, A. S. (2004). Quantifying the Bimodal Color-Magnitude Distribution of Galaxies. *ApJ*, 600:681–694.

Baldry, I. K., Glazebrook, K., and Driver, S. P. (2008). On the galaxy stellar mass function, the mass-metallicity relation and the implied baryonic mass function. *MNRAS*, 388:945–959.

Barbuy, B., Chiappini, C., and Gerhard, O. (2018). Chemodynamical history of the Galactic Bulge. *ArXiv e-prints*.

Bardeen, J. M., Steinhardt, P. J., and Turner, M. S. (1983). Spontaneous creation of almost scale-free density perturbations in an inflationary universe. *Phys. Rev. D*, 28:679–693.

Bechtol, K., Drlica-Wagner, A., Balbinot, E., Pieres, A., Simon, J. D., Yanny, B., Santiago, B., Wechsler, R. H., Frieman, J., Walker, A. R., Williams, P., Rozo, E., Rykoff, E. S., Queiroz, A., Luque, E., Benoit-Lévy, A., Tucker, D., Sevilla, I., Gruendl, R. A., da Costa, L. N., Fausti Neto, A., Maia, M. A. G., Abbott, T., Allam, S., Armstrong, R., Bauer, A. H., Bernstein, G. M., Bernstein, R. A., Bertin, E., Brooks, D., Buckley-Geer, E., Burke, D. L., Carnero Rosell, A., Castander, F. J., Covarrubias, R., D'Andrea, C. B., DePoy, D. L., Desai, S., Diehl, H. T., Eifler, T. F., Estrada, J., Evrard, A. E., Fernandez, E., Finley, D. A., Flaugher, B., Gaztanaga, E., Gerdes, D., Girardi, L., Gladders, M., Gruen, D., Gutierrez, G., Hao, J., Honscheid, K., Jain, B., James, D., Kent, S., Kron, R., Kuehn, K., Kuropatkin, N., Lahav, O., Li, T. S., Lin, H., Makler, M., March, M., Marshall, J., Martini, P., Merritt, K. W., Miller, C., Miquel, R., Mohr, J., Neilsen, E., Nichol, R., Nord, B., Ogando, R., Peoples, J., Petravick, D., Plazas, A. A., Romer, A. K., Roodman, A., Sako, M., Sanchez, E., Scarpine, V., Schubnell, M., Smith, R. C., Soares-Santos, M., Sobreira, F., Suchyta, E., Swanson, M. E. C., Tarle, G., Thaler, J., Thomas, D., Wester, W., Zuntz, J., and DES Collaboration (2015). Eight New Milky Way Companions Discovered in First-year Dark Energy Survey Data. *ApJ*, 807:50.

Behroozi, P. S., Wechsler, R. H., and Conroy, C. (2013). The Average Star Formation Histories of Galaxies in Dark Matter Halos from z = 0-8. *ApJ*, 770:57.

Behroozi, P. S., Wechsler, R. H., Lu, Y., Hahn, O., Busha, M. T., Klypin, A., and Primack, J. R. (2014). Mergers and Mass Accretion for Infalling Halos Both End Well Outside Cluster Virial Radii. *ApJ*, 787:156.

Bell, E. F., Zucker, D. B., Belokurov, V., Sharma, S., Johnston, K. V., Bullock, J. S., Hogg, D. W., Jahnke, K., de Jong, J. T. A., Beers, T. C., Evans, N. W., Grebel, E. K., Ivezić, Ž., Koposov, S. E., Rix, H.-W., Schneider, D. P., Steinmetz, M., and Zolotov, A. (2008). The Accretion Origin of the Milky Way's Stellar Halo. *ApJ*, 680:295–311.

Bellazzini, M., Beccari, G., Oosterloo, T. A., Galleti, S., Sollima, A., Correnti, M., Testa, V., Mayer, L., Cignoni, M., Fraternali, F., and Gallozzi, S. (2011). An optical and H i study of the dwarf Local Group galaxy VV124 = UGC4879. A gas-poor dwarf with a stellar disk? *A&A*, 527:A58.

Bellazzini, M., Oosterloo, T., Fraternali, F., and Beccari, G. (2013). Dwarfs walking in a row. The filamentary nature of the NGC 3109 association. *A&A*, 559:L11.

Belokurov, V. (2013). Galactic Archaeology: The dwarfs that survived and perished. *New A Rev.*, 57:100–121.

Belokurov, V., Irwin, M. J., Koposov, S. E., Evans, N. W., Gonzalez-Solares, E., Metcalfe, N., and Shanks, T. (2014). ATLAS lifts the Cup: discovery of a new Milky Way satellite in Crater. *MNRAS*, 441:2124–2133.

Belokurov, V., Zucker, D. B., Evans, N. W., Gilmore, G., Vidrih, S., Bramich, D. M., Newberg, H. J., Wyse, R. F. G., Irwin, M. J., Fellhauer, M., Hewett, P. C., Walton, N. A., Wilkinson, M. I., Cole, N., Yanny, B., Rockosi, C. M., Beers, T. C., Bell, E. F., Brinkmann, J., Ivezić, Ž., and Lupton, R. (2006). The Field of Streams: Sagittarius and Its Siblings. *ApJ*, 642:L137–L140.

Belokurov, V., Zucker, D. B., Evans, N. W., Kleyna, J. T., Koposov, S., Hodgkin, S. T., Irwin, M. J., Gilmore, G., Wilkinson, M. I., Fellhauer, M., Bramich, D. M., Hewett, P. C., Vidrih, S., De Jong, J. T. A., Smith, J. A., Rix, H.-W., Bell, E. F., Wyse, R. F. G., Newberg, H. J., Mayeur, P. A., Yanny, B., Rockosi, C. M., Gnedin, O. Y., Schneider, D. P., Beers, T. C., Barentine, J. C., Brewington, H., Brinkmann, J., Harvanek, M., Kleinman, S. J., Krzesinski, J., Long, D., Nitta, A., and Snedden, S. A. (2007). Cats and Dogs, Hair and a Hero: A Quintet of New Milky Way Companions. *ApJ*, 654:897–906.

Bennett, C. L., Halpern, M., Hinshaw, G., Jarosik, N., Kogut, A., Limon, M., Meyer, S. S., Page, L., Spergel, D. N., Tucker, G. S., Wollack, E., Wright, E. L., Barnes, C., Greason, M. R., Hill, R. S., Komatsu, E., Nolta, M. R., Odegard, N., Peiris, H. V., Verde, L., and Weiland, J. L. (2003). First-Year Wilkinson Microwave Anisotropy Probe (WMAP) Observations: Preliminary Maps and Basic Results. *ApJS*, 148:1–27.

Bensby, T., Alves-Brito, A., Oey, M. S., Yong, D., and Meléndez, J. (2011). A First Constraint on the Thick Disk Scale Length: Differential Radial Abundances in K Giants at Galactocentric Radii 4, 8, and 12 kpc. *ApJ*, 735:L46.

Bensby, T., Feltzing, S., Gould, A., Yee, J. C., Johnson, J. A., Asplund, M., Meléndez, J., Lucatello, S., Howes, L. M., McWilliam, A., Udalski, A., Szymański, M. K., Soszyński, I., Poleski, R., Wyrzykowski, Ł., Ulaczyk, K., Kozłowski, S., Pietrukowicz, P., Skowron, J., Mróz, P., Pawlak, M., Abe, F., Asakura, Y., Bhattacharya, A., Bond, I. A., Bennett, D. P., Hirao, Y., Nagakane, M., Koshimoto, N., Sumi, T., Suzuki, D., and Tristram, P. J. (2017). Chemical evolution of the Galactic bulge as traced by microlensed dwarf and subgiant stars. VI. Age and abundance structure of the stellar populations in the central sub-kpc of the Milky Way. *ArXiv e-prints*.

Bensby, T., Feltzing, S., Johnson, J. A., Gould, A., Adén, D., Asplund, M., Meléndez, J., Gal-Yam, A., Lucatello, S., Sana, H., Sumi, T., Miyake, N., Suzuki, D., Han, C., Bond, I., and Udalski, A. (2010). Chemical evolution of the Galactic bulge as traced by microlensed dwarf and subgiant stars. II. Ages, metallicities, detailed elemental abundances, and connections to the Galactic thick disc. *A&A*, 512:A41.

Bensby, T., Feltzing, S., and Lundström, I. (2003). Elemental abundance trends in the Galactic thin and thick disks as traced by nearby F and G dwarf stars. *A&A*, 410:527–551.

Bensby, T., Feltzing, S., and Oey, M. S. (2014). Exploring the Milky Way stellar disk. A detailed elemental abundance study of 714 F and G dwarf stars in the solar neighbourhood. *A&A*, 562:A71.

Bensby, T., Yee, J. C., Feltzing, S., Johnson, J. A., Gould, A., Cohen, J. G., Asplund, M., Meléndez, J., Lucatello, S., Han, C., Thompson, I., Gal-Yam, A., Udalski, A., Bennett, D. P., Bond, I. A., Kohei, W., Sumi, T., Suzuki, D., Suzuki, K., Takino, S., Tristram, P., Yamai, N., and Yonehara, A. (2013). Chemical evolution of the Galactic bulge as traced by microlensed dwarf and subgiant stars. V. Evidence for a wide age distribution and a complex MDF. *A&A*, 549:A147.

Benson, A. J., Lacey, C. G., Baugh, C. M., Cole, S., and Frenk, C. S. (2002). The effects of photoionization on galaxy formation - I. Model and results at z=0. *MNRAS*, 333:156–176.

Bertone, G., Hooper, D., and Silk, J. (2004). Particle dark matter: evidence, candidates and constraints. *Phys. Rep.*, 405:279–390.

Bertschinger, E. (2001). Multiscale Gaussian Random Fields and Their Application to Cosmological Simulations. *ApJS*, 137:1–20.

Besla, G., Kallivayalil, N., Hernquist, L., Robertson, B., Cox, T. J., van der Marel, R. P., and Alcock, C. (2007). Are the Magellanic Clouds on Their First Passage about the Milky Way? *ApJ*, 668:949–967.

Bigiel, F., Leroy, A., Walter, F., Brinks, E., de Blok, W. J. G., Madore, B., and Thornley, M. D. (2008). The Star Formation Law in Nearby Galaxies on Sub-Kpc Scales. *AJ*, 136:2846–2871.

Binney, J. (1977). The physics of dissipational galaxy formation. *ApJ*, 215:483–491.

Binney, J. (2013). Dynamics for galactic archaeology. *New A Rev.*, 57:29–51.

Binney, J., Gerhard, O., and Spergel, D. (1997). The photometric structure of the inner Galaxy. *MNRAS*, 288:365–374.

Binney, J. and Merrifield, M. (1998). *Galactic Astronomy*.

Binney, J. and Tremaine, S. (2008). *Galactic dynamics*. Princeton series in astrophysics. Princeton University Press, Princeton, NJ ; Oxford, 2. ed. edition.

Birnboim, Y. and Dekel, A. (2003). Virial shocks in galactic haloes? *MNRAS*, 345:349–364.

Blaña Díaz, M., Wegg, C., Gerhard, O., Erwin, P., Portail, M., Opitsch, M., Saglia, R., and Bender, R. (2017). Andromeda chained to the box - dynamical models for M31: bulge and bar. *MNRAS*, 466:4279–4298.

Bland-Hawthorn, J. and Gerhard, O. (2016). The Galaxy in Context: Structural, Kinematic, and Integrated Properties. *ARA&A*, 54:529–596.

Blitz, L. and Spergel, D. N. (1991). Direct evidence for a bar at the Galactic center. *ApJ*, 379:631–638.

Blumenthal, G. R., Pagels, H., and Primack, J. R. (1982). Galaxy formation by dissipationless particles heavier than neutrinos. *Nature*, 299:37.

Bond, J. R., Silk, J., and Kolb, E. W. (1982). The generation of isothermal perturbations in the very early universe. *ApJ*, 255:341–360.

Bond, J. R. and Szalay, A. S. (1983). The collisionless damping of density fluctuations in an expanding universe. *ApJ*, 274:443–468.

Bond, N. A., Ivezić, Ž., Sesar, B., Jurić, M., Munn, J. A., Kowalski, A., Loebman, S., Roškar, R., Beers, T. C., Dalcanton, J., Rockosi, C. M., Yanny, B., Newberg, H. J., Allende Prieto, C., Wilhelm, R., Lee, Y. S., Sivarani, T., Majewski, S. R., Norris, J. E., Bailer-Jones, C. A. L., Re Fiorentin, P., Schlegel, D., Uomoto, A., Lupton, R. H., Knapp, G. R., Gunn, J. E., Covey, K. R., Allyn Smith, J., Miknaitis, G., Doi, M., Tanaka, M., Fukugita, M., Kent, S., Finkbeiner, D., Quinn, T. R., Hawley, S., Anderson, S., Kiuchi, F., Chen, A., Bushong, J., Sohi, H., Haggard, D., Kimball, A., McGurk, R., Barentine, J., Brewington, H., Harvanek, M., Kleinman, S., Krzesinski, J., Long, D., Nitta, A., Snedden, S., Lee, B., Pier, J. R., Harris, H., Brinkmann, J., and Schneider, D. P. (2010). The Milky Way Tomography with SDSS. III. Stellar Kinematics. *ApJ*, 716:1–29.

Bournaud, F., Chapon, D., Teyssier, R., Powell, L. C., Elmegreen, B. G., Elmegreen, D. M., Duc, P.-A., Contini, T., Epinat, B., and Shapiro, K. L. (2011). Hydrodynamics of High-redshift Galaxy Collisions: From Gas-rich Disks to Dispersion-dominated Mergers and Compact Spheroids. *ApJ*, 730:4.

Bournaud, F., Daddi, E., Elmegreen, B. G., Elmegreen, D. M., Nesvadba, N., Vanzella, E., Di Matteo, P., Le Tiran, L., Lehnert, M., and Elbaz, D. (2008). Observations and modeling of a clumpy galaxy at z = 1.6. Spectroscopic clues to the origin and evolution of chain galaxies. *A&A*, 486:741–753.

Bournaud, F. and Elmegreen, B. G. (2009). Unstable Disks at High Redshift: Evidence for Smooth Accretion in Galaxy Formation. *ApJ*, 694:L158–L161.

Bournaud, F., Elmegreen, B. G., and Elmegreen, D. M. (2007). Rapid Formation of Exponential Disks and Bulges at High Redshift from the Dynamical Evolution of Clump-Cluster and Chain Galaxies. *ApJ*, 670:237–248.

Bournaud, F., Perret, V., Renaud, F., Dekel, A., Elmegreen, B. G., Elmegreen, D. M., Teyssier, R., Amram, P., Daddi, E., Duc, P.-A., Elbaz, D., Epinat, B., Gabor, J. M., Juneau, S., Kraljic, K., and Le Floch', E. (2014). The Long Lives of Giant Clumps and the Birth of Outflows in Gas-rich Galaxies at High Redshift. *ApJ*, 780:57.

Bovill, M. S. and Ricotti, M. (2009). Pre-Reionization Fossils, Ultra-Faint Dwarfs, and the Missing Galactic Satellite Problem. *ApJ*, 693:1859–1870.

Bovy, J., Rix, H.-W., and Hogg, D. W. (2012a). The Milky Way Has No Distinct Thick Disk. *ApJ*, 751:131.

Bovy, J., Rix, H.-W., Liu, C., Hogg, D. W., Beers, T. C., and Lee, Y. S. (2012b). The Spatial Structure of Mono-abundance Sub-populations of the Milky Way Disk. *ApJ*, 753:148.

Bovy, J., Rix, H.-W., Schlafly, E. F., Nidever, D. L., Holtzman, J. A., Shetrone, M., and Beers, T. C. (2016). The Stellar Population Structure of the Galactic Disk. *ApJ*, 823:30.

Boylan-Kolchin, M., Bullock, J. S., and Kaplinghat, M. (2011). Too big to fail? The puzzling darkness of massive Milky Way subhaloes. *MNRAS*, 415:L40–L44.

Boylan-Kolchin, M., Bullock, J. S., and Kaplinghat, M. (2012). The Milky Way's bright satellites as an apparent failure of ΛCDM. *MNRAS*, 422:1203–1218.

Boylan-Kolchin, M., Ma, C.-P., and Quataert, E. (2008). Dynamical friction and galaxy merging time-scales. *MNRAS*, 383:93–101.

Brook, C. B. and Di Cintio, A. (2015). Expanded haloes, abundance matching and too-big-to-fail in the Local Group. *MNRAS*, 450:3920–3934.

Brook, C. B., Di Cintio, A., Knebe, A., Gottlöber, S., Hoffman, Y., Yepes, G., and Garrison-Kimmel, S. (2014). The Stellar-to-halo Mass Relation for Local Group Galaxies. *ApJ*, 784:L14.

Brook, C. B., Kawata, D., Gibson, B. K., and Freeman, K. C. (2004). The Emergence of the Thick Disk in a Cold Dark Matter Universe. *ApJ*, 612:894–899.

Brook, C. B., Stinson, G., Gibson, B. K., Roškar, R., Wadsley, J., and Quinn, T. (2012). Hierarchical formation of bulgeless galaxies - II. Redistribution of angular momentum via galactic fountains. *MNRAS*, 419:771–779.

Brooks, A. (2008). *The role of gas in the evolution of disk galaxies*. PhD thesis, University of Washington.

Brooks, A. M., Papastergis, E., Christensen, C. R., Governato, F., Stilp, A., Quinn, T. R., and Wadsley, J. (2017). How to Reconcile the Observed Velocity Function of Galaxies with Theory. *ApJ*, 850:97.

Brooks, A. M. and Zolotov, A. (2014). Why Baryons Matter: The Kinematics of Dwarf Spheroidal Satellites. *ApJ*, 786:87.

Brown, T. M., Tumlinson, J., Geha, M., Simon, J. D., Vargas, L. C., VandenBerg, D. A., Kirby, E. N., Kalirai, J. S., Avila, R. J., Gennaro, M., Ferguson, H. C., Muñoz, R. R., Guhathakurta, P., and Renzini, A. (2014). The Quenching of the Ultra-faint Dwarf Galaxies in the Reionization Era. *ApJ*, 796:91.

Bruzual, G. and Charlot, S. (2003). Stellar population synthesis at the resolution of 2003. *MNRAS*, 344:1000–1028.

Bryan, G. L. and Norman, M. L. (1998). Statistical Properties of X-Ray Clusters: Analytic and Numerical Comparisons. *ApJ*, 495:80–99.

Buck, T., Dutton, A. A., and Macciò, A. V. (2016). Simulated ΛCDM analogues of the thin plane of satellites around the Andromeda galaxy are not kinematically coherent structures. *MNRAS*, 460:4348–4365.

Buck, T., Macciò, A. V., and Dutton, A. A. (2015). Evidence for Early Filamentary Accretion from the Andromeda Galaxy's Thin Plane of Satellites. *ApJ*, 809:49.

Buck, T., Macciò, A. V., Dutton, A. A., Obreja, A., and Frings, J. (2018a). NIHAO XV: The environmental impact of the host galaxy on galactic satellite and field dwarf

galaxies. *ArXiv e-prints*.

Buck, T., Macciò, A. V., Obreja, A., Dutton, A. A., Domínguez-Tenreiro, R., and Granato, G. L. (2017). NIHAO XIII: Clumpy discs or clumpy light in high-redshift galaxies? *MNRAS*, 468:3628–3649.

Buck, T., Ness, M., Obreja, A., Macciò, A. V., and Dutton, A. A. (2018b). Stars behind bars II: A cosmological formation scenario of the Milky Way's central stellar structure. *ArXiv e-prints*.

Buck, T., Ness, M. K., Macciò, A. V., Obreja, A., and Dutton, A. A. (2018c). Stars Behind Bars. I. The Milky Way's Central Stellar Populations. *ApJ*, 861:88.

Bullock, J. S. and Boylan-Kolchin, M. (2017). Small-Scale Challenges to the ΛCDM Paradigm. *ARA&A*, 55:343–387.

Bullock, J. S., Dekel, A., Kolatt, T. S., Kravtsov, A. V., Klypin, A. A., Porciani, C., and Primack, J. R. (2001). A Universal Angular Momentum Profile for Galactic Halos. *ApJ*, 555:240–257.

Bullock, J. S. and Johnston, K. V. (2005). Tracing Galaxy Formation with Stellar Halos. I. Methods. *ApJ*, 635:931–949.

Bullock, J. S., Kravtsov, A. V., and Weinberg, D. H. (2000). Reionization and the Abundance of Galactic Satellites. *ApJ*, 539:517–521.

Bundy, K., Bershady, M. A., Law, D. R., Yan, R., Drory, N., MacDonald, N., Wake, D. A., Cherinka, B., Sánchez-Gallego, J. R., Weijmans, A.-M., Thomas, D., Tremonti, C., Masters, K., Coccato, L., Diamond-Stanic, A. M., Aragón-Salamanca, A., Avila-Reese, V., Badenes, C., Falcón-Barroso, J., Belfiore, F., Bizyaev, D., Blanc, G. A., Bland-Hawthorn, J., Blanton, M. R., Brownstein, J. R., Byler, N., Cappellari, M., Conroy, C., Dutton, A. A., Emsellem, E., Etherington, J., Frinchaboy, P. M., Fu, H., Gunn, J. E., Harding, P., Johnston, E. J., Kauffmann, G., Kinemuchi, K., Klaene, M. A., Knapen, J. H., Leauthaud, A., Li, C., Lin, L., Maiolino, R., Malanushenko, V., Malanushenko, E., Mao, S., Maraston, C., McDermid, R. M., Merrifield, M. R., Nichol, R. C., Oravetz, D., Pan, K., Parejko, J. K., Sanchez, S. F., Schlegel, D., Simmons, A., Steele, O., Steinmetz, M., Thanjavur, K., Thompson, B. A., Tinker, J. L., van den Bosch, R. C. E., Westfall, K. B., Wilkinson, D., Wright, S., Xiao, T., and Zhang, K. (2015). Overview of the SDSS-IV MaNGA Survey: Mapping nearby Galaxies at Apache Point Observatory. *ApJ*, 798:7.

Buote, D. A. and Canizares, C. R. (1992). X-ray constraints on the shape of the dark matter in five Abell clusters. *ApJ*, 400:385–397.

Bureau, M., Aronica, G., Athanassoula, E., Dettmar, R.-J., Bosma, A., and Freeman, K. C. (2006). K-band observations of boxy bulges - I. Morphology and surface brightness profiles. *MNRAS*, 370:753–772.

Bureau, M. and Athanassoula, E. (2005). Bar Diagnostics in Edge-On Spiral Galaxies. III. N-Body Simulations of Disks. *ApJ*, 626:159–173.

Bureau, M. and Freeman, K. C. (1999). The Nature of Boxy/Peanut-Shaped Bulges in Spiral Galaxies. *AJ*, 118:126–138.

Burkert, A. (1995). The Structure of Dark Matter Halos in Dwarf Galaxies. *ApJ*, 447:L25–L28.

Burles, S., Nollett, K. M., and Turner, M. S. (2001). Big Bang Nucleosynthesis Predictions for Precision Cosmology. *ApJ*, 552:L1–L5.

Cacciato, M., Dekel, A., and Genel, S. (2012). Evolution of violent gravitational disc instability in galaxies: late stabilization by transition from gas to stellar dominance. *MNRAS*, 421:818–831.

Caldwell, N., Walker, M. G., Mateo, M., Olszewski, E. W., Koposov, S., Belokurov, V., Torrealba, G., Geringer-Sameth, A., and Johnson, C. I. (2017). Crater 2: An Extremely Cold Dark Matter Halo. *ApJ*, 839:20.

Carollo, D., Beers, T. C., Chiba, M., Norris, J. E., Freeman, K. C., Lee, Y. S., Ivezić, Ž., Rockosi, C. M., and Yanny, B. (2010). Structure and Kinematics of the Stellar Halos and Thick Disks of the Milky Way Based on Calibration Stars from Sloan Digital Sky Survey DR7. *ApJ*, 712:692–727.

Carr, B. J. (1978). On the cosmological density of black holes. *Comments on Astrophysics*, 7:161–173.

Cautun, M., Bose, S., Frenk, C. S., Guo, Q., Han, J., Hellwing, W. A., Sawala, T., and Wang, W. (2015). Planes of satellite galaxies: when exceptions are the rule. *ArXiv e-prints*.

Cautun, M. and Frenk, C. S. (2017). The tangential velocity excess of the Milky Way satellites. *MNRAS*, 468:L41–L45.

Cautun, M., Frenk, C. S., van de Weygaert, R., Hellwing, W. A., and Jones, B. J. T. (2014). Milky Way mass constraints from the Galactic satellite gap. *MNRAS*, 445:2049–2060.

Ceverino, D., Dekel, A., and Bournaud, F. (2010). High-redshift clumpy discs and bulges in cosmological simulations. *MNRAS*, 404:2151–2169.

Ceverino, D., Dekel, A., Mandelker, N., Bournaud, F., Burkert, A., Genzel, R., and Primack, J. (2012). Rotational support of giant clumps in high-z disc galaxies. *MNRAS*, 420:3490–3520.

Ceverino, D., Dekel, A., Tweed, D., and Primack, J. (2015). Early formation of massive, compact, spheroidal galaxies with classical profiles by violent disc instability or mergers. *MNRAS*, 447:3291–3310.

Ceverino, D., Klypin, A., Klimek, E. S., Trujillo-Gomez, S., Churchill, C. W., Primack, J., and Dekel, A. (2014). Radiative feedback and the low efficiency of galaxy formation in low-mass haloes at high redshift. *MNRAS*, 442:1545–1559.

Chabrier, G. (2003). Galactic Stellar and Substellar Initial Mass Function. *PASP*, 115:763–795.

Chan, T. K., Kereš, D., Oñorbe, J., Hopkins, P. F., Muratov, A. L., Faucher-Giguère, C.-A., and Quataert, E. (2015). The impact of baryonic physics on the structure of dark matter haloes: the view from the FIRE cosmological simulations. *MNRAS*, 454:2981–3001.

Chandrasekhar, S. (1943). Dynamical Friction. I. General Considerations: the Coefficient of Dynamical Friction. *ApJ*, 97:255.

Chang, J., Macciò, A. V., and Kang, X. (2013). The dependence of tidal stripping efficiency on the satellite and host galaxy morphology. *MNRAS*, 431:3533–3542.

Chiboucas, K., Jacobs, B. A., Tully, R. B., and Karachentsev, I. D. (2013). Confirmation of Faint Dwarf Galaxies in the M81 Group. *AJ*, 146:126.

Ciambur, B. C., Graham, A. W., and Bland-Hawthorn, J. (2017). Quantifying the (X/peanut)-shaped structure of the Milky Way - new constraints on the bar geometry. *MNRAS*, 471:3988–4004.

Cirasuolo, M., Afonso, J., Bender, R., Bonifacio, P., Evans, C., Kaper, L., Oliva, E., Vanzi, L., Abreu, M., Atad-Ettedgui, E., Babusiaux, C., Bauer, F. E., Best, P., Bezawada, N., Bryson, I. R., Cabral, A., Caputi, K., Centrone, M., Chemla, F., Cimatti, A., Cioni, M.-R., Clementini, G., Coelho, J., Daddi, E., Dunlop, J. S., Feltzing, S., Ferguson, A., Flores, H., Fontana, A., Fynbo, J., Garilli, B., Glauser, A. M., Guinouard, I., Hammer, J.-F., Hastings, P. R., Hess, H.-J., Ivison, R. J., Jagourel, P., Jarvis, M., Kauffman, G., Lawrence, A., Lee, D., Li Causi, G., Lilly, S., Lorenzetti, D., Maiolino, R., Mannucci, F., McLure, R., Minniti, D., Montgomery, D., Muschielok, B., Nandra, K., Navarro, R., Norberg, P., Origlia, L., Padilla, N., Peacock, J., Pedicini, F., Pentericci, L., Pragt, J., Puech, M., Randich, S., Renzini, A., Ryde, N., Rodrigues, M., Royer, F., Saglia, R., Sánchez, A., Schnetler, H., Sobral, D., Speziali, R., Todd, S., Tolstoy, E., Torres, M., Venema, L., Vitali, F., Wegner, M., Wells, M., Wild, V., and Wright, G. (2012). MOONS: a multi-object optical and near-infrared spectrograph for the VLT. In *Ground-based and Airborne Instrumentation for Astronomy IV*, volume 8446 of *Proc. SPIE*, page 84460S.

Clarkson, W., Sahu, K., Anderson, J., Smith, T. E., Brown, T. M., Rich, R. M., Casertano, S., Bond, H. E., Livio, M., Minniti, D., Panagia, N., Renzini, A., Valenti, J., and Zoccali, M. (2008). Stellar Proper Motions in the Galactic Bulge from Deep Hubble Space Telescope ACS WFC Photometry. *ApJ*, 684:1110–1142.

Clarkson, W. I., Sahu, K. C., Anderson, J., Rich, R. M., Smith, T. E., Brown, T. M., Bond, H. E., Livio, M., Minniti, D., Renzini, A., and Zoccali, M. (2011). The First Detection of Blue Straggler Stars in the Milky Way Bulge. *ApJ*, 735:37.

Cole, S., Percival, W. J., Peacock, J. A., Norberg, P., Baugh, C. M., Frenk, C. S., Baldry, I., Bland-Hawthorn, J., Bridges, T., Cannon, R., Colless, M., Collins, C., Couch, W., Cross, N. J. G., Dalton, G., Eke, V. R., De Propris, R., Driver, S. P., Efstathiou, G., Ellis, R. S., Glazebrook, K., Jackson, C., Jenkins, A., Lahav, O., Lewis, I., Lumsden,

S., Maddox, S., Madgwick, D., Peterson, B. A., Sutherland, W., and Taylor, K. (2005). The 2dF Galaxy Redshift Survey: power-spectrum analysis of the final data set and cosmological implications. *MNRAS*, 362:505–534.

Colless, M., Dalton, G., Maddox, S., Sutherland, W., Norberg, P., Cole, S., Bland-Hawthorn, J., Bridges, T., Cannon, R., Collins, C., Couch, W., Cross, N., Deeley, K., De Propris, R., Driver, S. P., Efstathiou, G., Ellis, R. S., Frenk, C. S., Glazebrook, K., Jackson, C., Lahav, O., Lewis, I., Lumsden, S., Madgwick, D., Peacock, J. A., Peterson, B. A., Price, I., Seaborne, M., and Taylor, K. (2001). The 2dF Galaxy Redshift Survey: spectra and redshifts. *MNRAS*, 328:1039–1063.

Collins, M. L. M., Chapman, S. C., Irwin, M. J., Martin, N. F., Ibata, R. A., Zucker, D. B., Blain, A., Ferguson, A. M. N., Lewis, G. F., McConnachie, A. W., and Peñarrubia, J. (2010). A Keck/DEIMOS spectroscopic survey of the faint M31 satellites AndIX, AndXI, AndXII and AndXIII†. *MNRAS*, 407:2411–2433.

Collins, M. L. M., Chapman, S. C., Rich, R. M., Ibata, R. A., Martin, N. F., Irwin, M. J., Bate, N. F., Lewis, G. F., Peñarrubia, J., Arimoto, N., Casey, C. M., Ferguson, A. M. N., Koch, A., McConnachie, A. W., and Tanvir, N. (2013). A Kinematic Study of the Andromeda Dwarf Spheroidal System. *ApJ*, 768:172.

Combes, F., Debbasch, F., Friedli, D., and Pfenniger, D. (1990). Box and peanut shapes generated by stellar bars. *A&A*, 233:82–95.

Combes, F. and Sanders, R. H. (1981). Formation and properties of persisting stellar bars. *A&A*, 96:164–173.

Conn, A. R., Ibata, R. A., Lewis, G. F., Parker, Q. A., Zucker, D. B., Martin, N. F., McConnachie, A. W., Irwin, M. J., Tanvir, N., Fardal, M. A., Ferguson, A. M. N., Chapman, S. C., and Valls-Gabaud, D. (2012). A Bayesian Approach to Locating the Red Giant Branch Tip Magnitude. II. Distances to the Satellites of M31. *ApJ*, 758:11.

Conn, A. R., Lewis, G. F., Ibata, R. A., Parker, Q. A., Zucker, D. B., McConnachie, A. W., Martin, N. F., Valls-Gabaud, D., Tanvir, N., Irwin, M. J., Ferguson, A. M. N., and Chapman, S. C. (2013). The Three-dimensional Structure of the M31 Satellite System; Strong Evidence for an Inhomogeneous Distribution of Satellites. *ApJ*, 766:120.

Conroy, C. and van Dokkum, P. G. (2012). The Stellar Initial Mass Function in Early-type Galaxies From Absorption Line Spectroscopy. II. Results. *ApJ*, 760:71.

Conroy, C. and Wechsler, R. H. (2009). Connecting Galaxies, Halos, and Star Formation Rates Across Cosmic Time. *ApJ*, 696:620–635.

Conroy, C., Wechsler, R. H., and Kravtsov, A. V. (2006). Modeling Luminosity-dependent Galaxy Clustering through Cosmic Time. *ApJ*, 647:201–214.

Cooper, A. P., Cole, S., Frenk, C. S., White, S. D. M., Helly, J., Benson, A. J., De Lucia, G., Helmi, A., Jenkins, A., Navarro, J. F., Springel, V., and Wang, J. (2010). Galactic stellar haloes in the CDM model. *MNRAS*, 406:744–766.

Courteau, S., Dutton, A. A., van den Bosch, F. C., MacArthur, L. A., Dekel, A., McIntosh, D. H., and Dale, D. A. (2007). Scaling Relations of Spiral Galaxies. *ApJ*, 671:203–225.

Crain, R. A., Schaye, J., Bower, R. G., Furlong, M., Schaller, M., Theuns, T., Dalla Vecchia, C., Frenk, C. S., McCarthy, I. G., Helly, J. C., Jenkins, A., Rosas-Guevara, Y. M., White, S. D. M., and Trayford, J. W. (2015). The EAGLE simulations of galaxy formation: calibration of subgrid physics and model variations. *MNRAS*, 450:1937–1961.

Crnojević, D., Sand, D. J., Zaritsky, D., Spekkens, K., Willman, B., and Hargis, J. R. (2016). Deep Imaging of Eridanus II and Its Lone Star Cluster. *ApJ*, 824:L14.

Daddi, E., Bournaud, F., Walter, F., Dannerbauer, H., Carilli, C. L., Dickinson, M., Elbaz, D., Morrison, G. E., Riechers, D., Onodera, M., Salmi, F., Krips, M., and Stern, D. (2010). Very High Gas Fractions and Extended Gas Reservoirs in z = 1.5 Disk Galaxies. *ApJ*, 713:686–707.

Dalcanton, J. J., Spergel, D. N., and Summers, F. J. (1997). The Formation of Disk Galaxies. *ApJ*, 482:659–676.

de Bernardis, P., Ade, P. A. R., Bock, J. J., Bond, J. R., Borrill, J., Boscaleri, A., Coble, K., Crill, B. P., De Gasperis, G., Farese, P. C., Ferreira, P. G., Ganga, K., Giacometti, M., Hivon, E., Hristov, V. V., Iacoangeli, A., Jaffe, A. H., Lange, A. E., Martinis, L., Masi, S., Mason, P. V., Mauskopf, P. D., Melchiorri, A., Miglio, L., Montroy, T., Netterfield, C. B., Pascale, E., Piacentini, F., Pogosyan, D., Prunet, S., Rao, S., Romeo, G., Ruhl, J. E., Scaramuzzi, F., Sforna, D., and Vittorio, N. (2000). A flat Universe from high-resolution maps of the cosmic microwave background radiation. *Nature*, 404:955–959.

de Blok, W. J. G., Walter, F., Brinks, E., Trachternach, C., Oh, S.-H., and Kennicutt, Jr., R. C. (2008). High-Resolution Rotation Curves and Galaxy Mass Models from THINGS. *AJ*, 136:2648–2719.

de Jong, R. S. (1996a). Near-infrared and optical broadband surface photometry of 86 face-on disk dominated galaxies. III. The statistics of the disk and bulge parameters. *A&A*, 313:45–64.

de Jong, R. S. (1996b). Near-infrared and optical broadband surface photometry of 86 face-on disk dominated galaxies. IV. Using color profiles to study stellar and dust content of galaxies. *A&A*, 313:377–395.

de Jong, R. S. and Consortium, . (2015). 4MOST - The new wide-field, high-multiplex spectroscopic survey facility for ESO's VISTA telescope. *IAU General Assembly*, 22:2255843.

De Lucia, G., Weinmann, S., Poggianti, B. M., Aragón-Salamanca, A., and Zaritsky, D. (2012). The environmental history of group and cluster galaxies in a Λ cold dark matter universe. *MNRAS*, 423:1277–1292.

De Silva, G. M., Freeman, K. C., Bland-Hawthorn, J., Martell, S., de Boer, E. W., Asplund, M., Keller, S., Sharma, S., Zucker, D. B., Zwitter, T., Anguiano, B., Bacigalupo, C.,

Bayliss, D., Beavis, M. A., Bergemann, M., Campbell, S., Cannon, R., Carollo, D., Casagrande, L., Casey, A. R., Da Costa, G., D'Orazi, V., Dotter, A., Duong, L., Heger, A., Ireland, M. J., Kafle, P. R., Kos, J., Lattanzio, J., Lewis, G. F., Lin, J., Lind, K., Munari, U., Nataf, D. M., O'Toole, S., Parker, Q., Reid, W., Schlesinger, K. J., Sheinis, A., Simpson, J. D., Stello, D., Ting, Y.-S., Traven, G., Watson, F., Wittenmyer, R., Yong, D., and Žerjal, M. (2015). The GALAH survey: scientific motivation. *MNRAS*, 449:2604–2617.

de Vaucouleurs, G. (1974). Structure, dynamics and statistical properties of galaxies. In Shakeshaft, J. R., editor, *The Formation and Dynamics of Galaxies*, volume 58 of *IAU Symposium*, pages 1–52.

Deason, A. J., McCarthy, I. G., Font, A. S., Evans, N. W., Frenk, C. S., Belokurov, V., Libeskind, N. I., Crain, R. A., and Theuns, T. (2011). Mismatch and misalignment: dark haloes and satellites of disc galaxies. *MNRAS*, 415:2607–2625.

Debattista, V. P., Gonzalez, O. A., Sanderson, R. E., El-Badry, K., Garrison-Kimmel, S., Wetzel, A., Faucher-Giguère, C.-A., and Hopkins, P. F. (2018). Formation, vertex deviation and age of the Milky Way's bulge: input from a cosmological simulation with a late-forming bar. *ArXiv e-prints*.

Debattista, V. P., Mayer, L., Carollo, C. M., Moore, B., Wadsley, J., and Quinn, T. (2006). The Secular Evolution of Disk Structural Parameters. *ApJ*, 645:209–227.

Debattista, V. P., Ness, M., Gonzalez, O. A., Freeman, K., Zoccali, M., and Minniti, D. (2017). Separation of stellar populations by an evolving bar: implications for the bulge of the Milky Way. *MNRAS*, 469:1587–1611.

Dehnen, W. and Aly, H. (2012). Improving convergence in smoothed particle hydrodynamics simulations without pairing instability. *MNRAS*, 425:1068–1082.

Dékány, I., Minniti, D., Catelan, M., Zoccali, M., Saito, R. K., Hempel, M., and Gonzalez, O. A. (2013). VVV Survey Near-infrared Photometry of Known Bulge RR Lyrae Stars: The Distance to the Galactic Center and Absence of a Barred Distribution of the Metal-poor Population. *ApJ*, 776:L19.

Dekel, A. and Birnboim, Y. (2006). Galaxy bimodality due to cold flows and shock heating. *MNRAS*, 368:2–20.

Dekel, A., Birnboim, Y., Engel, G., Freundlich, J., Goerdt, T., Mumcuoglu, M., Neistein, E., Pichon, C., Teyssier, R., and Zinger, E. (2009a). Cold streams in early massive hot haloes as the main mode of galaxy formation. *Nature*, 457:451–454.

Dekel, A., Sari, R., and Ceverino, D. (2009b). Formation of Massive Galaxies at High Redshift: Cold Streams, Clumpy Disks, and Compact Spheroids. *ApJ*, 703:785–801.

Dekel, A. and Silk, J. (1986). The origin of dwarf galaxies, cold dark matter, and biased galaxy formation. *ApJ*, 303:39–55.

Del Popolo, A. and Le Delliou, M. (2017). Small Scale Problems of the ΛCDM Model: A Short Review. *Galaxies*, 5:17.

di Cintio, A., Knebe, A., Libeskind, N. I., Yepes, G., Gottlöber, S., and Hoffman, Y. (2011). Too small to succeed? Lighting up massive dark matter subhaloes of the Milky Way. *MNRAS*, 417:L74–L78.

Di Matteo, P. (2016). The Disc Origin of the Milky Way Bulge. *PASA*, 33:e027.

Di Matteo, P., Gómez, A., Haywood, M., Combes, F., Lehnert, M. D., Ness, M., Snaith, O. N., Katz, D., and Semelin, B. (2015). Why the Milky Way's bulge is not only a bar formed from a cold thin disk. *A&A*, 577:A1.

Di Matteo, P., Haywood, M., Gómez, A., van Damme, L., Combes, F., Hallé, A., Semelin, B., Lehnert, M. D., and Katz, D. (2014). Mapping a stellar disk into a boxy bulge: The outside-in part of the Milky Way bulge formation. *A&A*, 567:A122.

Dicke, R. H. and Peebles, P. J. E. (1979). The big bang cosmology - enigmas and nostrums. In *General Relativity: An Einstein centenary survey*, pages 504–517.

Diemand, J., Kuhlen, M., and Madau, P. (2007). Formation and Evolution of Galaxy Dark Matter Halos and Their Substructure. *ApJ*, 667:859–877.

Diemand, J., Kuhlen, M., Madau, P., Zemp, M., Moore, B., Potter, D., and Stadel, J. (2008). Clumps and streams in the local dark matter distribution. *Nature*, 454:735–738.

Diemer, B., Mansfield, P., Kravtsov, A. V., and More, S. (2017). The Splashback Radius of Halos from Particle Dynamics. II. Dependence on Mass, Accretion Rate, Redshift, and Cosmology. *ApJ*, 843:140.

Djorgovski, S. and Davis, M. (1987). Fundamental properties of elliptical galaxies. *ApJ*, 313:59–68.

Dodelson, S. (2003). *Modern cosmology*.

Doménech-Moral, M., Martínez-Serrano, F. J., Domínguez-Tenreiro, R., and Serna, A. (2012). Formation of galaxies in Λcold dark matter cosmologies - I. The fine structure of disc galaxies. *MNRAS*, 421:2510–2530.

Domínguez-Tenreiro, R., Obreja, A., Granato, G. L., Schurer, A., Alpresa, P., Silva, L., Brook, C. B., and Serna, A. (2014). GRASIL-3D: an implementation of dust effects in the SEDs of simulated galaxies. *MNRAS*, 439:3868–3889.

Doroshkevich, A. G. (1970). The space structure of perturbations and the origin of rotation of galaxies in the theory of fluctuation. *Astrofizika*, 6:581–600.

Dressler, A., Lynden-Bell, D., Burstein, D., Davies, R. L., Faber, S. M., Terlevich, R., and Wegner, G. (1987). Spectroscopy and photometry of elliptical galaxies. I - A new distance estimator. *ApJ*, 313:42–58.

Drlica-Wagner, A., Bechtol, K., Rykoff, E. S., Luque, E., Queiroz, A., Mao, Y.-Y., Wechsler, R. H., Simon, J. D., Santiago, B., Yanny, B., Balbinot, E., Dodelson, S., Fausti Neto, A., James, D. J., Li, T. S., Maia, M. A. G., Marshall, J. L., Pieres, A., Stringer, K., Walker, A. R., Abbott, T. M. C., Abdalla, F. B., Allam, S., Benoit-Lévy, A., Bernstein, G. M., Bertin, E., Brooks, D., Buckley-Geer, E., Burke, D. L., Carnero Rosell, A., Carrasco Kind, M., Carretero, J., Crocce, M., da Costa, L. N., Desai, S., Diehl, H. T., Dietrich,

J. P., Doel, P., Eifler, T. F., Evrard, A. E., Finley, D. A., Flaugher, B., Fosalba, P., Frieman, J., Gaztanaga, E., Gerdes, D. W., Gruen, D., Gruendl, R. A., Gutierrez, G., Honscheid, K., Kuehn, K., Kuropatkin, N., Lahav, O., Martini, P., Miquel, R., Nord, B., Ogando, R., Plazas, A. A., Reil, K., Roodman, A., Sako, M., Sanchez, E., Scarpine, V., Schubnell, M., Sevilla-Noarbe, I., Smith, R. C., Soares-Santos, M., Sobreira, F., Suchyta, E., Swanson, M. E. C., Tarle, G., Tucker, D., Vikram, V., Wester, W., Zhang, Y., Zuntz, J., and DES Collaboration (2015). Eight Ultra-faint Galaxy Candidates Discovered in Year Two of the Dark Energy Survey. *ApJ*, 813:109.

Dubinski, J. and Carlberg, R. G. (1991). The structure of cold dark matter halos. *ApJ*, 378:496–503.

Dutton, A. A., Conroy, C., van den Bosch, F. C., Simard, L., Mendel, J. T., Courteau, S., Dekel, A., More, S., and Prada, F. (2011). Dark halo response and the stellar initial mass function in early-type and late-type galaxies. *MNRAS*, 416:322–345.

Dutton, A. A. and Macciò, A. V. (2014). Cold dark matter haloes in the Planck era: evolution of structural parameters for Einasto and NFW profiles. *MNRAS*, 441:3359–3374.

Dutton, A. A., Macciò, A. V., Frings, J., Wang, L., Stinson, G. S., Penzo, C., and Kang, X. (2016). NIHAO V: too big does not fail - reconciling the conflict between ΛCDM predictions and the circular velocities of nearby field galaxies. *MNRAS*, 457:L74–L78.

Dutton, A. A., Macciò, A. V., Mendel, J. T., and Simard, L. (2013a). Universal IMF versus dark halo response in early-type galaxies: breaking the degeneracy with the Fundamental Plane. *MNRAS*, 432:2496–2511.

Dutton, A. A., Obreja, A., Wang, L., Gutcke, T. A., Buck, T., Udrescu, S. M., Frings, J., Stinson, G. S., Kang, X., and Macciò, A. V. (2017). NIHAO XII: galactic uniformity in a ΛCDM universe. *MNRAS*, 467:4937–4950.

Dutton, A. A., Treu, T., Brewer, B. J., Marshall, P. J., Auger, M. W., Barnabè, M., Koo, D. C., Bolton, A. S., and Koopmans, L. V. E. (2013b). The SWELLS survey - V. A Salpeter stellar initial mass function in the bulges of massive spiral galaxies. *MNRAS*, 428:3183–3195.

Dutton, A. A. and van den Bosch, F. C. (2012). The angular momentum of disc galaxies: implications for gas accretion, outflows, and dynamical friction. *MNRAS*, 421:608–620.

Dutton, A. A., van den Bosch, F. C., Dekel, A., and Courteau, S. (2007). A Revised Model for the Formation of Disk Galaxies: Low Spin and Dark Halo Expansion. *ApJ*, 654:27–52.

Dwek, E., Arendt, R. G., Hauser, M. G., Kelsall, T., Lisse, C. M., Moseley, S. H., Silverberg, R. F., Sodroski, T. J., and Weiland, J. L. (1995). Morphology, near-infrared luminosity, and mass of the Galactic bulge from COBE DIRBE observations. *ApJ*, 445:716–730.

Efstathiou, G. (1992). Suppressing the formation of dwarf galaxies via photoionization. *MNRAS*, 256:43P–47P.

Efstathiou, G. and Jones, B. J. T. (1979). The rotation of galaxies - Numerical investigations of the tidal torque theory. *MNRAS*, 186:133–144.

Efstathiou, G., Kaiser, N., Saunders, W., Lawrence, A., Rowan-Robinson, M., Ellis, R. S., and Frenk, C. S. (1990). Largescale Clustering of IRAS Galaxies. *MNRAS*, 247:10P.

Eggen, O. J., Lynden-Bell, D., and Sandage, A. R. (1962). Evidence from the motions of old stars that the Galaxy collapsed. *ApJ*, 136:748.

Einasto, J. (1965). On the Construction of a Composite Model for the Galaxy and on the Determination of the System of Galactic Parameters. *Trudy Astrofizicheskogo Instituta Alma-Ata*, 5:87–100.

Einasto, J., Saar, E., Kaasik, A., and Chernin, A. D. (1974). Missing mass around galaxies - Morphological evidence. *Nature*, 252:111–113.

El-Badry, K., Bland-Hawthorn, J., Wetzel, A., Quataert, E., Weisz, D. R., Boylan-Kolchin, M., Hopkins, P. F., Faucher-Giguère, C.-A., Kereš, D., and Garrison-Kimmel, S. (2018). Where are the most ancient stars in the Milky Way? *ArXiv e-prints*.

El-Badry, K., Wetzel, A., Geha, M., Hopkins, P. F., Kereš, D., Chan, T. K., and Faucher-Giguère, C.-A. (2016). Breathing FIRE: How Stellar Feedback Drives Radial Migration, Rapid Size Fluctuations, and Population Gradients in Low-mass Galaxies. *ApJ*, 820:131.

Elbert, O. D., Bullock, J. S., Garrison-Kimmel, S., Rocha, M., Oñorbe, J., and Peter, A. H. G. (2015). Core formation in dwarf haloes with self-interacting dark matter: no fine-tuning necessary. *MNRAS*, 453:29–37.

Elmegreen, B. G., Bournaud, F., and Elmegreen, D. M. (2008). Bulge Formation by the Coalescence of Giant Clumps in Primordial Disk Galaxies. *ApJ*, 688:67–77.

Elmegreen, B. G. and Elmegreen, D. M. (2005). Stellar Populations in 10 Clump-Cluster Galaxies of the Hubble Ultra Deep Field. *ApJ*, 627:632–646.

Elmegreen, B. G. and Elmegreen, D. M. (2006). Observations of Thick Disks in the Hubble Space Telescope Ultra Deep Field. *ApJ*, 650:644–660.

Elmegreen, B. G., Elmegreen, D. M., Fernandez, M. X., and Lemonias, J. J. (2009). Bulge and Clump Evolution in Hubble Ultra Deep Field Clump Clusters, Chains and Spiral Galaxies. *ApJ*, 692:12–31.

Elmegreen, B. G., Elmegreen, D. M., Tompkins, B., and Jenks, L. G. (2017). Thick Disks in the Hubble Space Telescope Frontier Fields. *ApJ*, 847:14.

Elmegreen, D. M. (1998). *Galaxies and galactic structure*.

Elmegreen, D. M., Elmegreen, B. G., Ravindranath, S., and Coe, D. A. (2007). Resolved Galaxies in the Hubble Ultra Deep Field: Star Formation in Disks at High Redshift. *ApJ*, 658:763–777.

Faber, S. M. and Jackson, R. E. (1976). Velocity dispersions and mass-to-light ratios for elliptical galaxies. *ApJ*, 204:668–683.

Faber, S. M. and Lin, D. N. C. (1983). Is there nonluminous matter in dwarf spheroidal galaxies. *ApJ*, 266:L17–L20.

Fabian, A. C. (2012). Observational Evidence of Active Galactic Nuclei Feedback. *ARA&A*, 50:455–489.

Fall, S. M. and Efstathiou, G. (1980). Formation and rotation of disc galaxies with haloes. *MNRAS*, 193:189–206.

Fattahi, A., Navarro, J. F., Frenk, C. S., Oman, K., Sawala, T., and Schaller, M. (2017). Tidal stripping and the structure of dwarf galaxies in the Local Group. *ArXiv e-prints*.

Fattahi, A., Navarro, J. F., Sawala, T., Frenk, C. S., Sales, L. V., Oman, K., Schaller, M., and Wang, J. (2016). The cold dark matter content of Galactic dwarf spheroidals: no cores, no failures, no problem. *ArXiv e-prints*.

Faucher-Giguère, C.-A., Quataert, E., and Hopkins, P. F. (2013). Feedback-regulated star formation in molecular clouds and galactic discs. *MNRAS*, 433:1970–1990.

Ferguson, A. M. N., Johnson, R. A., Faria, D. C., Irwin, M. J., Ibata, R. A., Johnston, K. V., Lewis, G. F., and Tanvir, N. R. (2005). The Stellar Populations of the M31 Halo Substructure. *ApJ*, 622:L109–L112.

Ferland, G. J., Korista, K. T., Verner, D. A., Ferguson, J. W., Kingdon, J. B., and Verner, E. M. (1998). CLOUDY 90: Numerical Simulation of Plasmas and Their Spectra. *PASP*, 110:761–778.

Fillingham, S. P., Cooper, M. C., Pace, A. B., Boylan-Kolchin, M., Bullock, J. S., Garrison-Kimmel, S., and Wheeler, C. (2016). Under pressure: quenching star formation in low-mass satellite galaxies via stripping. *MNRAS*, 463:1916–1928.

Fitts, A., Boylan-Kolchin, M., Elbert, O. D., Bullock, J. S., Hopkins, P. F., Oñorbe, J., Wetzel, A., Wheeler, C., Faucher-Giguère, C.-A., Kereš, D., Skillman, E. D., and Weisz, D. R. (2017). fire in the field: simulating the threshold of galaxy formation. *MNRAS*, 471:3547–3562.

Fixsen, D. J. (2009). The Temperature of the Cosmic Microwave Background. *ApJ*, 707:916–920.

Flores, R. A. and Primack, J. R. (1994). Observational and theoretical constraints on singular dark matter halos. *ApJ*, 427:L1–L4.

Forbes, D. A., Beasley, M. A., Bekki, K., Brodie, J. P., and Strader, J. (2003). Galaxy Disruption in a Halo of Dark Matter. *Science*, 301:1217–1219.

Förster Schreiber, N. M., Genzel, R., Bouché, N., Cresci, G., Davies, R., Buschkamp, P., Shapiro, K., Tacconi, L. J., Hicks, E. K. S., Genel, S., Shapley, A. E., Erb, D. K., Steidel, C. C., Lutz, D., Eisenhauer, F., Gillessen, S., Sternberg, A., Renzini, A., Cimatti, A., Daddi, E., Kurk, J., Lilly, S., Kong, X., Lehnert, M. D., Nesvadba, N., Verma, A., McCracken, H., Arimoto, N., Mignoli, M., and Onodera, M. (2009). The SINS Survey: SINFONI Integral Field Spectroscopy of z ˜ 2 Star-forming Galaxies. *ApJ*, 706:1364–1428.

Förster Schreiber, N. M., Genzel, R., Lehnert, M. D., Bouché, N., Verma, A., Erb, D. K., Shapley, A. E., Steidel, C. C., Davies, R., Lutz, D., Nesvadba, N., Tacconi, L. J., Eisenhauer, F., Abuter, R., Gilbert, A., Gillessen, S., and Sternberg, A. (2006). SINFONI Integral Field Spectroscopy of z ˜ 2 UV-selected Galaxies: Rotation Curves and Dynamical Evolution. *ApJ*, 645:1062–1075.

Förster Schreiber, N. M., Shapley, A. E., Genzel, R., Bouché, N., Cresci, G., Davies, R., Erb, D. K., Genel, S., Lutz, D., Newman, S., Shapiro, K. L., Steidel, C. C., Sternberg, A., and Tacconi, L. J. (2011). Constraints on the Assembly and Dynamics of Galaxies. II. Properties of Kiloparsec-scale Clumps in Rest-frame Optical Emission of z ˜ 2 Star-forming Galaxies. *ApJ*, 739:45.

Fragkoudi, F., Di Matteo, P., Haywood, M., Gómez, A., Combes, F., Katz, D., and Semelin, B. (2017). Bars & boxy/peanut bulges in thin & thick discs: I. Morphology and *los* velocities of a fiducial model. *ArXiv e-prints*.

Fragkoudi, F., Di Matteo, P., Haywood, M., Schultheis, M., Khoperskov, S., Gómez, A., and Combes, F. (2018). The disc origin of the Milky Way bulge: Dissecting the chemo-morphological relations using N-body simulations and APOGEE. *ArXiv e-prints*.

Freeman, K., Ness, M., Wylie-de-Boer, E., Athanassoula, E., Bland-Hawthorn, J., Asplund, M., Lewis, G., Yong, D., Lane, R., Kiss, L., and Ibata, R. (2013). ARGOS - II. The Galactic bulge survey. *MNRAS*, 428:3660–3670.

Freeman, K. C. (1970). On the Disks of Spiral and So Galaxies. *ApJ*, 160:811.

Frenk, C. S. and White, S. D. M. (2012). Dark matter and cosmic structure. *Annalen der Physik*, 524:507–534.

Friedmann, A. (1922). Über die Krümmung des Raumes. *Zeitschrift fur Physik*, 10:377–386.

Frings, J., Macciò, A., Buck, T., Penzo, C., Dutton, A., Blank, M., and Obreja, A. (2017). The edge of galaxy formation - II. Evolution of Milky Way satellite analogues after infall. *MNRAS*, 472:3378–3389.

Fry, A. B., Governato, F., Pontzen, A., Quinn, T., Tremmel, M., Anderson, L., Menon, H., Brooks, A. M., and Wadsley, J. (2015). All about baryons: revisiting SIDM predictions at small halo masses. *MNRAS*, 452:1468–1479.

Fuhrmann, K. (1998). Nearby stars of the Galactic disk and halo. *A&A*, 338:161–183.

Gaia Collaboration, Brown, A. G. A., Vallenari, A., Prusti, T., de Bruijne, J. H. J., Mignard, F., Drimmel, R., Babusiaux, C., Bailer-Jones, C. A. L., Bastian, U., and et al. (2016a). Gaia Data Release 1. Summary of the astrometric, photometric, and survey properties. *A&A*, 595:A2.

Gaia Collaboration, Helmi, A., van Leeuwen, F., McMillan, P. J., Massari, D., Antoja, T., Robin, A., Lindegren, L., Bastian, U., and co-authors, . (2018). Gaia Data Release 2: Kinematics of globular clusters and dwarf galaxies around the Milky Way. *ArXiv*

e-prints.

Gaia Collaboration, Prusti, T., de Bruijne, J. H. J., Brown, A. G. A., Vallenari, A., Babusiaux, C., Bailer-Jones, C. A. L., Bastian, U., Biermann, M., Evans, D. W., and et al. (2016b). The Gaia mission. *A&A*, 595:A1.

Gallazzi, A., Charlot, S., Brinchmann, J., and White, S. D. M. (2006). Ages and metallicities of early-type galaxies in the Sloan Digital Sky Survey: new insight into the physical origin of the colour-magnitude and the Mg_2-σ_V relations. *MNRAS*, 370:1106–1124.

Gallazzi, A., Charlot, S., Brinchmann, J., White, S. D. M., and Tremonti, C. A. (2005). The ages and metallicities of galaxies in the local universe. *MNRAS*, 362:41–58.

Gamow, G. (1946). Expanding Universe and the Origin of Elements. *Physical Review*, 70:572–573.

Gamow, G. (1948). The Origin of Elements and the Separation of Galaxies. *Physical Review*, 74:505–506.

Gamow, G. and Teller, E. (1939). The Expanding Universe and the Origin of the Great Nebulæ. *Nature*, 143:116–117.

Gardner, E., Debattista, V. P., Robin, A. C., Vásquez, S., and Zoccali, M. (2014). N-body simulation insights into the X-shaped bulge of the Milky Way: kinematics and distance to the Galactic Centre. *MNRAS*, 438:3275–3290.

Garnavich, P. M., Jha, S., Challis, P., Clocchiatti, A., Diercks, A., Filippenko, A. V., Gilliland, R. L., Hogan, C. J., Kirshner, R. P., Leibundgut, B., Phillips, M. M., Reiss, D., Riess, A. G., Schmidt, B. P., Schommer, R. A., Smith, R. C., Spyromilio, J., Stubbs, C., Suntzeff, N. B., Tonry, J., and Carroll, S. M. (1998). Supernova Limits on the Cosmic Equation of State. *ApJ*, 509:74–79.

Garrison-Kimmel, S., Boylan-Kolchin, M., Bullock, J. S., and Kirby, E. N. (2014). Too big to fail in the Local Group. *MNRAS*, 444:222–236.

Garrison-Kimmel, S., Wetzel, A., Bullock, J. S., Hopkins, P. F., Boylan-Kolchin, M., Faucher-Giguère, C.-A., Kereš, D., Quataert, E., Sanderson, R. E., Graus, A. S., and Kelley, T. (2017). Not so lumpy after all: modelling the depletion of dark matter subhaloes by Milky Way-like galaxies. *MNRAS*, 471:1709–1727.

Geller, M. J. and Huchra, J. P. (1989). Mapping the universe. *Science*, 246:897–903.

Genel, S., Naab, T., Genzel, R., Förster Schreiber, N. M., Sternberg, A., Oser, L., Johansson, P. H., Davé, R., Oppenheimer, B. D., and Burkert, A. (2012). Short-lived Star-forming Giant Clumps in Cosmological Simulations of z $\sim$ 2 Disks. *ApJ*, 745:11.

Gennaro, M., Tchernyshyov, K., Brown, T. M., and Gordon, K. D. (2015). A New Method for Deriving the Stellar Birth Function of Resolved Stellar Populations. *ApJ*, 808:45.

Genzel, R., Burkert, A., Bouché, N., Cresci, G., Förster Schreiber, N. M., Shapley, A., Shapiro, K., Tacconi, L. J., Buschkamp, P., Cimatti, A., Daddi, E., Davies, R., Eisenhauer, F., Erb, D. K., Genel, S., Gerhard, O., Hicks, E., Lutz, D., Naab, T., Ott,

T., Rabien, S., Renzini, A., Steidel, C. C., Sternberg, A., and Lilly, S. J. (2008). From Rings to Bulges: Evidence for Rapid Secular Galaxy Evolution at z ˜ 2 from Integral Field Spectroscopy in the SINS Survey. *ApJ*, 687:59–77.

Genzel, R., Newman, S., Jones, T., Förster Schreiber, N. M., Shapiro, K., Genel, S., Lilly, S. J., Renzini, A., Tacconi, L. J., Bouché, N., Burkert, A., Cresci, G., Buschkamp, P., Carollo, C. M., Ceverino, D., Davies, R., Dekel, A., Eisenhauer, F., Hicks, E., Kurk, J., Lutz, D., Mancini, C., Naab, T., Peng, Y., Sternberg, A., Vergani, D., and Zamorani, G. (2011). The Sins Survey of z ˜ 2 Galaxy Kinematics: Properties of the Giant Star-forming Clumps. *ApJ*, 733:101.

Genzel, R., Tacconi, L. J., Eisenhauer, F., Förster Schreiber, N. M., Cimatti, A., Daddi, E., Bouché, N., Davies, R., Lehnert, M. D., Lutz, D., Nesvadba, N., Verma, A., Abuter, R., Shapiro, K., Sternberg, A., Renzini, A., Kong, X., Arimoto, N., and Mignoli, M. (2006). The rapid formation of a large rotating disk galaxy three billion years after the Big Bang. *Nature*, 442:786–789.

Genzel, R., Tacconi, L. J., Lutz, D., Saintonge, A., Berta, S., Magnelli, B., Combes, F., García-Burillo, S., Neri, R., Bolatto, A., Contini, T., Lilly, S., Boissier, J., Boone, F., Bouché, N., Bournaud, F., Burkert, A., Carollo, M., Colina, L., Cooper, M. C., Cox, P., Feruglio, C., Förster Schreiber, N. M., Freundlich, J., Gracia-Carpio, J., Juneau, S., Kovac, K., Lippa, M., Naab, T., Salome, P., Renzini, A., Sternberg, A., Walter, F., Weiner, B., Weiss, A., and Wuyts, S. (2015). Combined CO and Dust Scaling Relations of Depletion Time and Molecular Gas Fractions with Cosmic Time, Specific Star-formation Rate, and Stellar Mass. *ApJ*, 800:20.

Gerhard, O. (2002). The Galactic Bar. In Da Costa, G. S., Sadler, E. M., and Jerjen, H., editors, *The Dynamics, Structure & History of Galaxies: A Workshop in Honour of Professor Ken Freeman*, volume 273 of *Astronomical Society of the Pacific Conference Series*, page 73.

Ghez, A. M., Salim, S., Weinberg, N. N., Lu, J. R., Do, T., Dunn, J. K., Matthews, K., Morris, M. R., Yelda, S., Becklin, E. E., Kremenek, T., Milosavljevic, M., and Naiman, J. (2008). Measuring Distance and Properties of the Milky Way's Central Supermassive Black Hole with Stellar Orbits. *ApJ*, 689:1044–1062.

Gibbons, S. L. J., Belokurov, V., and Evans, N. W. (2017). A tail of two populations: chemo-dynamics of the Sagittarius stream and implications for its original mass. *MNRAS*, 464:794–809.

Gill, S. P. D., Knebe, A., and Gibson, B. K. (2004). The evolution of substructure - I. A new identification method. *MNRAS*, 351:399–409.

Gill, S. P. D., Knebe, A., and Gibson, B. K. (2005). The evolution of substructure - III. The outskirts of clusters. *MNRAS*, 356:1327–1332.

Gillessen, S., Eisenhauer, F., Trippe, S., Alexander, T., Genzel, R., Martins, F., and Ott, T. (2009). Monitoring Stellar Orbits Around the Massive Black Hole in the Galactic

Center. *ApJ*, 692:1075–1109.

Gillet, N., Ocvirk, P., Aubert, D., Knebe, A., Libeskind, N., Yepes, G., Gottlöber, S., and Hoffman, Y. (2015). Vast Planes of Satellites in a High-resolution Simulation of the Local Group: Comparison to Andromeda. *ApJ*, 800:34.

Gilmore, G., Randich, S., Asplund, M., Binney, J., Bonifacio, P., Drew, J., Feltzing, S., Ferguson, A., Jeffries, R., Micela, G., and et al. (2012). The Gaia-ESO Public Spectroscopic Survey. *The Messenger*, 147:25–31.

Gilmore, G. and Reid, N. (1983). New light on faint stars. III - Galactic structure towards the South Pole and the Galactic thick disc. *MNRAS*, 202:1025–1047.

Gilmore, G., Wyse, R. F. G., and Jones, J. B. (1995). A determination of the thick disk chemical abundance distribution: Implications for galaxy evolution. *AJ*, 109:1095–1111.

Gingold, R. A. and Monaghan, J. J. (1982). Kernel estimates as a basis for general particle methods in hydrodynamics. *Journal of Computational Physics*, 46:429–453.

Girardi, L., Williams, B. F., Gilbert, K. M., Rosenfield, P., Dalcanton, J. J., Marigo, P., Boyer, M. L., Dolphin, A., Weisz, D. R., Melbourne, J., Olsen, K. A. G., Seth, A. C., and Skillman, E. (2010). The ACS Nearby Galaxy Survey Treasury. IX. Constraining Asymptotic Giant Branch Evolution with Old Metal-poor Galaxies. *ApJ*, 724:1030–1043.

Gonzalez, O. A., Debattista, V. P., Ness, M., Erwin, P., and Gadotti, D. A. (2017). Peanut-shaped metallicity distributions in bulges of edge-on galaxies: the case of NGC 4710. *MNRAS*, 466:L93–L97.

Gonzalez, O. A., Gadotti, D. A., Debattista, V. P., Rejkuba, M., Valenti, E., Zoccali, M., Coccato, L., Minniti, D., and Ness, M. (2016). Comparing the properties of the X-shaped bulges of NGC 4710 and the Milky Way with MUSE. *A&A*, 591:A7.

Gonzalez, O. A., Rejkuba, M., Zoccali, M., Hill, V., Battaglia, G., Babusiaux, C., Minniti, D., Barbuy, B., Alves-Brito, A., Renzini, A., Gomez, A., and Ortolani, S. (2011). Alpha element abundances and gradients in the Milky Way bulge from FLAMES-GIRAFFE spectra of 650 K giants. *A&A*, 530:A54.

Gonzalez, O. A., Rejkuba, M., Zoccali, M., Valent, E., Minniti, D., and Tobar, R. (2013). Reddening and metallicity maps of the Milky Way bulge from VVV and 2MASS. III. The first global photometric metallicity map of the Galactic bulge. *A&A*, 552:A110.

Gott, III, J. R., Jurić, M., Schlegel, D., Hoyle, F., Vogeley, M., Tegmark, M., Bahcall, N., and Brinkmann, J. (2005). A Map of the Universe. *ApJ*, 624:463–484.

Gott, III, J. R. and Thuan, T. X. (1976). On the formation of spiral and elliptical galaxies. *ApJ*, 204:649–667.

Governato, F., Brook, C., Mayer, L., Brooks, A., Rhee, G., Wadsley, J., Jonsson, P., Willman, B., Stinson, G., Quinn, T., and Madau, P. (2010). Bulgeless dwarf galaxies and dark matter cores from supernova-driven outflows. *Nature*, 463:203–206.

Governato, F., Willman, B., Mayer, L., Brooks, A., Stinson, G., Valenzuela, O., Wadsley, J., and Quinn, T. (2007). Forming disc galaxies in ΛCDM simulations. *MNRAS*, 374:1479–1494.

Goz, D., Monaco, P., Granato, G. L., Murante, G., Domínguez-Tenreiro, R., Obreja, A., Annunziatella, M., and Tescari, E. (2016). Panchromatic Spectral Energy Distributions of simulated galaxies: results at redshift $z = 0$. *ArXiv e-prints*.

Graham, A. W. (2001). An Investigation into the Prominence of Spiral Galaxy Bulges. *AJ*, 121:820–840.

Granato, G. L., Lacey, C. G., Silva, L., Bressan, A., Baugh, C. M., Cole, S., and Frenk, C. S. (2000). The Infrared Side of Galaxy Formation. I. The Local Universe in the Semianalytical Framework. *ApJ*, 542:710–730.

Granato, G. L., Ragone-Figueroa, C., Domínguez-Tenreiro, R., Obreja, A., Borgani, S., De Lucia, G., and Murante, G. (2015). The early phases of galaxy clusters formation in IR: coupling hydrodynamical simulations with GRASIL-3D. *MNRAS*, 450:1320–1332.

Grand, R. J. J., Bustamante, S., Gómez, F. A., Kawata, D., Marinacci, F., Pakmor, R., Rix, H.-W., Simpson, C. M., Sparre, M., and Springel, V. (2018a). Origin of chemically distinct discs in the Auriga cosmological simulations. *MNRAS*, 474:3629–3639.

Grand, R. J. J., Gómez, F. A., Marinacci, F., Pakmor, R., Springel, V., Campbell, D. J. R., Frenk, C. S., Jenkins, A., and White, S. D. M. (2017). The Auriga Project: the properties and formation mechanisms of disc galaxies across cosmic time. *MNRAS*, 467:179–207.

Grand, R. J. J., Helly, J., Fattahi, A., Cautun, M., Cole, S., Cooper, A. P., Deason, A. J., Frenk, C., Gómez, F. A., Hunt, J. A. S., Marinacci, F., Pakmor, R., Simpson, C. M., Springel, V., and Xu, D. (2018b). Aurigaia: mock Gaia DR2 stellar catalogues from the Auriga cosmological simulations. *ArXiv e-prints*.

Gratton, R. G., Carretta, E., Matteucci, F., and Sneden, C. (2000). Abundances of light elements in metal-poor stars. IV. [Fe/O] and [Fe/Mg] ratios and the history of star formation in the solar neighborhood. *A&A*, 358:671–681.

Grebel, E. K., Gallagher, III, J. S., and Harbeck, D. (2003). The Progenitors of Dwarf Spheroidal Galaxies. *AJ*, 125:1926–1939.

Gregory, S. A. and Thompson, L. A. (1978). The Coma/A1367 supercluster and its environs. *ApJ*, 222:784–799.

Griffen, B. F., Ji, A. P., Dooley, G. A., Gómez, F. A., Vogelsberger, M., O'Shea, B. W., and Frebel, A. (2016). The Caterpillar Project: A Large Suite of Milky Way Sized Halos. *ApJ*, 818:10.

Guedes, J., Callegari, S., Madau, P., and Mayer, L. (2011). Forming Realistic Late-type Spirals in a ΛCDM Universe: The Eris Simulation. *ApJ*, 742:76.

Guedes, J., Mayer, L., Carollo, M., and Madau, P. (2013). Pseudobulge Formation as a Dynamical Rather than a Secular Process. *ApJ*, 772:36.

Guhathakurta, P. and Draine, B. T. (1989). Temperature fluctuations in interstellar grains. I - Computational method and sublimation of small grains. *ApJ*, 345:230–244.

Gunn, J. E. and Gott, III, J. R. (1972). On the Infall of Matter Into Clusters of Galaxies and Some Effects on Their Evolution. *ApJ*, 176:1.

Guo, Y., Ferguson, H. C., Bell, E. F., Koo, D. C., Conselice, C. J., Giavalisco, M., Kassin, S., Lu, Y., Lucas, R., Mandelker, N., McIntosh, D. M., Primack, J. R., Ravindranath, S., Barro, G., Ceverino, D., Dekel, A., Faber, S. M., Fang, J. J., Koekemoer, A. M., Noeske, K., Rafelski, M., and Straughn, A. (2015). Clumpy Galaxies in CANDELS. I. The Definition of UV Clumps and the Fraction of Clumpy Galaxies at $0.5 < z < 3$. *ApJ*, 800:39.

Guo, Y., Giavalisco, M., Ferguson, H. C., Cassata, P., and Koekemoer, A. M. (2012). Multi-wavelength View of Kiloparsec-scale Clumps in Star-forming Galaxies at z ˜ 2. *ApJ*, 757:120.

Gutcke, T. A., Stinson, G. S., Macciò, A. V., Wang, L., and Dutton, A. A. (2017). NIHAO - VIII. Circum-galactic medium and outflows - The puzzles of H I and O VI gas distributions. *MNRAS*, 464:2796–2815.

Guth, A. H. (1981). Inflationary universe: A possible solution to the horizon and flatness problems. *Phys. Rev. D*, 23:347–356.

Guth, A. H. and Pi, S.-Y. (1982). Fluctuations in the new inflationary universe. *Physical Review Letters*, 49:1110–1113.

Haardt, F. and Madau, P. (2005). Radiative Transfer in a Clumpy Universe. II. The Ultraviolet Extragalactic Background. *unpublished*.

Halverson, N. W., Leitch, E. M., Pryke, C., Kovac, J., Carlstrom, J. E., Holzapfel, W. L., Dragovan, M., Cartwright, J. K., Mason, B. S., Padin, S., Pearson, T. J., Readhead, A. C. S., and Shepherd, M. C. (2002). Degree Angular Scale Interferometer First Results: A Measurement of the Cosmic Microwave Background Angular Power Spectrum. *ApJ*, 568:38–45.

Hammer, F., Yang, Y., Fouquet, S., Pawlowski, M. S., Kroupa, P., Puech, M., Flores, H., and Wang, J. (2013). The vast thin plane of M31 corotating dwarfs: an additional fossil signature of the M31 merger and of its considerable impact in the whole Local Group. *MNRAS*, 431:3543–3549.

Hanany, S., Ade, P., Balbi, A., Bock, J., Borrill, J., Boscaleri, A., de Bernardis, P., Ferreira, P. G., Hristov, V. V., Jaffe, A. H., Lange, A. E., Lee, A. T., Mauskopf, P. D., Netterfield, C. B., Oh, S., Pascale, E., Rabii, B., Richards, P. L., Smoot, G. F., Stompor, R., Winant, C. D., and Wu, J. H. P. (2000). MAXIMA-1: A Measurement of the Cosmic Microwave Background Anisotropy on Angular Scales of 10'-5°. *ApJ*, 545:L5–L9.

Hargis, J. R., Willman, B., and Peter, A. H. G. (2014). Too Many, Too Few, or Just Right? The Predicted Number and Distribution of Milky Way Dwarf Galaxies. *ApJ*, 795:L13.

Harrison, E. R. (1970). Fluctuations at the Threshold of Classical Cosmology. *Phys. Rev. D*, 1:2726–2730.

Hawking, S. W. (1982). The development of irregularities in a single bubble inflationary universe. *Physics Letters B*, 115:295–297.

Hayden, M. R., Bovy, J., Holtzman, J. A., Nidever, D. L., Bird, J. C., Weinberg, D. H., Andrews, B. H., Majewski, S. R., Allende Prieto, C., Anders, F., Beers, T. C., Bizyaev, D., Chiappini, C., Cunha, K., Frinchaboy, P., García-Herńandez, D. A., García Pérez, A. E., Girardi, L., Harding, P., Hearty, F. R., Johnson, J. A., Mészáros, S., Minchev, I., O'Connell, R., Pan, K., Robin, A. C., Schiavon, R. P., Schneider, D. P., Schultheis, M., Shetrone, M., Skrutskie, M., Steinmetz, M., Smith, V., Wilson, J. C., Zamora, O., and Zasowski, G. (2015). Chemical Cartography with APOGEE: Metallicity Distribution Functions and the Chemical Structure of the Milky Way Disk. *ApJ*, 808:132.

Haywood, M., Di Matteo, P., Lehnert, M. D., Katz, D., and Gómez, A. (2013). The age structure of stellar populations in the solar vicinity. Clues of a two-phase formation history of the Milky Way disk. *A&A*, 560:A109.

Haywood, M., Di Matteo, P., Snaith, O., and Calamida, A. (2016). Hiding its age: the case for a younger bulge. *A&A*, 593:A82.

Haywood, M., Di Matteo, P., Snaith, O., and Lehnert, M. D. (2015). Clues to the formation of the Milky Way's thick disk. *A&A*, 579:A5.

Heckman, T. M. and Best, P. N. (2014). The Coevolution of Galaxies and Supermassive Black Holes: Insights from Surveys of the Contemporary Universe. *ARA&A*, 52:589–660.

Helmi, A. (2008). The stellar halo of the Galaxy. *A&A Rev.*, 15:145–188.

Helmi, A., White, S. D. M., de Zeeuw, P. T., and Zhao, H. (1999). Debris streams in the solar neighbourhood as relicts from the formation of the Milky Way. *Nature*, 402:53–55.

Herpich, J., Stinson, G. S., Dutton, A. A., Rix, H.-W., Martig, M., Roškar, R., Macciò, A. V., Quinn, T. R., and Wadsley, J. (2015). How to bend galaxy disc profiles: the role of halo spin. *MNRAS*, 448:L99–L103.

Herpich, J., Stinson, G. S., Rix, H.-W., Martig, M., and Dutton, A. A. (2017). How to bend galaxy disc profiles - II. Stars surfing the bar in Type-III discs. *MNRAS*, 470:4941–4955.

Hill, V., Lecureur, A., Gómez, A., Zoccali, M., Schultheis, M., Babusiaux, C., Royer, F., Barbuy, B., Arenou, F., Minniti, D., and Ortolani, S. (2011). The metallicity distribution of bulge clump giants in Baade's window. *A&A*, 534:A80.

Hirschmann, M., De Lucia, G., Wilman, D., Weinmann, S., Iovino, A., Cucciati, O., Zibetti, S., and Villalobos, Á. (2014). The influence of the environmental history on quenching star formation in a Λ cold dark matter universe. *MNRAS*, 444:2938–2959.

Ho, N., Geha, M., Munoz, R. R., Guhathakurta, P., Kalirai, J., Gilbert, K. M., Tollerud, E., Bullock, J., Beaton, R. L., and Majewski, S. R. (2012). Stellar Kinematics of the Andromeda II Dwarf Spheroidal Galaxy. *ApJ*, 758:124.

Hockney, R. W. and Eastwood, J. W. (1981). *Computer Simulation Using Particles*.

Hohl, F. (1971). Numerical Experiments with a Disk of Stars. *ApJ*, 168:343.

Hopkins, P. F., Cox, T. J., Younger, J. D., and Hernquist, L. (2009). How do Disks Survive Mergers? *ApJ*, 691:1168–1201.

Hopkins, P. F., Croton, D., Bundy, K., Khochfar, S., van den Bosch, F., Somerville, R. S., Wetzel, A., Keres, D., Hernquist, L., Stewart, K., Younger, J. D., Genel, S., and Ma, C.-P. (2010). Mergers in ΛCDM: Uncertainties in Theoretical Predictions and Interpretations of the Merger Rate. *ApJ*, 724:915–945.

Hopkins, P. F., Kereš, D., Murray, N., Quataert, E., and Hernquist, L. (2012). Stellar feedback and bulge formation in clumpy discs. *MNRAS*, 427:968–978.

Hopkins, P. F., Kereš, D., Oñorbe, J., Faucher-Giguère, C.-A., Quataert, E., Murray, N., and Bullock, J. S. (2014). Galaxies on FIRE (Feedback In Realistic Environments): stellar feedback explains cosmologically inefficient star formation. *MNRAS*, 445:581–603.

Howard, C. D., Rich, R. M., Clarkson, W., Mallery, R., Kormendy, J., De Propris, R., Robin, A. C., Fux, R., Reitzel, D. B., Zhao, H. S., Kuijken, K., and Koch, A. (2009). Kinematics at the Edge of the Galactic Bulge: Evidence for Cylindrical Rotation. *ApJ*, 702:L153–L157.

Howard, C. D., Rich, R. M., Reitzel, D. B., Koch, A., De Propris, R., and Zhao, H. (2008). The Bulge Radial Velocity Assay (BRAVA). I. Sample Selection and a Rotation Curve. *ApJ*, 688:1060–1077.

Howes, L. M., Asplund, M., Keller, S. C., Casey, A. R., Yong, D., Lind, K., Frebel, A., Hays, A., Alves-Brito, A., Bessell, M. S., Casagrande, L., Marino, A. F., Nataf, D. M., Owen, C. I., Da Costa, G. S., Schmidt, B. P., and Tisserand, P. (2016). The EMBLA survey - metal-poor stars in the Galactic bulge. *MNRAS*, 460:884–901.

Hoyle, F. (1949). On the Cosmological Problem. *MNRAS*, 109:365.

Hoyle, F. and Tayler, R. J. (1964). The Mystery of the Cosmic Helium Abundance. *Nature*, 203:1108–1110.

Hubble, E. (1929a). A Relation between Distance and Radial Velocity among Extra-Galactic Nebulae. *Proceedings of the National Academy of Science*, 15:168–173.

Hubble, E. P. (1925). NGC 6822, a remote stellar system. *ApJ*, 62.

Hubble, E. P. (1926). Extragalactic nebulae. *ApJ*, 64.

Hubble, E. P. (1929b). A spiral nebula as a stellar system, Messier 31. *ApJ*, 69.

Hubble, E. P. (1936). *Realm of the Nebulae*.

Hunter, D. A. and Elmegreen, B. G. (2006). Broadband Imaging of a Large Sample of Irregular Galaxies. *ApJS*, 162:49–79.

Hunter, J. D. (2007). Matplotlib: A 2d graphics environment. *Computing In Science & Engineering*, 9(3):90–95.

Hyde, J. B. and Bernardi, M. (2009). The luminosity and stellar mass Fundamental Plane of early-type galaxies. *MNRAS*, 396:1171–1185.

Ibata, R., Martin, N. F., Irwin, M., Chapman, S., Ferguson, A. M. N., Lewis, G. F., and McConnachie, A. W. (2007). The Haunted Halos of Andromeda and Triangulum: A Panorama of Galaxy Formation in Action. *ApJ*, 671:1591–1623.

Ibata, R. A., Famaey, B., Lewis, G. F., Ibata, N. G., and Martin, N. (2015). Eppur si Muove: Positional and Kinematic Correlations of Satellite Pairs in the Low Z Universe. *ApJ*, 805:67.

Ibata, R. A., Gilmore, G., and Irwin, M. J. (1994). A dwarf satellite galaxy in Sagittarius. *Nature*, 370:194–196.

Ibata, R. A., Ibata, N. G., Lewis, G. F., Martin, N. F., Conn, A., Elahi, P., Arias, V., and Fernando, N. (2014). A Thousand Shadows of Andromeda: Rotating Planes of Satellites in the Millennium-II Cosmological Simulation. *ApJ*, 784:L6.

Ibata, R. A., Lewis, G. F., Conn, A. R., Irwin, M. J., McConnachie, A. W., Chapman, S. C., Collins, M. L., Fardal, M., Ferguson, A. M. N., Ibata, N. G., Mackey, A. D., Martin, N. F., Navarro, J., Rich, R. M., Valls-Gabaud, D., and Widrow, L. M. (2013). A vast, thin plane of corotating dwarf galaxies orbiting the Andromeda galaxy. *Nature*, 493:62–65.

Ibata, R. A., Wyse, R. F. G., Gilmore, G., Irwin, M. J., and Suntzeff, N. B. (1997). The Kinematics, Orbit, and Survival of the Sagittarius Dwarf Spheroidal Galaxy. *AJ*, 113:634–655.

Inoue, S., Dekel, A., Mandelker, N., Ceverino, D., Bournaud, F., and Primack, J. (2016). Non-linear violent disc instability with high Toomre's Q in high-redshift clumpy disc galaxies. *MNRAS*, 456:2052–2069.

Inoue, S. and Saitoh, T. R. (2012). Natures of a clump-origin bulge: a pseudo-bulge like but old metal-rich bulge. *MNRAS*, 422:1902–1913.

Inoue, S. and Saitoh, T. R. (2014). Properties of thick discs formed in clumpy galaxies. *MNRAS*, 441:243–255.

Jeans, J. H. (1902). The Stability of a Spherical Nebula. *Philosophical Transactions of the Royal Society of London Series A*, 199:1–53.

Jeans, J. H. (1919). *Problems of cosmogony and stellar dynamics*.

Jenkins, A., Frenk, C. S., White, S. D. M., Colberg, J. M., Cole, S., Evrard, A. E., Couchman, H. M. P., and Yoshida, N. (2001). The mass function of dark matter haloes. *MNRAS*, 321:372–384.

Jethwa, P., Belokurov, V., and Erkal, D. (2016). The upper bound on the lowest mass halo. *ArXiv e-prints*.

Jiang, C. Y., Jing, Y. P., Faltenbacher, A., Lin, W. P., and Li, C. (2008). A Fitting Formula for the Merger Timescale of Galaxies in Hierarchical Clustering. *ApJ*, 675:1095–1105.

Jiang, F. and van den Bosch, F. C. (2015). Comprehensive assessment of the too big to fail problem. *MNRAS*, 453:3575–3592.

Johnson, C. I., Rich, R. M., Fulbright, J. P., Valenti, E., and McWilliam, A. (2011). Alpha Enhancement and the Metallicity Distribution Function of Plaut's Window. *ApJ*, 732:108.

Jones, E., Oliphant, T., Peterson, P., et al. (2001). SciPy: Open source scientific tools for Python. [Online; accessed <today>].

Jones, T. A., Swinbank, A. M., Ellis, R. S., Richard, J., and Stark, D. P. (2010). Resolved spectroscopy of gravitationally lensed galaxies: recovering coherent velocity fields in subluminous z ˜ 2-3 galaxies. *MNRAS*, 404:1247–1262.

Jonsson, P. (2006). SUNRISE: polychromatic dust radiative transfer in arbitrary geometries. *MNRAS*, 372:2–20.

Jonsson, P., Groves, B. A., and Cox, T. J. (2010). High-resolution panchromatic spectral models of galaxies including photoionization and dust. *MNRAS*, 403:17–44.

Jonsson, P. and Primack, J. R. (2010). Accelerating dust temperature calculations with graphics-processing units. *New A*, 15:509–514.

Jurić, M., Ivezić, Ž., Brooks, A., Lupton, R. H., Schlegel, D., Finkbeiner, D., Padmanabhan, N., Bond, N., Sesar, B., Rockosi, C. M., Knapp, G. R., Gunn, J. E., Sumi, T., Schneider, D. P., Barentine, J. C., Brewington, H. J., Brinkmann, J., Fukugita, M., Harvanek, M., Kleinman, S. J., Krzesinski, J., Long, D., Neilsen, Jr., E. H., Nitta, A., Snedden, S. A., and York, D. G. (2008). The Milky Way Tomography with SDSS. I. Stellar Number Density Distribution. *ApJ*, 673:864–914.

Kacharov, N., Battaglia, G., Rejkuba, M., Cole, A. A., Carrera, R., Fraternali, F., Wilkinson, M. I., Gallart, C. G., Irwin, M., and Tolstoy, E. (2017). Prolate rotation and metallicity gradient in the transforming dwarf galaxy Phoenix. *MNRAS*, 466:2006–2023.

Kahn, F. D. and Woltjer, L. (1959). Intergalactic Matter and the Galaxy. *ApJ*, 130:705.

Kaiser, N. and Squires, G. (1993). Mapping the dark matter with weak gravitational lensing. *ApJ*, 404:441–450.

Kalirai, J. S., Gilbert, K. M., Guhathakurta, P., Majewski, S. R., Ostheimer, J. C., Rich, R. M., Cooper, M. C., Reitzel, D. B., and Patterson, R. J. (2006). The Metal-poor Halo of the Andromeda Spiral Galaxy (M31)1,. *ApJ*, 648:389–404.

Kang, X., Mao, S., Gao, L., and Jing, Y. P. (2005). Are great disks defined by satellite galaxies in Milky-Way type halos rare in ΛCDM? *A&A*, 437:383–388.

Kannan, R., Macciò, A. V., Fontanot, F., Moster, B. P., Karman, W., and Somerville, R. S. (2015). From discs to bulges: effect of mergers on the morphology of galaxies. *MNRAS*, 452:4347–4360.

Karachentsev, I. D., Makarova, L. N., Makarov, D. I., Tully, R. B., and Rizzi, L. (2015). A new isolated dSph galaxy near the Local Group. *MNRAS*, 447:L85–L89.

Katz, N. (1992). Dissipational galaxy formation. II - Effects of star formation. *ApJ*, 391:502–517.

Kauffmann, G., Heckman, T. M., Tremonti, C., Brinchmann, J., Charlot, S., White, S. D. M., Ridgway, S. E., Brinkmann, J., Fukugita, M., Hall, P. B., Ivezić, Ž., Richards, G. T., and Schneider, D. P. (2003). The host galaxies of active galactic nuclei. *MNRAS*, 346:1055–1077.

Kauffmann, G., White, S. D. M., and Guiderdoni, B. (1993). The Formation and Evolution of Galaxies Within Merging Dark Matter Haloes. *MNRAS*, 264:201.

Kazantzidis, S., Kravtsov, A. V., Zentner, A. R., Allgood, B., Nagai, D., and Moore, B. (2004). The Effect of Gas Cooling on the Shapes of Dark Matter Halos. *ApJ*, 611:L73–L76.

Kazantzidis, S., Łokas, E. L., Callegari, S., Mayer, L., and Moustakas, L. A. (2011). On the Efficiency of the Tidal Stirring Mechanism for the Origin of Dwarf Spheroidals: Dependence on the Orbital and Structural Parameters of the Progenitor Disky Dwarfs. *ApJ*, 726:98.

Kazantzidis, S., Mayer, L., Callegari, S., Dotti, M., and Moustakas, L. A. (2017). The Effects of Ram-pressure Stripping and Supernova Winds on the Tidal Stirring of Disky Dwarfs: Enhanced Transformation into Dwarf Spheroidals. *ApJ*, 836:L13.

Keller, B. W., Wadsley, J., Benincasa, S. M., and Couchman, H. M. P. (2014). A super-bubble feedback model for galaxy simulations. *MNRAS*, 442:3013–3025.

Kennicutt, Jr., R. C. (1989). The star formation law in galactic disks. *ApJ*, 344:685–703.

Kennicutt, Jr., R. C. (1998). The Global Schmidt Law in Star-forming Galaxies. *ApJ*, 498:541–552.

Kereš, D., Katz, N., Weinberg, D. H., and Davé, R. (2005). How do galaxies get their gas? *MNRAS*, 363:2–28.

Kerr, F. J. and Lynden-Bell, D. (1986). Review of galactic constants. *MNRAS*, 221:1023–1038.

Kirby, E. N., Bullock, J. S., Boylan-Kolchin, M., Kaplinghat, M., and Cohen, J. G. (2014). The dynamics of isolated Local Group galaxies. *MNRAS*, 439:1015–1027.

Kirby, E. N., Cohen, J. G., Simon, J. D., Guhathakurta, P., Thygesen, A. O., and Duggan, G. E. (2017a). Triangulum II. Not Especially Dense After All. *ApJ*, 838:83.

Kirby, E. N., Rizzi, L., Held, E. V., Cohen, J. G., Cole, A. A., Manning, E. M., Skillman, E. D., and Weisz, D. R. (2017b). Chemistry and Kinematics of the Late-forming Dwarf Irregular Galaxies Leo A, Aquarius, and Sagittarius DIG. *ApJ*, 834:9.

Kirby, E. N., Simon, J. D., and Cohen, J. G. (2015). Spectroscopic Confirmation of the Dwarf Galaxies Hydra II and Pisces II and the Globular Cluster Laevens 1. *ApJ*,

810:56.

Kirkman, D., Tytler, D., Suzuki, N., O'Meara, J. M., and Lubin, D. (2003). The Cosmological Baryon Density from the Deuterium-to-Hydrogen Ratio in QSO Absorption Systems: D/H toward Q1243+3047. *ApJS*, 149:1–28.

Klimentowski, J., Łokas, E. L., Kazantzidis, S., Mayer, L., and Mamon, G. A. (2009a). Tidal evolution of discy dwarf galaxies in the Milky Way potential: the formation of dwarf spheroidals. *MNRAS*, 397:2015–2029.

Klimentowski, J., Łokas, E. L., Kazantzidis, S., Mayer, L., Mamon, G. A., and Prada, F. (2009b). The orientation and kinematics of inner tidal tails around dwarf galaxies orbiting the Milky Way. *MNRAS*, 400:2162–2168.

Klimentowski, J., Łokas, E. L., Kazantzidis, S., Prada, F., Mayer, L., and Mamon, G. A. (2007). Mass modelling of dwarf spheroidal galaxies: the effect of unbound stars from tidal tails and the Milky Way. *MNRAS*, 378:353–368.

Klypin, A., Karachentsev, I., Makarov, D., and Nasonova, O. (2015). Abundance of field galaxies. *MNRAS*, 454:1798–1810.

Klypin, A., Kravtsov, A. V., Valenzuela, O., and Prada, F. (1999). Where Are the Missing Galactic Satellites? *ApJ*, 522:82–92.

Knebe, A., Libeskind, N. I., Knollmann, S. R., Martinez-Vaquero, L. A., Yepes, G., Gottlöber, S., and Hoffman, Y. (2011). The luminosities of backsplash galaxies in constrained simulations of the Local Group. *MNRAS*, 412:529–536.

Knollmann, S. R. and Knebe, A. (2009). AHF: Amiga's Halo Finder. *ApJS*, 182:608–624.

Kobayashi, C. and Nakasato, N. (2011). Chemodynamical Simulations of the Milky Way Galaxy. *ApJ*, 729:16.

Koch, A. and Grebel, E. K. (2006). The Anisotropic Distribution of M31 Satellite Galaxies: A Polar Great Plane of Early-type Companions. *AJ*, 131:1405–1415.

Kollmeier, J. A., Zasowski, G., Rix, H.-W., Johns, M., Anderson, S. F., Drory, N., Johnson, J. A., Pogge, R. W., Bird, J. C., Blanc, G. A., Brownstein, J. R., Crane, J. D., De Lee, N. M., Klaene, M. A., Kreckel, K., MacDonald, N., Merloni, A., Ness, M. K., O'Brien, T., Sanchez-Gallego, J. R., Sayres, C. C., Shen, Y., Thakar, A. R., Tkachenko, A., Aerts, C., Blanton, M. R., Eisenstein, D. J., Holtzman, J. A., Maoz, D., Nandra, K., Rockosi, C., Weinberg, D. H., Bovy, J., Casey, A. R., Chaname, J., Clerc, N., Conroy, C., Eracleous, M., Gänsicke, B. T., Hekker, S., Horne, K., Kauffmann, J., McQuinn, K. B. W., Pellegrini, E. W., Schinnerer, E., Schlafly, E. F., Schwope, A. D., Seibert, M., Teske, J. K., and van Saders, J. L. (2017). SDSS-V: Pioneering Panoptic Spectroscopy. *ArXiv e-prints*.

Komatsu, E., Dunkley, J., Nolta, M. R., Bennett, C. L., Gold, B., Hinshaw, G., Jarosik, N., Larson, D., Limon, M., Page, L., Spergel, D. N., Halpern, M., Hill, R. S., Kogut, A., Meyer, S. S., Tucker, G. S., Weiland, J. L., Wollack, E., and Wright, E. L. (2009). Five-Year Wilkinson Microwave Anisotropy Probe Observations: Cosmological

Interpretation. *ApJS*, 180:330–376.

Koposov, S. E., Belokurov, V., Torrealba, G., and Evans, N. W. (2015a). Beasts of the Southern Wild: Discovery of Nine Ultra Faint Satellites in the Vicinity of the Magellanic Clouds. *ApJ*, 805:130.

Koposov, S. E., Casey, A. R., Belokurov, V., Lewis, J. R., Gilmore, G., Worley, C., Hourihane, A., Randich, S., Bensby, T., Bragaglia, A., Bergemann, M., Carraro, G., Costado, M. T., Flaccomio, E., Francois, P., Heiter, U., Hill, V., Jofre, P., Lando, C., Lanzafame, A. C., de Laverny, P., Monaco, L., Morbidelli, L., Sbordone, L., Mikolaitis, Š., and Ryde, N. (2015b). Kinematics and Chemistry of Recently Discovered Reticulum 2 and Horologium 1 Dwarf Galaxies. *ApJ*, 811:62.

Kordopatis, G., Wyse, R. F. G., Gilmore, G., Recio-Blanco, A., de Laverny, P., Hill, V., Adibekyan, V., Heiter, U., Minchev, I., Famaey, B., Bensby, T., Feltzing, S., Guiglion, G., Korn, A. J., Mikolaitis, Š., Schultheis, M., Vallenari, A., Bayo, A., Carraro, G., Flaccomio, E., Franciosini, E., Hourihane, A., Jofré, P., Koposov, S. E., Lardo, C., Lewis, J., Lind, K., Magrini, L., Morbidelli, L., Pancino, E., Randich, S., Sacco, G. G., Worley, C. C., and Zaggia, S. (2015). The Gaia-ESO Survey: characterisation of the [α/Fe] sequences in the Milky Way discs. *A&A*, 582:A122.

Kormendy, J. (1977). Brightness distributions in compact and normal galaxies. II - Structure parameters of the spheroidal component. *ApJ*, 218:333–346.

Kormendy, J. (2013). *Secular Evolution in Disk Galaxies*, page 1.

Kormendy, J. and Freeman, K. C. (2016). Scaling Laws for Dark Matter Halos in Late-type and Dwarf Spheroidal Galaxies. *ApJ*, 817:84.

Kormendy, J. and Ho, L. C. (2013). Coevolution (Or Not) of Supermassive Black Holes and Host Galaxies. *ARA&A*, 51:511–653.

Kormendy, J. and Kennicutt, Jr., R. C. (2004). Secular Evolution and the Formation of Pseudobulges in Disk Galaxies. *ARA&A*, 42:603–683.

Kravtsov, A., Vikhlinin, A., and Meshscheryakov, A. (2014). Stellar mass – halo mass relation and star formation efficiency in high-mass halos. *ArXiv e-prints*.

Kravtsov, A. V., Gnedin, O. Y., and Klypin, A. A. (2004). The Tumultuous Lives of Galactic Dwarfs and the Missing Satellites Problem. *ApJ*, 609:482–497.

Kuhlen, M., Madau, P., and Silk, J. (2009). Exploring Dark Matter with Milky Way Substructure. *Science*, 325:970.

Kuijken, K. and Gilmore, G. (1989). The Mass Distribution in the Galactic Disc - II - Determination of the Surface Mass Density of the Galactic Disc Near the Sun. *MNRAS*, 239:605–649.

Kunder, A., Koch, A., Rich, R. M., de Propris, R., Howard, C. D., Stubbs, S. A., Johnson, C. I., Shen, J., Wang, Y., Robin, A. C., Kormendy, J., Soto, M., Frinchaboy, P., Reitzel, D. B., Zhao, H., and Origlia, L. (2012). The Bulge Radial Velocity Assay (BRAVA). II. Complete Sample and Data Release. *AJ*, 143:57.

Kunder, A., Rich, R. M., Koch, A., Storm, J., Nataf, D. M., De Propris, R., Walker, A. R., Bono, G., Johnson, C. I., Shen, J., and Li, Z.-Y. (2016). Before the Bar: Kinematic Detection of a Spheroidal Metal-poor Bulge Component. *ApJ*, 821:L25.

Kunkel, W. E. and Demers, S. (1976). The Magellanic Plane. In Dickens, R. J., Perry, J. E., Smith, F. G., and King, I. R., editors, *The Galaxy and the Local Group*, volume 182 of *Royal Greenwich Observatory Bulletins*, page 241.

Laevens, B. P. M., Martin, N. F., Bernard, E. J., Schlafly, E. F., Sesar, B., Rix, H.-W., Bell, E. F., Ferguson, A. M. N., Slater, C. T., Sweeney, W. E., Wyse, R. F. G., Huxor, A. P., Burgett, W. S., Chambers, K. C., Draper, P. W., Hodapp, K. A., Kaiser, N., Magnier, E. A., Metcalfe, N., Tonry, J. L., Wainscoat, R. J., and Waters, C. (2015a). Sagittarius II, Draco II and Laevens 3: Three New Milky Way Satellites Discovered in the Pan-STARRS 1 3π Survey. *ApJ*, 813:44.

Laevens, B. P. M., Martin, N. F., Ibata, R. A., Rix, H.-W., Bernard, E. J., Bell, E. F., Sesar, B., Ferguson, A. M. N., Schlafly, E. F., Slater, C. T., Burgett, W. S., Chambers, K. C., Flewelling, H., Hodapp, K. A., Kaiser, N., Kudritzki, R.-P., Lupton, R. H., Magnier, E. A., Metcalfe, N., Morgan, J. S., Price, P. A., Tonry, J. L., Wainscoat, R. J., and Waters, C. (2015b). A New Faint Milky Way Satellite Discovered in the Pan-STARRS1 3π Survey. *ApJ*, 802:L18.

Laevens, B. P. M., Martin, N. F., Sesar, B., Bernard, E. J., Rix, H.-W., Slater, C. T., Bell, E. F., Ferguson, A. M. N., Schlafly, E. F., Burgett, W. S., Chambers, K. C., Denneau, L., Draper, P. W., Kaiser, N., Kudritzki, R.-P., Magnier, E. A., Metcalfe, N., Morgan, J. S., Price, P. A., Sweeney, W. E., Tonry, J. L., Wainscoat, R. J., and Waters, C. (2014). A New Distant Milky Way Globular Cluster in the Pan-STARRS1 3π Survey. *ApJ*, 786:L3.

Larson, R. B. (1974a). Dynamical models for the formation and evolution of spherical galaxies. *MNRAS*, 166:585–616.

Larson, R. B. (1974b). Effects of supernovae on the early evolution of galaxies. *MNRAS*, 169:229–246.

Larson, R. B. (1975). Models for the formation of elliptical galaxies. *MNRAS*, 173:671–699.

Larson, R. B. (1976). Models for the formation of disc galaxies. *MNRAS*, 176:31–52.

Leaman, R., Venn, K. A., Brooks, A. M., Battaglia, G., Cole, A. A., Ibata, R. A., Irwin, M. J., McConnachie, A. W., Mendel, J. T., and Tolstoy, E. (2012). The Resolved Structure and Dynamics of an Isolated Dwarf Galaxy: A VLT and Keck Spectroscopic Survey of WLM. *ApJ*, 750:33.

Lecureur, A., Hill, V., Zoccali, M., Barbuy, B., Gómez, A., Minniti, D., Ortolani, S., and Renzini, A. (2007). Oxygen, sodium, magnesium, and aluminium as tracers of the galactic bulge formation. *A&A*, 465:799–814.

Lee, C. T., Primack, J. R., Behroozi, P., Rodríguez-Puebla, A., Hellinger, D., and Dekel, A. (2017). Tidal Stripping and Post-Merger Relaxation of Dark Matter Halos: Causes

and Consequences of Mass Loss. *ArXiv e-prints*.

Lemaître, G. (1927). Un Univers homogène de masse constante et de rayon croissant rendant compte de la vitesse radiale des nébuleuses extra-galactiques. *Annales de la Société Scientifique de Bruxelles*, 47:49–59.

Li, T. S., Simon, J. D., Drlica-Wagner, A., Bechtol, K., Wang, M. Y., García-Bellido, J., Frieman, J., Marshall, J. L., James, D. J., Strigari, L., Pace, A. B., Balbinot, E., Zhang, Y., Abbott, T. M. C., Allam, S., Benoit-Lévy, A., Bernstein, G. M., Bertin, E., Brooks, D., Burke, D. L., Carnero Rosell, A., Carrasco Kind, M., Carretero, J., Cunha, C. E., D'Andrea, C. B., da Costa, L. N., DePoy, D. L., Desai, S., Diehl, H. T., Eifler, T. F., Flaugher, B., Goldstein, D. A., Gruen, D., Gruendl, R. A., Gschwend, J., Gutierrez, G., Krause, E., Kuehn, K., Lin, H., Maia, M. A. G., March, M., Menanteau, F., Miquel, R., Plazas, A. A., Romer, A. K., Sanchez, E., Santiago, B., Schubnell, M., Sevilla-Noarbe, I., Smith, R. C., Sobreira, F., Suchyta, E., Tarle, G., Thomas, D., Tucker, D. L., Walker, A. R., Wechsler, R. H., Wester, W., Yanny, B., and (DES Collaboration (2017). Farthest Neighbor: The Distant Milky Way Satellite Eridanus II. *ApJ*, 838:8.

Li, Y.-S. and White, S. D. M. (2008). Masses for the Local Group and the Milky Way. *MNRAS*, 384:1459–1468.

Li, Z.-Y. and Shen, J. (2012). The Vertical X-shaped Structure in the Milky Way: Evidence from a Simple Boxy Bulge Model. *ApJ*, 757:L7.

Libeskind, N. I., Frenk, C. S., Cole, S., Helly, J. C., Jenkins, A., Navarro, J. F., and Power, C. (2005). The distribution of satellite galaxies: the great pancake. *MNRAS*, 363:146–152.

Libeskind, N. I., Frenk, C. S., Cole, S., Jenkins, A., and Helly, J. C. (2009). How common is the Milky Way-satellite system alignment? *MNRAS*, 399:550–558.

Libeskind, N. I., Hoffman, Y., Tully, R. B., Courtois, H. M., Pomarède, D., Gottlöber, S., and Steinmetz, M. (2015). Planes of satellite galaxies and the cosmic web. *MNRAS*, 452:1052–1059.

Libeskind, N. I., Knebe, A., Hoffman, Y., and Gottlöber, S. (2014). The universal nature of subhalo accretion. *MNRAS*, 443:1274–1280.

Libeskind, N. I., Knebe, A., Hoffman, Y., Gottlöber, S., Yepes, G., and Steinmetz, M. (2011). The preferred direction of infalling satellite galaxies in the Local Group. *MNRAS*, 411:1525–1535.

Lifshitz, E. M. (1946). On the gravitational stability of the expanding universe. *Zhurnal Eksperimentalnoi i Teoreticheskoi Fiziki*, 16:587–602.

López-Corredoira, M. (2017). Absence of an X-shaped Structure in the Milky Way Bulge Using Mira Variable Stars. *ApJ*, 836:218.

Lovell, M. R., Eke, V. R., Frenk, C. S., and Jenkins, A. (2011). The link between galactic satellite orbits and subhalo accretion. *MNRAS*, 413:3013–3021.

Ludlow, A. D., Navarro, J. F., Springel, V., Jenkins, A., Frenk, C. S., and Helmi, A. (2009). The Unorthodox Orbits of Substructure Halos. *ApJ*, 692:931–941.

Lundmark, K. (1925). The Motions and the Distances of Spiral Nebulæ. *MNRAS*, 85:865.

Lütticke, R., Pohlen, M., and Dettmar, R.-J. (2004). Box- and peanut-shaped bulges. III. A new class of bulges: Thick Boxy Bulges. *A&A*, 417:527–539.

Lynden-Bell, D. (1967). Statistical mechanics of violent relaxation in stellar systems. *MNRAS*, 136:101.

Lynden-Bell, D. (1976). Dwarf galaxies and globular clusters in high velocity hydrogen streams. *MNRAS*, 174:695–710.

Ma, X., Hopkins, P. F., Wetzel, A. R., Kirby, E. N., Anglés-Alcázar, D., Faucher-Giguère, C.-A., Kereš, D., and Quataert, E. (2017). The structure and dynamical evolution of the stellar disc of a simulated Milky Way-mass galaxy. *MNRAS*, 467:2430–2444.

MacArthur, L. A., Courteau, S., and Holtzman, J. A. (2003). Structure of Disk-dominated Galaxies. I. Bulge/Disk Parameters, Simulations, and Secular Evolution. *ApJ*, 582:689–722.

Macciò, A. V., Frings, J., Buck, T., Penzo, C., Dutton, A. A., Blank, M., and Obreja, A. (2017). The edge of galaxy formation - I. Formation and evolution of MW-satellite analogues before accretion. *MNRAS*, 472:2356–2366.

Macciò, A. V., Udrescu, S. M., Dutton, A. A., Obreja, A., Wang, L., Stinson, G. R., and Kang, X. (2016). NIHAO X: reconciling the local galaxy velocity function with cold dark matter via mock H i observations. *MNRAS*, 463:L69–L73.

Madau, P., Shen, S., and Governato, F. (2014). Dark Matter Heating and Early Core Formation in Dwarf Galaxies. *ApJ*, 789:L17.

Maddox, S. J., Efstathiou, G., Sutherland, W. J., and Loveday, J. (1990). Galaxy correlations on large scales. *MNRAS*, 242:43P–47P.

Majewski, S. R., Schiavon, R. P., Frinchaboy, P. M., Allende Prieto, C., Barkhouser, R., Bizyaev, D., Blank, B., Brunner, S., Burton, A., Carrera, R., Chojnowski, S. D., Cunha, K., Epstein, C., Fitzgerald, G., Garcia Perez, A. E., Hearty, F. R., Henderson, C., Holtzman, J. A., Johnson, J. A., Lam, C. R., Lawler, J. E., Maseman, P., Meszaros, S., Nelson, M., Coung Nguyen, D., Nidever, D. L., Pinsonneault, M., Shetrone, M., Smee, S., Smith, V. V., Stolberg, T., Skrutskie, M. F., Walker, E., Wilson, J. C., Zasowski, G., Anders, F., Basu, S., Beland, S., Blanton, M. R., Bovy, J., Brownstein, J. R., Carlberg, J., Chaplin, W., Chiappini, C., Eisenstein, D. J., Elsworth, Y., Feuillet, D., Fleming, S. W., Galbraith-Frew, J., Garcia, R. A., Anibal Garcia-Hernandez, D., Gillespie, B. A., Girardi, L., Gunn, J. E., Hasselquist, S., Hayden, M. R., Hekker, S., Ivans, I., Kinemuchi, K., Klaene, M., Mahadevan, S., Mathur, S., Mosser, B., Muna, D., Munn, J. A., Nichol, R. C., O'Connell, R. W., Robin, A. C., Rocha-Pinto, H., Schultheis, M., Serenelli, A. M., Shane, N., Silva Aguirre, V., Sobeck, J. S., Thompson, B., Troup, N. W., Weinberg, D. H., and Zamora, O. (2015). The Apache Point Observatory Galactic Evolution Experiment (APOGEE). *ArXiv e-prints*.

Majewski, S. R., Schiavon, R. P., Frinchaboy, P. M., Allende Prieto, C., Barkhouser, R., Bizyaev, D., Blank, B., Brunner, S., Burton, A., Carrera, R., Chojnowski, S. D., Cunha, K., Epstein, C., Fitzgerald, G., García Pérez, A. E., Hearty, F. R., Henderson, C., Holtzman, J. A., Johnson, J. A., Lam, C. R., Lawler, J. E., Maseman, P., Mészáros, S., Nelson, M., Nguyen, D. C., Nidever, D. L., Pinsonneault, M., Shetrone, M., Smee, S., Smith, V. V., Stolberg, T., Skrutskie, M. F., Walker, E., Wilson, J. C., Zasowski, G., Anders, F., Basu, S., Beland, S., Blanton, M. R., Bovy, J., Brownstein, J. R., Carlberg, J., Chaplin, W., Chiappini, C., Eisenstein, D. J., Elsworth, Y., Feuillet, D., Fleming, S. W., Galbraith-Frew, J., García, R. A., García-Hernández, D. A., Gillespie, B. A., Girardi, L., Gunn, J. E., Hasselquist, S., Hayden, M. R., Hekker, S., Ivans, I., Kinemuchi, K., Klaene, M., Mahadevan, S., Mathur, S., Mosser, B., Muna, D., Munn, J. A., Nichol, R. C., O'Connell, R. W., Parejko, J. K., Robin, A. C., Rocha-Pinto, H., Schultheis, M., Serenelli, A. M., Shane, N., Silva Aguirre, V., Sobeck, J. S., Thompson, B., Troup, N. W., Weinberg, D. H., and Zamora, O. (2017). The Apache Point Observatory Galactic Evolution Experiment (APOGEE). *AJ*, 154:94.

Majewski, S. R., Skrutskie, M. F., Weinberg, M. D., and Ostheimer, J. C. (2003). A Two Micron All Sky Survey View of the Sagittarius Dwarf Galaxy. I. Morphology of the Sagittarius Core and Tidal Arms. *ApJ*, 599:1082–1115.

Malin, D. and Hadley, B. (1997). HI in Shell Galaxies and Other Merger Remnants. *PASA*, 14:52–58.

Mandelker, N., Dekel, A., Ceverino, D., DeGraf, C., Guo, Y., and Primack, J. (2017). Giant clumps in simulated high- z Galaxies: properties, evolution and dependence on feedback. *MNRAS*, 464:635–665.

Mandelker, N., Dekel, A., Ceverino, D., Tweed, D., Moody, C. E., and Primack, J. (2014). The population of giant clumps in simulated high-z galaxies: in situ and ex situ migration and survival. *MNRAS*, 443:3675–3702.

Mansfield, P., Kravtsov, A. V., and Diemer, B. (2017). Splashback Shells of Cold Dark Matter Halos. *ApJ*, 841:34.

Marchesini, D., D'Onghia, E., Chincarini, G., Firmani, C., Conconi, P., Molinari, E., and Zacchei, A. (2002). Hα Rotation Curves: The Soft Core Question. *ApJ*, 575:801–813.

Marigo, P., Girardi, L., Bressan, A., Groenewegen, M. A. T., Silva, L., and Granato, G. L. (2008). Evolution of asymptotic giant branch stars. II. Optical to far-infrared isochrones with improved TP-AGB models. *A&A*, 482:883–905.

Marinacci, F., Pakmor, R., and Springel, V. (2014). The formation of disc galaxies in high-resolution moving-mesh cosmological simulations. *MNRAS*, 437:1750–1775.

Martig, M., Bournaud, F., Croton, D. J., Dekel, A., and Teyssier, R. (2012). A Diversity of Progenitors and Histories for Isolated Spiral Galaxies. *ApJ*, 756:26.

Martig, M., Bournaud, F., Teyssier, R., and Dekel, A. (2009). Morphological Quenching of Star Formation: Making Early-Type Galaxies Red. *ApJ*, 707:250–267.

Martig, M., Fouesneau, M., Rix, H.-W., Ness, M., Mészáros, S., García-Hernández, D. A., Pinsonneault, M., Serenelli, A., Silva Aguirre, V., and Zamora, O. (2016). Red giant masses and ages derived from carbon and nitrogen abundances. *MNRAS*, 456:3655–3670.

Martin, N. F., Chambers, K. C., Collins, M. L. M., Ibata, R. A., Rich, R. M., Bell, E. F., Bernard, E. J., Ferguson, A. M. N., Flewelling, H., Kaiser, N., Magnier, E. A., Tonry, J. L., and Wainscoat, R. J. (2014). Spectroscopy of the Three Distant Andromedan Satellites Cassiopeia III, Lacerta I, and Perseus I. *ApJ*, 793:L14.

Martin, N. F., Geha, M., Ibata, R. A., Collins, M. L. M., Laevens, B. P. M., Bell, E. F., Rix, H.-W., Ferguson, A. M. N., Chambers, K. C., Wainscoat, R. J., and Waters, C. (2016a). Is Draco II one of the faintest dwarf galaxies? First study from Keck/DEIMOS spectroscopy. *MNRAS*, 458:L59–L63.

Martin, N. F., Ibata, R. A., Bellazzini, M., Irwin, M. J., Lewis, G. F., and Dehnen, W. (2004). A dwarf galaxy remnant in Canis Major: the fossil of an in-plane accretion on to the Milky Way. *MNRAS*, 348:12–23.

Martin, N. F., Ibata, R. A., Lewis, G. F., McConnachie, A., Babul, A., Bate, N. F., Bernard, E., Chapman, S. C., Collins, M. M. L., Conn, A. R., Crnojević, D., Fardal, M. A., Ferguson, A. M. N., Irwin, M., Mackey, A. D., McMonigal, B., Navarro, J. F., and Rich, R. M. (2016b). The PAndAS View of the Andromeda Satellite System. II. Detailed Properties of 23 M31 Dwarf Spheroidal Galaxies. *ApJ*, 833:167.

Martin, N. F., Nidever, D. L., Besla, G., Olsen, K., Walker, A. R., Vivas, A. K., Gruendl, R. A., Kaleida, C. C., Muñoz, R. R., Blum, R. D., Saha, A., Conn, B. C., Bell, E. F., Chu, Y.-H., Cioni, M.-R. L., de Boer, T. J. L., Gallart, C., Jin, S., Kunder, A., Majewski, S. R., Martinez-Delgado, D., Monachesi, A., Monelli, M., Monteagudo, L., Noël, N. E. D., Olszewski, E. W., Stringfellow, G. S., van der Marel, R. P., and Zaritsky, D. (2015). Hydra II: A Faint and Compact Milky Way Dwarf Galaxy Found in the Survey of the Magellanic Stellar History. *ApJ*, 804:L5.

Martínez-Delgado, D., Butler, D. J., Rix, H.-W., Franco, V. I., Peñarrubia, J., Alfaro, E. J., and Dinescu, D. I. (2005). The Closest View of a Dwarf Galaxy: New Evidence on the Nature of the Canis Major Overdensity. *ApJ*, 633:205–209.

Martínez-Delgado, D., D'Onghia, E., Chonis, T. S., Beaton, R. L., Teuwen, K., GaBany, R. J., Grebel, E. K., and Morales, G. (2015). A Stellar Tidal Stream Around the Whale Galaxy, NGC 4631. *AJ*, 150:116.

Martínez-Delgado, D., Romanowsky, A. J., Gabany, R. J., Annibali, F., Arnold, J. A., Fliri, J., Zibetti, S., van der Marel, R. P., Rix, H.-W., Chonis, T. S., Carballo-Bello, J. A., Aloisi, A., Macciò, A. V., Gallego-Laborda, J., Brodie, J. P., and Merrifield, M. R. (2012). Dwarfs Gobbling Dwarfs: A Stellar Tidal Stream around NGC 4449 and Hierarchical Galaxy Formation on Small Scales. *ApJ*, 748:L24.

Martinez-Valpuesta, I. and Gerhard, O. (2013a). Metallicity Gradients Through Disk Instability: A Simple Model for the Milky Way's Boxy Bulge. *ApJ*, 766:L3.

Martinez-Valpuesta, I. and Gerhard, O. (2013b). Metallicity Gradients Through Disk Instability: A Simple Model for the Milky Way's Boxy Bulge. *ApJ*, 766:L3.

Mashchenko, S., Wadsley, J., and Couchman, H. M. P. (2008). Stellar Feedback in Dwarf Galaxy Formation. *Science*, 319:174–.

Masseron, T. and Gilmore, G. (2015). Carbon, nitrogen and α-element abundances determine the formation sequence of the Galactic thick and thin discs. *MNRAS*, 453:1855–1866.

Mateo, M. L. (1998). Dwarf Galaxies of the Local Group. *ARA&A*, 36:435–506.

Mather, J. C., Cheng, E. S., Eplee, R. E., J., Isaacman, R. B., Meyer, S. S., Shafer, R. A., Weiss, R., Wright, E. L., Bennett, C. L., Boggess, N. W., Dwek, E., Gulkis, S., Hauser, M. G., Janssen, M., Kelsall, T., Lubin, P. M., Moseley, S. H., J., Murdock, T. L., Silverberg, R. F., Smoot, G. F., and Wilkinson, D. T. (1990). A Preliminary Measurement of the Cosmic Microwave Background Spectrum by the Cosmic Background Explorer (COBE) Satellite. *ApJ*, 354:L37.

Mayer, L., Governato, F., Colpi, M., Moore, B., Quinn, T., Wadsley, J., Stadel, J., and Lake, G. (2001). The Metamorphosis of Tidally Stirred Dwarf Galaxies. *ApJ*, 559:754–784.

Mayer, L., Kazantzidis, S., Mastropietro, C., and Wadsley, J. (2007). Early gas stripping as the origin of the darkest galaxies in the Universe. *Nature*, 445:738–740.

Mayer, L., Mastropietro, C., Wadsley, J., Stadel, J., and Moore, B. (2006). Simultaneous ram pressure and tidal stripping; how dwarf spheroidals lost their gas. *MNRAS*, 369:1021–1038.

Mayer, L., Tamburello, V., Lupi, A., Keller, B., Wadsley, J., and Madau, P. (2016). Clumpy high-z galaxies as a testbed for feedback-regulated galaxy formation. *ArXiv e-prints*.

McConnachie, A. W. (2012). The Observed Properties of Dwarf Galaxies in and around the Local Group. *AJ*, 144:4.

McConnachie, A. W. and Irwin, M. J. (2006a). Structural properties of the M31 dwarf spheroidal galaxies. *MNRAS*, 365:1263–1276.

McConnachie, A. W. and Irwin, M. J. (2006b). The satellite distribution of M31. *MNRAS*, 365:902–914.

McConnachie, A. W., Irwin, M. J., Ibata, R. A., Dubinski, J., Widrow, L. M., Martin, N. F., Côté, P., Dotter, A. L., Navarro, J. F., Ferguson, A. M. N., Puzia, T. H., Lewis, G. F., Babul, A., Barmby, P., Bienaymé, O., Chapman, S. C., Cockcroft, R., Collins, M. L. M., Fardal, M. A., Harris, W. E., Huxor, A., Mackey, A. D., Peñarrubia, J., Rich, R. M., Richer, H. B., Siebert, A., Tanvir, N., Valls-Gabaud, D., and Venn, K. A. (2009a). The remnants of galaxy formation from a panoramic survey of the region around M31. *Nature*, 461:66–69.

McConnachie, A. W., Irwin, M. J., Ibata, R. A., Dubinski, J., Widrow, L. M., Martin, N. F., Côté, P., Dotter, A. L., Navarro, J. F., Ferguson, A. M. N., Puzia, T. H., Lewis, G. F., Babul, A., Barmby, P., Bienaymé, O., Chapman, S. C., Cockcroft, R., Collins, M. L. M., Fardal, M. A., Harris, W. E., Huxor, A., Mackey, A. D., Peñarrubia, J., Rich, R. M., Richer, H. B., Siebert, A., Tanvir, N., Valls-Gabaud, D., and Venn, K. A. (2009b). The remnants of galaxy formation from a panoramic survey of the region around M31. *Nature*, 461:66–69.

McGaugh, S. S. (2012). The Baryonic Tully-Fisher Relation of Gas-rich Galaxies as a Test of ΛCDM and MOND. *AJ*, 143:40.

McGaugh, S. S., Lelli, F., and Schombert, J. M. (2016). Radial Acceleration Relation in Rotationally Supported Galaxies. *Physical Review Letters*, 117(20):201101.

McGaugh, S. S., Rubin, V. C., and de Blok, W. J. G. (2001). High-Resolution Rotation Curves of Low Surface Brightness Galaxies. I. Data. *AJ*, 122:2381–2395.

McWilliam, A. and Zoccali, M. (2010). Two Red Clumps and the X-shaped Milky Way Bulge. *ApJ*, 724:1491–1502.

Merritt, A., van Dokkum, P., Abraham, R., and Zhang, J. (2016). The Dragonfly nearby Galaxies Survey. I. Substantial Variation in the Diffuse Stellar Halos around Spiral Galaxies. *ApJ*, 830:62.

Merritt, D. and Sellwood, J. A. (1994). Bending instabilities in stellar systems. *ApJ*, 425:551–567.

Metz, M., Kroupa, P., and Jerjen, H. (2007). The spatial distribution of the Milky Way and Andromeda satellite galaxies. *MNRAS*, 374:1125–1145.

Metz, M., Kroupa, P., and Libeskind, N. I. (2008). The Orbital Poles of Milky Way Satellite Galaxies: A Rotationally Supported Disk of Satellites. *ApJ*, 680:287–294.

Miller, M. J. and Bregman, J. N. (2013). The Structure of the Milky Way's Hot Gas Halo. *ApJ*, 770:118.

Miller, M. J. and Bregman, J. N. (2015). Constraining the Milky Way's Hot Gas Halo with O VII and O VIII Emission Lines. *ApJ*, 800:14.

Minchev, I., Steinmetz, M., Chiappini, C., Martig, M., Anders, F., Matijevic, G., and de Jong, R. S. (2017). The Relationship between Mono-abundance and Mono-age Stellar Populations in the Milky Way Disk. *ApJ*, 834:27.

Minniti, D., Lucas, P. W., Emerson, J. P., Saito, R. K., Hempel, M., Pietrukowicz, P., Ahumada, A. V., Alonso, M. V., Alonso-Garcia, J., Arias, J. I., Bandyopadhyay, R. M., Barbá, R. H., Barbuy, B., Bedin, L. R., Bica, E., Borissova, J., Bronfman, L., Carraro, G., Catelan, M., Clariá, J. J., Cross, N., de Grijs, R., Dékány, I., Drew, J. E., Fariña, C., Feinstein, C., Fernández Lajús, E., Gamen, R. C., Geisler, D., Gieren, W., Goldman, B., Gonzalez, O. A., Gunthardt, G., Gurovich, S., Hambly, N. C., Irwin, M. J., Ivanov, V. D., Jordán, A., Kerins, E., Kinemuchi, K., Kurtev, R., López-Corredoira, M., Maccarone, T., Masetti, N., Merlo, D., Messineo, M., Mirabel, I. F., Monaco, L., Morelli, L., Padilla,

N., Palma, T., Parisi, M. C., Pignata, G., Rejkuba, M., Roman-Lopes, A., Sale, S. E., Schreiber, M. R., Schröder, A. C., Smith, M., , Jr., L. S., Soto, M., Tamura, M., Tappert, C., Thompson, M. A., Toledo, I., Zoccali, M., and Pietrzynski, G. (2010). VISTA Variables in the Via Lactea (VVV): The public ESO near-IR variability survey of the Milky Way. *New A*, 15:433–443.

Misner, C. W. (1968). The Isotropy of the Universe. *ApJ*, 151:431.

Mo, H., van den Bosch, F. C., and White, S. (2010). *Galaxy Formation and Evolution*.

Mo, H. J., Mao, S., and White, S. D. M. (1998). The formation of galactic discs. *MNRAS*, 295:319–336.

Molinari, S., Bally, J., Noriega-Crespo, A., Compiègne, M., Bernard, J. P., Paradis, D., Martin, P., Testi, L., Barlow, M., Moore, T., Plume, R., Swinyard, B., Zavagno, A., Calzoletti, L., Di Giorgio, A. M., Elia, D., Faustini, F., Natoli, P., Pestalozzi, M., Pezzuto, S., Piacentini, F., Polenta, G., Polychroni, D., Schisano, E., Traficante, A., Veneziani, M., Battersby, C., Burton, M., Carey, S., Fukui, Y., Li, J. Z., Lord, S. D., Morgan, L., Motte, F., Schuller, F., Stringfellow, G. S., Tan, J. C., Thompson, M. A., Ward-Thompson, D., White, G., and Umana, G. (2011). A 100 pc Elliptical and Twisted Ring of Cold and Dense Molecular Clouds Revealed by Herschel Around the Galactic Center. *ApJ*, 735:L33.

Monaghan, J. J. (1992). Smoothed particle hydrodynamics. *ARA&A*, 30:543–574.

Moody, C. E., Guo, Y., Mandelker, N., Ceverino, D., Mozena, M., Koo, D. C., Dekel, A., and Primack, J. (2014). Star formation and clumps in cosmological galaxy simulations with radiation pressure feedback. *MNRAS*, 444:1389–1399.

Moore, B. (1994). Evidence against dissipation-less dark matter from observations of galaxy haloes. *Nature*, 370:629–631.

Moore, B., Diemand, J., and Stadel, J. (2004). On the age-radius relation and orbital history of cluster galaxies. In Diaferio, A., editor, *IAU Colloq. 195: Outskirts of Galaxy Clusters: Intense Life in the Suburbs*, pages 513–518.

Moore, B., Ghigna, S., Governato, F., Lake, G., Quinn, T., Stadel, J., and Tozzi, P. (1999a). Dark Matter Substructure within Galactic Halos. *ApJ*, 524:L19–L22.

Moore, B., Ghigna, S., Governato, F., Lake, G., Quinn, T., Stadel, J., and Tozzi, P. (1999b). Dark Matter Substructure within Galactic Halos. *ApJ*, 524:L19–L22.

More, S., Diemer, B., and Kravtsov, A. V. (2015). The Splashback Radius as a Physical Halo Boundary and the Growth of Halo Mass. *ApJ*, 810:36.

More, S., van den Bosch, F. C., Cacciato, M., Skibba, R., Mo, H. J., and Yang, X. (2011). Satellite kinematics - III. Halo masses of central galaxies in SDSS. *MNRAS*, 410:210–226.

Morishita, T., Ichikawa, T., Noguchi, M., Akiyama, M., Patel, S. G., Kajisawa, M., and Obata, T. (2015). From Diversity to Dichotomy, and Quenching: Milky-Way-like and Massive Galaxy Progenitors at $0.5 < z < 3.0$. *ApJ*, 805:34.

Moster, B. P., Naab, T., and White, S. D. M. (2013). Galactic star formation and accretion histories from matching galaxies to dark matter haloes. *MNRAS*, 428:3121–3138.

Moster, B. P., Somerville, R. S., Maulbetsch, C., van den Bosch, F. C., Macciò, A. V., Naab, T., and Oser, L. (2010). Constraints on the Relationship between Stellar Mass and Halo Mass at Low and High Redshift. *ApJ*, 710:903–923.

Murata, K. L., Kajisawa, M., Taniguchi, Y., Kobayashi, M. A. R., Shioya, Y., Capak, P., Ilbert, O., Koekemoer, A. M., Salvato, M., and Scoville, N. Z. (2014). Evolution of the Fraction of Clumpy Galaxies at $0.2 < z < 1.0$ in the COSMOS Field. *ApJ*, 786:15.

Naab, T. and Ostriker, J. P. (2017). Theoretical Challenges in Galaxy Formation. *ARA&A*, 55:59–109.

Nataf, D. M., Udalski, A., Gould, A., Fouqué, P., and Stanek, K. Z. (2010). The Split Red Clump of the Galactic Bulge from OGLE-III. *ApJ*, 721:L28–L32.

Navarro, J. F., Frenk, C. S., and White, S. D. M. (1996). The Structure of Cold Dark Matter Halos. *ApJ*, 462:563.

Navarro, J. F., Frenk, C. S., and White, S. D. M. (1997a). A Universal Density Profile from Hierarchical Clustering. *ApJ*, 490:493–508.

Navarro, J. F., Frenk, C. S., and White, S. D. M. (1997b). A Universal Density Profile from Hierarchical Clustering. *ApJ*, 490:493.

Navarro, J. F., Ludlow, A., Springel, V., Wang, J., Vogelsberger, M., White, S. D. M., Jenkins, A., Frenk, C. S., and Helmi, A. (2010). The diversity and similarity of simulated cold dark matter haloes. *MNRAS*, 402:21–34.

Navarro, J. F. and Steinmetz, M. (2000). Dark Halo and Disk Galaxy Scaling Laws in Hierarchical Universes. *ApJ*, 538:477–488.

Nelson, D., Vogelsberger, M., Genel, S., Sijacki, D., Kereš, D., Springel, V., and Hernquist, L. (2013). Moving mesh cosmology: tracing cosmological gas accretion. *MNRAS*, 429:3353–3370.

Nelson, E. J., van Dokkum, P. G., Förster Schreiber, N. M., Franx, M., Brammer, G. B., Momcheva, I. G., Wuyts, S., Whitaker, K. E., Skelton, R. E., Fumagalli, M., Hayward, C. C., Kriek, M., Labbé, I., Leja, J., Rix, H.-W., Tacconi, L. J., van der Wel, A., van den Bosch, F. C., Oesch, P. A., Dickey, C., and Ulf Lange, J. (2016a). Where Stars Form: Inside-out Growth and Coherent Star Formation from HST Hα Maps of 3200 Galaxies across the Main Sequence at $0.7 < z < 1.5$. *ApJ*, 828:27.

Nelson, E. J., van Dokkum, P. G., Momcheva, I. G., Brammer, G. B., Wuyts, S., Franx, M., Förster Schreiber, N. M., Whitaker, K. E., and Skelton, R. E. (2016b). Spatially Resolved Dust Maps from Balmer Decrements in Galaxies at z ˜ 1.4. *ApJ*, 817:L9.

Ness, M., Debattista, V. P., Bensby, T., Feltzing, S., Roškar, R., Cole, D. R., Johnson, J. A., and Freeman, K. (2014). Young Stars in an Old Bulge: A Natural Outcome of Internal Evolution in the Milky Way. *ApJ*, 787:L19.

Ness, M., Freeman, K., Athanassoula, E., Wylie-de-Boer, E., Bland-Hawthorn, J., Asplund, M., Lewis, G. F., Yong, D., Lane, R. R., and Kiss, L. L. (2013a). ARGOS - III. Stellar populations in the Galactic bulge of the Milky Way. *MNRAS*, 430:836–857.

Ness, M., Freeman, K., Athanassoula, E., Wylie-de-Boer, E., Bland-Hawthorn, J., Asplund, M., Lewis, G. F., Yong, D., Lane, R. R., Kiss, L. L., and Ibata, R. (2013b). ARGOS - IV. The kinematics of the Milky Way bulge. *MNRAS*, 432:2092–2103.

Ness, M., Freeman, K., Athanassoula, E., Wylie-De-Boer, E., Bland-Hawthorn, J., Lewis, G. F., Yong, D., Asplund, M., Lane, R. R., Kiss, L. L., and Ibata, R. (2012). The Origin of the Split Red Clump in the Galactic Bulge of the Milky Way. *ApJ*, 756:22.

Ness, M., Hogg, D. W., Rix, H.-W., Martig, M., Pinsonneault, M. H., and Ho, A. Y. Q. (2016a). Spectroscopic Determination of Masses (and Implied Ages) for Red Giants. *ApJ*, 823:114.

Ness, M. and Lang, D. (2016). The X-shaped Bulge of the Milky Way Revealed by WISE. *AJ*, 152:14.

Ness, M., Zasowski, G., Johnson, J. A., Athanassoula, E., Majewski, S. R., García Pérez, A. E., Bird, J., Nidever, D., Schneider, D. P., Sobeck, J., Frinchaboy, P., Pan, K., Bizyaev, D., Oravetz, D., and Simmons, A. (2016b). APOGEE Kinematics. I. Overview of the Kinematics of the Galactic Bulge as Mapped By APOGEE. *ApJ*, 819:2.

Netzer, H. (2013). *The Physics and Evolution of Active Galactic Nuclei*.

Newberg, H. J., Yanny, B., Rockosi, C., Grebel, E. K., Rix, H.-W., Brinkmann, J., Csabai, I., Hennessy, G., Hindsley, R. B., Ibata, R., Ivezić, Z., Lamb, D., Nash, E. T., Odenkirchen, M., Rave, H. A., Schneider, D. P., Smith, J. A., Stolte, A., and York, D. G. (2002). The Ghost of Sagittarius and Lumps in the Halo of the Milky Way. *ApJ*, 569:245–274.

Nidever, D. L., Bovy, J., Bird, J. C., Andrews, B. H., Hayden, M., Holtzman, J., Majewski, S. R., Smith, V., Robin, A. C., García Pérez, A. E., Cunha, K., Allende Prieto, C., Zasowski, G., Schiavon, R. P., Johnson, J. A., Weinberg, D. H., Feuillet, D., Schneider, D. P., Shetrone, M., Sobeck, J., García-Hernández, D. A., Zamora, O., Rix, H.-W., Beers, T. C., Wilson, J. C., O'Connell, R. W., Minchev, I., Chiappini, C., Anders, F., Bizyaev, D., Brewington, H., Ebelke, G., Frinchaboy, P. M., Ge, J., Kinemuchi, K., Malanushenko, E., Malanushenko, V., Marchante, M., Mészáros, S., Oravetz, D., Pan, K., Simmons, A., and Skrutskie, M. F. (2014). Tracing Chemical Evolution over the Extent of the Milky Way's Disk with APOGEE Red Clump Stars. *ApJ*, 796:38.

Noeske, K. G., Weiner, B. J., Faber, S. M., Papovich, C., Koo, D. C., Somerville, R. S., Bundy, K., Conselice, C. J., Newman, J. A., Schiminovich, D., Le Floc'h, E., Coil, A. L., Rieke, G. H., Lotz, J. M., Primack, J. R., Barmby, P., Cooper, M. C., Davis, M., Ellis, R. S., Fazio, G. G., Guhathakurta, P., Huang, J., Kassin, S. A., Martin, D. C., Phillips, A. C., Rich, R. M., Small, T. A., Willmer, C. N. A., and Wilson, G. (2007). Star Formation in AEGIS Field Galaxies since z=1.1: The Dominance of Gradually Declining Star Formation, and the Main Sequence of Star-forming Galaxies. *ApJ*,

660:L43–L46.

Noguchi, M. (1998). Clumpy star-forming regions as the origin of the peculiar morphology of high-redshift galaxies. *Nature*, 392:253.

Noguchi, M. (1999). Early Evolution of Disk Galaxies: Formation of Bulges in Clumpy Young Galactic Disks. *ApJ*, 514:77–95.

Oñorbe, J., Boylan-Kolchin, M., Bullock, J. S., Hopkins, P. F., Kereš, D., Faucher-Giguère, C.-A., Quataert, E., and Murray, N. (2015). Forged in FIRE: cusps, cores and baryons in low-mass dwarf galaxies. *MNRAS*, 454:2092–2106.

Oñorbe, J., Garrison-Kimmel, S., Maller, A. H., Bullock, J. S., Rocha, M., and Hahn, O. (2014). How to zoom: bias, contamination and Lagrange volumes in multimass cosmological simulations. *MNRAS*, 437:1894–1908.

Obreja, A., Brook, C. B., Stinson, G., Domínguez-Tenreiro, R., Gibson, B. K., Silva, L., and Granato, G. L. (2014). The main sequence and the fundamental metallicity relation in MaGICC Galaxies: evolution and scatter. *MNRAS*, 442:1794–1804.

Obreja, A., Domínguez-Tenreiro, R., Brook, C., Martínez-Serrano, F. J., Doménech-Moral, M., Serna, A., Mollá, M., and Stinson, G. (2013). A Two-phase Scenario for Bulge Assembly in ΛCDM Cosmologies. *ApJ*, 763:26.

Obreja, A., Dutton, A. A., Macciò, A. V., Moster, B., Buck, T., van den Ven, G., Wang, L., Stinson, G. S., and Zhu, L. (2018a). NIHAO XVI: The properties and evolution of kinematically selected discs, bulges and stellar haloes. *ArXiv e-prints*.

Obreja, A., Macciò, A. V., Moster, B., Dutton, A. A., Buck, T., Stinson, G. S., and Wang, L. (2018b). Introducing galactic structure finder: the multiple stellar kinematic structures of a simulated Milky Way mass galaxy. *MNRAS*, 477:4915–4930.

Obreja, A., Stinson, G. S., Dutton, A. A., Macciò, A. V., Wang, L., and Kang, X. (2016). NIHAO VI. The hidden discs of simulated galaxies. *MNRAS*, 459:467–486.

Oh, S.-H., Hunter, D. A., Brinks, E., Elmegreen, B. G., Schruba, A., Walter, F., Rupen, M. P., Young, L. M., Simpson, C. E., Johnson, M. C., Herrmann, K. A., Ficut-Vicas, D., Cigan, P., Heesen, V., Ashley, T., and Zhang, H.-X. (2015). High-resolution Mass Models of Dwarf Galaxies from LITTLE THINGS. *AJ*, 149:180.

Oklopčić, A., Hopkins, P. F., Feldmann, R., Kereš, D., Faucher-Giguère, C.-A., and Murray, N. (2017). Giant clumps in the FIRE simulations: a case study of a massive high-redshift galaxy. *MNRAS*, 465:952–969.

Okuda, H., Maihara, T., Oda, N., and Sugiyama, T. (1977). 2.4-micron mapping of the galactic central region. *Nature*, 265:515.

Oman, K. A., Navarro, J. F., Fattahi, A., Frenk, C. S., Sawala, T., White, S. D. M., Bower, R., Crain, R. A., Furlong, M., Schaller, M., Schaye, J., and Theuns, T. (2015). The unexpected diversity of dwarf galaxy rotation curves. *MNRAS*, 452:3650–3665.

Oppenheimer, B. D. and Davé, R. (2006). Cosmological simulations of intergalactic medium enrichment from galactic outflows. *MNRAS*, 373:1265–1292.

Ostriker, J. P. and Peebles, P. J. E. (1973). A Numerical Study of the Stability of Flattened Galaxies: or, can Cold Galaxies Survive? *ApJ*, 186:467–480.

Ostriker, J. P., Peebles, P. J. E., and Yahil, A. (1974). The size and mass of galaxies, and the mass of the universe. *ApJ*, 193:L1–L4.

Overzier, R. A., Heckman, T. M., Tremonti, C., Armus, L., Basu-Zych, A., Gonçalves, T., Rich, R. M., Martin, D. C., Ptak, A., Schiminovich, D., Ford, H. C., Madore, B., and Seibert, M. (2009). Local Lyman Break Galaxy Analogs: The Impact of Massive Star-Forming Clumps on the Interstellar Medium and the Global Structure of Young, Forming Galaxies. *ApJ*, 706:203–222.

Papastergis, E., Cattaneo, A., Huang, S., Giovanelli, R., and Haynes, M. P. (2012). A Direct Measurement of the Baryonic Mass Function of Galaxies and Implications for the Galactic Baryon Fraction. *ApJ*, 759:138.

Papastergis, E., Giovanelli, R., Haynes, M. P., and Shankar, F. (2015). Is there a "too big to fail" problem in the field? *A&A*, 574:A113.

Papastergis, E. and Ponomareva, A. A. (2017). Testing core creation in hydrodynamical simulations using the HI kinematics of field dwarfs. *A&A*, 601:A1.

Papastergis, E. and Shankar, F. (2016). An assessment of the "too big to fail" problem for field dwarf galaxies in view of baryonic feedback effects. *A&A*, 591:A58.

Patel, S. G., van Dokkum, P. G., Franx, M., Quadri, R. F., Muzzin, A., Marchesini, D., Williams, R. J., Holden, B. P., and Stefanon, M. (2013). HST/WFC3 Confirmation of the Inside-out Growth of Massive Galaxies at $0 < z < 2$ and Identification of Their Star-forming Progenitors at $z \tilde{} 3$. *ApJ*, 766:15.

Pawlik, A. H. and Schaye, J. (2008). TRAPHIC - radiative transfer for smoothed particle hydrodynamics simulations. *MNRAS*, 389:651–677.

Pawlik, A. H. and Schaye, J. (2011). Multifrequency, thermally coupled radiative transfer with TRAPHIC: method and tests. *MNRAS*, 412:1943–1964.

Pawlowski, M. S., Famaey, B., Jerjen, H., Merritt, D., Kroupa, P., Dabringhausen, J., Lüghausen, F., Forbes, D. A., Hensler, G., Hammer, F., Puech, M., Fouquet, S., Flores, H., and Yang, Y. (2014). Co-orbiting satellite galaxy structures are still in conflict with the distribution of primordial dwarf galaxies. *MNRAS*, 442:2362–2380.

Pawlowski, M. S. and Kroupa, P. (2014). The Vast Polar Structure of the Milky Way Attains New Members. *ApJ*, 790:74.

Pawlowski, M. S., Kroupa, P., Angus, G., de Boer, K. S., Famaey, B., and Hensler, G. (2012). Filamentary accretion cannot explain the orbital poles of the Milky Way satellites. *MNRAS*, 424:80–92.

Pawlowski, M. S., Kroupa, P., and Jerjen, H. (2013). Dwarf galaxy planes: the discovery of symmetric structures in the Local Group. *MNRAS*, 435:1928–1957.

Pawlowski, M. S. and McGaugh, S. S. (2014). Perseus I and the NGC 3109 association in the context of the Local Group dwarf galaxy structures. *MNRAS*, 440:908–919.

Pawlowski, M. S., McGaugh, S. S., and Jerjen, H. (2015). The new Milky Way satellites: alignment with the VPOS and predictions for proper motions and velocity dispersions. *MNRAS*, 453:1047–1061.

Peñarrubia, J., Ma, Y.-Z., Walker, M. G., and McConnachie, A. (2014). A dynamical model of the local cosmic expansion. *MNRAS*, 443:2204–2222.

Peñarrubia, J., Navarro, J. F., and McConnachie, A. W. (2008). The Tidal Evolution of Local Group Dwarf Spheroidals. *ApJ*, 673:226–240.

Pedregosa, F., Varoquaux, G., Gramfort, A., Michel, V., Thirion, B., Grisel, O., Blondel, M., Prettenhofer, P., Weiss, R., Dubourg, V., Vanderplas, J., Passos, A., Cournapeau, D., Brucher, M., Perrot, M., and Duchesnay, E. (2011). Scikit-learn: Machine learning in Python. *Journal of Machine Learning Research*, 12:2825–2830.

Peebles, P. J. E. (1971). Rotation of Galaxies and the Gravitational Instability Picture. *A&A*, 11:377.

Peebles, P. J. E. (1980). *The large-scale structure of the universe*.

Peebles, P. J. E. (1982). Large-scale background temperature and mass fluctuations due to scale-invariant primeval perturbations. *ApJ*, 263:L1–L5.

Peebles, P. J. E. (1984). Dark matter and the origin of galaxies and globular star clusters. *ApJ*, 277:470–477.

Peeples, M. S. and Shankar, F. (2011). Constraints on star formation driven galaxy winds from the mass-metallicity relation at z= 0. *MNRAS*, 417:2962–2981.

Penzias, A. A. and Wilson, R. W. (1965). A Measurement of Excess Antenna Temperature at 4080 Mc/s. *ApJ*, 142:419–421.

Penzo, C., Macciò, A. V., Casarini, L., Stinson, G. S., and Wadsley, J. (2014). Dark MaGICC: the effect of dark energy on disc galaxy formation. Cosmology does matter. *MNRAS*, 442:176–186.

Pérez, F. and Granger, B. E. (2007). IPython: a system for interactive scientific computing. *Computing in Science and Engineering*, 9(3):21–29.

Perez, J., Valenzuela, O., Tissera, P. B., and Michel-Dansac, L. (2013). Clumpy disc and bulge formation. *MNRAS*, 436:259–265.

Perlmutter, S., Aldering, G., Goldhaber, G., Knop, R. A., Nugent, P., Castro, P. G., Deustua, S., Fabbro, S., Goobar, A., Groom, D. E., Hook, I. M., Kim, A. G., Kim, M. Y., Lee, J. C., Nunes, N. J., Pain, R., Pennypacker, C. R., Quimby, R., Lidman, C., Ellis, R. S., Irwin, M., McMahon, R. G., Ruiz-Lapuente, P., Walton, N., Schaefer, B., Boyle, B. J., Filippenko, A. V., Matheson, T., Fruchter, A. S., Panagia, N., Newberg, H. J. M., Couch, W. J., and Supernova Cosmology Project (1999). Measurements of Omega and Lambda from 42 High-Redshift Supernovae. *ApJ*, 517:565–586.

Perret, V., Renaud, F., Epinat, B., Amram, P., Bournaud, F., Contini, T., Teyssier, R., and Lambert, J.-C. (2014). Evolution of the mass, size, and star formation rate in high redshift merging galaxies. MIRAGE - A new sample of simulations with detailed

stellar feedback. *A&A*, 562:A1.

Peter, A. H. G., Rocha, M., Bullock, J. S., and Kaplinghat, M. (2013). Cosmological simulations with self-interacting dark matter - II. Halo shapes versus observations. *MNRAS*, 430:105–120.

Pfenniger, D. and Friedli, D. (1991). Structure and dynamics of 3D N-body barred galaxies. *A&A*, 252:75–93.

Phillips, J. I., Cooper, M. C., Bullock, J. S., and Boylan-Kolchin, M. (2015). Are rotating planes of satellite galaxies ubiquitous? *MNRAS*, 453:3839–3847.

Pietrukowicz, P., Kozłowski, S., Skowron, J., Soszyński, I., Udalski, A., Poleski, R., Wyrzykowski, Ł., Szymański, M. K., Pietrzyński, G., Ulaczyk, K., Mróz, P., Skowron, D. M., and Kubiak, M. (2015). Deciphering the 3D Structure of the Old Galactic Bulge from the OGLE RR Lyrae Stars. *ApJ*, 811:113.

Pizagno, J., Prada, F., Weinberg, D. H., Rix, H.-W., Pogge, R. W., Grebel, E. K., Harbeck, D., Blanton, M., Brinkmann, J., and Gunn, J. E. (2007). The Tully-Fisher Relation and its Residuals for a Broadly Selected Sample of Galaxies. *AJ*, 134:945–972.

Planck Collaboration, Ade, P. A. R., Aghanim, N., Armitage-Caplan, C., Arnaud, M., Ashdown, M., Atrio-Barandela, F., Aumont, J., Baccigalupi, C., Banday, A. J., and et al. (2014). Planck 2013 results. XVI. Cosmological parameters. *A&A*, 571:A16.

Pohlen, M., Martínez-Delgado, D., Majewski, S., Palma, C., Prada, F., and Balcells, M. (2004). Tidal Streams around External Galaxies. In Prada, F., Martinez Delgado, D., and Mahoney, T. J., editors, *Satellites and Tidal Streams*, volume 327 of *Astronomical Society of the Pacific Conference Series*, page 288.

Pontzen, A. and Governato, F. (2012). How supernova feedback turns dark matter cusps into cores. *MNRAS*, 421:3464–3471.

Pontzen, A., Roškar, R., Stinson, G. S., Woods, R., Reed, D. M., Coles, J., and Quinn, T. R. (2013). pynbody: Astrophysics Simulation Analysis for Python. Astrophysics Source Code Library, ascl:1305.002.

Pontzen, A. and Tremmel, M. (2018). Tangos: the agile numerical galaxy organization system. *ArXiv e-prints*.

Portail, M. (2016). Dynamical Modelling Of The Inner Galactic Barred Disk. In *Discs in galaxies (Discs 2016)*, page 32.

Portail, M., Gerhard, O., Wegg, C., and Ness, M. (2017a). Dynamical modelling of the galactic bulge and bar: the Milky Way's pattern speed, stellar and dark matter mass distribution. *MNRAS*, 465:1621–1644.

Portail, M., Wegg, C., and Gerhard, O. (2015a). Peanuts, brezels and bananas: food for thought on the orbital structure of the Galactic bulge. *MNRAS*, 450:L66–L70.

Portail, M., Wegg, C., Gerhard, O., and Martinez-Valpuesta, I. (2015b). Made-to-measure models of the Galactic box/peanut bulge: stellar and total mass in the bulge region. *MNRAS*, 448:713–731.

Portail, M., Wegg, C., Gerhard, O., and Ness, M. (2017b). Chemodynamical Modelling of the Galactic Bulge and Bar. *ArXiv e-prints*.

Press, W. H. and Schechter, P. (1974). Formation of Galaxies and Clusters of Galaxies by Self-Similar Gravitational Condensation. *ApJ*, 187:425–438.

Price, D. J. (2008). Modelling discontinuities and Kelvin Helmholtz instabilities in SPH. *Journal of Computational Physics*, 227:10040–10057.

Puech, M. (2010). Clumpy galaxies at z ˜ 0.6: kinematics, stability and comparison with analogues at other redshifts. *MNRAS*, 406:535–547.

Quillen, A. C. (2002). Growth of a Peanut-shaped Bulge via Resonant Trapping of Stellar Orbits in the Vertical Inner Lindblad Resonances. *AJ*, 124:722–732.

Quillen, A. C., Minchev, I., Sharma, S., Qin, Y.-J., and Di Matteo, P. (2014). A vertical resonance heating model for X- or peanut-shaped galactic bulges. *MNRAS*, 437:1284–1307.

Raha, N., Sellwood, J. A., James, R. A., and Kahn, F. D. (1991). A dynamical instability of bars in disk galaxies. *Nature*, 352:411.

Read, J. I., Agertz, O., and Collins, M. L. M. (2016). Dark matter cores all the way down. *MNRAS*, 459:2573–2590.

Read, J. I., Iorio, G., Agertz, O., and Fraternali, F. (2017). The stellar mass-halo mass relation of isolated field dwarfs: a critical test of ΛCDM at the edge of galaxy formation. *MNRAS*, 467:2019–2038.

Rees, M. J. and Ostriker, J. P. (1977). Cooling, dynamics and fragmentation of massive gas clouds - Clues to the masses and radii of galaxies and clusters. *MNRAS*, 179:541–559.

Revaz, Y., Arnaudon, A., Nichols, M., Bonvin, V., and Jablonka, P. (2016). Computational issues in chemo-dynamical modelling of the formation and evolution of galaxies. *A&A*, 588:A21.

Riess, A. G., Filippenko, A. V., Challis, P., Clocchiatti, A., Diercks, A., Garnavich, P. M., Gilliland, R. L., Hogan, C. J., Jha, S., Kirshner, R. P., Leibundgut, B., Phillips, M. M., Reiss, D., Schmidt, B. P., Schommer, R. A., Smith, R. C., Spyromilio, J., Stubbs, C., Suntzeff, N. B., and Tonry, J. (1998). Observational Evidence from Supernovae for an Accelerating Universe and a Cosmological Constant. *AJ*, 116:1009–1038.

Ritchie, B. W. and Thomas, P. A. (2001). Multiphase smoothed-particle hydrodynamics. *MNRAS*, 323:743–756.

Roberts, M. S. and Rots, A. H. (1973). Comparison of Rotation Curves of Different Galaxy Types. *A&A*, 26:483–485.

Robertson, B., Bullock, J. S., Cox, T. J., Di Matteo, T., Hernquist, L., Springel, V., and Yoshida, N. (2006). A Merger-driven Scenario for Cosmological Disk Galaxy Formation. *ApJ*, 645:986–1000.

Robertson, B., Yoshida, N., Springel, V., and Hernquist, L. (2004). Disk Galaxy Formation in a Λ Cold Dark Matter Universe. *ApJ*, 606:32–45.

Rojas-Arriagada, A., Recio-Blanco, A., de Laverny, P., Mikolaitis, Š., Matteucci, F., Spitoni, E., Schultheis, M., Hayden, M., Hill, V., Zoccali, M., Minniti, D., Gonzalez, O. A., Gilmore, G., Randich, S., Feltzing, S., Alfaro, E. J., Babusiaux, C., Bensby, T., Bragaglia, A., Flaccomio, E., Koposov, S. E., Pancino, E., Bayo, A., Carraro, G., Casey, A. R., Costado, M. T., Damiani, F., Donati, P., Franciosini, E., Hourihane, A., Jofré, P., Lardo, C., Lewis, J., Lind, K., Magrini, L., Morbidelli, L., Sacco, G. G., Worley, C. C., and Zaggia, S. (2017). The Gaia-ESO Survey: Exploring the complex nature and origins of the Galactic bulge populations. *A&A*, 601:A140.

Rojas-Arriagada, A., Recio-Blanco, A., Hill, V., de Laverny, P., Schultheis, M., Babusiaux, C., Zoccali, M., Minniti, D., Gonzalez, O. A., Feltzing, S., Gilmore, G., Randich, S., Vallenari, A., Alfaro, E. J., Bensby, T., Bragaglia, A., Flaccomio, E., Lanzafame, A. C., Pancino, E., Smiljanic, R., Bergemann, M., Costado, M. T., Damiani, F., Hourihane, A., Jofré, P., Lardo, C., Magrini, L., Maiorca, E., Morbidelli, L., Sbordone, L., Worley, C. C., Zaggia, S., and Wyse, R. (2014a). The Gaia-ESO Survey: metallicity and kinematic trends in the Milky Way bulge. *A&A*, 569:A103.

Rojas-Arriagada, A., Recio-Blanco, A., Hill, V., de Laverny, P., Schultheis, M., Babusiaux, C., Zoccali, M., Minniti, D., Gonzalez, O. A., Feltzing, S., Gilmore, G., Randich, S., Vallenari, A., Alfaro, E. J., Bensby, T., Bragaglia, A., Flaccomio, E., Lanzafame, A. C., Pancino, E., Smiljanic, R., Bergemann, M., Costado, M. T., Damiani, F., Hourihane, A., Jofré, P., Lardo, C., Magrini, L., Maiorca, E., Morbidelli, L., Sbordone, L., Worley, C. C., Zaggia, S., and Wyse, R. (2014b). The Gaia-ESO Survey: metallicity and kinematic trends in the Milky Way bulge. *A&A*, 569:A103.

Rubin, V. C., Ford, Jr., W. K., and Thonnard, N. (1978). Extended rotation curves of high-luminosity spiral galaxies. IV - Systematic dynamical properties, SA through SC. *ApJ*, 225:L107–L111.

Rubin, V. C., Ford, Jr., W. K., and Thonnard, N. (1980). Rotational properties of 21 SC galaxies with a large range of luminosities and radii, from NGC 4605 /R = 4kpc/ to UGC 2885 /R = 122 kpc/. *ApJ*, 238:471–487.

Rybizki, J., Just, A., and Rix, H.-W. (2017). Chempy: A flexible chemical evolution model for abundance fitting. Do the Sun's abundances alone constrain chemical evolution models? *A&A*, 605:A59.

Saito, R. K., Zoccali, M., McWilliam, A., Minniti, D., Gonzalez, O. A., and Hill, V. (2011). Mapping the X-shaped Milky Way Bulge. *AJ*, 142:76.

Saitoh, T. R. and Makino, J. (2009). A Necessary Condition for Individual Time Steps in SPH Simulations. *ApJ*, 697:L99–L102.

Samland, M. and Gerhard, O. E. (2003). The formation of a disk galaxy within a growing dark halo. *A&A*, 399:961–982.

Sánchez, S. F., Kennicutt, R. C., Gil de Paz, A., van de Ven, G., Vílchez, J. M., Wisotzki, L., Walcher, C. J., Mast, D., Aguerri, J. A. L., Albiol-Pérez, S., Alonso-Herrero, A., Alves, J., Bakos, J., Bartáková, T., Bland-Hawthorn, J., Boselli, A., Bomans, D. J., Castillo-Morales, A., Cortijo-Ferrero, C., de Lorenzo-Cáceres, A., Del Olmo, A., Dettmar, R.-J., Díaz, A., Ellis, S., Falcón-Barroso, J., Flores, H., Gallazzi, A., García-Lorenzo, B., González Delgado, R., Gruel, N., Haines, T., Hao, C., Husemann, B., Iglésias-Páramo, J., Jahnke, K., Johnson, B., Jungwiert, B., Kalinova, V., Kehrig, C., Kupko, D., López-Sánchez, Á. R., Lyubenova, M., Marino, R. A., Mármol-Queraltó, E., Márquez, I., Masegosa, J., Meidt, S., Mendez-Abreu, J., Monreal-Ibero, A., Montijo, C., Mourão, A. M., Palacios-Navarro, G., Papaderos, P., Pasquali, A., Peletier, R., Pérez, E., Pérez, I., Quirrenbach, A., Relaño, M., Rosales-Ortega, F. F., Roth, M. M., Ruiz-Lara, T., Sánchez-Blázquez, P., Sengupta, C., Singh, R., Stanishev, V., Trager, S. C., Vazdekis, A., Viironen, K., Wild, V., Zibetti, S., and Ziegler, B. (2012a). CALIFA, the Calar Alto Legacy Integral Field Area survey. I. Survey presentation. *A&A*, 538:A8.

Sánchez, S. F., Kennicutt, R. C., Gil de Paz, A., van de Ven, G., Vílchez, J. M., Wisotzki, L., Walcher, C. J., Mast, D., Aguerri, J. A. L., Albiol-Pérez, S., Alonso-Herrero, A., Alves, J., Bakos, J., Bartáková, T., Bland-Hawthorn, J., Boselli, A., Bomans, D. J., Castillo-Morales, A., Cortijo-Ferrero, C., de Lorenzo-Cáceres, A., Del Olmo, A., Dettmar, R.-J., Díaz, A., Ellis, S., Falcón-Barroso, J., Flores, H., Gallazzi, A., García-Lorenzo, B., González Delgado, R., Gruel, N., Haines, T., Hao, C., Husemann, B., Iglésias-Páramo, J., Jahnke, K., Johnson, B., Jungwiert, B., Kalinova, V., Kehrig, C., Kupko, D., López-Sánchez, Á. R., Lyubenova, M., Marino, R. A., Mármol-Queraltó, E., Márquez, I., Masegosa, J., Meidt, S., Mendez-Abreu, J., Monreal-Ibero, A., Montijo, C., Mourão, A. M., Palacios-Navarro, G., Papaderos, P., Pasquali, A., Peletier, R., Pérez, E., Pérez, I., Quirrenbach, A., Relaño, M., Rosales-Ortega, F. F., Roth, M. M., Ruiz-Lara, T., Sánchez-Blázquez, P., Sengupta, C., Singh, R., Stanishev, V., Trager, S. C., Vazdekis, A., Viironen, K., Wild, V., Zibetti, S., and Ziegler, B. (2012b). CALIFA, the Calar Alto Legacy Integral Field Area survey. I. Survey presentation. *A&A*, 538:A8.

Sandage, A. and Visvanathan, N. (1978). The color-absolute magnitude relation for E and So galaxies. II - New colors, magnitudes, and types for 405 galaxies. *ApJ*, 223:707–729.

Sanderson, R. E., Wetzel, A., Loebman, S., Sharma, S., Hopkins, P. F., Garrison-Kimmel, S., Faucher-Giguère, C.-A., Kereš, D., and Quataert, E. (2018). Synthetic Gaia surveys from the FIRE cosmological simulations of Milky-Way-mass galaxies. *ArXiv e-prints*.

Santos-Santos, I. M., Di Cintio, A., Brook, C. B., Macciò, A., Dutton, A., and Domínguez-Tenreiro, R. (2017). NIHAO XIV: Reproducing the observed diversity of dwarf galaxy rotation curve shapes in LCDM. *ArXiv e-prints*.

Sawala, T., Frenk, C. S., Fattahi, A., Navarro, J. F., Bower, R. G., Crain, R. A., Dalla Vecchia, C., Furlong, M., Helly, J. C., Jenkins, A., Oman, K. A., Schaller, M., Schaye,

J., Theuns, T., Trayford, J., and White, S. D. M. (2016). The APOSTLE simulations: solutions to the Local Group's cosmic puzzles. *MNRAS*, 457:1931–1943.

Sawala, T., Frenk, C. S., Fattahi, A., Navarro, J. F., Bower, R. G., Crain, R. A., Dalla Vecchia, C., Furlong, M., Jenkins, A., McCarthy, I. G., Qu, Y., Schaller, M., Schaye, J., and Theuns, T. (2015). Bent by baryons: the low-mass galaxy-halo relation. *MNRAS*, 448:2941–2947.

Sawala, T., Frenk, C. S., Fattahi, A., Navarro, J. F., Theuns, T., Bower, R. G., Crain, R. A., Furlong, M., Jenkins, A., Schaller, M., and Schaye, J. (2014). The chosen few: the low mass halos that host faint galaxies. *ArXiv e-prints*.

Scannapieco, C., Gadotti, D. A., Jonsson, P., and White, S. D. M. (2010). An observer's view of simulated galaxies: disc-to-total ratios, bars and (pseudo-)bulges. *MNRAS*, 407:L41–L45.

Scannapieco, C., White, S. D. M., Springel, V., and Tissera, P. B. (2011). Formation history, structure and dynamics of discs and spheroids in simulated Milky Way mass galaxies. *MNRAS*, 417:154–171.

Schechter, P. (1976). An analytic expression for the luminosity function for galaxies. *ApJ*, 203:297–306.

Schlaufman, K. C., Rockosi, C. M., Allende Prieto, C., Beers, T. C., Bizyaev, D., Brewington, H., Lee, Y. S., Malanushenko, V., Malanushenko, E., Oravetz, D., Pan, K., Simmons, A., Snedden, S., and Yanny, B. (2009). Insight into the Formation of the Milky Way Through Cold Halo Substructure. I. The ECHOS of Milky Way Formation. *ApJ*, 703:2177–2204.

Schmidt, B. P., Suntzeff, N. B., Phillips, M. M., Schommer, R. A., Clocchiatti, A., Kirshner, R. P., Garnavich, P., Challis, P., Leibundgut, B., Spyromilio, J., Riess, A. G., Filippenko, A. V., Hamuy, M., Smith, R. C., Hogan, C., Stubbs, C., Diercks, A., Reiss, D., Gilliland, R., Tonry, J., Maza, J., Dressler, A., Walsh, J., and Ciardullo, R. (1998). The High-Z Supernova Search: Measuring Cosmic Deceleration and Global Curvature of the Universe Using Type IA Supernovae. *ApJ*, 507:46–63.

Schmidt, M. (1959). The Rate of Star Formation. *ApJ*, 129:243.

Schölkopf, B., Smola, A., and Müller, K.-R. (1998). Nonlinear component analysis as a kernel eigenvalue problem. *Neural Computation*, 10(5):1299–1319.

Searle, L. and Zinn, R. (1978). Compositions of halo clusters and the formation of the galactic halo. *ApJ*, 225:357–379.

Sellwood, J. A. (2014). Secular evolution in disk galaxies. *Reviews of Modern Physics*, 86:1–46.

Sersic, J. L. (1968). *Atlas de Galaxias Australes*.

Shen, J., Rich, R. M., Kormendy, J., Howard, C. D., De Propris, R., and Kunder, A. (2010a). Our Milky Way as a Pure-disk Galaxy - A Challenge for Galaxy Formation. *ApJ*, 720:L72–L76.

Shen, S., Wadsley, J., and Stinson, G. (2010b). The enrichment of the intergalactic medium with adiabatic feedback - I. Metal cooling and metal diffusion. *MNRAS*, 407:1581–1596.

Shibuya, T., Ouchi, M., Kubo, M., and Harikane, Y. (2016). Morphologies of ˜190,000 Galaxies at z = 0-10 Revealed with HST Legacy Data. II. Evolution of Clumpy Galaxies. *ApJ*, 821:72.

Sievers, J. L., Bond, J. R., Cartwright, J. K., Contaldi, C. R., Mason, B. S., Myers, S. T., Padin, S., Pearson, T. J., Pen, U.-L., Pogosyan, D., Prunet, S., Readhead, A. C. S., Shepherd, M. C., Udomprasert, P. S., Bronfman, L., Holzapfel, W. L., and May, J. (2003). Cosmological Parameters from Cosmic Background Imager Observations and Comparisons with BOOMERANG, DASI, and MAXIMA. *ApJ*, 591:599–622.

Silk, J. (1968). Cosmic Black-Body Radiation and Galaxy Formation. *ApJ*, 151:459.

Silk, J. (1977). On the fragmentation of cosmic gas clouds. I - The formation of galaxies and the first generation of stars. *ApJ*, 211:638–648.

Silk, J. and Rees, M. J. (1998). Quasars and galaxy formation. *A&A*, 331:L1–L4.

Silva, L., Granato, G. L., Bressan, A., and Danese, L. (1998). Modeling the Effects of Dust on Galactic Spectral Energy Distributions from the Ultraviolet to the Millimeter Band. *ApJ*, 509:103–117.

Simon, J. D., Geha, M., Minor, Q. E., Martinez, G. D., Kirby, E. N., Bullock, J. S., Kaplinghat, M., Strigari, L. E., Willman, B., Choi, P. I., Tollerud, E. J., and Wolf, J. (2011). A Complete Spectroscopic Survey of the Milky Way Satellite Segue 1: The Darkest Galaxy. *ApJ*, 733:46.

Simpson, C. M., Grand, R. J. J., Gómez, F. A., Marinacci, F., Pakmor, R., Springel, V., Campbell, D. J. R., and Frenk, C. S. (2017). Quenching and ram pressure stripping of simulated Milky Way satellite galaxies. *ArXiv e-prints*.

Skrutskie, M. F., Cutri, R. M., Stiening, R., Weinberg, M. D., Schneider, S., Carpenter, J. M., Beichman, C., Capps, R., Chester, T., Elias, J., Huchra, J., Liebert, J., Lonsdale, C., Monet, D. G., Price, S., Seitzer, P., Jarrett, T., Kirkpatrick, J. D., Gizis, J. E., Howard, E., Evans, T., Fowler, J., Fullmer, L., Hurt, R., Light, R., Kopan, E. L., Marsh, K. A., McCallon, H. L., Tam, R., Van Dyk, S., and Wheelock, S. (2006). The Two Micron All Sky Survey (2MASS). *AJ*, 131:1163–1183.

Smith, R., Duc, P. A., Bournaud, F., and Yi, S. K. (2016). A Formation Scenario for the Disk of Satellites: Accretion of Satellites during Mergers. *ApJ*, 818:11.

Smoot, G., Bennett, C., Weber, R., Maruschak, J., Ratliff, R., Janssen, M., Chitwood, J., Hilliard, L., Lecha, M., Mills, R., Patschke, R., Richards, C., Backus, C., Mather, J., Hauser, M., Weiss, R., Wilkinson, D., Gulkis, S., Boggess, N., Cheng, E., Kelsall, T., Lubin, P., Meyer, S., Moseley, H., Murdock, T., Shafer, R., Silverberg, R., and Wright, E. (1990). COBE Differential Microwave Radiometers - Instrument design and implementation. *ApJ*, 360:685–695.

Smoot, G. F., Bennett, C. L., Kogut, A., Wright, E. L., Aymon, J., Boggess, N. W., Cheng, E. S., de Amici, G., Gulkis, S., Hauser, M. G., Hinshaw, G., Jackson, P. D., Janssen, M., Kaita, E., Kelsall, T., Keegstra, P., Lineweaver, C., Loewenstein, K., Lubin, P., Mather, J., Meyer, S. S., Moseley, S. H., Murdock, T., Rokke, L., Silverberg, R. F., Tenorio, L., Weiss, R., and Wilkinson, D. T. (1992). Structure in the COBE Differential Microwave Radiometer First-Year Maps. *ApJ*, 396:L1.

Snaith, O., Haywood, M., Di Matteo, P., Lehnert, M. D., Combes, F., Katz, D., and Gómez, A. (2015). Reconstructing the star formation history of the Milky Way disc(s) from chemical abundances. *A&A*, 578:A87.

Sohn, S. T., Anderson, J., and van der Marel, R. P. (2012). The M31 Velocity Vector. I. Hubble Space Telescope Proper-motion Measurements. *ApJ*, 753:7.

Somerville, R. S. and Davé, R. (2015). Physical Models of Galaxy Formation in a Cosmological Framework. *ARA&A*, 53:51–113.

Somerville, R. S., Primack, J. R., and Faber, S. M. (2001). The nature of high-redshift galaxies. *MNRAS*, 320:504–528.

Spergel, D. N., Bean, R., Doré, O., Nolta, M. R., Bennett, C. L., Dunkley, J., Hinshaw, G., Jarosik, N., Komatsu, E., Page, L., Peiris, H. V., Verde, L., Halpern, M., Hill, R. S., Kogut, A., Limon, M., Meyer, S. S., Odegard, N., Tucker, G. S., Weiland, J. L., Wollack, E., and Wright, E. L. (2007). Three-Year Wilkinson Microwave Anisotropy Probe (WMAP) Observations: Implications for Cosmology. *ApJS*, 170:377–408.

Spergel, D. N., Verde, L., Peiris, H. V., Komatsu, E., Nolta, M. R., Bennett, C. L., Halpern, M., Hinshaw, G., Jarosik, N., Kogut, A., Limon, M., Meyer, S. S., Page, L., Tucker, G. S., Weiland, J. L., Wollack, E., and Wright, E. L. (2003). First-Year Wilkinson Microwave Anisotropy Probe (WMAP) Observations: Determination of Cosmological Parameters. *ApJS*, 148:175–194.

Springel, V. (2010). E pur si muove: Galilean-invariant cosmological hydrodynamical simulations on a moving mesh. *MNRAS*, 401:791–851.

Springel, V., Frenk, C. S., and White, S. D. M. (2006). The large-scale structure of the Universe. *Nature*, 440:1137–1144.

Springel, V., Wang, J., Vogelsberger, M., Ludlow, A., Jenkins, A., Helmi, A., Navarro, J. F., Frenk, C. S., and White, S. D. M. (2008). The Aquarius Project: the subhaloes of galactic haloes. *MNRAS*, 391:1685–1711.

Springel, V., White, S. D. M., Jenkins, A., Frenk, C. S., Yoshida, N., Gao, L., Navarro, J., Thacker, R., Croton, D., Helly, J., Peacock, J. A., Cole, S., Thomas, P., Couchman, H., Evrard, A., Colberg, J., and Pearce, F. (2005). Simulations of the formation, evolution and clustering of galaxies and quasars. *Nature*, 435:629–636.

Stadel, J. (2013). PkdGRAV2: Parallel fast-multipole cosmological code. Astrophysics Source Code Library.

Stadel, J., Potter, D., Moore, B., Diemand, J., Madau, P., Zemp, M., Kuhlen, M., and Quilis, V. (2009). Quantifying the heart of darkness with GHALO - a multibillion particle simulation of a galactic halo. *MNRAS*, 398:L21–L25.

Stadel, J. G. (2001). *Cosmological N-body simulations and their analysis*. PhD thesis, UNIVERSITY OF WASHINGTON.

Steinmetz, M. and Navarro, J. F. (1999). The Cosmological Origin of the Tully-Fisher Relation. *ApJ*, 513:555–560.

Steinmetz, M., Zwitter, T., Siebert, A., Watson, F. G., Freeman, K. C., Munari, U., Campbell, R., Williams, M., Seabroke, G. M., Wyse, R. F. G., Parker, Q. A., Bienaymé, O., Roeser, S., Gibson, B. K., Gilmore, G., Grebel, E. K., Helmi, A., Navarro, J. F., Burton, D., Cass, C. J. P., Dawe, J. A., Fiegert, K., Hartley, M., Russell, K. S., Saunders, W., Enke, H., Bailin, J., Binney, J., Bland-Hawthorn, J., Boeche, C., Dehnen, W., Eisenstein, D. J., Evans, N. W., Fiorucci, M., Fulbright, J. P., Gerhard, O., Jauregi, U., Kelz, A., Mijović, L., Minchev, I., Parmentier, G., Peñarrubia, J., Quillen, A. C., Read, M. A., Ruchti, G., Scholz, R.-D., Siviero, A., Smith, M. C., Sordo, R., Veltz, L., Vidrih, S., von Berlepsch, R., Boyle, B. J., and Schilbach, E. (2006). The Radial Velocity Experiment (RAVE): First Data Release. *AJ*, 132:1645–1668.

Stewart, K. R., Bullock, J. S., Wechsler, R. H., and Maller, A. H. (2009). Gas-rich Mergers in LCDM: Disk Survivability and the Baryonic Assembly of Galaxies. *ApJ*, 702:307–317.

Stinson, G., Seth, A., Katz, N., Wadsley, J., Governato, F., and Quinn, T. (2006). Star formation and feedback in smoothed particle hydrodynamic simulations - I. Isolated galaxies. *MNRAS*, 373:1074–1090.

Stinson, G. S., Bailin, J., Couchman, H., Wadsley, J., Shen, S., Nickerson, S., Brook, C., and Quinn, T. (2010). Cosmological galaxy formation simulations using smoothed particle hydrodynamics. *MNRAS*, 408:812–826.

Stinson, G. S., Bovy, J., Rix, H.-W., Brook, C., Roškar, R., Dalcanton, J. J., Macciò, A. V., Wadsley, J., Couchman, H. M. P., and Quinn, T. R. (2013a). MaGICC thick disc - I. Comparing a simulated disc formed with stellar feedback to the Milky Way. *MNRAS*, 436:625–634.

Stinson, G. S., Brook, C., Macciò, A. V., Wadsley, J., Quinn, T. R., and Couchman, H. M. P. (2013b). Making Galaxies In a Cosmological Context: the need for early stellar feedback. *MNRAS*, 428:129–140.

Stinson, G. S., Dutton, A. A., Wang, L., Macciò, A. V., Herpich, J., Bradford, J. D., Quinn, T. R., Wadsley, J., and Keller, B. (2015). NIHAO III: the constant disc gas mass conspiracy. *MNRAS*, 454:1105–1116.

Stromberg, G. (1925). Analysis of radial velocities of globular clusters and non-galactic nebulae. *ApJ*, 61.

Swinbank, A. M., Smail, I., Longmore, S., Harris, A. I., Baker, A. J., De Breuck, C., Richard, J., Edge, A. C., Ivison, R. J., Blundell, R., Coppin, K. E. K., Cox, P., Gurwell, M., Hainline, L. J., Krips, M., Lundgren, A., Neri, R., Siana, B., Siringo, G., Stark, D. P., Wilner, D., and Younger, J. D. (2010). Intense star formation within resolved compact regions in a galaxy at z = 2.3. *Nature*, 464:733–736.

Tacchella, S., Dekel, A., Carollo, C. M., Ceverino, D., DeGraf, C., Lapiner, S., Mandelker, N., and Primack Joel, R. (2016). The confinement of star-forming galaxies into a main sequence through episodes of gas compaction, depletion and replenishment. *MNRAS*, 457:2790–2813.

Tacconi, L. J., Genzel, R., Neri, R., Cox, P., Cooper, M. C., Shapiro, K., Bolatto, A., Bouché, N., Bournaud, F., Burkert, A., Combes, F., Comerford, J., Davis, M., Schreiber, N. M. F., Garcia-Burillo, S., Gracia-Carpio, J., Lutz, D., Naab, T., Omont, A., Shapley, A., Sternberg, A., and Weiner, B. (2010). High molecular gas fractions in normal massive star-forming galaxies in the young Universe. *Nature*, 463:781–784.

Tacconi, L. J., Neri, R., Genzel, R., Combes, F., Bolatto, A., Cooper, M. C., Wuyts, S., Bournaud, F., Burkert, A., Comerford, J., Cox, P., Davis, M., Förster Schreiber, N. M., García-Burillo, S., Gracia-Carpio, J., Lutz, D., Naab, T., Newman, S., Omont, A., Saintonge, A., Shapiro Griffin, K., Shapley, A., Sternberg, A., and Weiner, B. (2013). Phibss: Molecular Gas Content and Scaling Relations in z ˜ 1-3 Massive, Main-sequence Star-forming Galaxies. *ApJ*, 768:74.

Tadaki, K.-i., Kodama, T., Tanaka, I., Hayashi, M., Koyama, Y., and Shimakawa, R. (2014). The Nature of Hα-selected Galaxies at z > 2. II. Clumpy Galaxies and Compact Star-forming Galaxies. *ApJ*, 780:77.

Tamburello, V., Mayer, L., Shen, S., and Wadsley, J. (2015). A lower fragmentation mass scale in high-redshift galaxies and its implications on giant clumps: a systematic numerical study. *MNRAS*, 453:2490–2514.

Tamburello, V., Rahmati, A., Mayer, L., Cava, A., Dessauges-Zavadsky, M., and Schaerer, D. (2016). Clumpy galaxies seen in H-alpha: inflated observed clump properties due to limited spatial resolution and sensitivity. *ArXiv e-prints*.

Tegmark, M., Blanton, M. R., Strauss, M. A., Hoyle, F., Schlegel, D., Scoccimarro, R., Vogeley, M. S., Weinberg, D. H., Zehavi, I., Berlind, A., Budavari, T., Connolly, A., Eisenstein, D. J., Finkbeiner, D., Frieman, J. A., Gunn, J. E., Hamilton, A. J. S., Hui, L., Jain, B., Johnston, D., Kent, S., Lin, H., Nakajima, R., Nichol, R. C., Ostriker, J. P., Pope, A., Scranton, R., Seljak, U., Sheth, R. K., Stebbins, A., Szalay, A. S., Szapudi, I., Verde, L., Xu, Y., Annis, J., Bahcall, N. A., Brinkmann, J., Burles, S., Castander, F. J., Csabai, I., Loveday, J., Doi, M., Fukugita, M., Gott, III, J. R., Hennessy, G., Hogg, D. W., Ivezić, Ž., Knapp, G. R., Lamb, D. Q., Lee, B. C., Lupton, R. H., McKay, T. A., Kunszt, P., Munn, J. A., O'Connell, L., Peoples, J., Pier, J. R., Richmond, M., Rockosi, C., Schneider, D. P., Stoughton, C., Tucker, D. L., Vanden Berk, D. E., Yanny, B., York,

D. G., and SDSS Collaboration (2004). The Three-Dimensional Power Spectrum of Galaxies from the Sloan Digital Sky Survey. *ApJ*, 606:702–740.

Teyssier, M., Johnston, K. V., and Kuhlen, M. (2012). Identifying Local Group field galaxies that have interacted with the Milky Way. *MNRAS*, 426:1808–1818.

Thomas, D., Maraston, C., Bender, R., and Mendes de Oliveira, C. (2005). The Epochs of Early-Type Galaxy Formation as a Function of Environment. *ApJ*, 621:673–694.

Tinker, J., Kravtsov, A. V., Klypin, A., Abazajian, K., Warren, M., Yepes, G., Gottlöber, S., and Holz, D. E. (2008). Toward a Halo Mass Function for Precision Cosmology: The Limits of Universality. *ApJ*, 688:709–728.

Tissera, P. B., White, S. D. M., and Scannapieco, C. (2012). Chemical signatures of formation processes in the stellar populations of simulated galaxies. *MNRAS*, 420:255–270.

Tollerud, E. J., Beaton, R. L., Geha, M. C., Bullock, J. S., Guhathakurta, P., Kalirai, J. S., Majewski, S. R., Kirby, E. N., Gilbert, K. M., Yniguez, B., Patterson, R. J., Ostheimer, J. C., Cooke, J., Dorman, C. E., Choudhury, A., and Cooper, M. C. (2012). The SPLASH Survey: Spectroscopy of 15 M31 Dwarf Spheroidal Satellite Galaxies. *ApJ*, 752:45.

Tollerud, E. J., Boylan-Kolchin, M., and Bullock, J. S. (2014). M31 satellite masses compared to ΛCDM subhaloes. *MNRAS*, 440:3511–3519.

Tollerud, E. J., Bullock, J. S., Strigari, L. E., and Willman, B. (2008). Hundreds of Milky Way Satellites? Luminosity Bias in the Satellite Luminosity Function. *ApJ*, 688:277–289.

Tollerud, E. J., Geha, M. C., Vargas, L. C., and Bullock, J. S. (2013). The Outer Limits of the M31 System: Kinematics of the Dwarf Galaxy Satellites And XXVIII & And XXIX. *ApJ*, 768:50.

Tollet, E., Macciò, A. V., Dutton, A. A., Stinson, G. S., Wang, L., Penzo, C., Gutcke, T. A., Buck, T., Kang, X., Brook, C., Di Cintio, A., Keller, B. W., and Wadsley, J. (2016). NIHAO - IV: core creation and destruction in dark matter density profiles across cosmic time. *MNRAS*, 456:3542–3552.

Tomozeiu, M., Mayer, L., and Quinn, T. (2016). The Evolution of Dwarf Galaxy Satellites with Different Dark Matter Density Profiles in the ErisMod Simulations. I. The Early Infalls. *ApJ*, 818:193.

Tonry, J. L., Dressler, A., Blakeslee, J. P., Ajhar, E. A., Fletcher, A. B., Luppino, G. A., Metzger, M. R., and Moore, C. B. (2001). The SBF Survey of Galaxy Distances. IV. SBF Magnitudes, Colors, and Distances. *ApJ*, 546:681–693.

Toomre, A. (1964). On the gravitational stability of a disk of stars. *ApJ*, 139:1217–1238.

Toomre, A. (1977). Mergers and Some Consequences. In Tinsley, B. M. and Larson, D. Campbell, R. B. G., editors, *Evolution of Galaxies and Stellar Populations*, page 401.

Torrealba, G., Koposov, S. E., Belokurov, V., and Irwin, M. (2016). The feeble giant. Discovery of a large and diffuse Milky Way dwarf galaxy in the constellation of

Crater. *MNRAS*, 459:2370–2378.

Trager, S. C., Faber, S. M., Worthey, G., and González, J. J. (2000). The Stellar Population Histories of Early-Type Galaxies. II. Controlling Parameters of the Stellar Populations. *AJ*, 120:165–188.

Tremonti, C. A., Heckman, T. M., Kauffmann, G., Brinchmann, J., Charlot, S., White, S. D. M., Seibert, M., Peng, E. W., Schlegel, D. J., Uomoto, A., Fukugita, M., and Brinkmann, J. (2004). The Origin of the Mass-Metallicity Relation: Insights from 53,000 Star-forming Galaxies in the Sloan Digital Sky Survey. *ApJ*, 613:898–913.

Trick, W. H., van de Ven, G., and Dutton, A. A. (2016). A spiral galaxy's mass distribution uncovered through lensing and dynamics. *MNRAS*, 463:3151–3168.

Trujillo-Gomez, S., Klypin, A., Primack, J., and Romanowsky, A. J. (2011). Galaxies in ΛCDM with Halo Abundance Matching: Luminosity-Velocity Relation, Baryonic Mass-Velocity Relation, Velocity Function, and Clustering. *ApJ*, 742:16.

Trujillo-Gomez, S., Schneider, A., Papastergis, E., Reed, D. S., and Lake, G. (2018). Another baryon miracle? Testing solutions to the 'missing dwarfs' problem. *MNRAS*, 475:4825–4840.

Tully, R. B. (1987). Nearby groups of galaxies. II - an all-sky survey within 3000 kilometers per second. *ApJ*, 321:280–304.

Tully, R. B., Courtois, H. M., Dolphin, A. E., Fisher, J. R., Héraudeau, P., Jacobs, B. A., Karachentsev, I. D., Makarov, D., Makarova, L., Mitronova, S., Rizzi, L., Shaya, E. J., Sorce, J. G., and Wu, P.-F. (2013). Cosmicflows-2: The Data. *AJ*, 146:86.

Tully, R. B., Libeskind, N. I., Karachentsev, I. D., Karachentseva, V. E., Rizzi, L., and Shaya, E. J. (2015). Two Planes of Satellites in the Centaurus A Group. *ApJ*, 802:L25.

Tyson, J. A., Valdes, F., and Wenk, R. A. (1990). Detection of systematic gravitational lens galaxy image alignments - Mapping dark matter in galaxy clusters. *ApJ*, 349:L1–L4.

Übler, H., Naab, T., Oser, L., Aumer, M., Sales, L. V., and White, S. D. M. (2014). Why stellar feedback promotes disc formation in simulated galaxies. *MNRAS*, 443:2092–2111.

Ural, U., Wilkinson, M. I., Read, J. I., and Walker, M. G. (2015). A low pre-infall mass for the Carina dwarf galaxy from disequilibrium modelling. *Nature Communications*, 6:7599.

Uttenthaler, S., Schultheis, M., Nataf, D. M., Robin, A. C., Lebzelter, T., and Chen, B. (2012). Constraining the structure and formation of the Galactic bulge from a field in its outskirts. FLAMES-GIRAFFE spectra of about 400 red giants around (l, b) = (0deg, -10deg). *A&A*, 546:A57.

Vale, A. and Ostriker, J. P. (2006). The non-parametric model for linking galaxy luminosity with halo/subhalo mass. *MNRAS*, 371:1173–1187.

van den Bosch, F. C., Burkert, A., and Swaters, R. A. (2001). The angular momentum content of dwarf galaxies: new challenges for the theory of galaxy formation. *MNRAS*, 326:1205–1215.

van den Bosch, F. C. and Ogiya, G. (2018). Dark matter substructure in numerical simulations: a tale of discreteness noise, runaway instabilities, and artificial disruption. *MNRAS*, 475:4066–4087.

van den Bosch, F. C., Ogiya, G., Hahn, O., and Burkert, A. (2018). Disruption of dark matter substructure: fact or fiction? *MNRAS*, 474:3043–3066.

van der Wel, A., Franx, M., van Dokkum, P. G., Skelton, R. E., Momcheva, I. G., Whitaker, K. E., Brammer, G. B., Bell, E. F., Rix, H.-W., Wuyts, S., Ferguson, H. C., Holden, B. P., Barro, G., Koekemoer, A. M., Chang, Y.-Y., McGrath, E. J., Häussler, B., Dekel, A., Behroozi, P., Fumagalli, M., Leja, J., Lundgren, B. F., Maseda, M. V., Nelson, E. J., Wake, D. A., Patel, S. G., Labbé, I., Faber, S. M., Grogin, N. A., and Kocevski, D. D. (2014). 3D-HST+CANDELS: The Evolution of the Galaxy Size-Mass Distribution since z = 3. *ApJ*, 788:28.

van Dokkum, P. G., Whitaker, K. E., Brammer, G., Franx, M., Kriek, M., Labbé, I., Marchesini, D., Quadri, R., Bezanson, R., Illingworth, G. D., Muzzin, A., Rudnick, G., Tal, T., and Wake, D. (2010). The Growth of Massive Galaxies Since z = 2. *ApJ*, 709:1018–1041.

Vásquez, S., Zoccali, M., Hill, V., Renzini, A., González, O. A., Gardner, E., Debattista, V. P., Robin, A. C., Rejkuba, M., Baffico, M., Monelli, M., Motta, V., and Minniti, D. (2013). 3D kinematics through the X-shaped Milky Way bulge. *A&A*, 555:A91.

Vera-Ciro, C. A., Helmi, A., Starkenburg, E., and Breddels, M. A. (2013). Not too big, not too small: the dark haloes of the dwarf spheroidals in the Milky Way. *MNRAS*, 428:1696–1703.

Verheijen, M. A. W. (2001). The Ursa Major Cluster of Galaxies. V. H I Rotation Curve Shapes and the Tully-Fisher Relations. *ApJ*, 563:694–715.

Vogelsberger, M., Genel, S., Springel, V., Torrey, P., Sijacki, D., Xu, D., Snyder, G., Nelson, D., and Hernquist, L. (2014). Introducing the Illustris Project: simulating the coevolution of dark and visible matter in the Universe. *MNRAS*, 444:1518–1547.

Vogelsberger, M., Zavala, J., and Loeb, A. (2012). Subhaloes in self-interacting galactic dark matter haloes. *MNRAS*, 423:3740–3752.

Volonteri, M. (2010). Formation of supermassive black holes. *A&A Rev.*, 18:279–315.

Wadsley, J. W., Keller, B. W., and Quinn, T. R. (2017). Gasoline2: a modern smoothed particle hydrodynamics code. *MNRAS*, 471:2357–2369.

Wadsley, J. W., Stadel, J., and Quinn, T. (2004). Gasoline: a flexible, parallel implementation of TreeSPH. *New A*, 9:137–158.

Wadsley, J. W., Veeravalli, G., and Couchman, H. M. P. (2008). On the treatment of entropy mixing in numerical cosmology. *MNRAS*, 387:427–438.

Wagoner, R. V., Fowler, W. A., and Hoyle, F. (1967). On the Synthesis of Elements at Very High Temperatures. *ApJ*, 148:3.

Walker, M. G., Mateo, M., Olszewski, E. W., Koposov, S., Belokurov, V., Jethwa, P., Nidever, D. L., Bonnivard, V., Bailey, III, J. I., Bell, E. F., and Loebman, S. R. (2016). Magellan/M2FS Spectroscopy of Tucana 2 and Grus 1. *ApJ*, 819:53.

Walker, M. G., McGaugh, S. S., Mateo, M., Olszewski, E. W., and Kuzio de Naray, R. (2010). Comparing the Dark Matter Halos of Spiral, Low Surface Brightness, and Dwarf Spheroidal Galaxies. *ApJ*, 717:L87–L91.

Walker, T. P., Steigman, G., Schramm, D. N., Olive, K. A., and Kang, H.-S. (1991). Primordial nucleosynthesis redux. *ApJ*, 376:51–69.

Walt, S. v. d., Colbert, S. C., and Varoquaux, G. (2011). The numpy array: A structure for efficient numerical computation. *Computing in Science and Engg.*, 13(2):22–30.

Wang, J., Frenk, C. S., and Cooper, A. P. (2013). The spatial distribution of galactic satellites in the Λ cold dark matter cosmology. *MNRAS*, 429:1502–1513.

Wang, J., Frenk, C. S., Navarro, J. F., Gao, L., and Sawala, T. (2012). The missing massive satellites of the Milky Way. *MNRAS*, 424:2715–2721.

Wang, L., Dutton, A. A., Stinson, G. S., Macciò, A. V., Penzo, C., Kang, X., Keller, B. W., and Wadsley, J. (2015). NIHAO project - I. Reproducing the inefficiency of galaxy formation across cosmic time with a large sample of cosmological hydrodynamical simulations. *MNRAS*, 454:83–94.

Warnick, K., Knebe, A., and Power, C. (2008). The tidal streams of disrupting subhaloes in cosmological dark matter haloes. *MNRAS*, 385:1859–1883.

Wechsler, R. H., Bullock, J. S., Primack, J. R., Kravtsov, A. V., and Dekel, A. (2002). Concentrations of Dark Halos from Their Assembly Histories. *ApJ*, 568:52–70.

Wegg, C. and Gerhard, O. (2013). Mapping the three-dimensional density of the Galactic bulge with VVV red clump stars. *MNRAS*, 435:1874–1887.

Wegg, C., Gerhard, O., and Portail, M. (2015). The structure of the Milky Way's bar outside the bulge. *MNRAS*, 450:4050–4069.

Weiland, J. L., Arendt, R. G., Berriman, G. B., Dwek, E., Freudenreich, H. T., Hauser, M. G., Kelsall, T., Lisse, C. M., Mitra, M., Moseley, S. H., Odegard, N. P., Silverberg, R. F., Sodroski, T. J., Spiesman, W. J., and Stemwedel, S. W. (1994). COBE diffuse infrared background experiment observations of the galactic bulge. *ApJ*, 425:L81–L84.

Weinberg, S. (1989). The cosmological constant problem. *Reviews of Modern Physics*, 61:1–23.

Weisz, D. R., Dalcanton, J. J., Williams, B. F., Gilbert, K. M., Skillman, E. D., Seth, A. C., Dolphin, A. E., McQuinn, K. B. W., Gogarten, S. M., Holtzman, J., Rosema, K., Cole, A., Karachentsev, I. D., and Zaritsky, D. (2011). The ACS Nearby Galaxy Survey Treasury. VIII. The Global Star Formation Histories of 60 Dwarf Galaxies in the Local Volume. *ApJ*, 739:5.

Weisz, D. R., Dolphin, A. E., Skillman, E. D., Holtzman, J., Gilbert, K. M., Dalcanton, J. J., and Williams, B. F. (2015). The Star Formation Histories of Local Group Dwarf

Galaxies. III. Characterizing Quenching in Low-mass Galaxies. *ApJ*, 804:136.

Wetzel, A. R., Deason, A. J., and Garrison-Kimmel, S. (2015). Satellite Dwarf Galaxies in a Hierarchical Universe: Infall Histories, Group Preprocessing, and Reionization. *ApJ*, 807:49.

Wetzel, A. R., Hopkins, P. F., Kim, J.-h., Faucher-Giguère, C.-A., Kereš, D., and Quataert, E. (2016). Reconciling Dwarf Galaxies with ΛCDM Cosmology: Simulating a Realistic Population of Satellites around a Milky Way-mass Galaxy. *ApJ*, 827:L23.

Wetzel, A. R., Tinker, J. L., Conroy, C., and van den Bosch, F. C. (2013). Galaxy evolution in groups and clusters: satellite star formation histories and quenching time-scales in a hierarchical Universe. *MNRAS*, 432:336–358.

Wetzel, A. R., Tinker, J. L., Conroy, C., and van den Bosch, F. C. (2014). Galaxy evolution near groups and clusters: ejected satellites and the spatial extent of environmental quenching. *MNRAS*, 439:2687–2700.

White, S. D. M. and Frenk, C. S. (1991). Galaxy formation through hierarchical clustering. *ApJ*, 379:52–79.

White, S. D. M. and Rees, M. J. (1978). Core condensation in heavy halos - A two-stage theory for galaxy formation and clustering. *MNRAS*, 183:341–358.

Willman, B. and Strader, J. (2012). "Galaxy," Defined. *AJ*, 144:76.

Wright, T. (1750). *An original theory or new hypothesis of the universe : founded upon general phaenomena of the visible creation; and particularly the Via the laws of nature, and solving by mathematical principles : the Lactea ...compris'd in nine familiar letters from the author to his friendand : illustrated with upward of thirty graven and mezzotinto plates ...*

Wuyts, S., Förster Schreiber, N. M., Genzel, R., Guo, Y., Barro, G., Bell, E. F., Dekel, A., Faber, S. M., Ferguson, H. C., Giavalisco, M., Grogin, N. A., Hathi, N. P., Huang, K.-H., Kocevski, D. D., Koekemoer, A. M., Koo, D. C., Lotz, J., Lutz, D., McGrath, E., Newman, J. A., Rosario, D., Saintonge, A., Tacconi, L. J., Weiner, B. J., and van der Wel, A. (2012). Smooth(er) Stellar Mass Maps in CANDELS: Constraints on the Longevity of Clumps in High-redshift Star-forming Galaxies. *ApJ*, 753:114.

Wuyts, S., Förster Schreiber, N. M., van der Wel, A., Magnelli, B., Guo, Y., Genzel, R., Lutz, D., Aussel, H., Barro, G., Berta, S., Cava, A., Graciá-Carpio, J., Hathi, N. P., Huang, K.-H., Kocevski, D. D., Koekemoer, A. M., Lee, K.-S., Le Floc'h, E., McGrath, E. J., Nordon, R., Popesso, P., Pozzi, F., Riguccini, L., Rodighiero, G., Saintonge, A., and Tacconi, L. (2011). Galaxy Structure and Mode of Star Formation in the SFR-Mass Plane from z ˜ 2.5 to z ˜ 0.1. *ApJ*, 742:96.

Yanny, B., Newberg, H. J., Kent, S., Laurent-Muehleisen, S. A., Pier, J. R., Richards, G. T., Stoughton, C., Anderson, Jr., J. E., Annis, J., Brinkmann, J., Chen, B., Csabai, I., Doi, M., Fukugita, M., Hennessy, G. S., Ivezić, Ž., Knapp, G. R., Lupton, R., Munn, J. A., Nash, T., Rockosi, C. M., Schneider, D. P., Smith, J. A., and York, D. G. (2000).

Identification of A-colored Stars and Structure in the Halo of the Milky Way from Sloan Digital Sky Survey Commissioning Data. *ApJ*, 540:825–841.

Yao, Y. and Wang, Q. D. (2007). The Galactic Central Diffuse X-Ray Enhancement: A Differential Absorption/Emission Analysis. *ApJ*, 666:242–246.

Yoachim, P. and Dalcanton, J. J. (2006). Structural Parameters of Thin and Thick Disks in Edge-on Disk Galaxies. *AJ*, 131:226–249.

York, D. G., Adelman, J., Anderson, Jr., J. E., Anderson, S. F., Annis, J., Bahcall, N. A., Bakken, J. A., Barkhouser, R., Bastian, S., Berman, E., Boroski, W. N., Bracker, S., Briegel, C., Briggs, J. W., Brinkmann, J., Brunner, R., Burles, S., Carey, L., Carr, M. A., Castander, F. J., Chen, B., Colestock, P. L., Connolly, A. J., Crocker, J. H., Csabai, I., Czarapata, P. C., Davis, J. E., Doi, M., Dombeck, T., Eisenstein, D., Ellman, N., Elms, B. R., Evans, M. L., Fan, X., Federwitz, G. R., Fiscelli, L., Friedman, S., Frieman, J. A., Fukugita, M., Gillespie, B., Gunn, J. E., Gurbani, V. K., de Haas, E., Haldeman, M., Harris, F. H., Hayes, J., Heckman, T. M., Hennessy, G. S., Hindsley, R. B., Holm, S., Holmgren, D. J., Huang, C.-h., Hull, C., Husby, D., Ichikawa, S.-I., Ichikawa, T., Ivezić, Ž., Kent, S., Kim, R. S. J., Kinney, E., Klaene, M., Kleinman, A. N., Kleinman, S., Knapp, G. R., Korienek, J., Kron, R. G., Kunszt, P. Z., Lamb, D. Q., Lee, B., Leger, R. F., Limmongkol, S., Lindenmeyer, C., Long, D. C., Loomis, C., Loveday, J., Lucinio, R., Lupton, R. H., MacKinnon, B., Mannery, E. J., Mantsch, P. M., Margon, B., McGehee, P., McKay, T. A., Meiksin, A., Merelli, A., Monet, D. G., Munn, J. A., Narayanan, V. K., Nash, T., Neilsen, E., Neswold, R., Newberg, H. J., Nichol, R. C., Nicinski, T., Nonino, M., Okada, N., Okamura, S., Ostriker, J. P., Owen, R., Pauls, A. G., Peoples, J., Peterson, R. L., Petravick, D., Pier, J. R., Pope, A., Pordes, R., Prosapio, A., Rechenmacher, R., Quinn, T. R., Richards, G. T., Richmond, M. W., Rivetta, C. H., Rockosi, C. M., Ruthmansdorfer, K., Sandford, D., Schlegel, D. J., Schneider, D. P., Sekiguchi, M., Sergey, G., Shimasaku, K., Siegmund, W. A., Smee, S., Smith, J. A., Snedden, S., Stone, R., Stoughton, C., Strauss, M. A., Stubbs, C., SubbaRao, M., Szalay, A. S., Szapudi, I., Szokoly, G. P., Thakar, A. R., Tremonti, C., Tucker, D. L., Uomoto, A., Vanden Berk, D., Vogeley, M. S., Waddell, P., Wang, S.-i., Watanabe, M., Weinberg, D. H., Yanny, B., Yasuda, N., and SDSS Collaboration (2000). The Sloan Digital Sky Survey: Technical Summary. *AJ*, 120:1579–1587.

Zahid, H. J., Geller, M. J., Kewley, L. J., Hwang, H. S., Fabricant, D. G., and Kurtz, M. J. (2013). The Chemical Evolution of Star-forming Galaxies over the Last 11 Billion Years. *ApJ*, 771:L19.

Zana, T., Dotti, M., Capelo, P. R., Bonoli, S., Haardt, F., Mayer, L., and Spinoso, D. (2017). External versus internal triggers of bar formation in cosmological zoom-in simulations. *ArXiv e-prints*.

Zasowski, G., Cohen, R. E., Chojnowski, S. D., Santana, F., Oelkers, R. J., Andrews, B., Beaton, R. L., Bender, C., Bird, J. C., Bovy, J., Carlberg, J. K., Covey, K., Cunha, K.,

Dell'Agli, F., Fleming, S. W., Frinchaboy, P. M., García-Hernández, D. A., Harding, P., Holtzman, J., Johnson, J. A., Kollmeier, J. A., Majewski, S. R., Mészáros, S., Munn, J., Muñoz, R. R., Ness, M. K., Nidever, D. L., Poleski, R., Román-Zúñiga, C., Shetrone, M., Simon, J. D., Smith, V. V., Sobeck, J. S., Stringfellow, G. S., Szigetiáros, L., Tayar, J., and Troup, N. (2017). Target Selection for the SDSS-IV APOGEE-2 Survey. *AJ*, 154:198.

Zasowski, G., Ness, M. K., García Pérez, A. E., Martinez-Valpuesta, I., Johnson, J. A., and Majewski, S. R. (2016). Kinematics in the Galactic Bulge with APOGEE. II. High-Order Kinematic Moments and Comparison to Extragalactic Bar Diagnostics. *ApJ*, 832:132.

Zavala, J., Frenk, C. S., Bower, R., Schaye, J., Theuns, T., Crain, R. A., Trayford, J. W., Schaller, M., and Furlong, M. (2016). The link between the assembly of the inner dark matter halo and the angular momentum evolution of galaxies in the EAGLE simulation. *MNRAS*, 460:4466–4482.

Zavala, J., Jing, Y. P., Faltenbacher, A., Yepes, G., Hoffman, Y., Gottlöber, S., and Catinella, B. (2009). The Velocity Function in the Local Environment from ΛCDM and ΛWDM Constrained Simulations. *ApJ*, 700:1779–1793.

Zel'dovich, Y. B. (1970). Gravitational instability: An approximate theory for large density perturbations. *A&A*, 5:84–89.

Zentner, A. R., Kravtsov, A. V., Gnedin, O. Y., and Klypin, A. A. (2005). The Anisotropic Distribution of Galactic Satellites. *ApJ*, 629:219–232.

Zhou, Y., Shen, J., Liu, C., Li, Z.-Y., Mao, S., Kunder, A., Rich, R. M., Zasowski, G., Fernandez-Trincado, J. G., Majewski, S. R., Lin, C.-C., Geisler, D., Tang, B., Villanova, S., Roman-Lopes, A., Schultheis, M., Nidever, D. L., Meza, A., Pan, K., and Bizyaev, D. V. (2017). Chemical Abundances and Ages of the Bulge Stars in APOGEE High-velocity Peaks. *ApJ*, 847:74.

Zhu, L., van de Ven, G., van den Bosch, R., Rix, H.-W., Lyubenova, M., Falcón-Barroso, J., Martig, M., Mao, S., Xu, D., Jin, Y., Obreja, A., Grand, R. J. J., Dutton, A. A., Maccio, A. V., Gomez, F. A., Walcher, J. C., García-Benito, R., Zibetti, S., and Sánchez, S. F. (2017a). The stellar orbit distribution in present-day galaxies inferred from the CALIFA survey. *ArXiv e-prints*.

Zhu, L., van den Bosch, R., van de Ven, G., Lyubenova, M., Falcón-Barroso, J., Meidt, S. E., Martig, M., Shen, J., Li, Z.-Y., Yildirim, A., Walcher, C. J., and Sanchez, S. F. (2017b). Orbital decomposition of CALIFA spiral galaxies. *ArXiv e-prints*.

Zoccali, M., Gonzalez, O. A., Vasquez, S., Hill, V., Rejkuba, M., Valenti, E., Renzini, A., Rojas-Arriagada, A., Martinez-Valpuesta, I., Babusiaux, C., Brown, T., Minniti, D., and McWilliam, A. (2014). The GIRAFFE Inner Bulge Survey (GIBS). I. Survey description and a kinematical map of the Milky Way bulge. *A&A*, 562:A66.

Zoccali, M., Hill, V., Lecureur, A., Barbuy, B., Renzini, A., Minniti, D., Gómez, A., and Ortolani, S. (2008). The metal content of bulge field stars from FLAMES-GIRAFFE spectra. I. Stellar parameters and iron abundances. *A&A*, 486:177–189.

Zoccali, M. and Valenti, E. (2016). The 3D Structure of the Galactic Bulge. *PASA*, 33:e025.

Zolotov, A., Brooks, A. M., Willman, B., Governato, F., Pontzen, A., Christensen, C., Dekel, A., Quinn, T., Shen, S., and Wadsley, J. (2012). Baryons Matter: Why Luminous Satellite Galaxies have Reduced Central Masses. *ApJ*, 761:71.

Zwicky, F. (1933). Die Rotverschiebung von extragalaktischen Nebeln. *Helvetica Physica Acta*, 6:110–127.

Acknowledgements

Before I start the usual listing of names let me say: If you think this thesis is important enough to look at these pages you deserve a great thank you. **THANK YOU!**

Finishing this thesis marks the end of extremely pleasant 4 years at MPIA and unbelievable 8 years in Heidelberg. At the same time it is a tremendous professional and personal accomplishment for me. Reaching this point was not possible without the support of so many people: family, friends and colleagues.

Above all, I like to thank my supervisor Andrea Macciò for giving me the opportunity to work with him first on my master thesis and then on this PhD project. I further like to thank Hans-Walter Rix for making this thesis possible by accepting me into his group. Without our special arrangement of continuing at MPIA and being long-distant supervised by Andrea from Abu Dhabi I couldn't have finished this thesis. I thank both of you for all the time and the freedom you gave me in finding my own projects and following my own interests. On top, you both gave me valuable insights into the physics of galaxies and their formation. Andrea, I especially thank you for all the good time I could spend in Abu Dhabi. I had great fun with you, especially on the roller coaster and the many other external group meetings.

I further like to thank Björn Malte Schäfer and Luca Amendola for accepting the extra work of being part of my thesis panel.

Certainly, without the support of my parents, Brigitte and Manfred, I wouldn't have come this far. Your support allowed me to study whatever I wanted which in my case was Astrophysics. And although you are still unfamiliar with my professional life, you still supported my every choice. I am incredibly happy to have you!

Mama und Papa Danke, dass ihr mich bis hierher immer unterstützt habt. Ohne euch hätte ich mein Ziel nie erreicht. Ich weiß, ihr hättet mich gerne näher bei euch, aber meine Neugierde treibt mich noch ein wenig weiter durch die Welt.

Lena und Fabian Ich danke euch einfach nur dafür, dass es euch gibt! Jede Minute mit euch ist einzigartig und immer wenn ich bei euch bin, fühle ich mich wirklich zu Hause.

Oma und Opa Ich möchte ebenfalls meinen Großeltern danken, vor allem Oma Friedel und Oma Mienchen. Ihr habt erheblich dazu beigetragen, dass meine Neugierde auf Wissenschaft herangewachsen ist. Ich danke natürlich auch meinen Opas, Opa Jürgen und Opa Paul, die aber leider nicht mehr da sind, um (hoffentlich) meinen Doktortitel mit mir zu feiern. Ganz besonders Opa Jürgen hat meine Persönlichkeit durch viele Abenteuer, Basteleien und Ausflüge stark geprägt. Ohne seinen Einfluss wäre ich wahrscheinlich nie auf die Idee gekommen, Physik zu studieren.

I consider myself incredibly lucky to be able to work at the MPIA with the most encouraging working environment I experienced. I also like thank the administrative and technical staff of the institute. In particular, I want to thank Uli Hiller for his amazing support with all IT problems and Carola Jordan as well as Ingrid Apfel for all administrative related things.

During my PhD I had the opportunity to work with many great people who contributed in one way or another to this thesis. I like to list some of them here:

Aaron A. Dutton Thank you for all the insights into galaxy formation, scaling relations and dark matter. It was a pleasure to work with you. I hope we continue our projects in the future.

Aura Obreja Thanks for providing so many code snippets and your very valuable feedback on my confusing paper drafts.

Volker Springel contributed to the coordination of the thesis goals as a member of the thesis committee and gave me the opportunity to take part in his group meetings at HITS.

Melissa Ness gave me insights into the observational part of the Astrophysics of the Milky Way.

Jakob Herpich showed me how to use pynbody and helped a lot in fixing bugs in my code.

Sven Buder is the best office mate I can imagine and the best barkeeper I know. Thanks for planning all the Königstuhl bars with me!

Office 217 This office made all my working days enjoyable. Many thanks to Sven Buder (again), Hans Baehr, Hector Hiss, Martin Schlecker, Sassa, Michael and Paolo. I will miss you!

Christina Eilers thanks for being around all the time I spent at MPIA, the last half a year was very boring without you.

Jonas Frings und Thales Gutcke Es war eine schöne Zeit mit euch in Abu Dhabi!

Die Neugassen WG Thanks for hosting me while writing my thesis! I can't imagine any better suited kitchen to write a PhD thesis! A special thanks goes to Mirjam. You made my life so much better during the final parts of my PhD! I love you!

A big thanks goes also to Johannes Esser, Asmita Bhandare, Morgan Fouesneau, Wilma Trick and Robert Grand for fun, scientific insights, suggestions and useful conversations. I further like to thank all my friends for wonderful 8 years in Heidelberg. Thanks, Simon and Marissa, Max and Lia, Philip and Franzi, Nadia, Paul and Judith, Valentin. Finally, I like to mention my friends from school, Timo, Lara, Sören and Daniel with whom I am still in contact and which I regularly meet. You are always interested in what I am doing and where I am when traveling the world. I enjoy the time with you!

I most probably for got to thank many people who contributed to my success. If you read this, I probably have to thank you. Sorry for missing you. So, thanks a lot!

This research made use of the PYNBODY package Pontzen et al. (2013) and the TANGOS tool (Pontzen and Tremmel 2018) to analyse the simulations. Thanks Andrew Pontzen for providing this software! GASOLINE2 was developed and written by Tom Quinn and James Wadsley and further developed by Ben Keller. Without their contributions, this thesis would have been impossible. I used the PYTHON package MATPLOTLIB (Hunter 2007) to display all figures in this work. Data analysis for this work made intensive use of the PYTHON library SciPy (Jones et al. 2001), in particular NumPy and IPython (Walt et al. 2011; Pérez and Granger 2007) as well as the PYTHON package ASTROPY (Astropy Collaboration et al. 2013).

Finally I like to acknowledge support from the Sonderforschungsbereich SFB 881 "The Milky Way System" (subproject A2) of the German Research Foundation (DFG). I gratefully acknowledge the Gauss Centre for Supercomputing e.V. (www.gauss-centre.eu) for funding this project by providing computing time on the GCS Supercomputer SuperMUC at Leibniz Supercomputing Centre (www.lrz.de). This research was carried out on the High Performance Computing resources at New York University Abu Dhabi; Simulations have been performed on the ISAAC cluster of the Max-Planck-Institut für Astronomie at the Rechenzentrum in Garching and the HYDRA and DRACO clusters at the Rechenzentrum in Garching. I greatly appreciate the contributions of all these computing allocations.

